

Sand-mud erosion
from a soil mechanical perspective

Proefschrift

ter verkrijging van de graad van doctor
aan de Technische Universiteit Delft,
op gezag van de Rector Magnificus prof.ir. K.C.A.M. Luyben,
voorzitter van het College voor Promoties,
in het openbaar te verdedigen op vrijdag 1 juli 2011 om 10:00 uur

door

Walter JACOBS
civiel ingenieur
geboren te Leidschendam

Dit proefschrift is goedgekeurd door de promotoren:

Prof.dr.ir. H.J. De Vriend
Prof.dr.ir. J.C. Winterwerp

Samenstelling promotiecommissie:

Rector Magnificus	voorzitter
Prof.dr.ir. H.J. De Vriend	Technische Universiteit Delft, promotor
Prof.dr.ir. J.C. Winterwerp	Technische Universiteit Delft, promotor
Prof.dr.ir. B.P. Boudreau	Dalhousie Universiteit, Halifax, Canada
Prof.dr. P.M.J. Herman	Radboud Universiteit Nijmegen
Prof.dr. M.A. Hicks	Technische Universiteit Delft
Dr.ir. P. le Hir	Ifremer, Brest, Frankrijk
Ir. W.G.M. van Kesteren	Deltares
Prof.dr.ir. M.J.F. Stive	Technische Universiteit Delft, reservelid

This research was supported by the Dutch Technology Foundation STW, the Applied Science Division of NWO and the technology program of the Ministry of Economic Affairs, under grant number DCB 6334: 'Eco-morphology of estuaries and tidal lagoons'.

ISBN 978-94-91211-65-2

Cover design by Hanneke Jacobs

Copyright © W. Jacobs, 2011

All rights reserved. No part of this publication may be reproduced or distributed in any form or by any means, or stored in a database or retrieval system, without the prior consent of the author.

Preface

The present thesis is the result of a Ph.D research project on erosion of sand-mud mixtures, which has been performed at the Hydraulic Engineering Section and the Environmental Fluid Mechanics Laboratory at Delft University of Technology. This research project was initiated as a follow-up of a previous project, performed by Mathijs van Ledden, which has been reported in the Ph.D. thesis ‘Sand-mud segregation in estuaries and tidal basins’ (Van Ledden, 2003). The former project has focussed on the numerical modelling of large-scale sand-mud behaviour in estuaries and tidal basins; the present study proceeded on one of the important recommendations of the work of Van Ledden (2003).

This research was supported by the Dutch Technology Foundation STW, the Applied Science Division of NWO and the technology program of the Ministry of Economic Affairs, under grant number DCB 6334 (‘Eco-morphology of estuaries and tidal lagoons’). Next to the current study, this research project involved another Ph.D project as well as a Postdoc project. The Ph.D project (Montserrat, 2011) involved field research on the interaction between estuarine benthic organisms and sand-mud behaviour. The Postdoc project, which was executed first by Maarten van der Vegt and later by Bram Van Prooijen, focussed on the driving forces for erosion of intertidal sediments and on the integration of the physical-biological study results in a numerical model.

This present can be divided into four parts. The first part (Chapters 1, 2 and 3) presents a literature survey on the characteristics and behaviour of sand-mud mixtures. Based on this survey, a new formulation for the erosion of sand-mud mixtures is theoretically derived. In the second part (Chapters 4, 5 and 6) laboratory results are presented on the individual parameters in the formulation as well as on small and large-scale flume tests. A discussion of the experimental results and a comparison with literature and the new formulation is presented in the third part (Chapter 7). The final part (Chapter 8) presents an experimental strategy for the collection of field data, as well as two new measuring techniques, which enable the in-situ characterization sand-mud mixtures. The conclusions drawn may prove useful for e.g. design purposes in engineering practice.

Abstract

Wetlands in tidal lagoons and estuaries form the shallow interfaces between terrestrial and aquatic ecosystems. Sustainable management of these wetlands requires both a thorough understanding and validated tools to predict their natural behaviour and development. The weakest link in our present understanding of the functioning of wetlands concerns the local dynamics of mudflats, which are characterised by multiple-scale complex interactions and feedbacks between hydrodynamics, (geo-)morphology and biology.

The multi-disciplinary STW (Netherlands Technology Foundation) project “Eco-morphology of estuaries and tidal lagoons” focuses on the dynamics of mudflats. The current thesis forms part of this research project. A soil mechanical approach is applied to study the erosion of sand-mud mixtures. In this thesis, erosion is defined as a morphodynamic process determined by the gross upward flux of sediments from the bed into the water column due to a flow exerted stress.

Current difficulties relating to the determination of a generic formulation for the erosion of sand-mud mixtures result from the lack of understanding of sand-mud behaviour. This generates confusion with respect to the characterising parameters for the mechanical and morphological behaviour of sediment mixtures. As a result, existing erosion formulations for sand-mud mixtures are generally highly empirical.

Furthermore, available techniques to simulate sand-mud erosion exhibit strongly varying forcing mechanisms, which hampers the quantitative comparison of experimental data. Finally, sediment characterisation procedures are generally highly labour-intensive, which does not comply with the increasing need for field data at high spatial and temporal resolution.

The overall objective of this thesis is, therefore, to improve the insight into the (erosion) behaviour of sand-mud mixtures. More specifically, parameters characterising mechanical and morphological behaviour of sand-mud mixtures are identified, a generic erosion formulation is derived and validated and *in-situ* sediment characterisation techniques for measuring mechanical and sedimentological parameters are developed.

Erosion properties are often linked to micro-scale sedimentological properties like clay and sand content. However, current study follows a soil mechanical approach, for which erosion is considered the soil mechanical failure of the sediment bed. Soil mechanical behaviour is described as a function of meso-scale bulk soil parameters. Examples are the packing density and plasticity, which characterize the soil structure and cohesiveness, respectively.

Sand-mud mixtures exhibit a granular skeleton when sand and/or silt particles are in mutual contact. The space between sand and silt particles is defined as the granular porosity. A cohesive clay-water matrix occurs when for sufficiently large clay contents individual sand and silt particles are prevented from settling out in suspension of clay in water. Cohesive properties are in geotechnical engineering commonly characterised

by the Atterberg limits. These limits are soil-specific water contents characterising the transitions between liquid, plastic and solid behaviour. The ratio of the plasticity index and the water content is expressed by the relative water content, which reflects the relation between pore water and water bonded by clay minerals.

An important advantage of the soil mechanical approach is that different types of sediment strength can be defined. The drained strength relates to cohesive and adhesive properties. The undrained sediment strength occurs when the typical time-scale of forcing-induced soil deformations is larger than the dissipation scale of subsequently generated pore water pressure gradients. The sediment strength varies between the drained (minimum) and undrained (maximum) strength.

A geotechnical approach is inevitable for studying the erosion behaviour of sand-mud mixtures. Different geotechnical failure mechanisms allow to distinguish between different erosion modes. Three erosion modes are distinguished: floc, surface and mass erosion. Based on this approach an erosion classification scheme and a generic erosion formulation are derived.

Floc erosion is the disruption of individual sediment flocs or part of these flocs when (relatively low) flow-induced peak stresses exceed the drained strength of unconsolidated flocs. Mass erosion is the undrained erosion of lumps of material from an over-consolidated bed when (relatively large) flow-induced stresses locally exceed the undrained bed strength.

Surface erosion is a drained process during which layers of flocs are removed. The surface erosion threshold equals the decreased bed strength upon exceedance by flow-induced stresses. The decrease in bed strength is explained as follows. Due to a turbulent flow the stress state of a soil changes, which induces small deformations of the bed and, consequently, negative pore water pressure gradients. This over-consolidated state implies that the soil strength initially equals the undrained shear strength. However, the negative gradients generate swelling (or dilation), yielding an inflow of water into the bed following Darcy's law. As a result, pore water pressure gradients dissipate and the sediment strength decreases.

The newly proposed surface erosion formulation applies this principle to relate the erosion rate to both the undrained strength and the coefficient of pore water pressure dissipation upon swelling. The latter is a function of the coefficient of volume variation and the permeability. The maximum surface erosion rate equals the downward propagation speed of the swelling front.

To limit the number of variables, this thesis focuses on artificially generated sediment mixtures. Mixtures are generated in a special experimental set-up. This allows to obtain reproducible soil samples, for which biological and physico-chemical effects can be excluded. Moreover, disturbances of the (delicate) soil structure, e.g. due to *in-situ* sample collection and/or transport to a laboratory, are avoided.

Numerous standardized geotechnical tests are executed on the artificially generated sand-mud mixtures to study the soil mechanical input parameters of the erosion formulation individually. Semi-empirical models are presented to predict the undrained shear strength and the coefficient of pore water pressure dissipation of sand-mud mixtures as a function of the relative water content and the granular

porosity. This enables the theoretical derivation of surface erosion properties following the newly proposed formulation.

Next, erosion experiments are performed to validate the new erosion scheme and formulation. Results of about 50 small-scale straight flume tests and three large-scale annular flume tests are presented. For both flume tests soil samples with varying composition, in terms of clay-silt and sand-silt ratio and clay mineralogy, are applied. Concentration profiles, erosion rates and erosion thresholds are analysed. A stochastic approach is applied to simulate the typical relation between bed shear stress and erosion rate.

Results indicate that the surface erosion rate for sand-mud mixtures may vary over orders of magnitude. This e.g. accounts for highly consolidated cohesive soils, sand-mud mixtures with a transitional structure, and loosely packed granular soils. Moreover, the erosion rate is rather sensitive to the permeability, especially for sand-mud mixtures which exhibit a transitional structure (between a granular skeleton and a clay-water matrix).

The order of magnitude of the measured erosion rates is established by substituting soil (mechanical) properties in the new surface erosion formulation. The fair agreement between simulated and observed erosion rates confirms the important role of the pore water pressure gradients as an additional bed strength, next to gravitational and/or cohesive forces. The agreement further supports the applicability of the new formulation for surface erosion of cohesive, granular and intermediate sediment mixtures. Finally, it indicates that the formulation forms an alternative for currently applied highly empirical erosion formulae.

Two new techniques are developed for *in-situ* measuring sediment properties and soil mechanical parameters. The Medusa RhoC device applies radiometric sedimentology to characterize intertidal sediments concerning the vertical distribution of the bulk density as well as depth-averaged sand and mud contents. The Hydraulic Permeability and Strength (HPS) probe records pore water pressure variations which result from the injection of small volumes of water into the sediment bed. The measurement results allow derivation of vertical profiles of the hydraulic conductivity, shear modulus and undrained shear strength.

Medusa RhoC and HPS probe data can be applied as input for the erosion formulation. Besides, both techniques are based on a proper physical background, in contrast with currently available *in-situ* techniques for characterising sediment behaviour. This enables the comparison of data obtained at different moments and/or at different locations. Furthermore, the measuring procedures are significantly faster than traditional methods. This facilitates both the large-scale mapping of the upper layer of intertidal sediment beds and the study of biological and/or morphological processes.

In conclusion, the current thesis is a step forward in the study of (the erosion of) sand-mud mixtures. It presents an extensive theoretical survey on sand-mud behaviour, which provides insights in the failure mechanisms and accompanying characterising soil parameters during the erosion of sand-mud mixtures. Additionally, the experimental results of geotechnical tests and flume experiments on artificially generated soils form a valuable data-set, as only few data on the (erosion) behaviour of

sand-mud mixtures is available in open literature.

The physically-founded surface erosion formulation significantly reduces the amount of empiricism compared to the current fully empirical formulations. This is especially important for the employment of the formulation in numerical models concerning the simulation of the behaviour of sand-mud mixtures in estuaries and tidal lagoons, on various temporal and spatial scales. The presented measuring devices may facilitate the determination of model-input parameters and the validation of the model results.

Although the current thesis studies artificially generated soils only, a similar soil mechanical approach can potentially be applied for natural intertidal sediments. This also concerns the proposed erosion formulation, which allows incorporating not only physical but also biological and chemical influences through the soil mechanical parameters. Finally, an experimental strategy is proposed for obtaining soil parameters required for the assessment of the mechanical and erosion behaviour of sediment beds.

W. Jacobs

July 2011

Samenvatting

Wetlands of draslanden in getijdenlagunes en estuaria vormen de ondiepe grensvlakken tussen terrestrische en aquatische ecosystemen. Duurzaam beheer van deze draslanden vereist zowel een grondige kennis en gevalideerde instrumenten waarmee hun natuurlijke gedrag en ontwikkeling voorspeld kan worden. De zwakste schakel in het huidige begrip van het functioneren van draslanden betreft de lokale dynamiek van inter-getijdengebieden, die gekenmerkt wordt door velerlei groot- en kleinschalige complexe interacties en terugkoppelingen tussen hydrodynamica, (geo-)morfologie en biologie.

Het multi-disciplinaire STW (Stichting voor Technische Wetenschappen) project "Eco-morfologie van estuaria en lagunes" richt zich op de dynamiek van inter-getijdengebieden. Het huidige proefschrift maakt deel uit van dit onderzoeksproject. Een grondmechanische benadering is toegepast om de erosie van zand-slib mengsels te bestuderen. In dit proefschrift is erosie gedefinieerd als een morfo-dynamisch proces bepaald door een bruto opwaartse flux van sediment van de bodem naar de waterkolom als gevolg van een waterstroom.

Momenteel bemoeilijkt een gebrek aan voldoende kennis van het gedrag van zand-slib mengsels het afleiden van een algemene formulering voor de erosie van zand-slib mengsels. Deze kennisleemte leidt tot verwarring met betrekking tot de kenmerkende parameters voor het mechanische en morfologische gedrag van sediment mengsels. Daarom hebben bestaande erosie formuleringen voor zand-slib mengsels over het algemeen een sterk empirisch karakter.

Voorts vertonen beschikbare technieken om zand-slib erosie te simuleren sterk variërende aandrijfmechanismen, die de kwantitatieve vergelijking van experimentele gegevens bemoeilijken. Ten slotte zijn procedures om sediment te karakteriseren over het algemeen zeer arbeidsintensief, wat niet aansluit op de toenemende behoefte aan veldgegevens met hoge ruimtelijke en temporele resolutie.

De algemene doelstelling van dit proefschrift is dan ook het verbeteren van het inzicht in het (erosie) gedrag van zand-slib mengsels. Dit is bewerkstelligd door parameters te identificeren die mechanische en morfologische gedrag van zand-slib mengsels bepalen, door het afleiden en valideren van een generieke erosie formulering en door het ontwikkelen van meettechnieken voor het in-situ karakteriseren van grondmechanische en sedimentologische parameters.

Erosie parameters zijn vaak gekoppeld aan micro-schaal sedimentologische eigenschappen zoals klei en zand gehalte. Echter, de huidige studie volgt een grondmechanische aanpak, waarbij erosie wordt beschouwd als het grondmechanisch falen van het sediment bed. Grondmechanisch gedrag wordt gekoppeld aan meso-schaal bulk bodemparameters. Voorbeelden hiervan zijn de pakkingsdichtheid en plasticiteit, die respectievelijk bodemstructuur en cohesiviteit karakteriseren.

Zand-slib mengsels vertonen een granulaair skelet als zand en/of silt deeltjes onderling in contact zijn. De ruimte tussen de zand en silt deeltjes wordt gedefinieerd

als de granulaire porositeit. Een cohesieve klei-water matrix treedt op wanneer voor een voldoende groot klei gehalte individuele zand en silt deeltjes niet bezinken in een suspensie van klei in water. Cohesieve eigenschappen worden in de geotechniek in het algemeen gekenmerkt door de Atterbergse grenzen. Deze grenzen zijn kenmerkende watergehaltes die de overgangen tussen vloeibaar, plastisch en vast grondgedrag bepalen. De verhouding tussen de plasticiteit index en het watergehalte wordt gereflecteerd door het relatieve watergehalte, welke de relatie tussen poriewater en water gebonden door kleimineralen weerspiegelt.

Een belangrijk voordeel van de grondmechanische aanpak is dat verschillende typen sedimentsterkte gedefinieerd kunnen worden. De gedraineerde sterkte reflecteert cohesieve en adhesieve grondeigenschappen. De ongedraineerde sediment sterkte treedt op wanneer de typische tijdschaal van geforceerde bodem vervormingen groter is dan de schaal waarop dientengevolge gegenereerde grondwater spanningsgradiënten dissiperen. De sediment sterkte varieert tussen de gedraineerde (minimum) en ongedraineerde (maximaal) sterkte.

Een geotechnische benadering is onvermijdelijk bij het bestuderen van het erosie gedrag van zand-slib mengsels. De identificatie van verschillende geotechnische faalmechanismen maakt het mogelijk om onderscheid te maken tussen verschillende typen erosie. Drie erosie typen zijn onderscheiden: flocculerende, oppervlakte en massa erosie. Op basis van deze benadering zijn zowel een classificatieschema voor verschillende typen erosie en een generieke erosie formulering afgeleid.

Vlocculerende erosie is het wegspoelen van individuele sedimentvlokken of een deel van die vlokken wanneer (relatief lage) stromingsgeïnduceerde piek schuifspanningen groter zijn dan de gedraineerde sterkte van niet-geconsolideerde vlokken. Massa erosie is de ongedraineerde erosie van brokken bodemmateriaal uit een over-geconsolideerde bodem wanneer (relatief grote) stromingsgeïnduceerde schuifspanningen lokaal groter zijn dan de ongedraineerde bodem sterkte.

Oppervlakte erosie is een gedraineerd proces waarbij laagjes van vlokken achtereenvolgens verwijderd worden. Het begin van oppervlakte erosie is gelijk aan de afgenomen bodem sterkte op het moment van overschrijden door stromingsgeïnduceerde schuifspanningen. De afname van de bodem sterkte is als volgt te verklaren. Als gevolg van een turbulente stroming verandert de spanningstoestand van een bodem waardoor kleine vervormingen van de bodem optreden en, derhalve, negatieve grondwater spanningsgradiënten gegenereerd worden. Deze over-geconsolideerde toestand betekent dat de bodem sterkte aanvankelijk gelijk is aan de ongedraineerde sterkte. Echter, de negatieve gradiënten genereren zwellen (of dilatatie), waardoor water de bodem instroomt volgens de wet van Darcy. Als gevolg daarvan nemen grondwater spanningsgradiënten af, en daardoor ook de sterkte van de bodem.

De nieuwe formulering voor oppervlakte erosie past dit principe toe door de erosie snelheid te koppelen aan zowel de ongedraineerde sterkte als de dissipatie coëfficiënt voor poriewater spanningen tijdens zwellen. De laatste parameter is een functie van de coëfficiënt van volume variatie en de permeabiliteit. De maximale oppervlakte erosie snelheid is gelijk aan de snelheid waarmee het zwellingsfront zich neerwaarts de bodem in verplaatst.

Om het aantal variabelen te beperken, richt dit proefschrift zich op kunstmatig gegenereerde sediment monsters. De monsters worden gegenereerd in een speciale experimentele opstelling. Op deze manier worden reproduceerbare bodemonsters verkregen, waarvoor biologische en fysisch-chemische effecten geen rol spelen. Bovendien worden op deze manier verstoringen van de (gevoelige) bodemstructuur, bijvoorbeeld ten gevolge van in-situ bemonstering en/of het transport naar een laboratorium, voorkomen.

Tal van gestandaardiseerde geotechnische testen zijn uitgevoerd op de kunstmatig gegenereerde zand-slib mengsels om op die manier de grond mechanische invoerparameters van de erosie formulering individueel te bestuderen. Semi-empirische modellen zijn gepresenteerd waarmee de ongedraineerde schuifsterkte en de dissipatie coëfficiënt voor spanningsgradiënten van zand-slib mengsels als functie van het relatieve watergehalte en de granulaire porositeit voorspeld kunnen worden. Op deze manier kunnen, aan de hand van de nieuwe formulering, oppervlakte erosie parameters theoretische worden afgeleid.

Vervolgens zijn erosie experimenten uitgevoerd om de nieuwe erosie classificatie en formulering te valideren. Resultaten zijn gepresenteerd van ongeveer 50 kleinschalige rechte stroomgoot experimenten en van drie grootschalige ringvormige stroomgoot proeven. Voor beide stroomgoot experimenten zijn grondmonsters met een wisselende samenstelling, wat betreft klei-silt en zand-slib verhouding en kleimineralogie, gebruikt. Concentratie profielen, erosie snelheden en het begin van erosie zijn geanalyseerd. Een stochastische benadering is toegepast om de typische relatie tussen bodemschuifspanning en erosie snelheid te simuleren.

Resultaten tonen aan dat de snelheid van oppervlakte erosie voor zand-slib mengsels kan variëren over ordes van grootte. Dit geldt bijvoorbeeld voor sterk geconsolideerde cohesieve gronden, zand-slib mengsels met een overgangsstructuur, en los gepakte granulaire bodems. Bovendien is de erosie snelheid gevoelig voor de permeabiliteit, in het bijzonder voor zand-slib mengsels met een overgangsstructuur (tussen een granulair skelet en een klei-water matrix).

De orde grootte van de gemeten erosie snelheid is gestaafd door grond(mechanische) eigenschappen te substitueren in de nieuwe formulering voor oppervlakte erosie. De goede overeenkomst tussen berekende en gemeten erosie parameters bevestigt het belang van grondwater spanningsgradiënten als een additionele bodemsterkte, naast de zwaartekracht en/of cohesiviteit. De overeenkomst ondersteunt verder de toepasbaarheid van de oppervlakte erosie formulering zowel voor sediment monsters met een cohesieve, granulaire en overgangsstructuur. Het geeft ten slotte aan dat de erosieformulering een alternatief vormt voor de momenteel toegepaste sterk-empirische erosie formules.

Twee nieuwe technieken zijn ontwikkeld waarmee sediment eigenschappen en grondmechanische parameters in-situ gemeten kunnen worden. Het Medusa RhoC apparaat past radiometrische sedimentologie toe om inter-getijde sedimenten te karakteriseren met betrekking tot de verticale dichtheidsverdeling en het dieptegemiddelde zand en slib gehalte. De Hydraulische Permeabiliteit en Sterkte (HPS) sonde meet waterspanningsvariëaties die resulteren van het injecteren van kleine hoeveelheden water in het sediment bed. Verticale profielen van de hydraulische

permeabiliteit, glijdingsmodulus en ongedraineerde schuifsterkte kunnen vervolgens worden afgeleid.

Meetgegevens van de Medusa RhoC en HPS sonde kunnen als input voor de erosie formulering worden toegepast. Daarnaast hebben beide meettechnieken een fysische achtergrond, in tegenstelling tot de momenteel beschikbare in-situ technieken voor het karakteriseren van bodemgedrag. Dit vergemakkelijkt het vergelijken van meetgegevens die op verschillende momenten en/of op verschillende locaties zijn verzameld. Bovendien zijn beide meetprocedures aanzienlijk sneller vergeleken met traditionele technieken. Dit is handig zowel voor de grootschalige kartering van de bovenste laag van inter-getijde bodems als voor de studie van biologische en/of morfologische processen.

Concluderend is dit proefschrift een stap voorwaarts in de studie van (de erosie van) zand-slib bodems. Een uitgebreide theoretische analyse van zand-slib gedrag is gepresenteerd, wat tot inzichten leidt in de faalmechanismen en de bijbehorende bepalende bodemparameters tijdens de erosie van zand-slib bodems. Bovendien vormen de experimentele resultaten van zowel de geotechnische proeven en de stroomgoot experimenten op de kunstmatig gegenereerde bodems een waardevolle data-set, aangezien slechts een beperkt aantal gegevens met betrekking tot het (erosie) gedrag van zand-slib bodems in de open literatuur beschikbaar zijn.

De fysisch afgeleide formulering voor oppervlakte erosie vermindert de mate van empirie vergeleken met de huidige empirische formuleringen. Dit is vooral van belang voor het toepassen van de formulering in numerieke modellen met betrekking tot het simuleren van het gedrag van zand-slib bodems in estuaria en lagunes, op verschillende temporele en ruimtelijke schalen. De gepresenteerde meetapparaten komen goed van pas om de invoer van deze modellen te bepalen en om de resultaten te valideren.

Hoewel dit proefschrift alleen kunstmatig gegenereerde bodems bestudeert, kan een soortgelijke grondmechanische aanpak ook worden toegepast op natuurlijke inter-getijde bodems. Dit geldt ook voor de erosie formulering, waarmee door middel van de grondmechanische parameters niet alleen het effect van fysische maar ook van biologische en chemische invloeden voorspeld kan worden. Ten slotte is een experimentele strategie voorgesteld om veldgegevens te verzamelen die vereist zijn om het grondmechanische en erosie gedrag van sediment bodems vast te stellen.

W. Jacobs

Juli 2011

Contents

Preface.....	i
Abstract.....	iii
Samenvatting.....	vii
1 Introduction.....	1
1.1 Intertidal areas in marine wetlands.....	1
1.2 Sand-mud mixtures and erosion	5
1.3 Problem definition.....	6
1.4 Objectives	7
1.5 Outline	7
2 Nature and erosion of mixed sediments.....	9
2.1 Micro-scale characteristics	9
2.2 Meso-scale characteristics	14
2.3 Macro and mega scale characteristics	20
2.4 Erosion behaviour.....	24
2.5 Conclusions.....	33
3 Erosion from a soil-mechanical perspective	35
3.1 Discussion of the critical state concept.....	35
3.2 New erosion classification	51
3.3 New surface erosion formulation	58
3.4 Conclusions.....	64
4 Material properties	65
4.1 Characteristics of artificial sediment mixtures	65
4.2 Undrained shear strength.....	70
4.3 Coefficient of volume variation	77
4.4 Permeability.....	85
4.5 Coefficient of pore water dissipation	90
4.6 Conclusions.....	91
5 Straight flume erosion experiments.....	93
5.1 Methods	93
5.2 Results and analysis	97

5.3	Discussion.....	105
5.4	Conclusions.....	116
6	Annular flume erosion experiments	119
6.1	Methods	119
6.2	Results.....	125
6.3	Discussion.....	133
6.4	Conclusions.....	138
7	Validation of new erosion approach	139
7.1	Validation of erosion classification	139
7.2	Validation of surface erosion formulation.....	150
7.3	Real world applicability.....	159
7.4	Conclusions.....	167
8	In-situ sediment measuring techniques.....	169
8.1	Medusa RhoC: in-situ sediment characterisation.....	169
8.2	Hydraulic Permeability and Strength (HPS) probe	180
8.3	Conclusions.....	193
9	Conclusions and recommendations	195
9.1	Research objectives	195
9.2	Conclusions.....	196
9.3	Strategy for assessing soil mechanical behaviour.....	199
9.4	Recommendations for further study	201
	References	203
	Appendix I: Grain size analyses	213
	Appendix II: Mineralogical analyses.....	214
	Appendix III: Results erosion tests CH 5.....	215
	Appendix IV: Soil sample properties CH 7.....	225
	List of symbols.....	231
	Acknowledgements.....	237
	Publications	239
	Curriculum Vitae	241

Chapter 1

Introduction

1.1 Intertidal areas in marine wetlands

Wetlands form the shallow interfaces between terrestrial and aquatic ecosystems. Examples of these wetlands are intertidal flats and tidal marshes in systems without (tidal lagoons) or with a fresh water input (estuaries). Examples of a tidal lagoon and an estuary in the Netherlands are shown in Figure 1 and Figure 2, respectively. Wetlands in marine wetlands are important ecosystems, as they are associated with high levels of biodiversity (Heip *et al.*, 1995). They form an area of high production by flora and fauna and, therefore, provide habitat as spawning grounds and nurseries for numerous species and host large numbers of migrating birds.

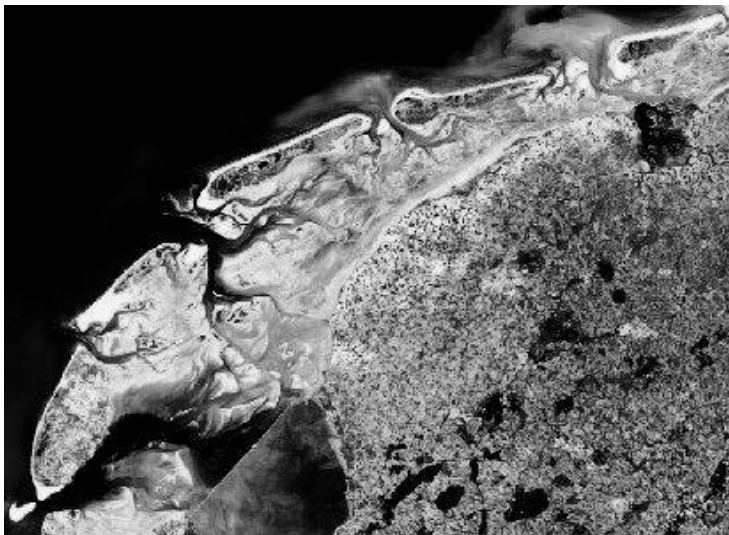


Figure 1. Satellite image of the Wadden Sea tidal lagoon in the Netherlands (horizontal scale ~120 km), showing a network of tidal channels between tidal flats behind barrier islands (www.waddensea-secretariat.org).

In spite of their importance and irreplaceable value, wetlands all over the world are under pressure and many of these systems are severely stressed. This is mainly caused by the world-wide increasing population density along coasts, which generates increasing economical (e.g. fishing, shipping), recreational and flood-protection related activities. National and international legislation and regulation to safeguard wetlands and to promote their sustainable development become therefore stricter, for instance in the form of the Ramsar Convention or the European Bird Directive.



Figure 2. Example of an intertidal sediment shore in the Western Scheldt estuary in the Netherlands. The level of the sediment bed drops from the tidal marsh with vegetation in front (flooding during spring tide only), to the unprotected sediment bed with patches of vegetation in the middle (flooding during each tidal-cycle), towards the shallow channels and foreshore in the background (permanently submersed).

Managing authorities therefore have to execute environmental impact assessments to predict and counteract c.q. mitigate the consequences of infrastructural and other management action on wetlands. Current examples in the Netherlands are compensating measures for the deepening of the Western Scheldt estuary fairway towards Antwerp, or the impact assessment of natural gas production on the long-term (ecological) development of the Wadden Sea.

Sustainable management and the design and execution of compensating measures requires a thorough understanding and validated tools for the prediction of the natural behaviour and development of these wetlands. This understanding is to be quantified in the form of algorithms, which can be implemented in numerical models describing and predicting the behaviour and development of wetlands.

The composition of the sediment bed is an important characteristic of intertidal areas. It governs sediment mobility, hence transport and deposition of sediments. The dynamics of these sediments also relate to the generation and migration of small-scale

bed-morphology, such as ripples. On the other hand, bed-features affect in their turn, subsequently, local hydrodynamics and, therefore, local water-bed exchange processes and the sediment composition.

The sediment composition in general and the sand-mud ratio in particular also govern the suitability for biological activity. The mud content is a good indicator of biological activity, as organic material mainly binds to fine graded, muddy sediments. Due to the large spatial and temporal variation of the sand-mud ratio, biological activity also exhibits strong variations, which is further enhanced by seasonal effects of sun light and/or temperature.

However, biology can also strongly influence sediment dynamics and the composition of sediments beds in intertidal areas. For example, mussels and algae mats can stabilise and trap large amounts of sediments, whereas surface deposit feeders can destabilise the bed, e.g. by grazing on micro algae (e.g. Widdows and Brinsley, 2002). Other species enhance the vertical mixing of sediments as they burrow through the sediment bed (i.e. bioturbation). Examples of both sediment stabilisation and bioturbation by biota are shown in Figure 3.

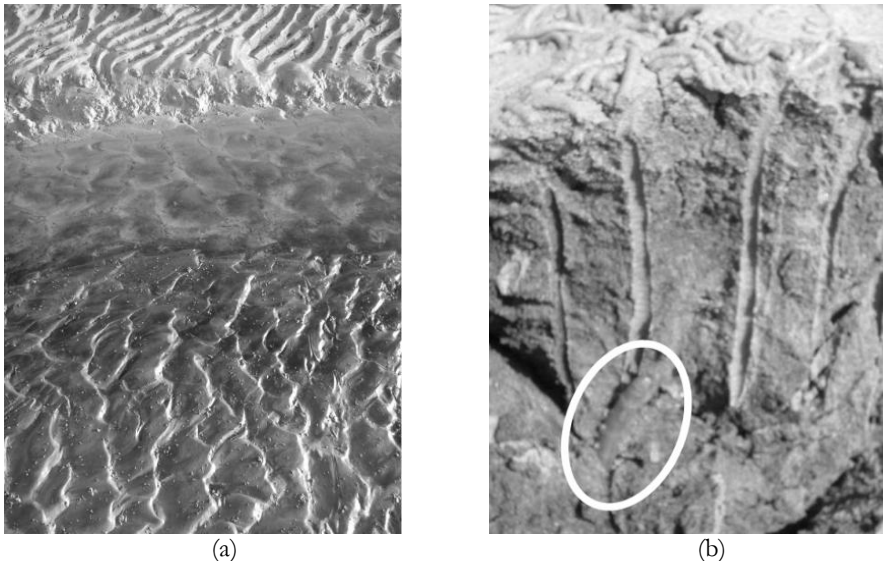


Figure 3. Examples of biota affecting sediment stability in the Western Scheldt estuary in the Netherlands. Stabilisation by algae mats (dark patches) is shown (a) along a small channel (middle of photo, horizontal scale ~ 1 m), with a muddy inner bend with algae at the bottom and a sandy outer bend at the top. The varying small-scale bed-morphological features relate to sediment composition, hydrodynamic conditions and degree of biological activity. In (b) destabilisation of the sediment bed by the burrow-digging *Arenicola Marina* (encircled) is shown. This lug worm loosens and mixes the (dark-coloured) subsoil with air and (light-coloured) surficial sediments (vertical scale ~ 10 cm).

The relations between sediment composition, on the one hand, and bed-morphology and biota, on the other, illustrate the complex interactions and feedbacks between hydrodynamics, (geo-)morphology and biology as observed in intertidal areas in estuaries and tidal lagoons. Moreover, these interactions and feedbacks are characterised by large temporal and spatial variations. De Vriend (1991) argues that the recognition of these (micro, meso, macro and mega) scales and interactions is inevitable for studying morphodynamical phenomena and processes. Small scale processes are driven by larger scale processes; but small scale non-linear processes can affect larger scale effects as well. Table 1 applies these scales to categorize some typical morphological phenomena and processes in marine wetlands, with special attention to (the erosion of) sand-mud mixtures. Interactions and feedback between different scales are indicated by the arrows.

The complicated interactions and feed-back in the functioning of wetlands hamper the prediction of natural and human-induced developments, as well as the design of required compensating measures at a sufficient level of accuracy. The weakest link in our present understanding concerns the local dynamics of mudflats. More in particular, these local dynamics concerns the relation between driving forces and erodibility, the generation and propagation of bed forms, the interaction between bed stability and micro/meso benthos (i.e. bottom-dwelling fauna) and the validation of process-based algorithms for the behaviour of sand-mud mixtures. These topics are subject of the multi-disciplinary STW (Netherlands Technology Foundation) project “Eco-morphology of estuaries and tidal lagoons”. The current study is part of this project and focuses on the erosion of sand-mud mixtures. Whereas this study concentrates on physical effects, another part of the project focuses on sediment-biota interactions and their influence on morphodynamics (Montserrat, 2011).

Table 1. Typical spatial and temporal scales for phenomena and processes in estuaries and tidal lagoons related to the erosion of intertidal sand-mud mixtures (after De Vriend, 1991).

Typical scales:	Space	Time	Phenomena	Processes
Mega	> 10 km	> 10 yr	Tidal basin, estuary, lagoon	Sediment supply, climate, tide, extreme events, geological history
Macro	100 m – 10 km	1 mnth – 10 yr	Tidal flat, channels, bed stratification	Sediment transport, currents, waves
Meso	1 cm – 100 m	1 hr - 1 mnth	Sediment structure, geotechnical bulk properties	Erosion, consolidation, biological processes
Micro	< 1 cm	< 1 hr	Granular and mineral sediment composition	Particle bonding: cohesive, adhesive

1.2 Sand-mud mixtures and erosion

Sediment beds in estuaries and tidal lagoons are often characterised by alternating muddy and sandy areas. Generally, mud is found in relatively sheltered areas (e.g. along embankments), whereas sandy beds occur in more exposed areas (e.g. channels). Sand consists of relatively coarse particles. Mud is a mixture of silt and clay particles, organic material, gas and water. Particle size is generally applied to distinguish between sediment mixtures. Figure 4 illustrates the relation between the particles size of sand, silt and clay.

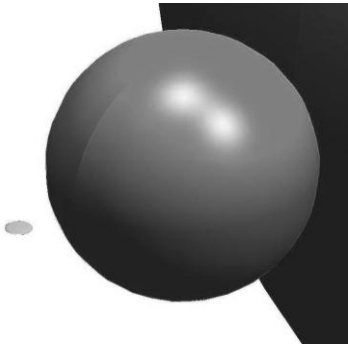


Figure 4. Schematic depiction of the large variety in size of (from left to right) a disc-shaped clay particle and a spherical silt and (part of a) sand particle. Most standards apply a size-classification defining clay as particles smaller than 2 μm , silt between 2 and 63 μm and sand as particles larger than 63 μm .

Another important characteristic of sediment mixtures is the mineralogical composition, which varies for clay particles, on the one hand, and sand and silt, on the other. The typical clay mineralogy characterises the cohesive forces between clay particles as well as the binding of water and organic material. This cohesion and binding are both strongly influenced by physico-chemical effects (e.g. salinity). As a result, mud in the natural environment always forms aggregates. These are open structures, which are much larger than the individual clay particle size (e.g. Winterwerp and Van Kesteren, 2004).

Table 1 illustrates that mega-scale system properties determine micro-scale sediment properties. This illustrates the importance of recognising large scale system characteristics to compare the (erosion) behaviour of sand-mud mixtures in different systems. An example is the relation between sedimentological properties of the catchment area on the clay mineralogy and clay-silt ratio in a marine system.

Erosion is often defined in sedimentological and morphological studies as the net downward movement of the bed level resulting from simultaneous pick-up and deposition of sediments. This implies that net erosion can be zero, although a significant water-bed exchange of sediments may occur. Also in e.g. mineralogy, hydrology and geology a similar definition for erosion is applied. An example is the (chemical, biological or physical) weathering of rocks (e.g. Mitchell, 1976).

In this thesis however, erosion is defined as the morphodynamic process of the removal (or: resuspension, pick-up) of sediments from a sediment bed due to a water-exerted force. This implies that erosion is the gross upward flux of sediments from the bed into the water column.

Furthermore, this thesis focuses on the erosion of mixtures of sand, silt and clay by means of a uni-directional turbulent flow. The scale of interest is the meso/macro scale (see Table 1). The erosion of mud containing organic matter and/or gas, the effect of various physico-chemical influences, or erosion due to cyclic loading of (wind or ship) waves is not considered. However, the study exhibits a generic character to facilitate the ‘translation’ of the results to natural sediments and conditions.

1.3 Problem definition

Currently no generic formulation for the erosion of sand-mud mixtures exists due to the general lack of understanding of sand-mud behaviour. Very few studies on the physical behaviour of sand-mud mixtures have been published in the open literature. Studies on the erosion of sand and mud mainly focus on these fractions individually, rather than on mixtures of the two, although intertidal mud almost always forms a mixture with sand.

Besides, the morphological behaviour of mud is mainly characterised by the properties of the mud-aggregates, rather than by the properties of individual particles. However, properties of the mud-aggregates are often not anticipated for in formulations describing morphological behaviour. Experimental results indicate that simply combining existing erosion formulations for sand and mud is inadequate to describe the erosion behaviour of mixtures. Besides, existing studies are often highly empirical and not based on sound physical principles.

Many more studies have been executed on the relation between biota effects and bed-stability. However, there is a lack of integration of these studies, as biota-effects are often based on single-species experimental studies. Furthermore, attention has been focussed almost exclusively on the very surface of the sediment bed. Little study has been devoted on the effects of both physical and biological effects on the properties of the subsoil, which is important when considering morphological behaviour at larger time scales (e.g. the erosion of consolidated sediment beds).

The lack of sound physical (cf. geotechnical) principles in both physically and biologically oriented studies generates confusion on the parameters characterising the mechanical and morphological behaviour of sand-mud mixtures. As a result, various interpretations of terms as bed stability, erosion threshold and sediment strength exist. The same goes for the onset for cohesive behaviour; it is still unclear how to define the transition from granular to cohesive behaviour.

Another important consequence of the ambiguity in characterising and parameterising sand-mud behaviour is the application of measurement techniques with strongly varying forcing mechanisms to study erosion. The combination of different forcing mechanisms and sediment characterisations makes it extremely difficult to quantitatively compare data obtained at different institutes in different parts of the world. Finally, sediment characterisation is generally executed by core collection and subsequent laboratory analyses. This procedure is highly labour-intensive and does not comply with the increasing need for field data of high spatial and temporal resolution.

1.4 Objectives

The general objective of this thesis is to improve insight into (the erosion of) sand-mud mixtures as found in the sediment bed of intertidal flats in marine wetlands. Three more specific objectives are formulated next.

The first objective is to clarify the parameters determining the mechanical behaviour of sand-mud mixtures, as well as those determining the transition between granular and cohesive behaviour. The second objective is to theoretically derive a generic formulation for the erosion of sand-mud mixtures under uni-directional flow conditions. The formulation should account for varying sediment composition, structure and history. Furthermore, the formulation should enable incorporation of chemical and biological effects in future studies. The final objective is to discuss the practical implications of the newly derived (erosion) approach, to demonstrate its practical applicability and to introduce new *in-situ* experimental techniques to obtain required input-parameters.

These three objectives are important steps towards a generic erosion formulation for natural sand-mud beds, enabling the incorporation of physical, biological and chemical influences. In order to limit the number of variables this thesis focuses on artificially generated sediment mixtures without biological and chemical influences.

1.5 Outline

An overview of the characteristics of mixed sediments, ranging from micro to mega temporal and spatial scales, as well as of the classifications of these mixtures is presented in Chapter 2. Additionally, this chapter presents a literature review on the state-of-the-art knowledge of the erosion behaviour of sand-mud mixtures. The theory of soil mechanical behaviour is summarized in Chapter 3. The parameters determining soil behaviour, a new erosion classification scheme and an erosion formulation for sand-mud mixtures are derived from this theory. Next, the determining soil mechanical properties are individually studied for artificially generated sediment mixtures as functions of varying sediment compositions and packing degree (Chapter 4).

Chapter 5 and 6 present experimental results of erosion tests in a small-scale straight flume and a large-scale annular flume, respectively. Results of both experimental studies are compared and discussed in view of the new erosion approach (Chapter 3) in Chapter 7. The practical applicability of the new approach is discussed in Chapter 8 by presenting two new *in-situ* techniques for soil (behaviour) characterisation. We conclude, in Chapter 9, with a summary of the major findings of this thesis and with suggestions and recommendations for further study.

Chapter 2

Nature and erosion of mixed sediments

Sand and mud in the marine environment appear in a variety of sizes, shapes and materials. In addition, they form aggregates due to inter-molecular forces. To study the morphodynamic behaviour (e.g. erosion) of mixed sediments it is important to obtain insight in the complex characteristics and driving forces at different spatial and temporal scales. Sections 2.1, 2.2 and 2.3 consider the dynamics of fines at micro (particle), meso (bulk properties) and macro/mega scale (tidal flats and marine systems). The subsequent two sections deal with studies on the erosion of sand-mud mixtures. First, the erosion of granular and cohesive soils are discussed separately (Section 2.4), followed by the erosion of mixtures and natural sediment beds, including the effect of biota. Finally, attention is paid to the erosion threshold in relation to the sediment strength. Parts of this chapter are based on Jacobs (2006).

2.1 Micro-scale characteristics

2.1.1 Granular composition

The most common way to classify sediments is by grain size, which is expressed by the particle diameter (d [m]). The sediment fractions occurring in estuaries and tidal lagoons are sand, silt and clay (Table 2). Mud is a mixture of clay and silt, but can also contain organic material, gas and water. Natural soils in marine systems often contain a mixture of different fractions. These mixtures are generally characterized by a size distribution based on percentages of weight, which are usually presented as frequency distribution curves and/or as cumulative (probability) curves (Figure 5). The frequency distribution curve has generally a normal (Gaussian) distribution. The median diameter (d_{50} [m]) in Figure 6 is the size for which 50% of a soil is finer by weight. The particle sizes d_5 [m] and d_{95} [m] represent fractions for which 5% and 95% is finer by weight, respectively.

The mean diameter (d_m [m]) differs from the median diameter, as it is the average of the frequency distribution curve. d_m is the average of the percentages of dry weight (p_i) of fractions (\bullet_i) with grain size d_i ($d_m = \sum p_i d_i$). The standard deviation (σ_d [-]) is determined by the difference between d_5 and d_{95} and is the best overall measure to

express the sorting of a soil. Another parameter to express the spreading of sediments over various size-classes is the uniformity coefficient d_{60}/d_{10} , with d_{10} [m] and d_{60} [m] as particle sizes for which 10% and 60% is finer by weight, respectively. A uniform grain size distribution (i.e. well a sorted soil) occurs for $\sigma_d < 1.35$, for which the frequency distribution is narrow and the cumulative distribution rather steep. Poorly sorted samples with a wide frequency distribution curve ($\sigma_d > 1.35$) contain a variety of sizes.

It is important to realize that a well-sorted and a poorly-sorted mixture has a different spreading of particle sizes over the various size-classes, but can have similar d_{50} . This implies that d_{50} and d_m are not always appropriate to characterise soils, whereas the combination of d_{50} or d_m with σ_d or d_{90}/d_{10} is much more suitable. This explains that in many geotechnical studies the mechanical behaviour of sediment mixtures is related to parameters reflecting the sorting of soils (e.g. Mitchell, 1976).

Table 2. Classification of dry sediments based on grain size. Both the English and Dutch names of the various fractions are denoted.

English (BS 1377)	Dutch (NEN 5104)	Min. d [μm]	Max. d [μm]
Clay	Lutum	> 0	2
Silt	Silt	2	63
Mud, fines	Modder, slib	> 0	63
Sand	Zand	63	2000

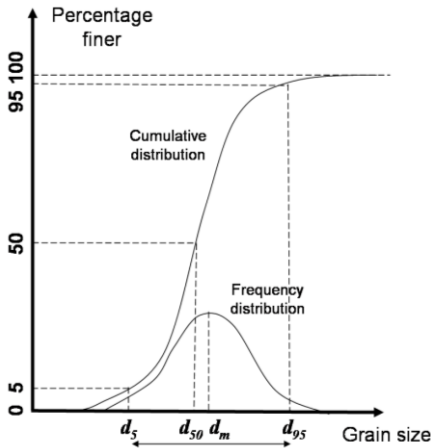


Figure 5. Cumulative and frequency distribution by percentages of weight, as a function of particle grain size.

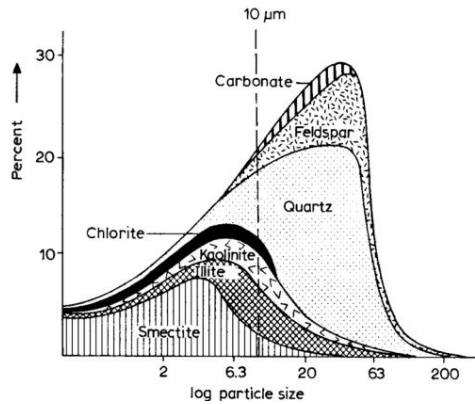


Figure 6. Example of a mineralogical fraction analysis for Mississippi alluvial mud (Weaver, 1989).

The solids content (ξ_i [%]) reflects the dry mass ($M_{dry,i}$ [kg]) of fraction \mathbf{i} to the total dry mass of a soil ($M_{dry,tot}$ [kg]):

$$\xi_i = \frac{M_{dry,i}}{M_{dry,tot}} 100\% \quad (2.1)$$

In this way the sand ξ_{sa} [%], silt ξ_{si} [%], clay ξ_{cl} [%] and mud content ξ_{mu} [%] are distinguished (Table 2). Organic matter is indicated by ξ_{om} [%] and can have various sizes. The sum of all ξ_i equals unity, which indicates that ξ_i does not reflect the relation between sediments and the total volume of a soil. This relation is further elaborated in Section 2.2.

The grain sizes defining the transition between different size classes (Table 2) are not identical in different countries. Both in the Dutch standards (NEN 5104) and in the British Standards (BS 1377) a grain size of 2 μm is applied to distinguish between clay and silt. However, the American Standards (ASTM D422) apply 5 μm at this transition.

Figure 6 shows a typical example of the result of a mineralogical analysis on an alluvial mud. Weaver (1989) argues that this example is representative for mixed sediments, as it displays the most common clay minerals found in the marine environment: kaolinite, illite, smectite and chlorite. Therefore, it is generally assumed that the mud fraction contains all clay minerals, which confirms the 63 μm limit as an appropriate discriminator between sand and mud. Furthermore, it is arbitrary to apply a specific grain size to distinguish between clay and silt, as clay minerals (e.g. kaolinite and smectite) occur for grain sizes larger than 2 - 5 μm .

2.1.2 Mineralogy and cohesive bonding

Lithogenous sediments, such as sands and clays, originate from the weathering of rocks. Biogenous sediments (organic material) are remnants of organisms and consist mainly of carbonate, opal and calcium phosphate. Finally, hydrogenous sediments are precipitates from sea water or interstitial water (Van Rijn, 1993). The genetic origin determines sediment characteristics such as shape and specific surface. Identifying the mineral composition of sediments allows to distinguish between cohesive and non-cohesive sediments, as well as between silicates and non-silicates. Silicates such as quartz, feldspar and clay minerals are lithogenous sediments which appear in a variety of shapes and structures.

Quartz and feldspar are silicates composed of three-dimensional silica tetrahedra. Clay minerals are phyllo-silicates¹, which consist of two-dimensional silica tetrahedra combined with gibbsite (i.e. aluminium oxide) or brucite octahedra (i.e. magnesium-hydroxide). The combination of six silicon tetrahedra forms a tetrahedral silica sheet and four gibbsite or four brucite octahedral, resulting in an octahedral sheet. Different combinations of tetrahedral and octahedral sheets yield different clay minerals.

The most common clay minerals in the marine environment are kaolinite, illite, montmorillonite (e.g. smectite, bentonite) and chlorite. Table 3 summarizes the

¹ 'Phyllo' is Greek for 'leaf'.

properties of these minerals (see also Mitchell, 1976; Winterwerp and Van Kesteren, 2004). The main differences between these minerals concern the structure and type of inter-molecular bonding. This is illustrated by the Scanning Electron Microscope (SEM) images in Figure 7.

Different mineral composition indicates different mechanical behaviour. For example, the specific surface area (A_s , [m²]) of a clay mineral in combination with its net layer charge determines the exposure to cations in the pore water. Interactions between clay and the physico-chemical properties of pore water generate cohesion², which is the bonding force between similar molecules.

Table 3. Important properties of the four most common clay minerals in the marine environment (Mitchell, 1976).

	Kaolinite	Smectite	Illite	Chlorite
Specific surface area [m ² ·g ⁻¹]	10-20	50-120	60-100	-
CEC [meq·(100g) ⁻¹]	3-15	80-150	10-40	10-40
Type of bonding	Hydrogen	v.d. Waals	K ions	Brucite
Bonding between sheets	Strong	Very weak	strong	Strong
Cohesiveness	Low	High	Medium	-
Plasticity	Low	High	Medium	-
Swelling	Low	High	Low	None
Activity [-]	0.4	7	0.9	-

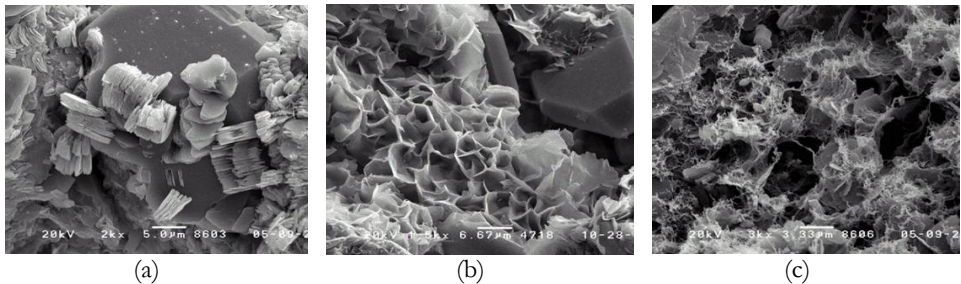


Figure 7. SEM images (www.omnilabs.com) of kaolinite (a), smectite (b) and illite (c). Their structure varies from left to right from rather regular and dense, to regular and open, and irregular and open. The presence of a silt / quartz particle ($d \approx 10 \mu\text{m}$) in (a) and (b) indicates the scale.

Negatively charged clay particles generate repulsive inter-particle forces. The ζ -potential [V] is a measure for these repulsive forces. The negative charge attracts positively charged cations in the interstitial water. However, these cations have simultaneously the tendency to diffuse away due to the lower cation-concentration in the surrounding pore water (Winterwerp and Van Kesteren, 2004). These two counteracting processes result in a cloud of cations around clay particles, which is

²The word 'Cohesion' follows from the Latin word 'cohaerere' which means 'stick' or 'stay together'.

called the diffusive double layer. Within this layer at a specific distance, the negative charge of clay particles is neutralized by cations. When the distance between two clay particles exceeds the diffusive double layer, the net force becomes attractive. This attractive force is referred to as the cohesive force.

The thickness of the double diffusive layer (i.e. the distance at which repulsive and attractive forces are equal) and the magnitude of the net attractive force depend both on the clay mineralogy and the concentration of clay particles in the surrounding fluid. An example is the *pH* [-], which is an absolute measure of the hydrogen ions concentration. In marine systems the *pH* is around 7.5 - 8. *pH* and salinity are related, which explains that an increasing salinity generates a decreasing thickness of the diffusive double layer and, consequently, larger cohesive forces.

Equilibrium exists between cations adsorbed to a particle and cations in the surrounding fluid. This equilibrium is expressed by the Sodium Adsorption Ratio (*SAR* [(meq·l⁻¹)^{0.5}]). Low *SAR* indicates a thin double diffusive layer. *SAR* is a useful parameter to quantify the effects of cations on the mechanical properties of cohesive soils (Winterwerp and Van Kesteren, 2004).

Winterwerp and Van Kesteren (2004) also refer to ‘apparent cohesion’, which has a different origin as ‘physico-chemical’ cohesion. Apparent cohesion occurs when the time-scale of loading is small compared to the time scale of the response (i.e. deformations) of a soil. This difference in time-scale generates negative pore water pressure gradients, which act as an apparent bonding force within a soil (see further Chapter 3).

2.1.3 Organic matter and adhesive bonding

Sediments in estuaries and tidal lagoons also contain non-silicates like salts, carbonates, sulphides, oxides and hydroxides. The occurrence of non-silicates depends on the local chemical conditions, such as the presence of oxygen, iron, magnesium, calcium and manganese. A comprehensive overview of biological constituents and characteristics as well as geo-microbiological processes and their effect on geotechnical properties is given by Mitchell and Santamarina (2005).

Organic matter often occurs as Extra-cellular Polymeric Substances (EPS). De Brouwer *et al.* (2002) discuss the role of EPS as a bonding agent in intertidal sediments. EPS is either imported into a system, or originates from local sources within the sediment bed or water column. The organic matter content is often characterised by the Chlorophyll-a content [$\mu\text{g}\cdot\text{g}^{-1}$]. This green pigment allows plants and algae to obtain energy by means of photosynthesis. Organic matter in the sediment bed also occurs as micro and macro-organisms. This is more elaborated in Section 2.3.3.

Organic matter (e.g. polymers) in mud appears as particulate or dissolved matter, which may be neutral or charged. Contrary to charged organic matter, neutral organic matter or poly-saccharides play an important role in the natural environment due to their ability to adhere to clay particles (Winterwerp and Van Kesteren, 2004). An example of polymeric bonding between particles is shown in Figure 8.

The adhesive force between particles depends on the type of EPS and the number of polymeric bonds. This number depends on the specific surface area of clay particles

A_s [$\text{m}^2 \cdot \text{g}^{-1}$], which relates to the clay mineralogy (see Table 3). It is important to realize that adhesion is the physical attraction between different substances or molecules, in contrast with cohesion, which is the physical-chemical attraction of similar molecules. Adhesion, together with cohesion, has a significant effect on the dynamics of fine sediments in the marine environment.



Figure 8. SEM image showing adhesive bonding of glass beads by polymeric strings (Paterson, 1997). The average size of the beads is around $50 \mu\text{m}$.

2.2 Meso-scale characteristics

2.2.1 Geotechnical bulk properties

This section presents an overview of geotechnical bulk parameters, which relate to soil-mechanical and morphological behaviour of sediment beds. Flemming and Delafontaine (2000) show that in studies relating sediment properties and sediment dynamics, often confusion arises concerning the distinction between mass contents and volume fractions. They argue that ‘concentration’ is frequently confused with the term ‘content’.

The distinction between ‘concentration’ and ‘content’ is especially important in case of cohesive sediments. For a sandy sediment bed, all particles have identical specific density ($\sim 2650 \text{ kg} \cdot \text{m}^{-3}$). This implies that the volume concentration of one particle in relation to the total volume is equal to its mass content in relation to the total mass. However, cohesive sediments form flocs, which have a significantly lower specific density than their primary particles. This implies that the volume concentration of flocs is much larger than its mass content.

The relation between the volume of solids and the total soil volume is defined as:

$$\phi_{sed} = 1 - n \quad (2.2)$$

where ϕ_{sed} [-] is the volume concentration of sediment and n [-] is the porosity:

$$n = \frac{V_{por}}{V_{tot}} \quad (2.3)$$

V_{por} [m³] is the volume of pores and V_{tot} [m³] is the total volume of a sample. The void ratio e [-] is closely related to the porosity:

$$e = \frac{V_{por}}{V_{sed}} = \frac{n}{1-n} \quad (2.4)$$

where V_{sed} [m³] is the volume occupied by solids. The volume concentrations for sand, silt, clay and mud are given by ϕ_{sa} [-], ϕ_{si} [-], ϕ_{cl} [-] and ϕ_{mu} [-], respectively:

$$\phi_{sed} = \phi_{sa} + \phi_{si} + \phi_{cl} = \phi_{sa} + \phi_{mu} \quad (2.5)$$

The relation between solids mass and total soil mass is given by the bulk density:

$$\rho_{bulk} = S n \rho_w + S(1-n)\rho_{sed} \quad (2.6)$$

where S [-] is the degree of saturation to gas, ρ_{sed} the specific density of sediment (~2650 kg·m⁻³) and ρ_w the density of water (1000 kg·m⁻³ for fresh water and ~1030 kg·m⁻³ for sea water). In the current study it is assumed that $S = 1$. The dry density is defined as:

$$\rho_{dry} = \rho_{sed}(1-n) = \phi_{sed}\rho_{sed} \quad (2.7)$$

Another way to characterise the mass concentration of solids in relation to the total mass is the water content [%]:

$$W = \frac{M_w}{M_{sed}} 100\% = \frac{\rho_w}{\rho_{sed}} \frac{1}{1-n} 100\% \quad (2.8)$$

where M_w [kg] is the mass of water and M_{sed} [kg] the mass of dry sediment. It should be noted that W can be larger than 100%. Furthermore, it is important to distinguish between water in the pores (free water) and water bonded by the clay minerals (bonded water). The latter depends on the clay mineralogy.

In Section 2.1.1 the solids content ξ_i is discussed. It reflects the dry mass of fraction i in relation to the total dry mass of solids. The solids fraction ψ_i [%] is the volume-equivalent of ξ_i . It is defined as the volume of a fraction i in relation to the total volume of solids in a sample. The sum of all solids fractions equals unity. In case all fractions have similar specific densities, ξ_i and ψ_i are equal, in which case:

$$\psi_i = \frac{\phi_i}{\phi_{sed}} 100\% \quad (2.9)$$

The geotechnical bulk parameters discussed so far concern the packing of a soil. However, for fines cohesive properties are also important. In geotechnical engineering these properties are commonly characterised by the consistency limits or Atterberg Limits (Skempton, 1965). These limits represent water contents defining the transition from liquid to plastic behaviour (Liquid Limit: LL [%]), and from plastic to solid behaviour (Plastic Limit: PL [%]). The difference between LL and PL is the Plasticity Index (PI [%]):

$$PI = LL - PL \quad (2.10)$$

Figure 9 illustrates the definition of the Atterberg Limits. The remoulded (undrained shear) strength of sediments at the *LL* is generally around 1 kPa, and around 100 kPa at the *PL*.

PI is the difference in water content between *LL* and *PL* for which a sediment mixture exhibits plastic behaviour. It depends on the clay content, the clay mineralogy and the chemical properties of the pore water. *PI* is also defined as:

$$PI = A(\xi_{cl} - \xi_{cl,0}) \quad (2.11)$$

where *A* [-] is the activity of a soil and $\xi_{cl,0}$ [%] the offset for cohesive behaviour. *A* characterises the water-binding property of a soil which can vary considerably (0 - 10) as a function of clay mineralogy, pore water characteristics and polymeric bonding. Van Paassen (2002) shows that *A* increases with increasing pore water salinity. Samples are generally considered cohesive when *PI* > 7%. Numerous empirical relations between *PI* and soil behaviour (e.g. permeability, strength, etc) occur in geotechnical engineering studies.

The Liquidity Index *LI* [-] combines packing with cohesive properties:

$$LI = \frac{W-PL}{PI} \quad (2.12)$$

LI is generally applied for consolidated soils with $PL < W < LL$, resulting in $0 < LI < 1$. However, natural sand-mud mixtures in marine systems often exhibit $W > LL$, which requires extrapolating *LI* to values of two or more. Winterwerp and Van Kesteren (2004) argue that this extrapolation may lead to inaccuracies, e.g. when relating *LI* to the undrained shear strength.

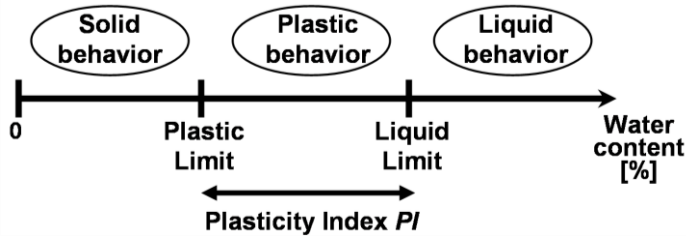


Figure 9. The Atterberg Limits reflect the transitions in water content for which the behaviour of a soil changes from solid to plastic (*PL*) and from plastic to liquid (*LL*). The difference between these water contents is the plasticity index *PI*.

Alternatively, the activity or swelling potential of clays can be derived from specific surface area measurements using methylene blue (see e.g. Verhoef, 1992; Santamarina, 2002). The hydrated form of this chemical compound is blue coloured. Methylene blue adsorbs to clay minerals by replacing the cations in the diffusive double layer. Unadsorbed methylene blue forms a blue halo around a soil sample on a filter paper. The maximum amount of adsorbed methylene blue is a measure for the specific surface area. Although this method is indirect, it is quicker compared to the determination of the Atterberg Limits and only a few grams of material are required.

2.2.2 Network structures in mixed sediments

The structure of soils is important for their mechanical behaviour. This structure depends on the volume concentration of solids in combination with cohesive properties. A granular skeleton occurs when sand and/or silt particles are in mutual contact, which forms a relatively stiff skeleton due to constrained particle movements. Figure 10 illustrates four possible packing densities of a granular skeleton. Particles can be cemented (I), which may occur during the formation of sedimentary rock. Cementation due to deposition of dissolved matter (e.g. carbonates, see Mitchell, 1976) is beyond the scope of the current study. When grains are in mutual contact, they form either a densely packed (II), or a loosely packed (III) skeleton. Quick sand occurs when sand and silt grains do not form a skeleton (IV).

In case sand and/or silt particles are not in mutual contact, and when the pore water not only contains water but also clay, a clay-water matrix may occur (Figure 10 (V)). Such a matrix only occurs at a (cohesive) strength, which is large enough to keep sand and silt particles in suspension.

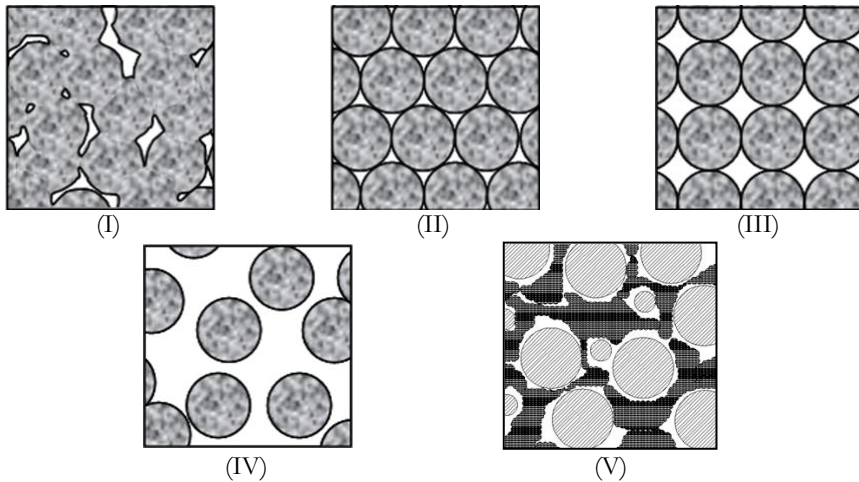


Figure 10. Schematized packing densities for mixtures of sand and silt. Below the minimum granular porosity particles are cemented (I), which occurs e.g. for sedimentary rock. A densely (II) or a loosely (III) packed skeleton may occur when sand and/or silt grains are in mutual contact. When sand and/or silt grains are not in contact (IV), quicksand or a clay-water matrix (V) might occur, depending on the occurrence of clay.

The porosity of a soil with spherical, uniform grains varies between 25% and 48%. The maximum porosity of a granular skeleton ($n_{sasi,max}$ [%]) occurs for the loosest packing of a granular skeleton (Winterwerp and Van Kesteren, 2004). Van Kesteren (1996) takes a first step to depict not only the solids contents (mass), but also the effect of these contents on the structure (volume) in a ternary diagram (Figure 11, see also van Ledden *et al.*, 2004). These diagrams are commonly used to illustrate mass contents and to classify soils by dividing these triangles into sub-zones. Flemming (2000) applies

ternary diagrams to classify sediments of a wide range of marine systems around the world.

The limit for the occurrence of a sand skeleton applied by Van Ledden *et al.* (2004) follows from Merckelbach (2000), with a sand network structure for $\phi_{sa} > 40$ -50%. The limits for a sand and silt skeleton shown in Figure 11 depend on the packing density and the sand and silt content, respectively. For the remainder of the triangle, a clay-water matrix occurs. The transition from cohesive to non-cohesive behaviour is represented by the horizontal line in Figure 11, for which $\zeta_{cl} = \zeta_{cl,0}$. Van Ledden *et al.* (2004) subdivide the triangle into six zones (see the Roman numerals (see also Table 4) to distinguish between different modes of sand-mud behaviour. Furthermore, a specific relation exists between ζ_{cl} and ζ_{si} for each marine system. This clay-silt ratio limits the possible modes occurring in a specific marine system.

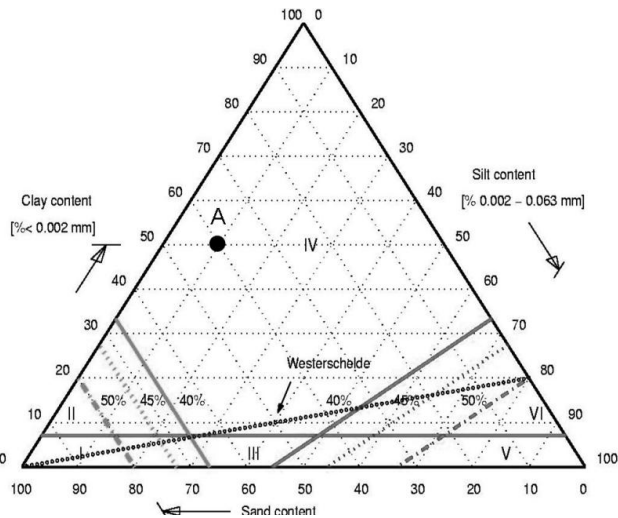


Figure 11. Classification of sediment mixtures in a ternary diagram (Van Ledden *et al.*, 2004). The horizontal axes represent ζ_{sa} , the left diagonal axes ζ_{cl} and the right diagonal axes ζ_{si} . For point 'A' $\zeta_{sa} = 40\%$, $\zeta_{cl} = 50\%$ and $\zeta_{si} = 10\%$. The percentages next to the diagonal lines in the left and right lower corners of the triangle indicate the water contents for which sand and silt-dominated structures occur. The horizontal line represents the transition between cohesive and non-cohesive behaviour. The dotted diagonal line depicts a constant clay-silt ratio, in this case for Western Scheldt sediments.

Table 4. Different bed types for sand-mud mixtures according the diagram in Figure 11.

Number	Cohesion	Skeleton
I	No	Sand
II	Yes	Sand
III	No	Mixed
IV	Yes	Clay
V	No	Silt
VI	Yes	Silt

The granular porosity n_{sasi} [-] is defined as the space between sand and silt particles, which is for a saturated soil occupied by water and clay particles:

$$n_{sasi} = n + \psi_{cl}(1 - n) \quad (2.13)$$

where ψ_{cl} equals ζ_{cl} for identical specific density of all fractions. Eq. (2.13) shows that the transition between cohesive and granular behaviour not only depends on the clay content, but also on the porosity. The importance of the network structure for this transition is indicated by Van Ledden (2003), who gives an overview of the threshold for cohesive behaviour in relation to $\zeta_{cl,0}$ ($\zeta_{cl,0} \approx 5 - 15\%$).

Sand and silt influence each other's skeleton, which is only partly incorporated by Van Ledden *et al.* (2004). The solids fractions at which these skeletons become affected by the other fraction are around 15% for sand and 30% for silt. For $\psi_{sa} > 15\%$ and/or $\psi_{si} > 30\%$, $n_{sasi,max}$ follows from (Winterwerp and Van Kesteren, 2004):

$$n_{sasi,max} = \frac{n_{si,max}(100 - (100 - n_{si,max})\psi_{sa}) - \psi_{cl}}{100 - \psi_{cl}} \quad \text{for } 0\% < \psi_{sa} < 86\% \quad (2.14)$$

$$n_{sasi,max} = n_{sa,max} - (100 - n_{sa,max})(100 - \psi_{sa}) \quad \text{for } 86\% < \psi_{sa} < 100\% \quad (2.15)$$

where $n_{si,max}$ [%] and $n_{sa,max}$ [%] are the maximum porosity for a purely silty or purely sandy soil. By replacing the maximum porosities in Eq. (2.14) and (2.15) with the minimum porosities $n_{si,min}$ [%] and $n_{sa,min}$ [%], it is possible to determine the minimum granular porosity $n_{sasi,min}$ [%] in a similar way.

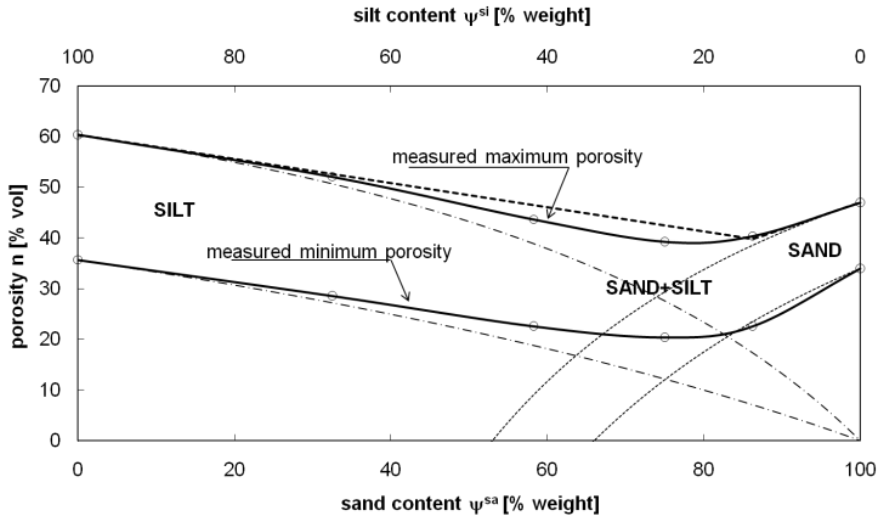


Figure 12. Minimum and maximum granular porosity as a function of the volume fraction of sand (Winterwerp and Van Kesteren, 2004), based on Eq. (2.14) and (2.15).

Figure 12 shows the separate maximum and minimum porosity of sand and silt for mixtures of sand and silt, as well as the combined maximum and minimum granular porosities (n_{sasi} [-]). The porosities $n_{sasi,min}$ and $n_{sasi,max}$ subdivide the figure into three different regimes, which relate to the schematized plots of Figure 10. Samples for which $n_{sasi} < n_{sasi,min}$ refer to sedimentary rock as shown in Figure 10 (I), which is beyond the scope of the current study. For $n_{sasi,min} < n_{sasi} < n_{sasi,max}$ sand and/or silt grains form a granular skeleton (II or III). For $n_{sasi} > n_{sasi,max}$ (IV) grains are not in mutual contact and a clay-water matrix may occur (see also Figure 10 (V)). It is argued that a soil can only exhibit cohesive properties when $n_{sasi} > n_{sasi,max}$. The plasticity (i.e. cohesive strength) of a clay-water matrix depends on ζ_{cl} and A , as shown by Eq. (2.11).

2.3 Macro and mega scale characteristics

2.3.1 Driving forces

Sections 2.3.2 - 2.3.4 discuss dynamics and characteristics of mixed sediments relevant to the water-bed exchange on a macro and mega scale, both in time and space. The climatological conditions mainly determine the presence and character of mixed sediments. These conditions are for example important for the local and non-local hydrodynamic forcing conditions, the frequency and character of extreme events, the effect of climate changes, the amount of sunlight (biological activity), the temperature and precipitation rate, tidal forcing and the marine and/or fluvial sediment supply rate.

The geological history of the substratum of a tidal basin and its catchment area is also important. This history especially concerns the mineralogy of fines and the degree of consolidation of old deposited layers. The relation between macro/mega-scale driving forces and sediment dynamics in tidal basins are extensively discussed in sedimentological studies, for example by Reading (1986) and Perillo (1995).

2.3.2 Stratification of the sediment bed

Segregation of sand and mud occurs at a variety of spatial and temporal scales. Van Ledden (2003) studies sand-mud segregation in Dutch estuaries with a numerical model. Vertically stratified mixed beds are often the result of different depositional characters of sand and mud. Sand deposition is often in-phase with the flow velocity gradient, whereas the deposition of fines often exhibits a time lag resulting from the longer settling times of fines. This explains the occurrence of successive layers of sand and mud. E.g. Van den Berg (1981) discusses the seasonal layering of mixed sediments in the Eastern Scheldt Estuary in the Netherlands. De Boer (1979) discusses convolute lamination in purely granular beds, which results from air entrapment during the rapid inundation during flood.

Sediment beds in intertidal areas also exhibit a strong chemical stratification, which is important as chemical properties have a significant effect on cohesive and adhesive properties (the presence and type of biota depends on chemical properties,

see Section 2.1.3). The salinity (which affects *pH*) of the interstitial water influences the cohesiveness (Van Paassen, 2002), which explains the effect of precipitation on the stability of intertidal flats (Tolhurst *et al.*, 2006).

Within the sediment bed, numerous processes influence the stratification of mixed sediments. The main processes are consolidation and swelling (see Chapter 3 and 4) and reworking/mixing of the bed by physical (e.g. waves) and/or biological processes. These processes are shortly discussed next.

2.3.3 Biological processes

Biological processes significantly influence the dynamics of fine sediments on intertidal flats (Black and Paterson, 1997; Whitehouse *et al.*, 2000 and Widdows *et al.*, 2000). The current study focuses on the stability of (intertidal) sediment beds of marine systems in North-Western Europe. Generally, these areas do not contain much vegetation, but exhibit various meso/macro scale biological processes. These processes and their interaction with bulk properties are shortly discussed.

Biological activity induces stabilization, destabilization, mixing and/or alternation of the bed roughness. These effects appear in various combinations and exhibit complicated interactions with both biological and physical processes. Further, biological activity varies at multiple temporal (seasonal, diurnal, tidal) and spatial (salinity gradient, height with respect to MSL) scales. Murray *et al.* (2002), Widdows and Brinsley (2002) and Le Hir *et al.* (2007a) give a thorough overview of studies on the relation between biology and the stability of intertidal sediment beds.

Mussel and oyster beds reduce wave action and flow velocities and trap sediments as they filter fines from the water column (Van Duren *et al.*, 2006). Filtered fines are deposited as faecal pellets (Prins *et al.*, 1996), which change the grain size distribution and exhibit different mechanical behaviour compared to individual fines. Bioturbation or reworking of the sediment bed (e.g. by *Heteromastus filiformis* or *Arenicola marina*) results in vertical transport of particles, as well as in the re-oxygenisation of anaerobic sediments (e.g. Gillet and Gorman, 2002). Both processes have a significant effect on the physical, chemical and biological properties of the sediment bed, which determine bulk soil properties.

The most common stabilizers are benthic diatoms (microphytobenthos), which mainly occur on muddy sediments (Orvain *et al.*, 2003). Diatoms produce EPS which causes adhesion between particles and, therefore, enhances the stability of the bed (Paterson, 1997; Yallop, 2000; Lucas *et al.*, 2003). De Boer (1981), Montserrat *et al.* (2008) and Montserrat (2011) nicely illustrate the stabilizing effect of diatoms. They defaunate part of an intertidal flat which nicely shows the relation between morphology and biota. Montserrat *et al.* (2008) and Montserrat (2011) show that after defaunation, the Chlorophyll-a content initially increased due to the absence of diatom-grazers. Examples are the mud snail (*Macoma Baltica*, e.g. Widdows *et al.*, 1998) and the mud shrimp *Hydrobia ulvae* (Orvain, 2003, 2006). Subsequently, the population of grazers increased due to the availability of food (i.e. diatoms). Finally, the increased number of grazers reduced the population of diatoms to numbers comparable to the

control plots. A similar phenomenon occurs at a seasonal scale, as the population of diatoms strongly relates to the availability of sunlight.

Many studies (e.g. Austen *et al.*, 1999) address the variety of biological effects and occurring complex interactions. Some effects can even be counteracting. This is illustrated by the effect of the ragworm (*Nereis Diversicolor*), which exhibits stabilizing as well as destabilizing effects (e.g. Banta *et al.* 1999; Fernandes *et al.*, 2006). These complex and sometimes counteracting interactions, as well as the fact that most studies consider a single species on a single temporal and/or spatial scale only, often result in site-specific and non-generic relations between sediment properties and biota.

2.3.4 Sedimentological interactions

Sedimentological interactions exist when comparing the composition of sediment samples collected at various locations along the length (on a mega scale) of a specific tidal system. Flemming (2000) shows that more or less constant clay-silt ratios exist in different marine systems. This ratio is 3 (3 times more silt than clay) for the Dyfi Estuary in Wales, around 1 for the Danish Wadden Sea and 0.2-0.25 for Dutch estuaries and tidal inlets.

A probable explanation (Van Kesteren, 2006) for the occurrence of this ratio follows from the settling behaviour of fines. Clay and silt particles are deposited simultaneously, as they occur in aggregates or flocs (Winterwerp and Van Kesteren, 2004). The entrapment of silt in these flocs depends on their adhesive and cohesive bonding properties, which depend on clay mineralogy, the amount of organic material and the prevailing hydrodynamic and chemical conditions. This implies that specific conditions in an estuary generate flocs with a specific relation between clay and silt. However, it is questionable to what extent larger silt particles are entrapped, or settle individually. This implies that segregation between clay and silt might occur and that the assumption of a constant ratio is less applicable for mud which contains relatively large silt particles.

The second interaction occurs between ξ_{cl} and ξ_{om} . As discussed in Section 2.1.3, polymers adhere to the surface of clay particles, which explains the importance of A_s . This parameter depends on the clay mineralogy in a specific marine system, which suggests a constant relation between ξ_{cl} and ξ_{om} . This is confirmed by Hedges and Keil (1995) and Middelburg and Herman (2007).

Finally, relations exist between mud content and bulk density. The cohesive properties of the clay fraction determine the binding capacities of mud and thus the volume fraction of flocs in a soil. This indicates a unique relation between ξ_{mu} and ρ_{bulk} , as for each marine system unique relations exist between ξ_{cl} and ξ_{si} , as well as between ξ_{cl} and A . Next, it is possible to derive the sediment composition and density of an *in-situ* sample, given the clay-silt ratio and A , from its sand content alone. This is confirmed by Flemming and Delafontaine (2000) for different marine systems. They argue that this relation reflects the local environmental conditions.

2.3.5 Western Scheldt sediments

Field experiments in the framework of the current study were executed at tidal flats in the Western Scheldt Estuary (51.04° - 51.81° N; 3.23° - 4.39° E) in the Netherlands (Figure 13). This tide-dominated and well-mixed estuary is the downstream part of the River Scheldt and has a length of 350 km. Sediments in the Western Scheldt Estuary have either a marine or fluvial origin (Verlaan, 1998). The poorly sorted sand fraction exhibits decreasing d_{50} from 175 μm at the seaward side to 125 μm near Antwerp close to the Dutch-Belgian border. The average sand content decreases over the same stretch from around 80% to 40%. Spatial segregation occurs between different morphological elements (Van Eck, 1999), with coarser sediments in the channels and finer sediments on the intertidal flats along the banks of the estuary. Flats in the middle of the estuary exhibit a mixture of these fractions.

The composition of Western Scheldt sediments is discussed by the clay-silt ratio in Figure 11 and by Table 4. Figure 13 and Table 5 show the clay mineralogy at four locations (Fontaine (2004)). It is shown that Western Scheldt clay deposits contain a mixture of smectite and illite, with smaller amounts of kaolinite and chlorite. The illite mainly results from erosion of ‘Boonse klei’ within the estuary. The relatively high smectite content results from erosion of ‘Ieperse klei’ in the Strait of Dover, after which these clay particles are transported into the Western Scheldt by tidal action.

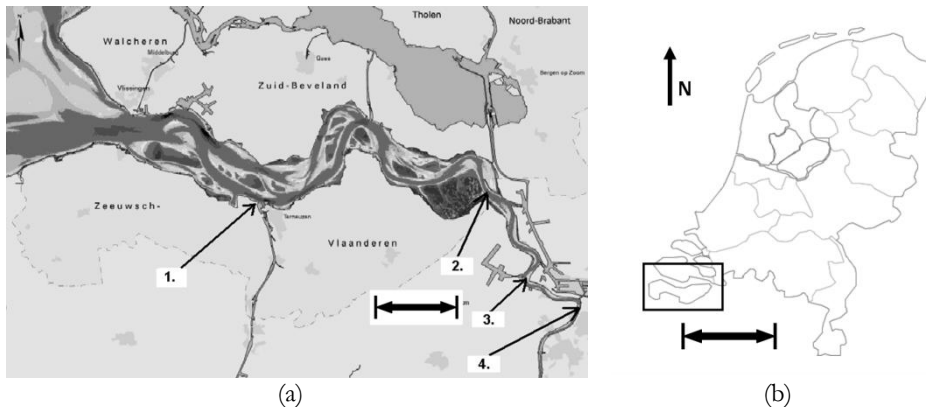


Figure 13. Western Scheldt Estuary (a) with the numbers indicating the sampling locations shown in Table 5 (Van Eck, 1999). The Estuary is indicated on the map of the Netherlands (b). The arrows in the left and right panel refer to 10 and 100 km, respectively.

Table 5. Mineralogy of the clay fraction in the Western Scheldt Estuary, after Fontaine (2004). The sample locations refer to the numbers indicated in Figure 13(a).

Sample location	Kaolinite [%]	Illite [%]	Smectite [%]	Chlorite [%]
1.	8	15	77	some
2.	17	44	39	none
3.	31	49	20	none
4.	31	51	18	some

2.4 Erosion behaviour

The current study defines erosion as the morphodynamic process of the removal of sediment grains and/or aggregates (i.e. flocs or lumps of material) from a sediment bed due to a waterflow-induced force. Erosion properties involve an erosion threshold (τ_e [Pa]) and an erosion rate or flux (E [$\text{kg}\cdot\text{m}^{-2}\cdot\text{s}^{-1}$]). The first concerns the bed shear stress (τ_b [Pa]), at which particles start to erode. The second parameter is the amount of material which is removed from a specific surface area per unit of time.

This section gives an overview of studies on the erosion of sand-mud mixtures. First, erosion modes and bed forms are discussed, followed by erosion formulae obtained from various laboratory and field studies. Laboratory studies mostly consider artificially generated granular, cohesive and/or mixed sediment beds. Field studies often relate the erosion of natural sediments to the combined effect of physical, biological and chemical influences. Furthermore, different field and laboratory techniques to measure τ_e and E are discussed. Also the definitions of the bed shear stress, the erosion threshold and the strength of the bed are considered.

2.4.1 Erosion modes and bed forms

Different erosion modes and bed forms occur for mixed sediments. The distinction between erosion modes is based on the individual or the combined removal of particles from the bed. Subsequently, material is transported as suspended load and/or as bed load. Transport by suspended load is generally related to fines, and bed load to coarser material. Bed load transport often occurs by means of migrating bed forms, which occur as more or less regular patterns on the surface of the bed. Both longitudinal (parallel to the flow direction, e.g. ribbons and ridges) and transverse (perpendicular to the flow direction, e.g. ripples and dunes) bed forms occur. Van Rijn (1993) gives an overview of bed forms in granular beds, whereas Flood (1983) and Dyer (1986) discuss bed forms in cohesive beds.

Van Rijn (1993) argues that longitudinal grooves and ridges with a typical spacing of 0.01 to 1 m, as well as meandering grooves and flute marks or spoon-shaped depressions with a more random character exist. These features are generated at large velocities. Also mini-ripples occur for cohesive sediments. These exhibit a typical length-scale of around 0.1 m and a height of around 5 mm, and are observed at velocities of around $0.3 \text{ m}\cdot\text{s}^{-1}$ and bed shear stresses of 0.2 Pa.

Torfs (1995) observed bed forms in non-cohesive sand-mud mixtures. Fine particles were washed out from the upper part of the sediment bed for $\tau_b > \tau_e$. For larger τ_b ripples occur, which indicate bed load transport. At increasing ζ_{mu} this behaviour changed completely: the bed exhibited an undulating appearance for moderate flow conditions. The sediment composition of these undulations after the tests was homogeneous in relation to the initial composition, which indicates the simultaneous erosion of sand and mud. For denser mixtures lumps of material were randomly removed from the bed, with a sudden start of the erosion.

A variety of bed forms and related erosion modes occur for mixed sediments. Sometimes it appears difficult to distinguish between erosion modes and bed forms,

for example in case of flute marks. Some refer to these features as bed forms, whereas others define them as erosion features. Winterwerp and Van Kesteren (2004) give an overview of erosion modes for cohesive sediments. This classification distinguishes between floc erosion (stochastic process during which individual flocs are disrupted), surface erosion (continuous and uniform process) and mass erosion (random disruption of relatively large aggregates). The occurrence and character of these modes depend on the relation between the bed shear stress and the strength of the bed (Figure 27). This classification is more fundamentally discussed in Chapter 3.

2.4.2 Granular beds

Formulations for the erosion of granular beds are generally derived from the force balance on individual particles. Stabilising forces are either gravity-induced, or result from phenomena like hiding, inter-locking or armouring. Three important types of flow-induced destabilising forces exist. The first is a vertical lift due to lower pressure above particles as a result of the contraction of streamlines. The second and third are horizontal drag forces resulting from particle roughness and from a region of low pressure behind particles.

Shields (1936) experimentally derived a stability criterion (Figure 14) for mono-disperse sand ($d_{50} > 100 \mu\text{m}$), with the destabilising forces reflected by the Reynolds particle number ($Re_* [-]$), and the stabilising force by the Shields parameter ($\theta_{cr} [-]$):

$$\theta_{cr} = \frac{|\tau_e|}{(\rho_{bulk} - \rho_w)gd_{50}} \quad (2.16)$$

$$Re_* = \frac{u_* d}{\nu_w} = \frac{\rho_w u_* d}{\eta_w} \quad (2.17)$$

where g [$\text{m}\cdot\text{s}^{-2}$] is the gravitational acceleration, u_* [$\text{m}\cdot\text{s}^{-1}$] ($=\sqrt{\tau_b/\rho_w}$) the friction velocity, ν_w [$\text{m}^2\cdot\text{s}^{-1}$] the kinematic viscosity of water, τ_e [Pa] the bed shear stress for the initiation of motion and η_w [$\text{kg}\cdot\text{m}^{-1}\cdot\text{s}^{-1}$] the dynamic viscosity of water.

It is important to realize that the Shields criterion only applies to well-sorted and relatively coarse, non-cohesive sand. This implies that phenomena like hiding and exposure (e.g. Egiazaroff, 1965) and the filling of voids by smaller particles as encountered for multiple-sized sediments, are not taken into account.

In literature it is recognized that the Shields criterion does not apply to fine sands. Van Rijn (1993) gives an overview of various experimental studies dealing with the erosion of fine sands. These studies show that fine sand beds may exhibit cohesive-like behaviour for $d_{50} < 40 \mu\text{m}$. This follows from observed erosion of aggregates which disintegrate downstream. This is probably due to apparent cohesion (Section 2.1.2). Roberts *et al.* (1998) are one of the few to relate packing density to τ_e . They studied the erosion behaviour of granular mixtures containing a variety of particle sizes. Decreasing particle size generated a decreasing erosion threshold and increasing erosion rate for $d_{50} > 100 \mu\text{m}$. For $d_{50} < 100 \mu\text{m}$, the threshold increased and the erosion rate decreased for decreasing d_{50} , with typical values of τ_e between 0.05 and 1.3 Pa (for $\rho_{bulk} \approx 1850 \text{ kg}\cdot\text{m}^{-3}$).

Mono-disperse granular beds generally erode continuously and uniformly for $\tau_b > \tau_e$. The erosion rate of mono-disperse granular sediments is often described by a pick-up function, e.g. by Fernandez-Luque (1974):

$$E = \alpha \rho_{sed} (\Delta g d)^{0.5} (\theta - \theta_{cr})^{1.5} \quad (2.18)$$

where α [-] is an empirical coefficient, Δ [-] the specific density of sediments, $\theta = u_*^2 / (\Delta g d)$ and $\theta_{cr} = u_{*,cr}^2 / (\Delta g d_{50})$. Not many studies define the erosion rate of granular beds containing multiple-sized fractions. Van Rijn (1993) distinguishes between a single-fraction and a multi-fraction method to determine transport rates. The latter method incorporates sorting effects by considering complete size distributions.

It is concluded from the results of Roberts *et al.* (1998) that to understand the erosion of granular sediments it is insufficient to solely consider force balances. Besides frictional and gravitational forces, packing density and apparent cohesion are also important. This is illustrated by the occurrence of the erosion of large aggregates from the fine-grained bed of the Yellow River, China (Van Maren *et al.*, 2009). In conclusion, formulations for both τ_e and E for granular sediments are highly empirical. Only the initiation of motion for mono-disperse sands is based on a physical consideration (force balance).

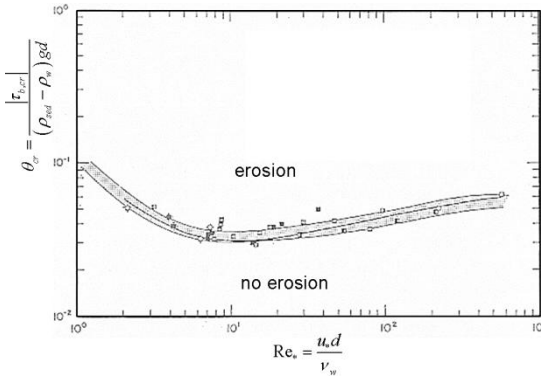


Figure 14. Shields stability criterion for mono-disperse granular sediments, with the stabilising force as a function of the destabilising force (Shields, 1936).

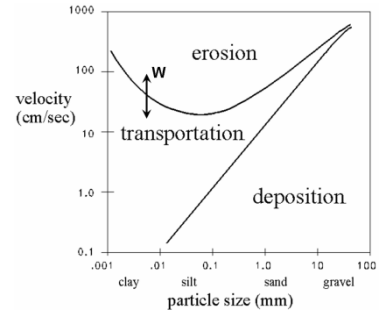


Figure 15. Hjulstrom stability criterion. The arrow indicates the effect of varying water content W (Dyer, 1986).

2.4.3 Cohesive beds

The stabilising force for cohesive beds (i.e. beds with a dominant clay-water matrix) results from gravity, packing density and cohesive and adhesive bonding forces. Clay mineralogy, chemical composition of the pore water and presence of organic matter can be more important than particle size and bed density. The large variety of physical, chemical and biological properties (see Sections 2.1, 2.2 and 2.3), explains the empirical character of existing erosion formulae for cohesive sediments.

Van Rijn (1993), Whitehouse *et al.* (2000) and Winterwerp and van Kesteren (2004) list most studies on the erosion of cohesive sediments. This section summarizes the most important studies.

A number of studies attempt to derive a Shields-type stability criterion for cohesive sediments. An example is the Hjulstrom curve (Dyer, 1986), as shown in Figure 15. This criterion is fairly descriptive, as it only incorporates the effect of varying W , but not the effect of clay mineralogy and/or network structure. Therefore, Dyer (1986) discourages the use of these criteria to describe and classify the stability of cohesive sediments.

Righetti and Lucarelli (2007) give an overview of previous studies on τ_e for cohesive sediments. Most studies relate τ_e to properties similar to ρ_{bulk} and d_{50} . Others acknowledge the importance of internal structure, consolidation and stress history. For example Panagiotopoulos *et al.* (1997) and Torfs (1995) focus on the changing erosion behaviour due to the transition from cohesive to non-cohesive behaviour. They explain this transition by the decreased internal friction angle of sediment grains for $\xi_{mu} > 30\%$. Torfs (1995) defines a ‘transitional regime’ for $\xi_{cl} = 7 - 13\%$. Partheniades (1962, 1965) found that erosion occurs at all mean $\tau_b > 0$. This indicates that τ_e equals or approaches zero. Also other studies argue that it is difficult to determine the ‘true’ initiation of movement for cohesive beds, as flocs are eroded for $\tau_b > 0$.

Most studies present empirical formulations, which do not give insight into determining bed properties for erosion. Van Rijn (1993) gives an overview of these studies. Typical values for τ_e range between 0.1 and 5 Pa. Le Hir *et al.* (2007a) argue that τ_e is around 0.1 - 1 Pa for consolidating mud, and 1 - 10 Pa for consolidated mud. Only Smerdon and Beasley (1959) relate τ_e to the plasticity of the bed (although for dense mixtures only):

$$\tau_e = 0.163 \cdot PI^{0.84} \quad (2.19)$$

This formulation acknowledges the importance of cohesive and adhesive properties.

The surface erosion rate for cohesive sediments generally yields:

$$E = f(\tau_b - \tau_e, \varphi_1, \varphi_2, \varphi_3, \dots) \quad (2.20)$$

The excess bed shear stress ($\tau_b - \tau_e$) reflects the destabilising force, and the bed properties φ_i the stabilising bed properties. Partheniades (1962, 1965) and Ariathurai (1974) combined these properties in the erosion parameter M [$\text{kg}\cdot\text{m}^{-2}\cdot\text{s}^{-1}$], which leads to the well-known Ariathurai-Partheniades formulation for the erosion of cohesive sediments:

$$E = M \left(\frac{\tau_b - \tau_e}{\tau_e} \right), \text{ for } \tau_b > \tau_e \quad (2.21)$$

with M typically varying between $0.01 \cdot 10^{-3}$ and $0.50 \cdot 10^{-3} \text{ kg}\cdot\text{m}^{-2}\cdot\text{s}^{-1}$. These values follow from numerous studies (see for an overview Winterwerp and Van Kesteren, 2004) on the erosion of artificially generated and natural soils. The variability of M follows e.g. from the temporal and spatial variation of the cohesive properties of the bed. Because of its simplicity, the Ariathurai-Partheniades equation is commonly used.

Eq. (2.21) applies to well-consolidated ($\rho_{bulk} \approx 1400 - 1800 \text{ kg}\cdot\text{m}^{-3}$), homogeneously mixed sediment beds. This implies that τ_e and M can be assumed constant over the upper few mm's of the sediment bed. For increasing depth, τ_e and M are not constant due to differences in density as a result of consolidation. Freshly-deposited beds exhibit strong vertical gradients in bed strength and erosion resistance in the upper mm's of the bed due to ongoing consolidation. Therefore, Mehta and Partheniades (1979) proposed an alternative formulation for floc erosion:

$$E = M_f \exp \left\{ \alpha_1 \left(\frac{\tau_b - \tau_e(z)}{\tau_e(z)} \right)^{\alpha_2} \right\} \quad (2.22)$$

with the floc erosion parameter M_f typically between $0.003 \cdot 10^{-3} - 5 \cdot 10^{-3} \text{ kg}\cdot\text{m}^{-2}\cdot\text{s}^{-1}$, α_1 (5 - 15 [-]) and α_2 (0.5 - 1 [-]) are empirical parameters and $\tau_e(z)$ typically 0.01 - 0.1 Pa.

Parchure and Mehta (1985) discuss the erosion of stratified and uniform sediment beds in an annular flume. They argue that stratified, freshly deposited sediments generally represent the upper portion of the active sediment layer (concerning water-bed exchange processes) in the marine environment. The lower layer is more uniform due to the higher degree of consolidation and the effect of biological (bioturbation) and physical (waves) mixing processes. Parchure and Mehta (1985) model a stratified and a uniform bed in the laboratory. Concentration profiles typically occurring for stratified (Figure 16(a)) and uniform beds (Figure 16(b)) are linked to vertical density profiles (see Figure 16(c) and (d)).

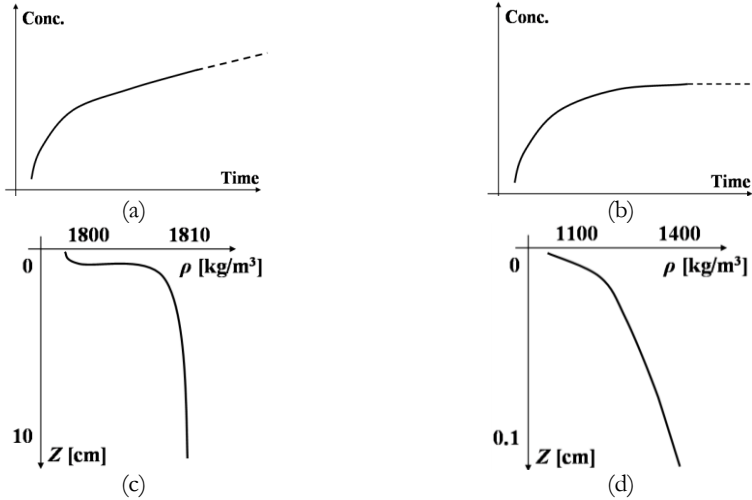


Figure 16. Typical concentration profiles as a function of depth (Z [m]) as observed for unlimited erosion (a) and depth-limited erosion (b), which represent Type I and Type II erosion, respectively. According to Parchure and Mehta (1985), these profiles relate to uniform compacted beds with vertical density profiles (c) and to freshly deposited soft sediments in a stratified bed (d). The concentration becomes constant (b) when the with depth increasing erosion threshold equals the applied bed shear stress. Note the different horizontal and vertical scales.

Erosion properties of cohesive sediment beds are generally derived from the concentration in time, which results from the net effect of erosion and deposition:

$$h \frac{\partial c}{\partial t} = E - D \quad (2.23)$$

where D [$\text{kg}\cdot\text{m}^{-2}\cdot\text{s}^{-1}$] is the deposition rate, c [$\text{g}\cdot\text{l}^{-1}$] the depth-averaged suspended sediment concentration, h [m] the water depth and t [s] time.

The initial parts of the concentration profiles in Figure 16(a) and (b) are similar. In this initial phase it is assumed that $E \gg D$, where D can either be small or zero. The decrease of $\partial c / \partial t$ in the next phase is either generated by an increasing τ_e ($\tau_e \rightarrow \tau_b$) with depth, or by an increasing deposition rate. The latter implies that after an increase of τ_b , the settling of particles requires some time (due to flocculation) to adjust to the new level of turbulence, resulting in a time lag between E and D . The second parts of the concentration profiles shown in Figure 16(a) and (b) are not similar. Parchure and Mehta (1985) define Type I erosion as depth-limited erosion ($\partial c / \partial t = E - D = 0$) and Type II erosion as unlimited erosion ($\partial c / \partial t > 0$ and thus $E - D > 0$).

Parchure and Mehta (1985) argue that deposition was not important during their experiments. They relate the occurrence of Type I erosion to an increasing bed strength for increasing depth. The varying strength results from consolidation and/or associated physico-chemical changes, or from segregation during deposition, which results in laminae with varying τ_e . They also suggest that both τ_b and τ_e should be considered as stochastic variables (i.e. the sum of a mean value and a turbulent fluctuation: $\tau_i = \bar{\tau}_i + \hat{\tau}_i$).

Most studies on the occurrence of Type I and II erosion neglect deposition. Mehta and Partheniades (1979) show experimental results for erosion tests on stratified and uniform (kaolinite) beds in an annular flume. The erosion rate for stratified beds tends to zero due to a increase of τ_e with depth. The time at which the concentration reached 90% of the asymptotic concentration was around 4 hours. Results for homogeneously mixed beds show that the erosion rate became constant ($E > 0$) after periods up to 48 hours. Similar results are found in a straight flume by Partheniades (1962, 1965), who applied natural mud instead of inorganic kaolinite. Both a stratified bed containing loose flocs ($W = 110\%$) and a consolidated bed at field moisture content were applied. The strength of the stratified bed varied significantly over the upper 5 cm, whereas the strength of the consolidated bed exhibited small variations over the upper 1.5 cm.

Amos *et al.* (1992) were the first to identify Type I and II erosion in the field using an *in-situ* annular flume. Amos *et al.* (1992) distinguish between Type Ia and Type Ib erosion. The first is characterised by an erosion rate asymptotically decreasing with time. Type Ia is a surface phenomenon associated with the erosion of unconsolidated, small (~ 0.1 mm) organic pellets and was observed for areas with significant benthic activity. Erosion stopped when all pellets were eroded. Type Ib erosion also exhibits an asymptotically decreasing erosion rate with time. But in this case relatively large and irregular aggregates (> 7 mm) erode, which subsequently fall apart during bed load transport. Amos *et al.* (1992) argue that Type Ib is constrained due to self-armouring of the bed in time.

2.4.4 Mixed beds

Sand and mud have a combined effect on the plasticity and network structure of mixed beds (see Sections 2.1 and 2.2). This implies that it is not sufficient to simply combine the erosion formulations for granular and cohesive beds in order to determine an erosion formulation for sediment mixtures. This section summarizes laboratory and field studies on the erosion of sediment mixtures. First the transition between cohesive and non-cohesive behaviour, as applied in these studies, is discussed.

Although non-cohesive sand-mud mixtures do not exhibit cohesive properties, their erosion behaviour is significantly influenced by even small amounts of mud. In general, the erosion threshold increases and the erosion rate decreases with increasing mud content. However, most erosion studies do not define a clear transition between cohesive and non-cohesive soils. Van Ledden (2003) gives an overview of critical mud ($\xi_{mu,0}$ [%]) and critical clay contents as applied by various authors: $\xi_{cl,0} = 5 - 10\%$ (Dyer, 1986; Raudkivi, 1990); $\xi_{cl,0} = 5 - 15\%$ (Alvarez-Hernandez, 1990); $\xi_{mu,0} = 3 - 15\%$ (Mitchener and Torfs, 1996); $\xi_{mu,0} = 20 - 30\%$ and $\xi_{cl,0} = 5 - 7\%$ (Houwing, 2000); $\xi_{mu,0} = 4\%$ for kaolinite-mud and $\xi_{cl,0} = 3 - 4\%$, and $\xi_{mu,0} = 13\%$ for montmorillonite-mud and $\xi_{cl,0} = 3 - 5\%$ clay (Torfs, 1995).

As most studies consider mass contents rather than volume fractions, a large variation occurs for $\xi_{cl,0}$ and $\xi_{mu,0}$. Volume fractions are much more appropriate when considering the structure of soils, as discussed in Section 2.2 and illustrated by Figure 12. Furthermore, the volume fraction of mud depends on the amount of water bonded to clay particles, which relates to the plasticity, see Eq. (2.11). The transition between cohesive and non-cohesive mixtures depends on the volume fraction of mud. This explains that this transition should not only be related to the (dry) mass content of mud, but also to its plasticity.

Van Rijn (1993), Van Ledden (2003) and Winterwerp and Van Kesteren (2004) give an overview of studies on the erosion of mixed sediments. Most of these studies apply empirical relations between τ_e , on the one hand, and ρ_{bulk} , ξ_{cl} or ξ_{mu} , on the other. E is generally defined by applying the Ariathurai-Partheniades equation shown in Eq. (2.21), with the erosion parameter M as an empirical lump parameter which combines physical, chemical and biological influences.

Van Ledden (2003) proposes formulations for the erosion of (mixtures of) sand and mud, both for the non-cohesive and cohesive regime. The transport of sand and mud is not related in the non-cohesive regime, as it is assumed that particles are individually eroded. This assumption is affirmed by Torfs (1995), who observes fines being washed out from a non-cohesive bed, as well as ripples indicating bed load transport. The erosion rate of sand is based on the pick-up function of Van Rijn (1993). M for both sand and fines is related to ρ_{sed} , d_{50} and v_w . Heuristic formulations are proposed for cohesive mixtures, with a coupling between sand and mud. Sand is passively eroded in cohesive aggregates and sand and mud exhibit erosion rates proportional to their mass contents. The erosion parameter for this regime is based on the Ariathurai-Partheniades approach.

Van Ledden (2003) also proposes formulations for τ_e for cohesive and non-cohesive beds, based on experimental results of Torfs (1995). In these formulations τ_e

for sand is modified for the presence of mud. The erosion threshold increases, decreases or remains constant for increasing ζ_{mu} . This agrees with experimental results, as for increasing ζ_{mu} , τ_e either increases due to more cohesion (e.g. Torfs, 1995; Panagiotopoulos *et al.*, 1997; Houwing, 2000) or decreases due to decreasing bed density (e.g. Williamson and Ockenden 1993). A variety of other explanations occurs for the behaviour of τ_e due to the addition of mud. For example, Mitchener and Torfs (1996) suggest that τ_e decreases due to a smoother bed, whereas Panagiotopoulos *et al.* (1997) argue that τ_e increases due to a decreasing angle of repose between grains.

There are two main advantages to the approach of Van Ledden (2003). The first is that it provides one set of formulations for the full range of sediment mixtures (from granular to cohesive), which is convenient for e.g. numerical model simulations. The second is that the transition between cohesive and non-cohesive behaviour is physically founded (See Section 2.2.2). However, the formulations for both τ_e and E are still highly empirical, as they lack a proper theoretical background.

There is no conceptual framework to combine, classify and quantify the effects of biological, chemical and physical processes on the parameters determining the erosion of mixed sediments. Therefore, erosion formulations are highly empirical and not generic. However, Winterwerp and Van Kesteren (2004) consider erosion as a geotechnical failure mechanism of the sediment bed, with permeability as one of the determining material parameters. They propose a new erosion formulation for mixed sediments, covering the range from non-cohesive to cohesive beds. In potential, this formulation offers the conceptual framework as discussed.

Also Sanford and Maa (2001) suggest the importance of the permeability for the stability of sediment beds. They argue that the time-scale of the eroding forces in relation to the time-scale of erosion determines whether erosion is unlimited (type I) or depth-limited (type II). This qualitatively acknowledges the distinction between cohesion and apparent cohesion. Also Mastbergen and Van den Berg (2003) emphasize the importance of permeability. They argue that shear dilatancy (i.e. deformations due to a shearing force) of a sediment bed generates negative pore water pressure gradients. The rate at which these pressures dissipate relates to the permeability. The new erosion formulation of Winterwerp and Van Kesteren (2004) is further elaborated in Chapter 3.

2.4.5 Natural beds

Sections 2.1.2, 2.1.3 and 2.3.3 show that physico-chemical and biological effects significantly influence bulk soil parameters as cohesion and adhesion, and, therefore, erosion. A number of studies exist on the effect of physico-chemical parameters on erosion, which are systematically discussed by Kandiah (1974) and Ariathurai and Arulanandan (1978). They show that increasing *SAR*, *pH* and temperature generate an increasing thickness of the diffusive double layer and, therefore, decreasing cohesiveness and increasing erodibility. Contrary to this, increasing salinity generates decreasing erodibility.

The effect of biota on cohesive sediment dynamics in the intertidal zone is significant. However, difficulties arise concerning the up-scaling of biological effects

for morphodynamic macro or mega scale studies, as only limited causal relationships exist. Le Hir *et al.* (2007a) discuss that although many studies agree on the importance of biota on sediment stability, sediment transport studies rarely account for these effects. They attribute this paradox to the difficulty of both simultaneously coupling physical and biological processes and the occurring ‘biodiversity’ (many species, strong heterogeneity, opposite effects on sediment stability). Widdows and Brinsley (2002) argue that interactions between biotic and abiotic factors and their combined influence on the behaviour of inter-tidal sediments are complex and poorly characterized.

First attempts to incorporate biological effects in large-scale and long-term numerical model simulations were taken by Wood and Widdows (2002, 2003), Knaapen *et al.* (2003) and Paarlberg *et al.* (2005). The latter two studies apply the morphodynamic model proposed by Van Ledden (2003). All three studies incorporate biological activity by means of empirical formulations for τ_e and M .

Next to the non-generic character of relations between the effect of biota and bed stability, other problems also arise. Often only τ_e is determined, whereas the effect of biota on M is also important, as both τ_e and M determine E . The latter is for example important when τ_b exceeds τ_e of a biofilm, and the subsoil starts to erode.

However, the main problem concerning the parameterization of biological effects appears to be the identification of the appropriate material parameters in relation to erosion. This is affirmed by Defew *et al.* (2002), who study the stabilisation (by biota) of intertidal flats in different systems. Sediment beds are compared concerning water content, microphytobenthic biomass and nature of the sediment bed. They acknowledge the difficulty in finding a universal proxy parameter for bed stability. This is attributed to the complex and contradicting relations between sediment stability and varying biological and physical factors. They conclude that the current challenge is to bridge the gap between the understanding of small and large scale properties and processes, in order to produce system-wide relations.

Orvain *et al.* (2007) consider stabilisation effects of diatoms. They illustrate the need for a multi-disciplinary approach, as contradictory relations are found for the relation between bed stability and chlorophyll-a content and/or carbohydrate fractions (e.g. EPS). Therefore, they argue that these are not relevant parameters to predict the erodibility of mudflats in the south-west of France. It is concluded that microphytobenthic development is not necessarily the primary cause of sediment stabilisation, as other parameters like clay content and density also play a role.

To find appropriate material parameters, the combined effect of physical, biological and chemical influences on the stability of the sediment bed should be considered. However, studies on natural inter-tidal sediments are rarely multidisciplinary; often only one of these influences is considered at a time, whereas other influences are not, or only partially, considered.

2.4.6 Erosion threshold and sediment strength

Various (laboratory and *in-situ*) experimental set-ups exist to study erosion behaviour. However, Black and Paterson (1997), Tolhurst *et al.* (2000a,b), Watts *et al.* (2003), Jonsson *et al.* (2006) and Widdows *et al.* (2007) show that erosion

characteristics obtained with different devices often do not correlate. Two main reasons occur for these poor correlations. The first is the variation between the different devices concerning the nature of the hydrodynamic forcing applied to the bed. Straight, annular and racetrack flumes induce horizontal flows, whereas e.g. the CSM (Cohesive Strength Meter) applies a vertical jet.

The second reason concerns the various definitions for bed strength and erosion threshold. Sometimes different types of τ_e are defined. For example, Widdows *et al.* (2007) suggest that there are possibly two τ_e : one for deposited flocs and one for aggregates of the bed. Others identify separate erosion thresholds for mass erosion and biofilms. The identification of multiple τ_e for particular sediment beds also originates from the confusion concerning the occurrence of varying definitions for the bed strength. Generally, differences between adhesion, cohesion and apparent cohesion are not recognized. This explains that although bed strength and τ_e often correlate, they can differ by orders of magnitude.

This large variation is illustrated by experimental results for the erosion threshold for cohesive sediments. For shear flows $\tau_e \approx 0.1 - 10$ Pa (Le Hir *et al.*, 2007a), whereas τ_e determined with a CSM is generally in the range of kPa's (e.g. Tolhurst *et al.*, 1999). Also other studies argue that markedly higher τ_e are found for devices which impose a vertical jet instead of a horizontal flow. Partheniades (1971) suggests that vertical jets do not indicate sediment erodibility, but reflect an aspect of sediment strength. This is confirmed by Watts *et al.* (2003), who find a correlation between data obtained by a CSM and a fall cone penetrometer (Hansbo, 1957). The latter device is similar to the Swedish fall cone used to determine *LL*.

Also Bassoullet and Le Hir (2007) find much larger values for τ_e of intertidal sediments than expected, by applying a handheld torvane. The bed strength measured by the fall cone, as well as by the vane, is in both studies referred to as the undrained shear strength. The fall cone, the torvane as well as the CSM typically find strengths in the range of kPa's. This indicates that the CSM device measures the undrained shear strength rather than τ_e . Chapter 3 further elaborates the different definitions for τ_e and bed strength.

2.5 Conclusions

Sand-mud mixtures on intertidal flats exhibit many different appearances and properties. Additionally, both the driving forces and the dynamics of sediment mixtures occur at a variety of different temporal and spatial scales, which are also mutually related. This indicates that a multiple-scale approach is required to understand morphodynamic processes like erosion. Mineralogy classifies sediment on a micro-scale. Cohesion and adhesion occur at a similar scale, and are both influenced by pore water characteristics. Apparent cohesion originates from different time-scales of the hydrodynamic forcing and the response of the bed.

On a meso-scale sediment volume fractions are more appropriate than mass contents when considering bulk properties in relation to the structure of soils. For sand-mud mixtures a sand-silt skeleton or a clay-water matrix might occur, characterised by the granular porosity and plasticity index, respectively. The transition between these structures is considered as the onset of cohesive behaviour. Macro and mega-scale characteristics of intertidal sand-mud mixtures reveal the vertical and horizontal stratification of physical, biological and physico-chemical properties. This indicates the importance of complex parameters like stress history, anisotropy and mode of occurrence for intertidal sediment dynamics.

As a result of these multiple-scale processes, it seems almost impossible to generate a conceptual framework in which parameters determining the stability of sediment beds can be combined, classified and quantified. However, relations occur between the clay content on the one hand, and the silt content, organic matter content and bulk density on the other. These relations depend on specific mixtures of minerals as found in (parts of) marine systems and are convenient as they significantly limit the amount of parameters required to quantify and characterise mixed sediments. Known relations between the sand and mud content are sufficient to determine silt content, clay content, organic matter content, bulk density and plasticity index.

The consideration of erosion formulations for granular and cohesive sediment beds provides insight into the parameters determining joint erosion of both types of sediments. As sand and mud have a combined effect on these parameters, it is not sufficient to combine existing formulations for granular and cohesive beds in order to derive a formulation for sediment mixtures. One of the difficulties to obtain a combined formulation is the lack of a general definition for the transition between cohesive and non-cohesive behaviour, which is often related to the clay or mud content only. This results in a variety of empirical relations between material parameters and the erosion threshold and erosion parameter.

Erosion studies on natural intertidal sediments provide relations which exhibit an even stronger empirical and sometimes contradicting character. Furthermore, confusion arises concerning the definitions of the bed strength and the erosion threshold. This leads to the conclusion that erosion studies on natural intertidal sediments can only be qualitatively compared at present. In general, it appears that there is a lack of understanding concerning the mechanisms in the sediment bed preceding and during erosion. The recognition of these mechanisms and accompanying material parameters is required to (1) relate micro-scale properties and processes to mechanical behaviour, to (2) obtain more generic erosion formulations, and to (3) distinguish between different erosion modes.

The current study focuses on these three items. The aim is to generate a conceptual framework which enables the combination, classification and quantification of the effects of biological, chemical and physical processes on the parameters determining the erosion of mixed sediments. A geotechnical approach is applied to relate meso scale-characteristics to the mechanical behaviour of soils. In this way micro-scale characteristics are lumped in bulk soil properties, which enables relating soil behaviour to soil structure. A new erosion formulation is theoretically derived and tested for artificially generated sediment mixtures.

Chapter 3

Erosion from a soil-mechanical perspective

To advance our understanding of the mechanisms of the sediment bed preceding and during erosion of mixed sediment beds, a soil mechanical approach is followed. The first part of this chapter (Section 3.1) discusses the Critical State Model (CSM) of Schofield and Wroth (1968). This is a well-known model in geotechnical engineering, which applies independently measurable material parameters to characterise the yielding/failure behaviour of consolidated granular and cohesive soils. The discussion of the CSM forms a framework for idealised soil behaviour, which is applied for both the new erosion approach and on the results of geotechnical tests as presented in this thesis. The second part of this chapter examines on the new erosion approach proposed by Winterwerp and van Kesteren (2004). The enhanced insight into the theoretical background of bed strength and failure modes following from the discussion of the CSM is the basis for both a classification scheme for erosion modes (Section 3.2) and for a formulation for surface erosion (Section 3.3). It is assumed that surface erosion plays a dominant role in estuaries and similar systems.

3.1 Discussion of the critical state concept

3.1.1 General description of the CSM

The critical state concept of Schofield and Wroth (1968) describes how and when yielding of a soil occurs. The discussion of this model forms a framework for idealised soil behaviour, which is applied in the current thesis to illustrate saturated soil behaviour upon and during erosion. There are multiple conceptual approaches to model soil behaviour. As for all models, the CSM is an idealisation of observed soil behaviour. The model relates the characteristics of a two-phase mixture (sediment and water) to mechanical behaviour. The state of a soil indicates a specific relationship of packing and applied forcing. In the Critical State Model the packing of soils is characterised by the specific volume v [-], which is the total volume divided by the volume of solids.

However, v is a relatively unknown parameter in hydraulic engineering. Therefore, in the current thesis v is replaced by the void ratio e [-], which is the volume of voids

divided by the volume of solids. The current thesis further applies the porosity n [-], which is the volume of voids divided by the total volume. The relation between v , e and n is shown in Table 6. The replacement of v by e in the visualisation and accompanying relations of the Critical State model is justified by the linear relation between the two parameters. Table 6 shows the relation between v and e and other (soil mechanical) parameters characterizing packing (see also Section 2.2.1).

The principal effective stresses ($\sigma_{1,2,3}$ [Pa]) reflect in the current thesis the stresses on a volume of soil in the x - y - z space. For consolidated sediment beds lateral stresses are assumed equal ($\sigma_2 = \sigma_3$), so that stresses on a soil can be regarded in a two-dimensional plane. This is shown in the Mohr diagram in Figure 17, which illustrates the mathematical relation between the principal stresses σ_1 and σ_3 , and the effective shear (τ [Pa]) and normal stress (σ [Pa]). The failure envelope for these stresses yields:

$$\tau = c + \sigma \tan \phi \quad (3.1)$$

where ϕ [-] is the internal friction angle and c [Pa] the bed strength for zero normal stress. This bed strength is an effective stress, which equals the total stress (σ_{tot} [Pa]) minus the pore water pressure p_w [Pa]:

$$\sigma = \sigma_{tot} - p_w \quad (3.2)$$

In this thesis tension stresses on a sediment bed are positive and compressive stresses negative, which is the opposite of what is generally applied in geotechnical engineering.

Table 6. Relations between geotechnical parameters which characterize soil packing density.

	ϕ_s	n	e	v
ϕ_s	-	$1 - n$	$1/(1 + e)$	$1/v$
n	$1 - \phi_s$	-	$e/(1 + e)$	$(v - 1)/v$
e	$(1 - \phi_s)\phi_s$	$n/(1 - n)$	-	$v - 1$
v	$1/\phi_s$	$1/(1 - n)$	$1 + e$	-

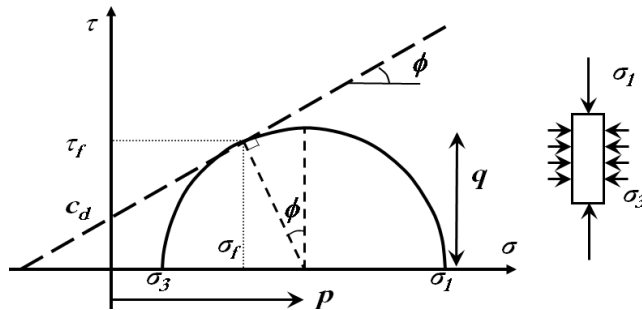


Figure 17. Mohr diagram showing the relation between the principal stresses (σ_1 and σ_3), and the effective shear (τ) and normal stress (σ). The dashed diagonal line is the drained Mohr-Coulomb failure envelope, with τ_f and σ_f as the shear and normal stress upon failure. The isotropic (p) and deviatoric (q) stresses are shown. The right panel shows the principal stresses on a soil typical for consolidated sediment beds.

For drained conditions, ϕ equals the maximum friction angle ϕ_{max} and c the drained bed strength c_d [Pa]. Typical values for ϕ_{max} yield $30^\circ - 45^\circ$ for sand; $27.5^\circ - 32.5^\circ$ for loosely – densely packed silt; and $17.5^\circ - 22.5^\circ$ for freshly deposited to heavily consolidated clays. Typical values for c_d yield 0 for sand; 2 – 10 Pa for loosely – densely packed silt; and $> 0 - 25$ Pa for freshly deposited to heavily consolidated clays (Schofield and Wroth, 1968; Terzaghi and Peck, 1967).

For undrained conditions, ϕ is in the current thesis assumed zero and c is the undrained bed strength c_u [Pa], which implies a horizontal failure envelope in the Mohr diagram. Typical vales for c_u for freshly deposited sediments are (much) lower than 10 kPa, and for consolidated soils larger than 100 kPa (Schofield and Wroth, 1968). In the current study mixtures of sand and mud are considered, with relatively large variations concerning composition and packing. For this reason c_d and c_u may vary over the indicated ranges.

To describe and quantify two or three-dimensional soil behaviour in terms of stresses and strains, tensor analysis is required (see e.g. Schofield and Wroth (1968) and Winterwerp and Van Kesteren (2004)). The stress tensor reflects the combined effect of the three principal stresses, and is graphically represented in the principal stress state in Figure 18. The three principal stressse are the normals to three mutually orthogonal principal cleavage planes (through any point P) which have zero shear stress components.

Figure 18 visualizes the stress state in terms of an isotropic stress (p [Pa]) and a deviatoric stress (q [Pa]). The isotropic stress is the mean of the principal stresses and follows the space diagonal. The deviatoric stress is the stress tensor minus the isotropic stress and is located on the triangular plane perpendicular to the space diagonal. Isotropic stresses tend to change the volume of a stressed body, whereas deviatoric stresses may also generate distortion.

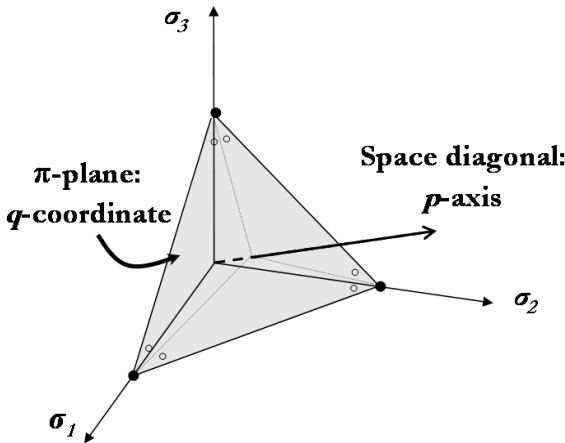


Figure 18. Relation between the principal stresses (σ_i) and the isotropic (p) and deviatoric stress (q). The π -plane runs perpendicular to the space diagonal.

The current study focuses on the two-dimensional case only, as the principal stresses in the horizontal plane are assumed identical ($\sigma_2 = \sigma_3$). Then, the magnitude of p and q is determined by:

$$p = \frac{1}{3}(\sigma_1 + 2\sigma_3) \quad (3.3)$$

$$q = \frac{1}{2}(\sigma_1 - \sigma_3) \quad (3.4)$$

From the Mohr diagram (Figure 17) it follows that p is the average of the principal stresses (σ -coordinate of the centre of the Mohr circle), and q the radius of the circle.

Substitution of $(\sigma_f, \tau_f) = (p - q \cdot \sin \phi, q \cdot \cos \phi)$ in Eq. (3.1) leads to a failure envelope for effective stresses in p - q space:

$$q = c \cos \phi + p \sin \phi = c^* + p \tan \phi^* \quad (3.5)$$

with $c^* [\text{Pa}] = c \cdot \cos \phi$ and $\tan \phi^* = \sin \phi$. Substitution of $\phi = \phi_{max}$ in Eq. (3.5) leads to the formulation of the drained strength (i.e. the deviatoric stress at $p = 0$, yielding a maximum friction angle) $c_d^* [\text{Pa}]$:

$$c_d^* = c \cos \phi_{max} \quad (3.6)$$

For undrained and water saturated conditions no volume variations occur under loading conditions, which implies that upon loading no pore water pressures are dissipated. This implies that the bed strength $c_u^* [\text{Pa}]$ at undrained failure equals the total axial stress imposed on a soil (Figure 17). Hence, the bed strength in the p - q diagram at failure under undrained conditions equals twice the undrained shear strength:

$$c_u^* = \sigma_1 - \sigma_3 = 2c_u \quad (3.7)$$

The physical meaning of c_d^* and c_u^* becomes apparent in the following pages, e.g. in Figure 21.

The Mohr diagram does not illustrate the direction of the total stresses. Therefore, it can be applied only to determine limiting stress states. The CSM on the other hand, enables the visualisation of both the direction of stresses and the soil responses before and during yielding. The state of a soil in the CSM is visualised in the p - q - e space (Figure 19). This state indicates the relation between the packing of a soil (e) and the isotropic (p) and deviatoric stress (q). Upon loading, the state of a soil moves along a specific stress path to a new stable state. The character of a stress path is determined by the direction and magnitude of the applied stresses.

The yield plane or curve forms the boundary for all possible stable states of a soil. For variations of the state of a soil within (i.e. along) a yield curve, a soil is considered stable. When the state of a soil reaches a yield curve during loading, yielding occurs, which is characterised by irreversible deformations. This means that grains re-arrange, and that volume variations may occur. These deformations generate a soil with a different structure and, therefore, different properties. The Critical State Model of Schofield and Wroth (1968) applies the Granta-gravel model for granular mixtures and

the Cam-clay model for cohesive mixtures³. Both models are discussed in the present study, as we focus on sediment mixtures with both granular and cohesive properties.

As noted, the Critical State Model and the Cam-clay model are idealisations of observed soil behaviour; also other models are being applied. For example, Roscoe and Burland (1968) present the Modified Cam-clay model. Main difference between the Cam-clay and the Modified Cam-clay models are the shape of the yield curves, which are reflected as droplets and ellipses, respectively. For simplicity, the current thesis only refers to the Cam-clay model. It is further noted that the main objection to the Cam-clay model concerns the idealisation of soil behaviour on the dry side of yield curves, as peak strengths which occur for observed soil behaviour are not incorporated.

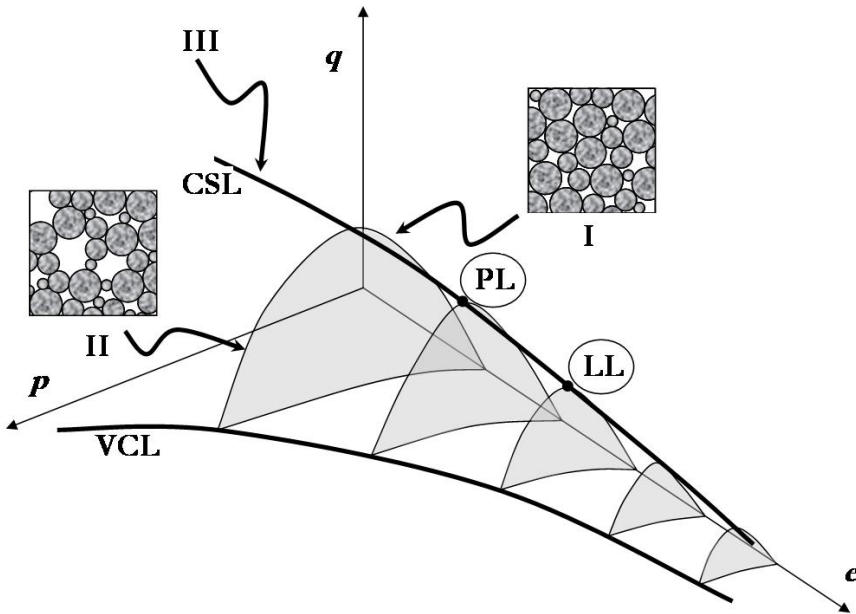


Figure 19. Three-dimensional depiction of the Cam-clay model (redrawn after Schofield and Wroth, 1968). Large and small (grey-shaded) yield curves relate to densely and loosely packed soils, respectively. Two soil behaviours at yielding occur at either side of the CSL: ‘dry’ (I) and ‘wet’ (II). ‘Dry’ and ‘wet’ refer to the appearance of a soil upon yielding: pore volume increase and inward pore water flow (I) or pore volume decrease and outward pore water flow (II). Yielding in the CS is indicated by ‘III’. Also the location of the states at PL and LL are shown indicatively.

Figure 19 shows a family of yield curves forming a failure envelope in the $p-q-e$ space. This envelope forms a stable-state boundary surface; states beyond this surface are not stable. Failure at the top of a yield curve occurs at constant volume, and

³ The names Granta and Cam refer to, respectively, the upper and lower reach of the river passing the laboratory where Andrew Schofield and Peter Wroth worked.

therefore depicts the critical state (CS) of a soil. The Critical State Line (CSL) connects CS of all yield curves. The Virgin Compression Line (VCL) determines the maximum isotropic stress of a yield curve at $q = 0$. Yielding occurs when the state of a sample reaches the stable-state boundary surface (i.e. the edge of a yield curve in a p - q plane). Upon yielding, the state of a sample moves along the yield envelope in the p - q - e plane.

Figure 20 shows the projections of the VCL and the CSL on the e - $\ln p$ plane. Both lines are parallel, which is typical to granular material ($\ln p_{VCL} \approx 2 \cdot \ln p_{CSL}$). This implies similar relations for VCL and CSL:

$$e = e_{VCL} - \lambda \ln \frac{p}{p_0}, \text{ for VCL} \quad (3.8)$$

$$e = e_{CSL} - \lambda \ln \frac{p}{p_0}, \text{ for CSL} \quad (3.9)$$

where e_{VCL} [-] and e_{CSL} [-] are initial void ratios (with the specific volume v replaced by e), p_0 [Pa] the pore water pressure and λ [-] the slope of the VCL and CSL. λ is a measure of volume variations as a function of isotropic pressure changes.

For the Granta-gravel model yield curves run parallel to the p - q plane, whereas for the Cam-clay model e varies for varying p . This is illustrated by Figure 20, which shows the projections of the yield curves on the $\ln p$ - e plane, reflected by Swelling Lines (SL). This line represents the states of a soil during drained (un)loading conditions. For the Granta-gravel model the SL runs parallel to the $\ln p$ axis (Figure 20(a)), which is in contrast with the SL in the Cam-clay model (Figure 20(b)). Therefore, additional information is required to describe the Cam-clay model:

$$e = e_{SL} - \kappa \ln \frac{p}{p_0}, \text{ for SL} \quad (3.10)$$

where e_{SL} [-] is the initial void ratio and κ [-] the slope of the swelling line.

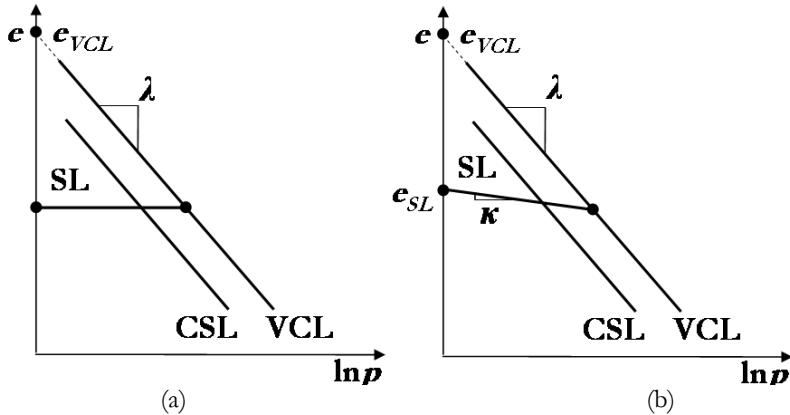


Figure 20. Two-dimensional depictions of the Granta-gravel model (a) and the Cam-clay model (b). The CSL and VCL are parallel in the e - $\ln p$ plane and yield curves run parallel to the p axis (see SL) for the Granta-gravel model, contrary to the Cam-clay model.

Both λ and κ are soil-material properties, which relate to the coefficient of volume variation (m_v [$\text{m}^2 \cdot \text{N}^{-1}$]). The subscript \cdot_v indicates vertical direction (we assume homogeneity in the horizontal direction). Volume variations can occur as a result of both compaction/consolidation and dilation/swelling. The formulation for m_v yields:

$$m_v = \frac{1}{(1+e_0)} \frac{de}{d\sigma'_v} \quad (3.11)$$

where e_0 [-] is the initial void ratio (identical to e_{VCL} in Eq. (3.8)) and σ'_v [Pa] the vertical principal effective stress (comparable to p in Eq. (3.8)). Eq. (3.11) follows from substituting Eq. (3.3) in Eq. (3.8).

Deformations which increase or decrease the pore volume generate pore water pressure gradients. The combination of m_v with the permeability (k_v [$\text{m} \cdot \text{s}^{-1}$]) leads to the coefficient of pore water dissipation (c_v [$\text{m}^2 \cdot \text{s}^{-1}$]):

$$c_v = \frac{k_v}{m_v \rho_w g} \quad (3.12)$$

Another commonly used name for c_v is the consolidation coefficient. However, c_v can characterise the dissipation of pore water pressure gradients both during swelling (negative gradients) as during consolidation (positive gradients). For granular mixtures, k_v is relatively large and m_v relatively small, resulting in large c_v . For cohesive mixtures, k_v is relatively small and m_v relatively large, resulting in small c_v .

Next to the either parallel or diagonal character of yield curves (represented by the SL) in the e - $\ln p$ plane, another important difference exists between the Cam-clay and Granta-gravel model. Figure 19 shows that for zero isotropic stress ($p = 0$) the deviatoric stress is also zero ($q = 0$). However, for the Cam-clay model $q > 0$ for $p = 0$, as shown in Figure 21(a). This implies that at zero isotropic stress a resisting stress for distortion exists, which is the 'true' cohesive (and adhesive) bonding strength c_d^* of cohesive material. Figure 21(b) shows that for a decreasing size of yield curves (i.e. larger e , e.g. for fresher/softer deposits), c_d^* approaches zero. For granular soils no cohesive stresses occur and, therefore, $c_d^* = 0$ in the Granta-gravel model.

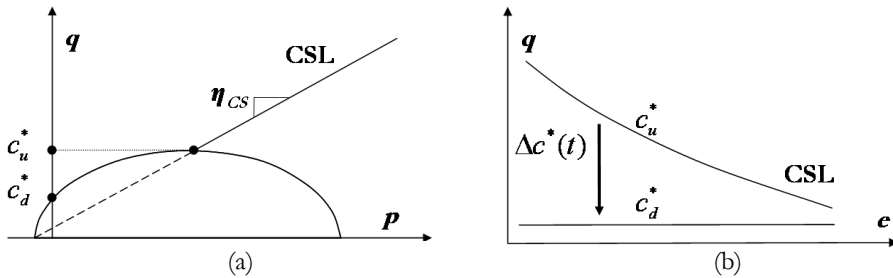


Figure 21. Two-dimensional views of yield curves. Left, the CSL is projected on the p - q plane. It is emphasized that p can be smaller than zero (yielding tensile stresses), which is for simplicity not shown in Figure 19. In the right panel the CSL is projected on the e - q plane. The 'true' cohesive strength c_d^* and the undrained strength c_u^* are depicted, with c_u^* decreasing to c_d^* for increasing e .

Chapter 2 distinguishes between cohesion and apparent cohesion. This originates from a difference in time-scale between the hydrodynamic forcing and the response (i.e. deformation) of a soil. When the soil-response is relatively slow, pore water pressure gradients occur. The slow dissipation of these gradients is characterised by c_v and referred to as consolidation or swelling, resulting from compression or extension, respectively.

Swelling originates from distortion (resulting in pore volume increase) and/or unloading of a soil, and is accompanied by negative pore water pressures gradients which generate an inward pore water flow. During this dissipation process, the under-pressure stiffens the granular skeleton and reflects an apparent bonding strength. The strength is referred to as the apparent cohesive strength ($c^*(t)$ [Pa]), which decreases in time due to swelling from c_u^* towards c_d^* as illustrated in Figure 21(b):

$$c_u^*(t) = c_d^* + \Delta c^*(t) \quad (3.13)$$

It is noted that the term ‘cohesive’ is confusing when considering apparent cohesion. Cohesion is defined as the mutual bonding strength between similar molecules. This indicates that the cohesive strength (c_d^*) is a micro-scale material parameter. Δc^* and c_u^* depend on packing density as they result from negative pore water pressure gradients. Therefore, these parameters are considered meso-scale parameters and apparent cohesion a meso-scale phenomenon.

The maximum deviatoric stress for stable soils ($c^* = c_u^*$) occurs for undrained conditions when pore water pressures have not yet dissipated ($t = 0$). It is noted that c_u^* can be orders of magnitude larger than c_d^* . Furthermore, the behaviour of c_u^* as a function of e depends on the shape of the yield curves. The shape of yield curves as a function of varying granular composition, PI and void ratio is not known. Therefore, no physical relation exists for c_u^* as a function of these parameters.

Loading results in a different stress state, following a stress path in the p - q plane, which characterises the response of a soil (until failure). For granular material stress paths always form straight lines in the p - q plane (Figure 21(a)), as friction between grains results in linearly increasing shear stresses for increasing normal stresses (Coulomb’s law). The slope of a stress path in the p - q plane is given by:

$$\eta = \frac{dq}{dp} \quad (3.14)$$

The projection of the CSL on the p - q plane forms a special stress path which reaches each yield curve at maximum q . The slope of this path (η_{CS} [-]) is a soil-material parameter:

$$q = \eta_{CS} p = \frac{6 \sin \phi}{3 - \sin \phi} p \quad (3.15)$$

where η_{CS} typically varies between 0.7 – 1.2 for muddy ($\phi \leq 20^\circ$) and sandy ($\phi \leq 30^\circ$) sediments, respectively.

Schofield and Wroth (1968) link the stability criterion ($q = \eta_{CS} \cdot p$, see Eq. (3.15)) to the theory of plasticity, which results in the formulation for a yield curve:

$$|q| = \eta_{CS} p \left(1 - \ln \frac{p}{p_A} \right) \quad (3.16)$$

where p_A [Pa] is the isotropic stress at the CS for a soil 'A'. Substituting Eq. (3.9) and (3.10) in Eq. (3.16) gives a formulation for yield curves in the Cam-clay model:

$$|q| = \frac{\eta_{CS} p}{\lambda - \kappa} (\lambda - \kappa + e_{CSL} - e_A - \lambda \ln p) \quad (3.17)$$

where e_A [-] is the void ratio of a soil 'A'. A close relation between the Cam-clay and Granta-gravel model exists: the latter model is a sub-set of the first, as Eq. (3.17) reduces to Eq. (3.18) for $\kappa = 0$:

$$|q| = \frac{\eta_{CS} p}{\lambda} (\lambda + e_{CSL} - e_A - \lambda \ln p) \quad (3.18)$$

Eq. (3.18) yields a formulation for yield curves in the Granta-gravel model, which also follows from substituting Eq. (3.9) in Eq. (3.16).

3.1.2 Soil response to loading in the CSM

This section applies the theory of the Critical State Model to soil behaviour resulting from loading. Figure 19 shows that large yield curves are related to more densely packed soils, and small curves to more loosely packed (e.g. freshly deposited) soils. A small yield curve implies that the soil is stable for limited loading conditions. More densely packed beds with larger yield curves are stable for a larger range of loading conditions. Yielding occurs when the stress state of a soil reaches the yield envelope when moving along a stress path in the p - q plane.

Varying e results from deformations. Plastic deformations are irreversible and elastic deformations are reversible. For granular as well as cohesive mixtures plastic deformations occur upon yielding. These irreversible deformations result in compaction or dilation. The initial and final states of plastic deformations are located on different yield curves.

However, loading conditions for which a soil is not yielding lead to different responses for granular and cohesive soils. Granular mixtures exhibit a rigid response during which no deformations occur. For cohesive soils elastic deformations occur with an initial and final state within the same yield curve. This implies that upon unloading, the state of the soil returns to its original state as the soil fabric is still intact, which is reflected by varying e along yield curves of the Cam-clay model. During reversible deformations the pore volume changes due to pore water flow induced by pore water pressure gradients. It is noted that the application of the term 'consolidation' is sometimes confusing, e.g. concerning the volume decrease of freshly-deposited flocs with time. The open structure of freshly-deposited flocs indicates that the volume decrease is initially dominated by irreversible compaction.

Upon yielding three types of soil behaviour may occur (Figure 22). Two of these types exhibit volume variations. Contraction occurs when the total volume of a soil decreases during yielding, which typically occurs for loosely packed soils. During dilation the total volume increases, which occurs for more densely packed soils.

In the CSM hardening occurs when normal stresses (\sim isotropic stresses) are relatively large compared to shear stresses (\sim deviatoric stresses). As a result, the distance between particles and the pore volume decrease. For softening a relatively large shear stress is required to increase the pore volume. The result of hardening is compaction; the result of softening dilation. The third kind of yielding occurs at the critical state, during which no pore volume variations occur (Figure 22(c)). This type of yielding occurs for a specific relation between the packing and p and q .

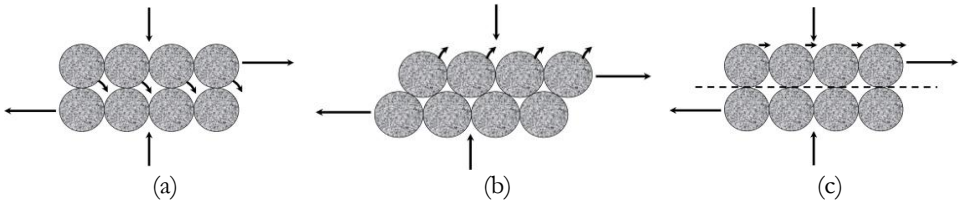


Figure 22. Schematic depiction of three types of yielding of a soil due to different combinations of shear and normal stresses: contraction (a), dilation (b) and yielding at the critical state (c).

Next, the different types of yielding that result from anisotropic ($q > 0$) loading conditions are visualized in Figure 23. After yielding (i.e. reaching the edge of a yield curve), the state of a sample continues to move along the imposed stress path until it reaches a new stable state on the CSL. Before it reaches this stable state, deformations continue due to the imposed deviatoric and isotropic stresses.

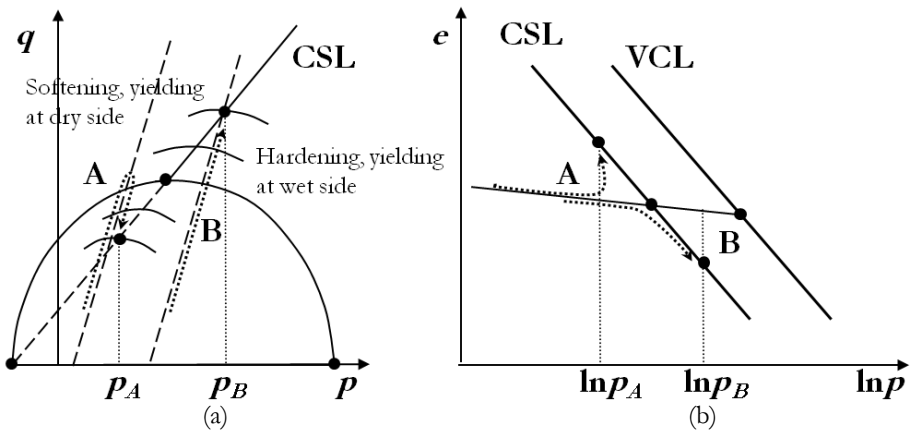


Figure 23. Two-dimensional graphs of the CSM showing different types of yielding in both the p - q plane (a) and the e - $\ln p$ plane (b). The dotted arrows 'A' in (a) and (b) indicate the process of softening; the dotted arrow 'B' in (a) and (b) indicates the process of hardening.

When the imposed stress path follows the CSL, yielding occurs at the critical state, after which the state moves along the CSL to another yield curve in the p - q - e space. The occurrence of hardening or softening depends on the location at which the

imposed stress path reaches the yield curve relative to the critical state. Hardening occurs when the yield curve is reached below the critical state, softening when yielding occurs above the critical state.

Softening results in dilation as the pore volume increases during yielding. During this process water flows into the soil as a result of a negative pore water pressure gradient. Therefore, samples which exhibit this type of yielding are referred to as ‘strong at yielding’, due to the additional bonding of apparent cohesion. Figure 23 shows that for $q > \eta_{CS}p$ soils are strong at yielding (indicated by ‘A’). Figure 23 indicates that during softening the state moves to a smaller yield curve. This is visualized by moving along the dry side of the 3-D failure envelope towards larger e in Figure 19. Due to the inflow of pore water, these soils appear as ‘dry’ during yielding. An example of ‘dry’ yielding occurs when walking on the beach along the shoreline. Locally, the pressure of your foot results in dilation and thus an increase of the pore volume. The sand around your feet appears ‘dry’, as an inward flux of water into the larger pore volume occurs.

Hardening results in compaction. A tendency to a decrease of the pore volume generates a positive pore water pressure gradient, which generates an outflow of pore water. A hardening soil is, therefore, referred to as ‘weak at yielding’, as the effective stress decreases due to the increased pore water pressure. Figure 23 shows that for $p > p_{CSL}$ soils are weak at yielding (indicated by ‘B’) and that hardening results in a larger yield curve. This is visualized by moving along the wet side of the 3-D failure envelope towards larger e in Figure 19. Due to the outflow of excess water, hardening results in a ‘wet’ appearance. The ‘wet’ side of yield curves is indicated by ‘B’ in Figure 23.

Yielding can also occur at isotropic ($q = 0$) loading conditions. In that case the stress path equals the projection of the VCL on the p - q plane, which equals the p -axis. This is typically the case during own-weight consolidation (also referred to as ‘normal consolidation’ or ‘virgin compression’) of freshly deposited sediments. However, the state of a soil at a certain depth is not located on the VCL as the deviatoric stress is always larger than zero due to the load of an overlying sediment in combination with internal friction between grains. This implies that the stress state of a consolidated soil at rest (i.e. no other loading conditions than an overlying layer of sediment) is always located on the so-called K_0 -stress path (or confined stress path).

The K_0 -stress path runs parallel to (and in-between) the CSL and the VCL in the e - $\ln p$ plane (Figure 24), which is inherent to granular soils. K_0 is also referred to as the coefficient of earth pressure at rest. The subscript 0 indicates zero horizontal strain. K_0 is the ratio between the horizontal and vertical principal stresses:

$$K_0 = \frac{\sigma_{1,2}}{\sigma_3} \approx 1 - \sin \phi_{max} \quad (3.19)$$

It is noted that the maximum internal stress of soils on the K_0 -stress path is lower than c_u^* , as K_0 reaches yield curves at q smaller than at the CSL. During a one-dimensional compression test, such as the Oedometer test (see Chapter 4), the stress path of a soil follows the K_0 -stress path.

K_0 typically varies between 0.3 – 0.5 for sand ($\phi_{max} = 45^\circ - 30^\circ$) and 0.8 – 0.6 for clay ($\phi_{max} = 10^\circ - 20^\circ$). The formulation for the slope of the K_0 -stress path in the p - q plane follows from substituting Eq. (3.19) in Eq. (3.3) and (3.4):

$$q = \frac{\sin \phi}{2 - \sin \phi} p = \eta_{K_0} p \quad (3.20)$$

Eq. (3.20) implies that η_{K_0} typically varies between 0.2 – 0.35 ($\phi_{max} = 10^\circ - 30^\circ$).

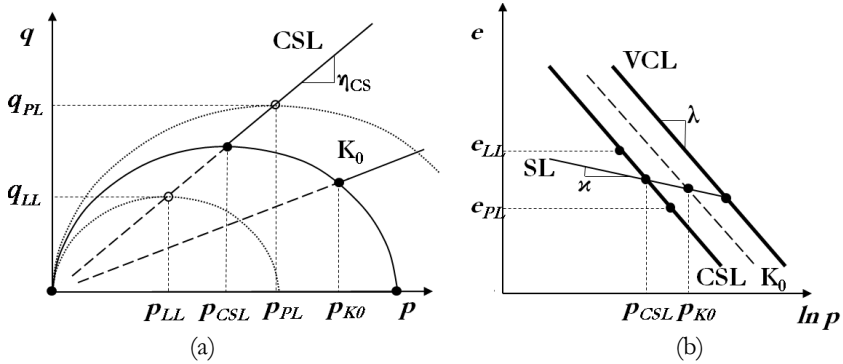


Figure 24. Two-dimensional projections e as a function of $\ln p$ in the right panel. The slope of the SL (swelling line) and VCL (b) indicate the swelling and consolidation indices, respectively. Also the K_0 -line and the projections of PL and LL are shown, the latter two are located on a smaller and larger yield curve, respectively.

Stress paths can generate both a drained or undrained response. The occurrence of a drained or undrained response depends on the relation between the typical time scales of the forcing condition and the dissipation rate of the generated pore water pressures. If these scales are of the same order of magnitude, a drained response is expected. For a relatively slow soil response an undrained response occurs.

Drained stress paths (i.e. initial and final state on the same yield curve) always run along the plane of a yield curve in the p - q plane. This implies that in the Cam-clay model e varies along a drained stress path, which results from an in or outflow of pore water. In the Granta-gravel model the yield curves run in a plane perpendicular to the e -axis, implying no volume variations along a drained stress path. For an undrained response no pore volume variations occur. Therefore, undrained stress paths always run in a plane perpendicular to the e -axis. This implies that along undrained stress paths the state of a cohesive soil reaches a number of yield curves. Undrained behaviour typically occurs when the permeability and, therefore, the coefficient of pore water dissipation is relatively low.

The transition between a drained and an undrained response is indicated by the Pécelet number Pe_w [-]. It relates the deformation rate of a soil to the rate of dissipation of pore water pressure gradients, which are generated by these deformations:

$$Pe_w = \frac{v\ell}{c_v} \quad (3.21)$$

where V [m/s] is a velocity characterising the deformation rate and l [m] a typical length scale. Figure 25 shows the relation between the Péclet number and the relative pore water pressure. The latter is indicated as the actual pore water pressure divided by the undrained pore water pressure.

Fully drained conditions occur when the deformation rate equals the dissipation rate ($Pe_w \leq 1$). Fully undrained conditions occur for $Pe_w > 10$, for which the advection rate should be an order of magnitude larger than the dissipation rate. Pe_w characterizes a sediment bed for undrained conditions only, as it relates to the undrained pore water pressure p_u^w [Pa], which occurs at $q = c_u^*$. The actual pore water pressure p_w decreases with time towards zero: at $p = 0$ we find $q = c_d^*$.

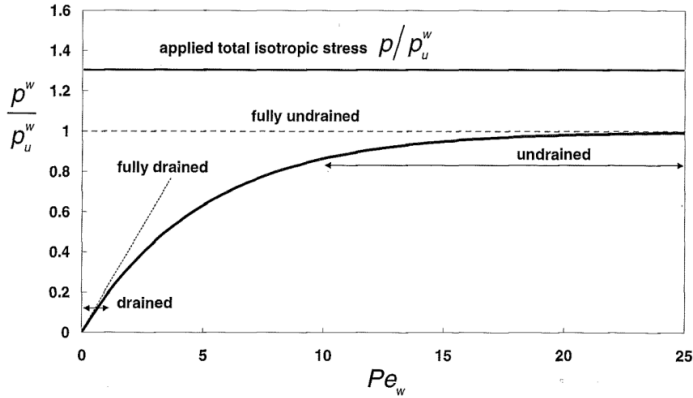


Figure 25. Pore water pressure as a function of the Péclet number, where p^w [Pa] is the actual pore water pressure and p_u^w [Pa] the undrained pore water pressure (Winterwerp and van Kesteren, 2004). For $Pe_w \leq 1$ fully drained conditions occur and for $Pe_w > 10$ undrained conditions.

Figure 24(b) shows the swelling line (SL) and the swelling index κ . SL runs along a yield curve in the Cam-clay model. Upon unloading, the state of a cohesive soil runs along SL with decreasing p . Soils for which $p < p_{K_0}$ (on the same yield curve) are over-consolidated, which is expressed by the Over-Consolidation Ratio:

$$OCR = \frac{p_{K_0}}{p} \tag{3.22}$$

where p_{K_0} [Pa] is the isotropic stress at the crossing of the K_O -line and the yield curve (see Figure 24), and p the actual isotropic stress. OCR is a measure for the stress history, as it indicates the potential response of a soil for specific current and previous loading conditions. For $OCR > 1$ the bed is over-consolidated, which generates swelling, and for $OCR < 1$ the bed is under-consolidated, which generates consolidation. Light and heavy over-consolidation occur for $p_{CSL} < p < p_{K_0}$ and $p < p_{CSL}$, respectively.

The plasticity index PI indicates the difference in water content of a remoulded soil at two different consistency levels: the plastic limit (PL) and the liquid limit (LL), as discussed in Chapter 2. Figure 19 and Figure 24 show the relative positions of LL and PL in the CSM. As expected, LL lies on a smaller yield curve than PL , due to the larger water content at LL . Both LL and PL are located on the CSL. As PI relates to the material property λ (i.e. slope of CSL), it is a convenient parameter to characterise soils. Remoulding occurs when mechanically stirring a soil and simultaneously adding water.

3.1.3 Examples of soil responses to varying loading conditions

This section discusses two examples showing the soil responses resulting from two different loading-unloading cycles. The first example illustrates the typical conditions during an Oedometer test, whereas the second example illustrates soil responses during a shear vane test. These examples provide background information for the discussion of the results of both tests in Chapter 4. For simplicity, we assume $q = 0$ at $p = 0$ in the accompanying figures, which implies that $c_d^* = 0$ Pa.

The first example deals with the drained loading-unloading-loading cycle ‘ABC’-‘CD’-‘DCE’ along an anisotropic and confined stress path (K_0) as shown in Figure 26. After imposing a compressive load, the soil initially consolidates (as $p_B > p_A$ and $OCR < 1$), during which the state moves from ‘A’ to ‘B’. Upon yielding on the wet side at ‘B’, hardening occurs. Next, the stress state moves towards a larger yield curve within the three-dimensional failure envelope along the K_0 -stress path towards ‘C’, as is shown in Figure 26(d). Along ‘BC’ and ‘AB’ plastic and elastic deformations occur, respectively.

Upon decreasing the compressive load ($p = p_D$), the soil becomes over-consolidated and starts to swell (as $p_D < p_C$ and $OCR > 1$). During swelling elastic deformations occur. As these deformations are reversible, the stress state would move along the same SL upon reloading ($p = p_E$). ‘A’ and ‘D’ exhibit similar stress levels (p -ordinates), although their mechanical behaviour is different as both states are located on different yield surfaces.

Because $\eta_1 < \eta_{CS}$, yielding (from ‘B’ to ‘C’) results in hardening. However, for a steeper slope of the stress path ($\eta = \eta_2 > \eta_{CS}$), yielding induces softening. Furthermore, the initial conditions are important for the mechanical behaviour of soils. Figure 26 shows that different stress paths occur for identical loading conditions ($p = p_C$) and composition (constant ξ_{sa} and PI), but different e . ‘ABC’ indicates both reversible and (after yielding) irreversible deformations. However, ‘DC’ indicates that for similar loading conditions but different initial condition, no yielding but only reversible deformations occur.

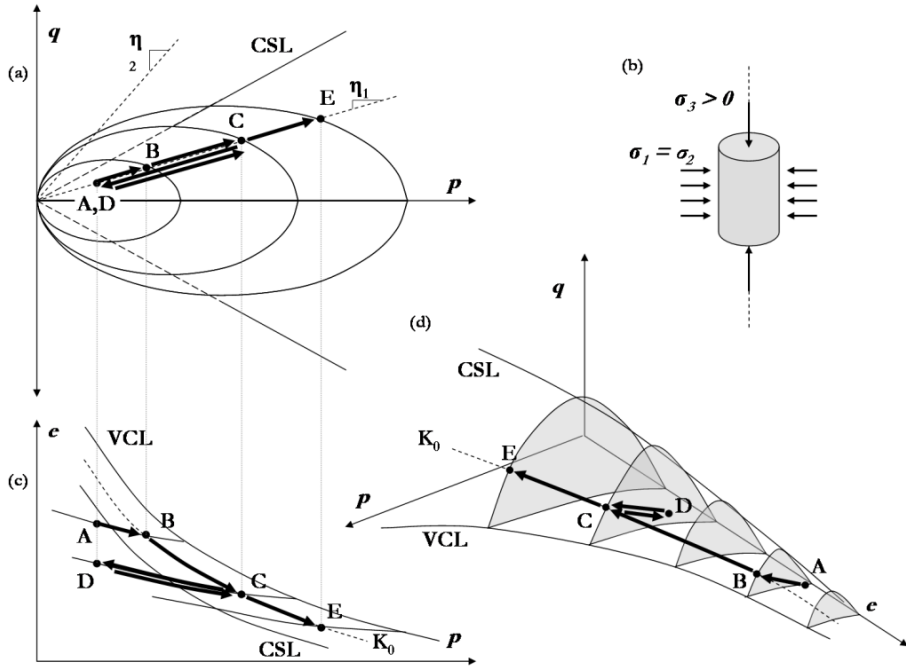


Figure 26. Cam-clay model showing soil responses during the anisotropic drained loading-unloading-loading cycle ‘ABC’-‘CD’-‘DCE’. Two-dimensional views (a and c) as well as a three-dimensional view of the yield curves are shown (d). In (b) the confined loading conditions are schematized, which typically occur during Oedometer tests.

The second example shows the undrained soil responses ‘FG’, ‘HIG’ and ‘JKG’ (Figure 27), which result from anisotropic loading typical for a shear vane test. The rotational speed of the vane is relatively large compared to the deformation rate of the soil, which implies undrained yielding. c_u^* is derived from the torque required to rotate a vane within a cylindrically shaped soil sample under undrained conditions. When executing a shear vane test at constant rotational speed a soil is continuously being remoulded. This implies that the final stress state is always located on the CSL. It has been argued before that $q_{CSL} = c_u^*$, which is the maximum remoulded strength of a soil.

The initial stress states ‘F’, ‘H’ and ‘J’ are located on different yield surfaces (Figure 27(b)). The initial void ratios are identical ($e_F = e_H = e_J$). As conditions during the test are undrained (constant e), stress states are forced to migrate in a plane perpendicular to the e -axis (Figure 27(b)). However, the states at ‘F’, ‘H’ and ‘J’ exhibit different *OCR*. The degree of over-consolidation increases when moving from ‘J’ to ‘F’ and further to ‘H’. These different initial conditions result in different yielding behaviours, as is illustrated by Figure 27(a) and (c). Figure 27(c) shows the soil strength as a function of the rotation angle of the vane. Next, the different stress paths are discussed individually.

Upon loading, a soil with initial state 'F', moves up the yield curve (a) maintaining constant e . At the CS, the soil is continuously yielding (due to the applied torque) without volume variations. For stress path 'HIG' the state is initially located on a larger yield curve than 'F'. After migrating along this yield plane, yielding occurs on the dry side. This implies negative pore water pressure gradients and apparent cohesion, which generates the peak in (c). After yielding, the state migrates for constant e along the 3-D failure envelope towards the CSL. It is noted that for a soil consisting of flocs the peak in (c) may also be generated by thixotropy (e.g. floc breakup).

For stress path 'JKG' the state is initially located on a smaller yield curve than 'F'. Upon reaching this curve, the soil appears weak at yielding. This results from yielding on the wet side, which implies the generation of positive pore water pressure gradients. Next, the state moves along the failure envelope at constant e towards the CSL.

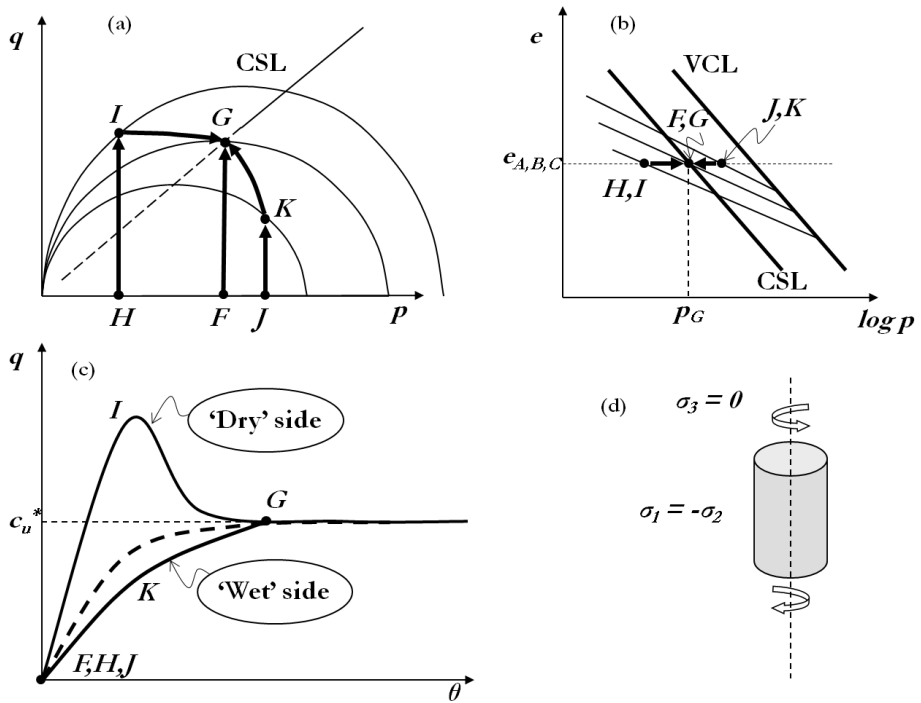


Figure 27. Cam-clay model showing soil responses during soil responses 'FG', 'HIG', 'JKG' for anisotropic undrained loading conditions during a shear vane test. (a) and (b) show two-dimensional views of yield curves; in (c) the soil strength is plotted as a function of the vane's rotation angle. In (d) the loading conditions are schematized. 'HIG' and 'JKG' exhibit yielding on the dry and wet side, respectively. The dashed line in (c) indicates 'FG'.

It appears that the stress paths of ‘HIG’ and ‘JKG’ are located above and below ‘FG’ in Figure 27(c), respectively. This reflects the occurrence of negative and positive pore water pressure gradients, which induce larger (‘HIG’) and smaller (‘JKG’) effective stresses. Larger effective stress implies increased shearing resistance and, therefore, larger c_u^* . This example illustrates the effects of various stress histories on soil behaviour. Although for all three cases the sample composition and void ratio are similar, the mechanical behaviour is completely different. However, it is shown that the shear vane test enables the determination of c_u^* (as final state on CSL), independently of the loading history (i.e. varying OCR at the initial state). This illustrates that c_u^* is a soil-material parameter.

3.2 New erosion classification

3.2.1 Introduction

The current study considers erosion as the yielding of a soil due to a turbulent flow. Winterwerp and van Kesteren (2004) present a classification scheme for the erosion of cohesive sediment mixtures (Figure 28). It distinguishes three erosion modes: floc erosion, surface erosion and mass erosion. As Winterwerp and van Kesteren (2004) discuss these modes descriptively, this section presents a more fundamental discussion.

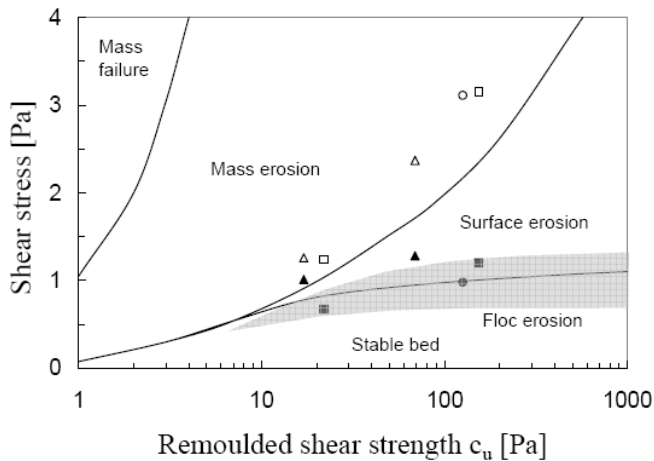


Figure 28. Classification of erosion modes for cohesive soils with the bed shear stress as a function of the bed strength (Winterwerp and van Kesteren, 2004). It is shown that, depending on the applied loading condition, a soil (constant c_u) can exhibit different erosion modes.

The different types of soil behaviour as discussed in Section 3.2.1 are related to the erosion modes shown in Figure 28. The occurrence of these modes depends on the type and magnitude of the hydrodynamic forcing (Section 3.2.2), the relation between the time scales of the pore water pressure dissipation rate and the driving forces (drained/undrained behaviour), and the actual stress state of the sediment bed in relation to its stress history. Section 3.2.3 discusses different erosion modes.

3.2.2 Hydrodynamic forcing

In geotechnical engineering generally concerns the effect of loading on (consolidated) soils. The magnitude and character of these loading conditions is generally known. However, loading on a sediment bed due to the typical hydrodynamic forcing resulting from a turbulent flow is much less understood. This section describes these hydrodynamics just above the water-bed interface, as well as the stresses generated within the upper layer of the sediment bed. To determine the type of yielding, it is required to translate the hydrodynamic forcing to deviatoric and isotropic stresses.

However, not much is known of the stresses within the upper layer of the sediment bed resulting from the hydrodynamics just above a permeable interface. Ample information is available concerning turbulence in open channel flows, for both hydraulically smooth and rough beds. For example Kim *et al.* (1987) show the existence of turbulence correlations between normal and shear stresses near a wall. However, these relations apply for the turbulent boundary layer only. It is unclear yet if these correlations also apply to stresses within the permeable interface.

Natural geophysical flows are turbulent and impose a combination of shear and normal stresses on the sediment bed. Turbulent fluctuations for both shear and normal stresses are often described by ensembles. However, instantaneous fluctuations of the flow are important for erosion. Therefore, the instantaneous shear and normal stress at the sediment bed ($\hat{\tau}_b$ [Pa] and $\hat{\sigma}_b$ [Pa]) should be considered, and not their ensemble averages.

At turbulence-scale bursting phenomena occur, which are coherent and organized motions whose growth and breakdown occur periodically (Nezu and Nakagawa, 1993). Following Taylor's hypothesis (i.e. frozen-turbulence approach), a constant relation exists between the time (T [s]) and length-scale (L [m]) of these bursts ($T = L/u$), with u [m/s] as a velocity scale). This implies that a spatial treatment of these bursts is adequate.

Bursting phenomena are generally classified by the quadrant theory, which is based on spatial characteristics (e.g. Nezu and Nakagawa, 1993). This theory leads to two important forcing mechanisms for erosion, which are indicated by the block arrows in Figure 29. The cyclic character of the bursting phenomena follows from the combined effect of a shear stress and an alternating up and downward directed normal stress. The outward directed resultant stress generates a lift-force. The inward directed resultant stress leads to a build-up of pore water pressures, which decrease the effective stress within the bed. This forcing mechanism can be compared with liquefaction resulting from cyclic wave loading.

The organized motions just above the bed generate a relation between shear and normal stresses within the upper layer of the bed. However, this relation is currently unknown. The shear and normal stresses $\hat{\tau}_b$ and $\hat{\sigma}_b$ at a permeable interface must be related to the organized motions above the bed. Breugem (2005) describes the influence of wall permeability on laminar and turbulent flow, although the pores at the interface are relatively large compared to those in a typical consolidated sediment bed. It remains unclear (1) what the relation between $\hat{\tau}_b$ and $\hat{\sigma}_b$ is, (2) if this relation is constant for varying flow velocities, and (3) what the effect of the stochastic character of the flow is. Uittenbogaard (2008) argues that normal and shear stresses at the water-bed interface are equally important, which only partly solves (1).

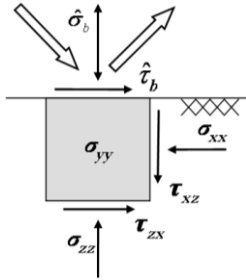


Figure 29. Stress-balance on a soil at the surface of a sediment bed. The block arrows indicate the resultant stresses of the hydrodynamic forcing.

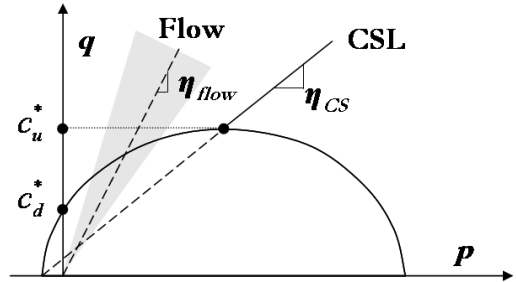


Figure 30. Stress path representing stresses within the upper layer of the bed resulting from hydrodynamic forcing. The yield curve is reached on the wet side; the grey-shaded reflects the stochastic flow character.

It is important to realize that the shear and normal stress on a sediment bed do not reflect the principal stresses within the bed. The coordinate system of the principal stresses rotates over an unknown angle due to the hydrodynamic forcing. This implies that the translation of $\hat{\tau}_b$ and $\hat{\sigma}_b$ to the principal stresses and/or p_b and q_b (isotropic and deviatoric stresses within the sediment bed) is not straightforward. Furthermore, the principal stresses are a function of flow conditions, material properties (K_0 and bulk density) and thickness of the eroding layer (see the stress-balance in Figure 29).

As their functions and relations are unknown at present, it is therefore not yet possible to generate p_b and q_b within the sediment bed. First, a more thorough study is required to gain more insight into this topic, especially on the relation between $\hat{\tau}_b$ and $\hat{\sigma}_b$. However, this mainly fluid-dynamical topic is beyond the scope of the current study, which principally focuses on the relation between geotechnical behaviour and erosion properties.

To reflect the mechanical behaviour of a sediment bed during erosion in the CSM, two assumptions are made concerning stress paths induced by hydrodynamic forcing. The first assumes a linear relation between p_b and q_b for varying flow velocities, independent of the direction of $\hat{\sigma}_b$. The second assumption states that the slope of the

flow-induced stress path $\eta_{flow} [-] = \alpha \cdot \eta_{CS}$, which implies that $q_b (= f(\rho_b))$ varies for different soil types ($\eta_{CS} \approx 1.4 - 2.4$ for clay and sand, respectively), see Eq. (3.15).

The current study assumes that the dimensionless coefficient $\alpha = 2$. This implies (1) that the flow-induced stress state always reaches yield curves on the dry side (Figure 30), and (2) that hydrodynamically generated deviatoric stresses within the upper layer of the bed are more important than isotropic stresses, which is based on the following consideration. The effect of $\hat{\tau}_b$ on the stresses within the bed is dissipated over a relatively short vertical distance, due to internal friction between grains. The effect of horizontal gradients of stresses induced by $\hat{\sigma}_b$ is more important for erosion as these gradients generate horizontal stress gradients and, therefore, distortion, within the upper layer of the bed.

Most studies on the erosion of sediments relate erosion properties to τ_b only (see Chapter 2), rather than to the combined effect of τ_b and σ_b . However, the erosion threshold is generally derived from observations on the mobilisation of sediments from the bed (sand) and/or from extrapolation of erosion rates (fines). The combined effect of τ_b and σ_b is then implicitly accounted for. This implies that the initiation of motion relates to this combined effect, rather than to the bed shear stress only.

From practical considerations, the erosion threshold τ_e in the current study is also represented by a shear stress, though representing both shear and normal stresses. The same assumption is made for τ_b . Also for reasons of simplicity, the drained and undrained bed strength are indicated by c_d and c_u rather than by the deviatoric drained and undrained bed strength c_d^* and c_u^* , respectively.

It is further noted that for most erosion devices the relation between flow velocity and bed shear stress is calibrated by applying the Shields stability criterion. As the ratio between shear and normal stresses may vary for erosion devices, care should be taken when applying the Shields stability criterion to calibrate shear stresses.

3.2.3 Erosion modes following from a geotechnical approach

Freshly deposited sediment beds, as well as the upper layer of normally consolidated beds, consist of freshly deposited and loosely packed flocs; this is schematically shown in Figure 31. Floc erosion is the disruption of individual flocs or parts of flocs. This occurs when flow-induced peak stresses exceed the strength of unconsolidated flocs and/or their mutual cohesive/adhesive bonds. Figure 31 shows that the inflow of water to replace a removed floc is not restricted, which implies that the typical time-scales of erosion and inflow of water are similar. Therefore, the only stabilising factor for floc erosion is c_d .

Floc erosion strongly relates to the stochastic character of turbulent flows. The floc erosion threshold ($\tau_{e,f}$ [Pa]) equals the drained strength of sediment beds (c_d). Floc erosion occurs for $\hat{\tau}_b \geq c_d$, where $\hat{\tau}_b$ [Pa] reflects peak stresses larger than the mean stress $\bar{\tau}_b$. Also the stochastic character of the bed strength is important, especially for natural sediment beds which exhibit significant spatial variation. The floc erosion parameter M_f [$\text{kg} \cdot \text{m}^{-2} \cdot \text{s}^{-1}$] should be related to the stochastic character of c_d .

Contrary to floc erosion, surface erosion is more related to the characteristics of the sediment bed rather than to the characteristics of the flow. Therefore, surface erosion is related to $\bar{\tau}_b$ rather than to $\hat{\tau}_b$. It can be argued that a stochastic approach to distinguish between floc and surface erosion explains the typical relation between τ_b and E for cohesive soils (see Partheniades (1962, 1965) and Figure 32). The linear increase of E for increasing τ_b indicates that at increasing flow velocities, not only $\hat{\tau}_b$ but also $\bar{\tau}_b$ is important (see also Van Prooijen and Winterwerp, 2010). The threshold for surface erosion ($\tau_{e,s}$ [Pa]) occurs for $\bar{\tau}_b = c_d$.

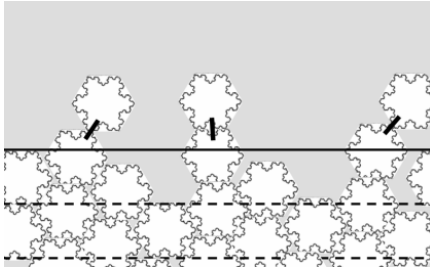


Figure 31. Schematised sediment bed with layers of flocs, with freshly deposited flocs on top. The vertical scale between the dashed lines indicates the floc size.

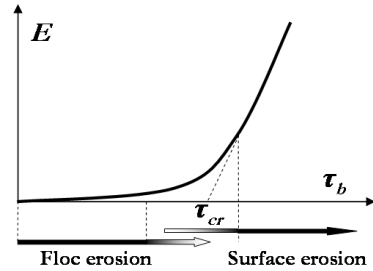


Figure 32. Typical relation between τ_b and the erosion rate E for cohesive soils. It has been suggested that the left part reflects floc erosion, and the right part surface erosion.

This study defines surface erosion as a drained erosion process at which layers of flocs are removed. During surface erosion the strength of a sediment bed slowly (i.e. in a drained manner) decreases until an erodible bed surface is obtained. The process of surface erosion is illustrated in Figure 33, which shows normally consolidated soils with initial stress states on the K_0 -line.

Due to turbulent flow shear stresses, the stress state of a soil changes and negative pore water pressures gradients are generated. These pressure gradients induce swelling, which concerns the flow of water into the bed following Darcy's law. The inflow decreases the bed strength. Surface erosion starts when the internal strength is exceeded by the flow-exerted stress (see Figure 33).

Upon the removal of flocs, underlying sediments become over-consolidated. Swelling occurs when a layer of sediments with a thickness larger than about twice the typical floc size (as $p_{VCL} \approx 2 \cdot q_{CSL}$) is eroded. During swelling the stress state moves along a yield surface towards the q -axis. As a result, the internal stress of the bed reduces towards c_d , as $\Delta c \rightarrow 0$ (see Figure 21(b) and Eq. (3.13)). By definition, surface erosion is a drained process, which implies that it occurs for $c_d \leq \bar{\tau}_b < c_u$. The surface erosion rate (E_s [$\text{kg} \cdot \text{m}^{-2} \cdot \text{s}^{-1}$]) is limited by the pore water pressure dissipation rate.

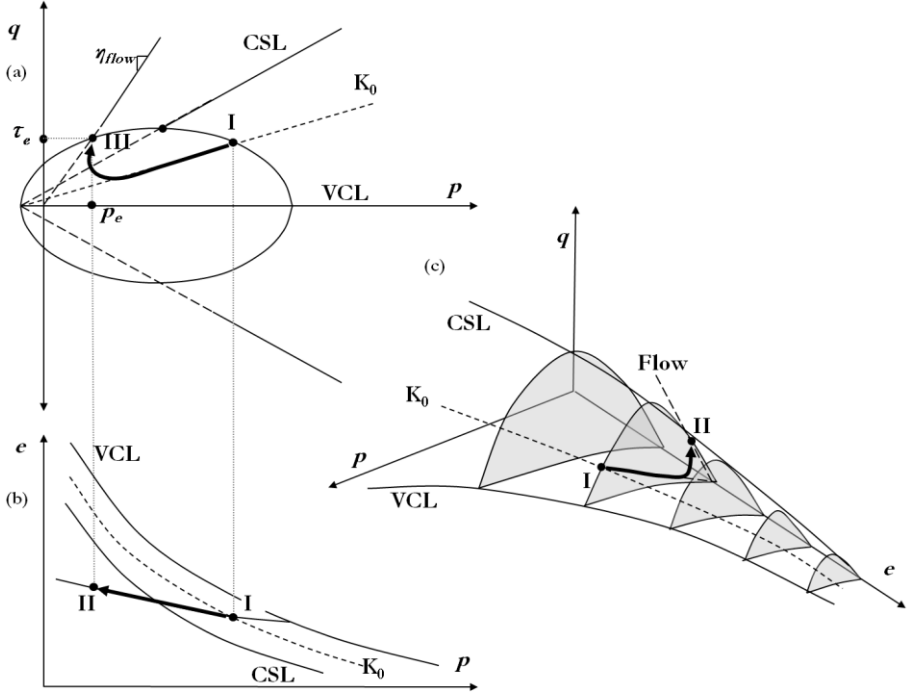


Figure 33. CSM showing the stress states of a sediment bed during surface erosion. Shear stresses exerted by a turbulent flow generate a negative pore water pressure gradient. This over-consolidated state induces swelling ('I-II'). Finally, surface erosion occurs in 'II' along the hydrodynamic stress path on the dry side of the yield curves.

Mass erosion is defined as erosion of lumps of material from an over-consolidated bed, i.e. before pore water pressure gradients are dissipated. This occurs when the forcing conditions locally exceed the undrained strength of the bed ($\hat{\tau}_b > c_u$). The onset of mass erosion is often accompanied by cracks or failure planes perpendicular to the flow direction. Upon erosion, lumps of material are disrupted from the bed, which results in an irregular bed. Winterwerp and Van Kesteren (2004) give a criterion for the threshold of mass erosion:

$$\tau_{e,m} \equiv \frac{1}{2} f_w \rho_w u^2 > f_w (2 - 5) c_u \quad (3.23)$$

where f_w is a dimensionless friction factor ($\sim 2 \cdot 10^{-3}$). The term $\frac{1}{2} \rho_w u^2$ equals the so-called stagnation stress, which should be larger than $2 - 5 \cdot c_u$ to generate mass erosion.

The values '2' and '5' relate to two geotechnical failure mechanisms. The first relates to ductile failure (Figure 34) resulting from compression under confined conditions. Failure occurs when the deviatoric stress exceeds $2 \cdot c_u$ (see Section 3.1.1 and Eq. (3.7)). The second mechanism relates to the theory of Prandtl, which describes the ultimate bearing capacity of a soil during vertical loading (Figure 35). This

mechanism exhibits shear failure surfaces accompanied by plastic deformations. Prandtl found that failure occurred for a deviatoric stress q exceeding $(2+\pi)c_u \approx 5c_u$.

The mass erosion rate is likely to correlate with c_u as well. Also, small irregularities of the surface of the sediment bed may influence the mass erosion rate. This indicates the importance of the stochastic character of both the flow and the undrained strength of the bed. Furthermore, it is noted that undrained responses not only occur for cohesive material, as purely granular mixtures can also exhibit undrained behaviour (e.g. mass erosion in the silty bed of the Yellow river, see Van Maren *et al.*, 2009).

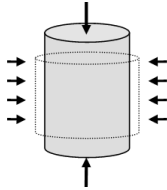


Figure 34. Ductile failure of a soil, see also Figure 26.

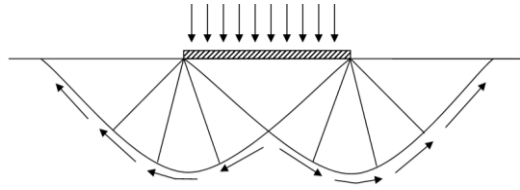


Figure 35. Shear failure of a soil following the theory of Prandtl.

The scheme in Figure 36 proposes a classification for erosion modes based on a geotechnical approach. It distinguishes different erosion modes by relating the drained and undrained sediment strength to the erosion threshold. A stable bed occurs when turbulent stress fluctuations ($\hat{\tau}_b$) do not exceed the drained strength of the bed (c_d). When these fluctuations exceed c_d , flocs are locally eroded (i.e. floc erosion). Surface erosion occurs when $\bar{\tau}_b$ is larger than c_d , but smaller than the undrained strength (c_u). Finally, mass erosion occurs when $\hat{\tau}_b$ exceeds c_u .

It is noted that according to this scheme floc and surface erosion may occur simultaneously when $\hat{\tau}_b > c_d$ and $\bar{\tau}_b < c_d$. The same accounts for surface and mass erosion, which may simultaneously occur when $\hat{\tau}_b > c_u$ and $\bar{\tau}_b < c_u$. Furthermore, the erosion rates for floc and mass erosion are expected to strongly relate to the stochastic character of the flow.

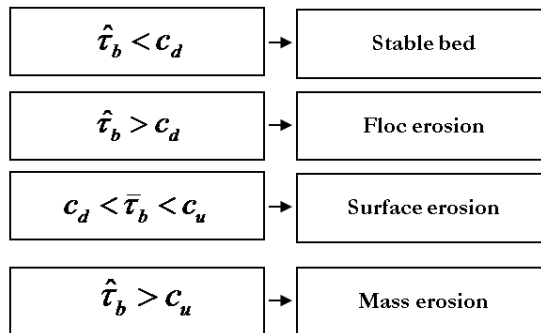


Figure 36. New classification scheme for erosion modes based on erosion thresholds, reflected by the drained and undrained strength of the bed, in relation to the mean and turbulent component of the deviatoric stress.

3.3 New surface erosion formulation

In this section a new formulation for the surface erosion rate is derived. This formulation is to a large extent based on the formulation proposed by Winterwerp and Van Kesteren (2004) for surface erosion of cohesive sediments:

$$E = M_E(\tau_b - \tau_e)\rho_{dry}, \text{ for } \tau_b > \tau_e \quad (3.24)$$

$$M_E = \frac{c_v \phi_{s,0}}{10d_{50,m}c_u} \quad (3.25)$$

where E [$\text{kg}\cdot\text{m}^2\cdot\text{s}^{-1}$] is an erosion rate, M_E [$\text{m}\cdot\text{Pa}^{-1}\cdot\text{s}^{-1}$] an erosion parameter, $\phi_{s,0}$ [-] the volume concentration of the sediment bed at the onset of swelling, $d_{50,m}$ the median particle size of the mud fraction, τ_b [Pa] the bed shear stress and τ_e [Pa] the erosion threshold. The latter two parameters reflect the combined effect of normal and shear stresses (see Section 3.2.2). Figure 37(a) indicates that the formulation shows a favourable agreement with some experimental data.

The current thesis presents a more accurate and more complete derivation of the formulation for surface erosion compared to the derivation presented by Winterwerp and Van Kesteren (2004). In addition, the formulation aimed not only at cohesive sediments, but also at sand-mud mixtures. Erosion experiments are executed to verify whether the formulation may be applied to both types of sediment beds.

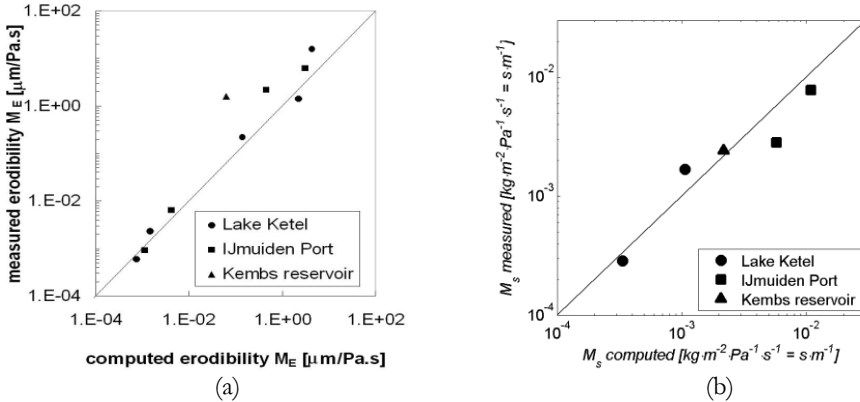


Figure 37. The left panel shows measured erodibility as a function of theoretically derived data using the formulation of Winterwerp and van Kesteren (2004). In (b) the same measured data as in (a) is shown, but now as a function of theoretically derived erodibilities following Eq. (3.36), with $n_{fr} = 2.55$.

In the following, the hydrodynamic forcing is assumed constant in time. Furthermore, the bed is initially stable, which indicates a normally consolidated bed ($OCR = 1$) with no pore water pressure gradients and, therefore, no pore water flow. The strength of a normally consolidated bed equals c_d . Upon loading due to flow-induced deformations and/or over-consolidation upon erosion, the strength of a soil

equals c_u , due to negative pore water pressure. As discussed, the strength of sediment beds decreases during surface erosion from c_u towards c_d due to swelling.

Let us consider the behaviour of an over-consolidated bed. During swelling the pore water pressures gradients resulting from the over-consolidated state are dissipated. This process compares to one-dimensional consolidation, which is described by the Gibson diffusion-advection equation (Gibson *et al.*, 1976):

$$\frac{\partial e}{\partial t} + (1 + e)^2 \left(\frac{\rho_{sed} - \rho_w}{\rho_w} \right) \frac{\partial}{\partial z} \left(\frac{k}{(1+e)^2} \right) + \frac{(1+e)^2}{g\rho_w} \frac{\partial}{\partial z} \left(\frac{k}{1+e} \frac{\partial \sigma'_z}{\partial z} \right) = 0 \quad (3.26)$$

with σ'_z [Pa] as the effective vertical stress. Eq. (3.26) is expressed in Eulerian co-ordinates, in contrast with the Lagrangian co-ordinates in the classical Gibson equation.

The consideration of the co-ordinate system concerns the boundary conditions close to the water-bed interface. In case of erosion, sedimentation and/or consolidation the moving boundary (Lagrange co-ordinate system) at this interface becomes rather complicated. The Eulerian co-ordinate system uses a fixed co-ordinate system in space, which is more convenient for morphological numerical studies. Therefore, the current study applies the Eulerian co-ordinate system approach.

By assuming (1) constant permeability and (2) the occurrence of only small deformations, which implies a small difference between the actual and initial void ratio, the advection term in Eq. (3.26) drops out. Furthermore, by substituting the pore water pressures gradient diffusion coefficient c_v (Eq. (3.12)), Eq. (3.26) reduces to the one-dimensional consolidation equation proposed by Terzaghi (1940):

$$\frac{\partial \sigma'_z}{\partial t} - c_v \frac{\partial^2 \sigma'_z}{\partial z^2} = 0 \quad (3.27)$$

The Terzaghi equation applies to the final phase of consolidation (i.e. not for freshly deposited flocs).

The typical time-scale for swelling (i.e. reversed consolidation) follows from the solution of Eq. (3.27):

$$T_s \propto \frac{z^2}{\pi c_v} \quad (3.28)$$

where z [m] is the depth below the water-bed interface. The swelling velocity (V_s [m·s⁻¹]) is obtained by differentiating Eq. (3.28) to time:

$$V_s = \frac{dz}{dt} = \frac{\pi c_v}{2z} \approx \frac{c_v}{z} \quad (3.29)$$

Eq. (3.29) implies that V_s is inversely proportional to z (Figure 38(a)). When substituting V_s for V in Eq. (3.21), and by assuming drained conditions ($Pe_w \leq 1$), Eq. (3.29) equals Eq. (3.21) as $V_s \leq c_v/\ell$.

During swelling the erosion depth $\delta_e(t)$ [m] and the length scale reflecting the diffusion process $\delta_s(t)$ [m] are important. At $z = \delta_e(t)$ the internal stresses in the sediment bed resulting from turbulent flow equal the remoulded shear strength of the bed (sediment bed is locally at its critical state). For $z < \delta_e(t)$, $c^* = c_d$, which indicates

that the strength of the bed equals the sum of cohesive and adhesive bonding forces. The layer becomes mobile when flow induced stresses exceed c_d .

For $z > \delta_s(t)$ the strength of the bed has not significantly decreased and still equals c_u^* . The location of $\delta_s(t)$ depends on the hydraulic forcing in the bed, the erosion velocity (V_e [$\text{m}\cdot\text{s}^{-1}$]) and the soil characteristic c_v . In case of no erosion ($\tau_b < \tau_{e,s}^*$), the dissipation of pore water pressure gradients continues, as shown in Figure 38(a). Initially, V_s is infinitely large for small δ_s as is indicated by Eq. (3.29). The increase of δ_s with time implies that the path-length of the transport of water from the surface into the sediment bed increases, which implies that for $\lim_{t \rightarrow \infty} V_s = 0$.

The strength of the upper layer of the sediment bed decreases during swelling. Erosion starts when $\bar{\tau}_b$ exceeds $\tau_{e,s}$ ($\approx c_d$). The maximum erosion rate equals the downward propagation speed of the swelling front. These identical velocities result in constant δ_s , as shown in Figure 38(b). Furthermore, the initial deformation rate of the bed is larger for larger τ_b , which implies larger V_s and a faster decrease of the strength of the bed. This indicates an earlier start of erosion and therefore, smaller δ_s .

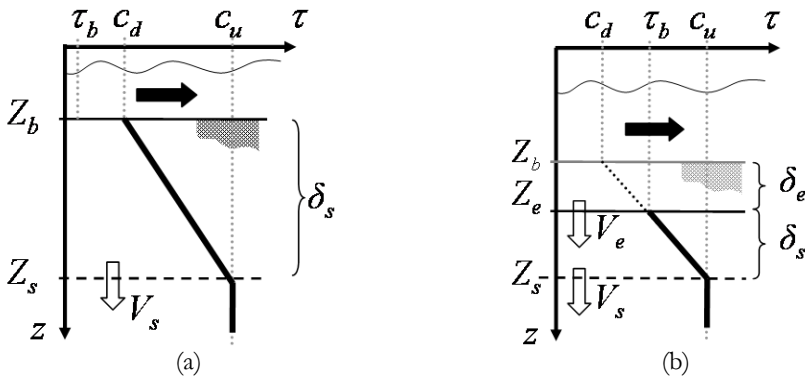


Figure 38. Schematized vertical distributions of the bed strength of a swelling, non-eroding bed (a) and a swelling, eroding bed (b). In (a) the flow only generates small deformations resulting in dilation, whereas in (b) swelling results from over-consolidation due to the removal of sediments. In (b) δ_s is constant as the hydrodynamic forcing, the erosion velocity and the bed characteristics are constant in time. δ_s is here indicated at a depth for which the bed strength is e.g. 99% of c_u .

The strength at the surface of a normally consolidated bed equals c_d , by definition. Therefore, the drained strength is considered as the ‘true’ erosion threshold for surface erosion. This only applies to cohesive sediments, as for purely granular mixtures also the properties of individual grains become important. Furthermore, it is assumed that the strength of the bed linearly increases with depth to c_u for $z > \delta_s(t) + \varepsilon$, where ε is an infinitesimal distance below $\delta_s(t)$ (for $\lim_{z \rightarrow \infty} V_s = 0$).

As the current study focuses on a stationary flow over homogeneous beds, the hydrodynamic forcing, the erosion velocity and the bed characteristics are constant in

time. Therefore, also V_s is constant in time. This implies that V_s only depends on V_e for stationary flow and a homogeneous bed, and that the exact values of δ_s and ε are not important. The thickness of the erosion layer follows from geometry (Figure 38(b)):

$$\delta_e = \delta_s \frac{\tau_b - c_d}{c_u - c_d} \quad (3.30)$$

So far, the derivation of a new formulation for surface erosion agrees with the derivation discussed in Winterwerp and Van Kesteren (2004). However, the next part of the derivation deviates from this approach. It is assumed that a cohesive bed consists of layers of deposited flocs, as schematically shown in Figure 31. It is further assumed that a cohesive bed erodes by means of the successively removal of these layers. This implies that the typical value for δ_e equals the floc size D_f [m]. Following the fractal approach for cohesive soils (Kranenburg, 1994) the volume concentration of a floc ϕ_f [-] yields:

$$\phi_f = \phi_s \left(\frac{D_f}{D_p} \right)^{3-n_{fr}} \quad (3.31)$$

where ϕ_s [-] is the volume concentration of solids (i.e. primary particles), D_p [m] the diameter of primary particles and n_{fr} [-] the fractal dimension.

By substituting $\phi_f = 1$ (per definition for consolidated soils) and by substituting the median grain size of mud $d_{50,m}$ [m] for D_p and $\phi_{s,0}$ for ϕ_s , δ_e becomes:

$$\delta_e = D_f = d_{50,m} \phi_{s,0}^{1/(n_{fr}-3)} \quad (3.32)$$

By substituting δ_e in Eq. (3.29) a maximum value for V_s is obtained. V_s and V_e are equal for an eroding bed, this leads to a formulation for the maximum erosion velocity $V_{e,max}$ [$m \cdot s^{-1}$] for which drained failure occurs:

$$V_{e,max} = \frac{c_v}{\delta_e} = \frac{c_v}{d_{50,m} \phi_{s,0}^{1/(n_{fr}-3)}} \quad (3.33)$$

It is important to realize that this maximum V_e occurs for $\tau_b = c_u$, for which δ_e is maximum and equal to δ_s . For $c_d < \tau_b < c_u$, $\delta_s > \delta_e$ and $V_e < V_{e,max}$.

By substituting Eq. (3.29) and Eq. (3.32) into the time derivative of Eq. (3.30), and by assuming $c_u \gg c_d$ and $V_e = V_s$, a formulation for the surface erosion velocity is derived:

$$V_e = V_s \frac{\tau_b - c_d}{c_u - c_d} = \frac{c_v}{\delta_e c_u} (\tau_b - c_d) \quad (3.34)$$

As expected, Eq. (3.34) reduces to Eq. (3.33) for $\tau_b = c_u$. The combination of Eq. (3.34) with the density of the sediment bed leads to a new formulation for surface erosion:

$$E_s = M_s (\tau_b - \tau_e) \text{ for } \tau_b > \tau_e \quad (3.35)$$

$$M_s = \frac{c_v \rho_{dry}}{\delta_e c_u} = \frac{c_v \rho_{dry}}{d_{50,m} \phi_{s,0}^{1/(n_{fr}-3)} c_u} \quad (3.36)$$

where E_s [$\text{kg}\cdot\text{m}^{-2}\cdot\text{s}^{-1}$] is the surface erosion rate and M_s [$\text{kg}\cdot\text{m}^{-2}\cdot\text{s}^{-1}\cdot\text{Pa}^{-1} = \text{s}\cdot\text{m}^{-1}$] the surface erosion parameter. M_s is a function of the coefficient of pore water dissipation and the undrained strength, which are further elaborated in Chapter 4. The relation between erosion and these two geotechnical material parameters reduces the amount of empiricism compared to the currently used fully empirical formulations.

The term with the fractal dimension replaces the factor ‘10’ in the formula proposed by Winterwerp and Van Kesteren (2004), Eq. (3.25). The fractal dimension for flocs in the water column varies between 1.4 to 1.7 - 2.2 for fragile flocs (marine snow) and for strong flocs in estuaries and coastal waters, respectively. For consolidated flocs within the sediment bed n_{fr} varies between 2.65 for cohesive flocs, to around 2.85 for sandier sediments (Winterwerp and Van Kesteren, 2004).

For sand-mud mixtures with a granular porosity close to its maximum, $\phi_{s,0}$ typically varies between 0.5 - 0.7 for $\rho_{bulk} = 1800 - 2100 \text{ kg}\cdot\text{m}^{-3}$, respectively. This implies that $\phi_{s,0}^{1/(3-n_{fr})}$ varies between 0.36 and 0.09 for $n_{fr} = 2.65$ and 2.85 ($\rho_{bulk} \approx 2100 \text{ kg}\cdot\text{m}^{-3}$), respectively; and between 0.14 and 0.01 for $n_{fr} = 2.65$ and 2.85 ($\rho_{bulk} \approx 1800 \text{ kg}\cdot\text{m}^{-3}$), respectively. As a result, E_s decreases for sandier sediments as well as for decreasing $\phi_{s,0}$ (i.e. decreasing ρ_{bulk}). Figure 37(b) shows that the new formulation for surface erosion (Eq. (3.36)) shows a favourable agreement with the experimental data of Winterwerp and Van Kesteren (2004). The applied fractal dimension ($n_{fr} = 2.55$) to obtain optimal agreement agrees with the expected n_{fr} for relatively loosely packed cohesive soils ($W \approx 80 - 300\%$).

Figure 39 shows the time-variation of V_s , V_e , δ_s and δ_e for increasing ((a) and (c)) and decreasing ((b) and (d)) flow velocity. Initially the bed is not eroding (for $0 < t < t_c$), although dilation occurs due to hydrodynamic forcing. In this period V_s decreases with time due to increasing δ_s . For $t > t_c$ erosion starts. The subscript \cdot_c indicates that from this moment onward δ_s is constant in time, which results from equal V_s and V_e , as indicated by Figure 39(a) and (b) and by the identical slopes of both z_s and z_e as a function of time in Figure 39(c) and (d). The latter two figures show that δ_s is indeed constant in time.

Figure 39(a) and (c) show the effect of the sudden increase of τ_b , whereas Figure 39(b) and (d) show the response of the bed after a sudden decrease of τ_b . For increasing τ_b both V_s and V_e increase, resulting in smaller δ_s . This decrease of δ_s implies that when the bed adjusts to a new forcing condition, V_e is larger than V_s . This is indicated by the larger slope of Z_e compared to Z_s in Figure 39(c). In the period that V_e is larger than V_s , a sudden increase of the amount of eroded material is expected. The contrary is expected for a sudden decrease of τ_b , as shown in Figure 39(b) and (d). When the bed is adjusting to the new forcing condition, temporarily no erosion occurs, as δ_s has to increase first. In this way the bed strength (i.e. τ_e) can decrease, so that erosion occurs for the ‘new’ τ_b .

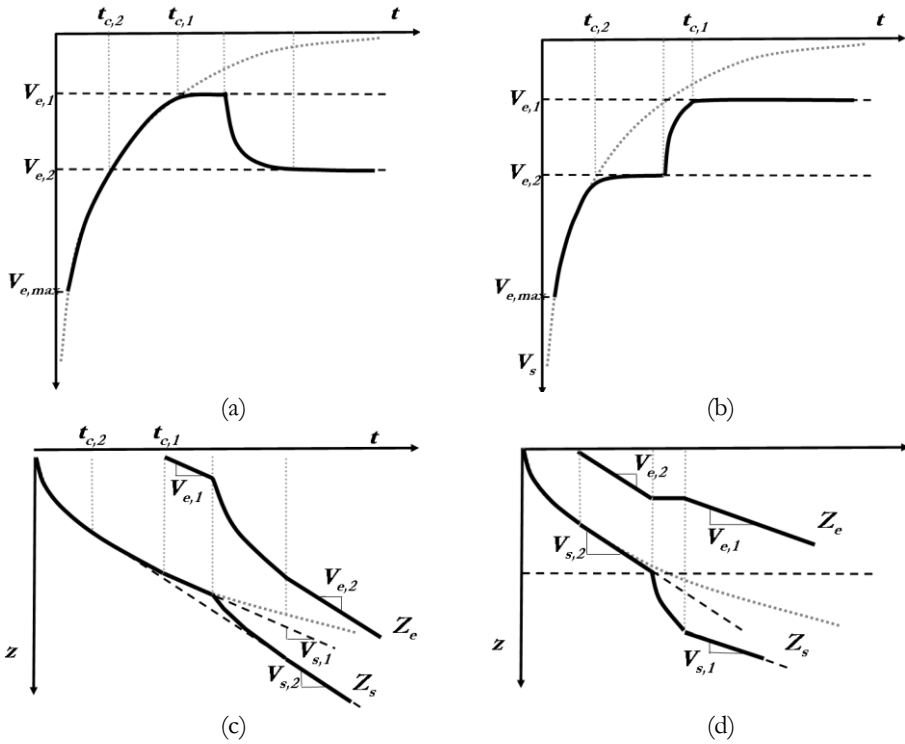


Figure 39. Schematic graphs showing the effect of varying erosion velocities $V_{e,i}$ (a and b) induced by varying flow velocities on the response of homogenous sediment beds (c and d). In (a) V_e increases from $V_{e,1}$ to $V_{e,2}$. In (b) V_e is initially relatively large ($V_{e,2}$), before it decreases to $V_{e,1}$. Figures (c) and (d) show the effect of varying V_e on Z_s and Z_e as a function of time, respectively for the conditions shown in (a) and (b). The grey-dotted lines show the response of a bed in case of no erosion.

The effects of biota on erosion properties can be incorporated in the geotechnical approach as discussed. The enhanced bonding between particles due to adhesion directly affects c_d and, therefore, the erosion thresholds of floc and surface erosion, as well as the erosion rate of floc erosion. Adhesive bonding mainly occurs for fines. Therefore, direct effects of biota are expected to occur for muddy beds. The mixing/reworking of the bed by biota changes the composition of the bed and/or the physico-chemical properties, which are both important for the granular skeleton and plasticity. The effect of both properties is reflected in the new formulation by the material properties c_v and c_u . This indicates that mixing by biota has an indirect effect on erosion properties. These indirect effects can occur both for muddy and sandy beds, and are especially important for the rates of surface and mass erosion, as well as for the erosion threshold for mass erosion.

3.4 Conclusions

The distinction between drained and undrained behaviour is important to understand cohesive and granular soil behaviour. Drained strength refers to cohesion and adhesion, whereas undrained strength also incorporates the effect of negative pore water pressure gradients. The latter generate an additional strength, which is referred to as apparent cohesion. When no distinction is made between drained and undrained strength, confusion concerning the sediment strength discussed in Chapter 2 may easily occur.

The recognition of the definition for bed strength in combination with the acknowledgement of the importance of the stochastic character of turbulent flow enabled the characterisation of a new classification for erosion modes. Floc erosion concerns the removal of individual flocs due to turbulent peak stresses exceeding the drained bed strength. Surface erosion is less dependent of the stochastic character of the flow. It concerns the overall drained failure of subsequent layers of the sediment bed upon the mean flow induced stress exceeding the drained bed strength. Mass erosion occurs when turbulent peak stresses exceed the undrained strength of the bed, which implies that mass erosion is strongly related to the stochastic character of the flow.

A formulation for surface erosion is derived following a geotechnical approach. This formulation incorporates independently measurable material parameters. The derivation is partly based on the approach of Winterwerp and Van Kesteren (2004), and partly new as also the fractal dimension of the bed is incorporated. The formulation significantly reduces the amount of empiricism compared to currently used fully empirical formulations. Additionally, it enables the incorporation of biota-effect.

In conclusion, the new approach for water-bed exchange of sediments as proposed in this chapter is promising, although the relation between normal and shear stresses induced by a turbulent flow, on the one hand, and deviatoric and isotropic stresses, on the other, is not fully understood. Following chapters present experimental results, which are compared with the newly proposed erosion classification and formulation.

Chapter 4

Material properties

The undrained shear strength (c_u) and the coefficient of pore water pressure dissipation (c_v) are characterising mechanical parameters for soil behaviour. The behaviour of c_u (Section 4.2) and c_v (Section 4.5) are discussed as a function of plasticity and granular packing. c_v is a function of the coefficient of volume variation m_v (Section 4.3) and permeability k_v (Section 0). Artificial sediment mixtures are generated (Section 4.1) to obtain reproducible soil samples, and to exclude biological and physico-chemical effects. The reasoning is that if the relation between c_u and c_v (current chapter) on the one hand, and erosion on the other can be demonstrated for physical (bulk) parameters (Chapter 7), the effect of biological and physico-chemical influences on erosion/soil behaviour can be incorporated in a similar way. Parts of this chapter have been published in Jacobs *et al.* (2007a,b; 2010).

4.1 Characteristics of artificial sediment mixtures

4.1.1 Soil sample generation

The current study focuses on the mechanical behaviour of sediment mixtures with varying sand and mud content and varying structure. This implies that $n_{sasi} \approx 40 - 60\%$ (see Section 2.2), hence $n \approx 35 - 50\%$ and $\rho_{bulk} \approx 1700 - 2000 \text{ kg}\cdot\text{m}^{-3}$ ($W \approx 20 - 40\%$) for $\xi_{cl} \approx 5 - 20\%$. These characteristics indicate relatively dense soils with relatively large ξ_{sa} . The sand and silt fractions have d_{50} comparable to Western Scheldt sediments (Section 2.3.5). ρ_{bulk} and W (oven-drying at 105°C for 24 hours) are determined following ASTM 2216.

Sediment mixtures are artificially generated using a dedicated experimental laboratory set-up (Figure 40(a)) at a constant temperature of 19°C . First, the individual fractions are oven-dried to disaggregate the material. Next, sand, silt and clay are manually mixed for around 10 minutes. The dry mixture is subsequently placed in a cylindrical container with a removable bottom-lid (Figure 40(b)). Small holes (diameter = 3 mm) in the bottom and top-lid allow the passage of water and gas; paper filters at both ends retain the grains.

Direct saturation by pouring water on top of dry sediment mixtures causes blocking of small pores by the surface tension of water, which then generates partly-saturated soil samples. Therefore, the containers with dry sediments are placed in an exsiccator to remove air by lowering the pressure to ~ 200 mbar. Next, the exsiccator is filled with CO_2 , after which the pressure is lowered again to replace enclosed air in the voids of the mixture with CO_2 .

Subsequently, mixtures are left for 24 hours in the exsiccator, in which a layer of water is present. The combination of the low pressure (reduced surface tension), 100% humidity and the attractive forces of the negatively charged clay particles enables water molecules to 'activate' clay particles in the smallest pores. Longer tests showed that the most significant part of the increase of W occurs well within 24 hours.

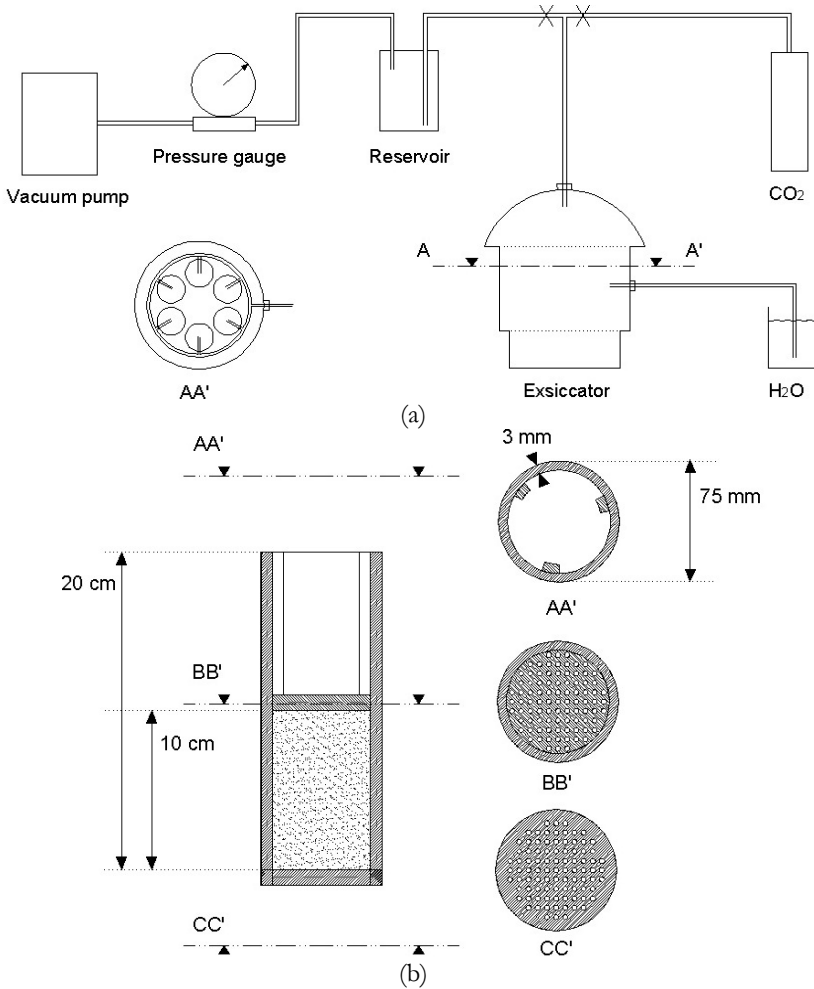


Figure 40. Schematized depictions of the experimental set-up to saturate dry mixtures (a) and of a cylindrical plastic container holding the soil samples (b).

The second part of the saturation process concerns the placement of a layer of 10 cm de-aired and demineralised water on top of the soil samples using the difference between the atmospheric and reduced pressure within the exsiccator. Subsequently, water percolated through the mixture, thereby completing the saturation procedure. The pressure induced by the water column (1 kPa) corresponds with the target strength of the soil samples. Therefore, no consolidation is anticipated. The volume of water (~ 0.5 litre) is sufficiently large to fill all pores and to dissolve all enclosed gas ($\sim 3.8 \cdot 10^{-4}$ mol of CO_2).

The saturation degree of the soil samples treated this way is about 100%. The relatively dense packing prevents segregation of the fractions during the saturation process. This experimental procedure generates reproducible and isotropic soil samples. This implies the absence of pore water pressure gradients, which would initiate swelling or consolidation.

4.1.2 Micro-scale properties

Before elaborating on the properties of the sediment mixtures, the characteristics of the individual sand, silt and clay fractions, as used in the current study, are discussed. Grain size analyses were executed to determine ζ_{cl} , ζ_{si} and ζ_{sa} of the purchased sand, silt and clays. The choice for a specific method to determine the grain size distribution is arbitrary, as results obtained by different methods may exhibit large variations (e.g. McCave, 2006; EC MAST-I, 1993) due to varying de-flocculation and calibration methods.

Grain size distributions were determined by a Sedigraph, two Malvern Laser Sizers and three Coulter Counters. Tests were executed at different institutes by experienced operators following international standards. Results for sand ($\zeta_{sa} \approx 98\%$) and silt ($\zeta_{sa} \approx 20\%$, $\zeta_{si} \approx 75\%$) are consistent for all methods. Yet, significant differences exist for ζ_{cl} of the clays, both between different and similar methods employed at different institutes (Appendix I).

ζ_{cl} was found to vary between 14 - 31% for kaolinite, 14 - 65% for illite and 3 - 54% for bentonite. In general, the larger ζ_{cl} are found using the Sedigraph method. For practical reasons the Sedigraph results are used in the current study (Table 7) to determine the required amounts of (purchased) sand, silt and clay to generate sand-mud mixtures.

Table 7. Results of Sedigraph grain size analyses on purchased sand, silt and clays.

	Sand	Silt	Kaolinite	Illite	Bentonite
ζ_{sa} [%]	99	18	0	0	7
ζ_{si} [%]	1	78	69	35	39
ζ_{cl} [%]	0	4	31	65	54
d_{50} [μm]	180	30	4	2	2
A	-	-	0.67	0.78	1.34

X-ray diffraction analyses were executed on the clay fraction smaller than $2\ \mu\text{m}$ to determine clay mineralogy (Appendix II). The results indicate that the (purchased) bentonite used in this study consist of bentonite minerals only. The illite sediments contain around 50% illite and 50% kaolinite minerals, with negligible amounts of montmorillonite minerals. It is also found that both the kaolinite and illite sediments contain small amounts of quartz. However, no information is available on the mineralogy of the clay sediments for the fraction larger than $2\ \mu\text{m}$, which may still contain clay minerals and/or quartz. Finally, the specific density was experimentally determined, which is about $2650\ \text{kg}\cdot\text{m}^{-3}$ for all fractions.

4.1.3 Meso-scale (bulk) properties

The Atterberg Limits of the clays are determined following Head (1980) and ASTM 4318. For the current study, LL is determined using a Swedish fall cone (BS 1377). Results for the artificial soils, which exhibit varying structural and mineralogical composition are shown in an activity plot (Figure 41). A follows from Eq. (2.11) and yields 0.67, 0.59 and 1.34 for kaolinite, illite and bentonite, respectively. For kaolinite and bentonite the offset for cohesive behaviour $\xi_{cl,0}$ is approximately zero; for illite $\xi_{cl,0} = 10\%$.

PI is not determined for all artificial soil samples (for practical reasons), but indirectly determined by multiplying A with $(\xi_{cl} - \xi_{cl,0})$. This also enables the expression of the plasticity of granular soils, whose PI is too low to be determined experimentally. This extrapolated plasticity index (PI^* [%]) yields:

$$PI^* = A(\xi_{cl} - \xi_{cl,0}) \quad (4.1)$$

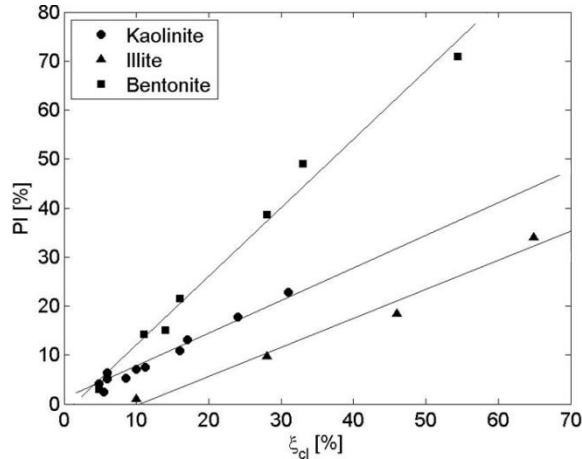


Figure 41. Activity plot indicating PI as a function of ξ_{cl} for sand-mud mixtures with varying structural and mineralogical composition. The slope reflects the clay's activity A and the ordinate indicates the offset for cohesive behaviour $\xi_{cl,0}$.

Section 2.2.1 discusses why the Liquidity Index LI is not convenient to characterise cohesive soils with relatively large W . However, to properly characterise sand-mud mixtures it is necessary to combine the Atterberg Limits (\sim cohesiveness) with the degree of packing. Therefore, the relative water content (W_{rel} [-]) is introduced:

$$W_{rel} = \frac{W}{PI} \quad (4.2)$$

W_{rel} enables the classification of mixtures with varying \mathcal{A} , ξ_{cl} and W , which is convenient when comparing soils from different marine systems or with different initial conditions due to consolidation. In the current study PI is replaced by PI^* to determine W_{rel} .

Sand-mud mixtures exhibit either a granular skeleton or a clay-water matrix, characterised by the porosity of the granular skeleton (n_{sasi} [-]) consisting of sand and silt (Section 2.2.2). The discriminator between these structures is the maximum granular porosity (i.e. the loosest packing) $n_{sasi,max}$ [-], whereas $n_{sasi,min}$ [-] reflects the minimum granular porosity (i.e. the densest packing).

Transitions in soil structure are indicated in Figure 42. Minimum and maximum granular porosities of six artificial mixtures of sand and silt are determined by a geotechnical institute following a procedure based on ASTM 4254 (see Figure 42). Van Kesteren (2008) determined an empirical function for $n_{sasi,max}$:

$$\begin{aligned} n_{sasi,max} = & n_{si,max} - n_{si,max}(1 - n_{si,max})\psi_{sasi} + \\ & (a - 1 + 4n_{sa,max} - n_{si,max} - 2n_{si,max}^2)\psi_{sasi}^2 - \\ & (2a - 1 + 3n_{sa,max} - n_{si,max} - n_{si,max}^2)\psi_{sasi}^3 + a\psi_{sasi}^4 \end{aligned} \quad (4.3)$$

where $n_{sa,max}$ [-] and $n_{si,max}$ [-] are the maximum porosities of soils consisting of 100% sand and silt, respectively. When assuming identical specific densities for sand and silt (see previous section), ψ_{sasi} [-] reflects ξ_{sa} [-] in relation to ξ_{si} [-]:

$$\psi_{sasi} = \frac{\xi_{sa}}{\xi_{sa} + \xi_{si}} \quad (4.4)$$

The dimensionless coefficient $a = 0.39$ follows from:

$$a = \frac{a_1 + a_2 + a_3 + a_4}{a_5} \quad (4.5)$$

with $a_1 = n_{si,max}(1 + 2\psi_{sasi,min} - 3\psi_{sasi,min}^2)$, $a_2 = \psi_{sasi,min}^2(-1 + 4\psi_{sasi,min} - 3\psi_{sasi,min}^2)$, $a_3 = n_{sa,max}(-8\psi_{sasi,min} + 9\psi_{sasi,min}^2)$, $a_4 = 2\psi_{sa,min} - 3\psi_{sasi,min}^2$, $a_5 = 2\psi_{sa,min} - 6\psi_{sasi,min}^2 + 4\psi_{sasi,min}^3$. $\psi_{sasi,min}$ [-] at minimum $n_{sasi,max}$ equals 0.77 and 0.64, respectively for $n_{sasi,max}$ and $n_{sasi,min}$.

Eq. (4.3) can also describe $n_{sasi,min}$ if we replace $n_{si,max}$ ($= 0.61$) by $n_{si,min}$ ($= 0.43$) and $n_{sa,max}$ ($= 0.50$) by $n_{sa,min}$ ($= 0.38$). Then Eq. (4.3) can also describe the transition between sediments with a sand-silt skeleton and sedimentary rock. Figure 42 indicates that $n_{sasi,min}$ and $n_{sasi,max}$ are functions of the ratio of the volume fractions of sand and silt. Note that at constant n_{sasi} both the dominant structure and packing density

$(n_{sasi}/n_{sasi,max})$ may vary. Both variations can significantly affect soil mechanical behaviour.

It is emphasized that ψ_i relates to the volume fraction of a specific sediment fraction and ξ_i to its mass content. Although ψ_i equals ξ_i for identical specific density, the current thesis distinguishes between both parameters: ψ_i is applied when discussing packing density, ξ_i is applied when discussing the ratio of (dry) sediments.

As water binds to clay, a relation between ξ_{si} and ξ_{cl} (Section 2.3.4) also implies a relation between ξ_{si} and W (see also Section 2.3.4). This ratio is illustrated by the dashed line in Figure 42. The slope of this line relates to the water-bonding capacities (PI) of clay. This implies that the transition between a granular skeleton and a clay-water matrix depends on the characteristics of sand and silt on the one hand, and on PI on the other. Both $n_{sasi}/n_{sasi,max}$ and PI exhibit typical value ranges for individual marine system.

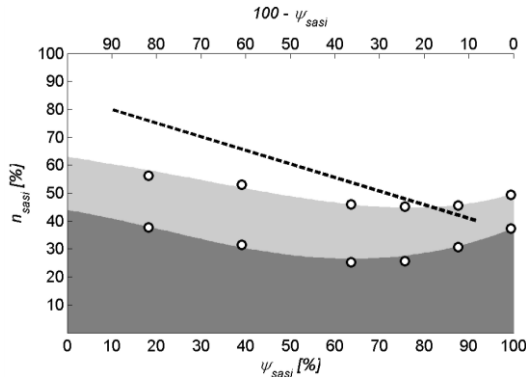


Figure 42. Granular porosity as a function of the sand-silt volume fraction ratio. The shaded areas indicate different structures: clay-water matrix (top), sand-silt skeleton (middle) and sedimentary rock (bottom). The markers represent experimental data fitted with Eq. (4.3). The line reflects typical soil compositions for sand-mud mixtures at constant clay-silt ratio.

4.2 Undrained shear strength

4.2.1 Experimental procedure

The undrained shear strength is determined with a shear vane test, which is a well-known geotechnical test (NEN 5106, BS 1377, ASTM 4648 and Head, 1980). The soil behaviour during this test is discussed in detail in Section 3.1.3, and illustrated by Figure 27. Tests are executed using the Anton Paar Physica MCR 301 rheometer of the *Centre Ifremer de Brest* (Jacobs *et al.*, 2010) using a six-bladed vane with a diameter of 2.2 cm and a height of 1.6 cm. The vane is rotated at constant rate (1 rpm) for 10

revolutions. Table 8, Figure 43 and Figure 44 give the composition and bulk properties of the sand-mud mixtures examined in this section.

Compositions of the artificial sediments are chosen such that the effect of the transition between a sand-silt skeleton and a clay-water matrix on c_u can be studied. Figure 44, in combination with Table 8, indicates that the transition between a sand-silt skeleton and a clay-water matrix occurs at $PI^* \approx 7$. This transition agrees with plasticity charts (PI as a function of LL), which are classification schemes for cohesive soils based on empirical data (Casagrande, 1932). W_{rel} at this transition amounts to 4.5 and 3 for kaolinite and bentonite, respectively. These values are derived from Table 8 and agree with calculated values (combining Eq. (2.13) and Eq. (4.2)). However, constant W_{rel} at the transition for soils with varying clay mineralogy is expected. A possible cause for the variation of W_{rel} is the inaccuracy in determining ζ_{cl} (and $\zeta_{cl,0}$).

Table 8. Composition and bulk properties of soil samples tested with a shear vane. For set 1, 2 and 5 the clay-silt ratios are 0.25, 0.4 and 0.25, respectively. For set 3 and 4 the sand-silt ratio is 0.8 and 0.5, respectively. The clay mineralogy for set 1 – 4 is kaolinite and for set 5 bentonite.

	N_o	ζ_{cl} [%]	ζ_{si} [%]	ζ_{sa} [%]	ψ_{sasi} [%]	ρ_{bulk} [kg·m ⁻³]	W [%]	n_{sasi} [%]	PI^* [%]	W_{rel} [-]
Set 1	1.	2	8	90	92	1994	23	39	1.4	17.0
	2.	5	19	76	80	1992	24	41	3.3	7.1
	3.	6	24	70	74	1983	24	42	4.1	5.8
	4.	11	45	44	50	1885	31	51	7.7	4.0
	5.	16	64	20	24	1768	42	60	11.0	3.8
Set 2	6.	2	5	93	95	1965	25	41	1.4	18.4
	7.	4	10	86	90	2015	22	39	2.8	8.0
	8.	7	19	74	80	1966	25	44	5.2	4.9
	9.	12	30	58	66	1873	32	52	8.3	3.9
	10.	17	42	42	50	1815	37	58	11.4	3.2
Set 3	11.	3	19	78	80	2050	20	36	2.1	9.7
	12.	5	19	76	80	2017	22	39	3.3	6.6
	13.	6	19	75	80	1983	24	42	4.1	5.8
	14.	7	18	74	80	1956	26	45	5.1	5.1
	15.	8	18	74	80	1944	27	46	5.6	4.8
Set 4	16.	2	49	49	50	2100	17	33	1.7	10.6
	17.	5	47	47	50	1994	23	41	3.8	6.2
	18.	8	46	46	50	1965	25	45	5.8	4.3
	19.	12	41	47	54	1873	32	52	8.1	4.0
	20.	16	42	42	50	1786	40	59	11.4	3.5
Set 5	21.	2	8	90	92	1976	25	40	2.8	8.9
	22.	5	19	76	80	1991	24	41	6.7	3.5
	23.	6	24	70	75	1981	24	42	8.3	2.9
	24.	11	44	45	50	1818	37	55	15.5	2.4
	25.	16	63	21	25	1711	48	63	22.0	2.2

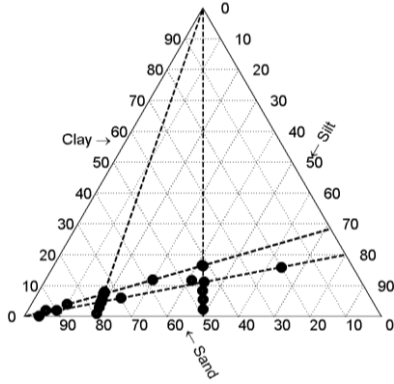


Figure 43. Ternary diagram relating ζ_{cl} , ζ_{si} and ζ_{sa} for all soil samples indicated in Table 8. The dashed lines indicate constant clay-silt (left-right) and constant sand-silt ratios (top-bottom).

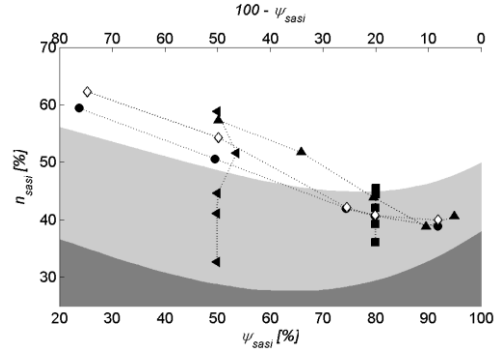


Figure 44. Granular porosity as a function of the sand-silt volume fraction ratio for all soil samples indicated in Table 8: set 1 (●), 2 (▲), 3 (■), 4 (◀) and 5 (◇, bentonite). Increasing ζ_{cl} yields a transition from a sand-silt skeleton to a clay-water matrix.

4.2.2 Results and discussion

Figure 45 displays the results of the shear vane measurements. Only small differences were found between the results of sets 1, 2, 3 and 4, although their structures are significantly different. Larger differences were found due to different clay mineralogy, as soil samples with bentonite exhibit generally larger c_u . Furthermore, minimum strengths of about 0.1 and 0.5 kPa were found for mixtures with kaolinite and bentonite, respectively.

The combination of Figure 45 with the structural classification indicated in Figure 44 enables a qualitative explanation of the behaviour of c_u . Generally, c_u is expected to increase with increasing cohesiveness (i.e. increasing ζ_{cl} and PI) and/or increasing packing density (i.e. increasing n_{sasi} and/or decreasing W). This behaviour is only partly reflected by the results, as Figure 45(a) indicates that c_u first decreases and, subsequently, increases with increasing ζ_{cl} . Figure 45(b) indicates that with increasing ρ_{bulk} , c_u first decreases and, subsequently sharply increases.

Schofield and Wroth (1968) argue that c_u at LL is 1 - 3 kPa. This explains that c_u of all tested soils is just below 1 kPa, as W of all soil samples is just above LL . Furthermore, results agree with Mitchell (1976) and Van Kesteren *et al.* (1997):

$$c_u = 10^{0.4LI^2 - 2.3LI + 2.2} \quad \text{for } 0 < LI < 2.5 \quad (4.6)$$

Eq. (4.6) is compared with the experimental results in Figure 45(c) for soil samples for which the Atterberg limits are directly determined. Eq. (4.6) only applies for mixtures with a dominant clay-water matrix and relatively low W . For granular soils and freshly deposited sediments (large W) $LI \gg 2.5$. Therefore, extrapolating Eq. (4.6) to $LI > 2.5$ is questionable (see Section 2.2.1).

The transition ($\zeta_{cl} \approx 7.5\%$ and $\rho_{bulk} \approx 1950 \text{ kg}\cdot\text{m}^{-3}$) in the behaviour of c_u agrees with the transition in dominant structure. c_u increases with increasing ζ_{cl} and increasing ρ_{bulk} in case of a dominant clay-water matrix; c_u decreases with increasing ζ_{cl} and increasing ρ_{bulk} for a dominant sand-silt skeleton. Adding water and/or clay to a soil with a dominant sand-silt skeleton generates an increase of the granular porosity, which yields decreasing c_u .

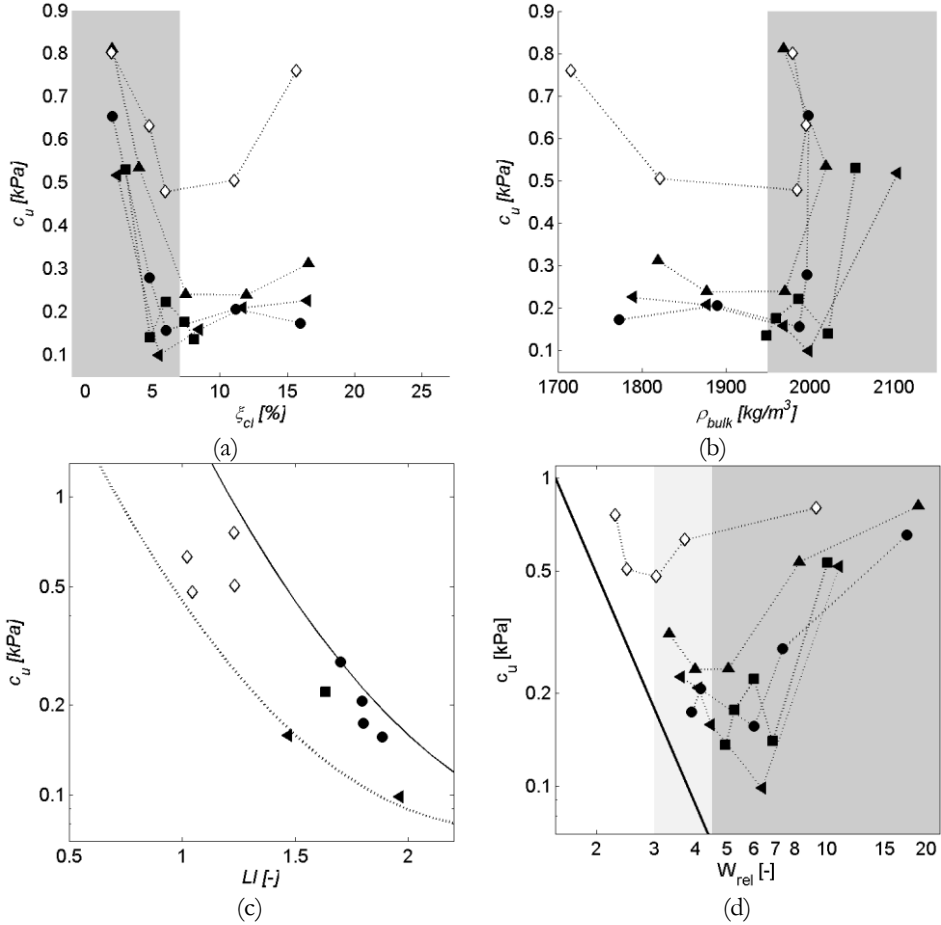


Figure 45. Undrained shear strength as a function of ζ_{cl} (a), ρ_{bulk} (b) and W_{rel} (d) for set 1 (●), 2 (▲), 3 (■), 4 (◄) and 5 (◇, bentonite). The grey-shaded areas indicate a sand-silt skeleton. The relation between LI and c_u is indicated in (c), with the continuous line representing Eq. (4.6) and the dotted line the lower limit of c_u following Mitchell (1976). The continuous line in (d) represents Eq. (4.7) and the light-grey shaded area indicates a sand-silt skeleton for soils with bentonite.

Figure 45(d) indicates that c_u increases with decreasing W_{rel} (i.e. increasing ξ_{cl}) for a clay-water matrix, and decreases for a sand-silt skeleton. W_{rel} at the transition between these structures agrees with the structural classification indicated in Figure 44. These two behaviours illustrate the combined effect of a non-cohesive granular skeleton and a cohesive matrix. Next, both behaviours are individually discussed and, subsequently, combined following a theoretically derived model suggested by Van Kesteren (2008).

The strength of a clay-water matrix depends on the relation between PI and W . The solid line in Figure 45(d) represents measured c_u of mixtures of clay and water, which are artificially generated following the same procedure as discussed in Section 4.1.1. The straight line indicates a power law relation between W_{rel} and c_u :

$$c_{u,clw} = B_1 W_{rel}^{B_2} \quad (4.7)$$

where $c_{u,clw}$ [Pa] is c_u of a clay-water mixture and B_1 ($= 2770$ Pa) and B_2 ($= -2.5$) are empirical coefficients. Such a power law function agrees with the fractal approach for the geotechnical behaviour of cohesive sediments following Kranenburg (1994). Eq. (4.7) enables the comparison of c_u of clay-water mixtures with varying W , ξ_{cl} and/or mineralogy. Figure 45(d) indicates that for a dominant clay-water matrix c_u of sand-mud mixtures approaches Eq. (4.7) for decreasing W_{rel} .

The behaviour of c_u as a function of W_{rel} for mixtures with a granular skeleton is based on Bagnold (1954). c_u of granular skeletons depends on the relation between the actual and the maximum (densest packing) volume concentration of sand and silt. Bagnold (1954) proposes the so-called linear concentration, which is the ratio of the grain diameter D and the free dispersion distance L (Figure 46). L is the distance between adjacent grains for which they have the same configuration as in the densest packing. The formulation for the linear concentration λ [-] relates to the grain volume fractions by:

$$\lambda = \frac{1}{(\phi_{sasi}/\phi_{sasi,max})^{-1/3} - 1} \quad (4.8)$$

where ϕ_{sasi} ($= 1 - n_{sasi}$) is the actual and $\phi_{sasi,max}$ ($= 1 - n_{sasi,min}$) the maximum volume concentration of sand and/or silt.

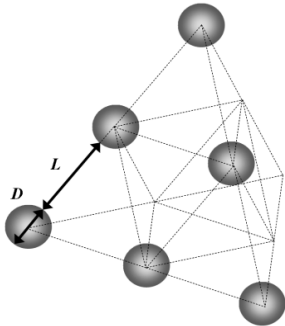


Figure 46. Schematic depiction showing the particle diameter (D) and free dispersion distance (L) of a granular sediment mixture. The linear concentration λ is the ratio between D and L (Bagnold, 1954).

The effect on c_u of the granular fraction increases with increasing λ (denser packing), which is described by an exponential function as indicated in Figure 47(a):

$$\frac{c_u}{c_{u,clw}} = e^{\alpha\lambda} \quad (4.9)$$

where α ($= 0.12$ [-]) is an empirical parameter. Figure 47(a) confirms the significance of the relation between $\phi_{sasi,max}$ and ϕ_{sasi} for the behaviour of c_u for granular soils, as all data, including those with bentonite, nicely follow Eq. (4.9). Figure 47(a) further indicates that for mixtures with relatively large λ , i.e. a densely packed sand-silt skeleton and little mud, $c_u/c_{u,clw}$ becomes rather sensitive for varying λ . As ϕ_{sasi} tends to $\phi_{sasi,max}$ (Figure 47(b)) the granular porosity is minimal, which implies that for small differences in packing density relatively large variations of c_u are expected. Figure 45 also illustrates that c_u is rather sensitive to small variations of $\rho_{bulk} > 1950 \text{ kg}\cdot\text{m}^{-3}$.

Substitution of Eq. (4.7) in Eq. (4.9) gives a formulation for c_u as a function of W_{rel} and λ for (non)cohesive mixtures of sand and mud:

$$c_u = B_1 \cdot W_{rel}^{B_2} \cdot e^{\alpha\lambda} \quad (4.10)$$

Figure 48 illustrates Eq. (4.10) for soils with varying sand content (a) and varying density (b), both for constant clay-silt ratio (1:4) and clay-mineralogy (kaolinite). Figure 48(a) further indicates that varying ξ_{sa} does not influence c_u at relatively large W_{rel} (large W). This implies that when sand and silt particles are not in mutual contact, c_u is determined by $c_{u,clw}$ only. For relatively small W_{rel} , addition of sand results in a sharp increase of c_u , as ϕ_{sasi} tends to $\phi_{sasi,max}$. This sharp increase occurs for larger W_{rel} when ξ_{sa} increases, as ϕ_{sasi} increases and tends to $\phi_{sasi,max}$. Therefore, ϕ_{sasi} tends to $\phi_{sasi,max}$ for relatively large W .

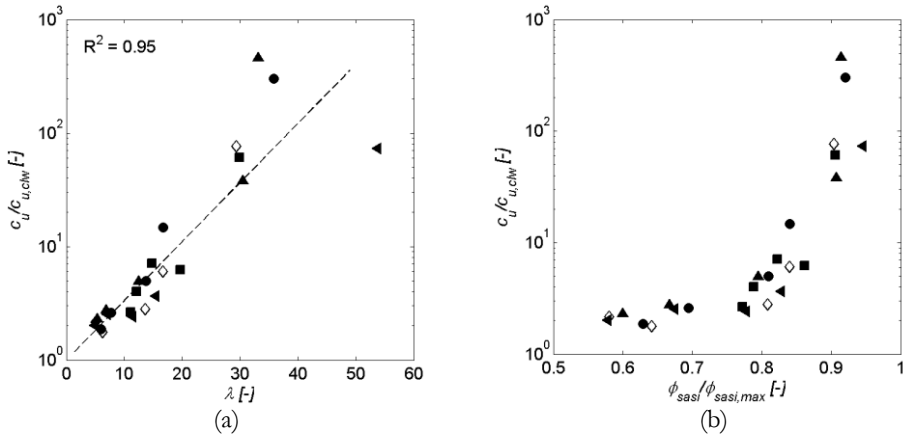


Figure 47. Total c_u divided by $c_{u,clw}$ as a function of the linear concentration (a) and as a function of the volume concentration of sand and silt divided by the maximum concentration (b) for set 1 (●), 2 (▲), 3 (■), 4 (◄) and 5 (◊, bentonite). Larger λ implies a denser packing of sand and silt.

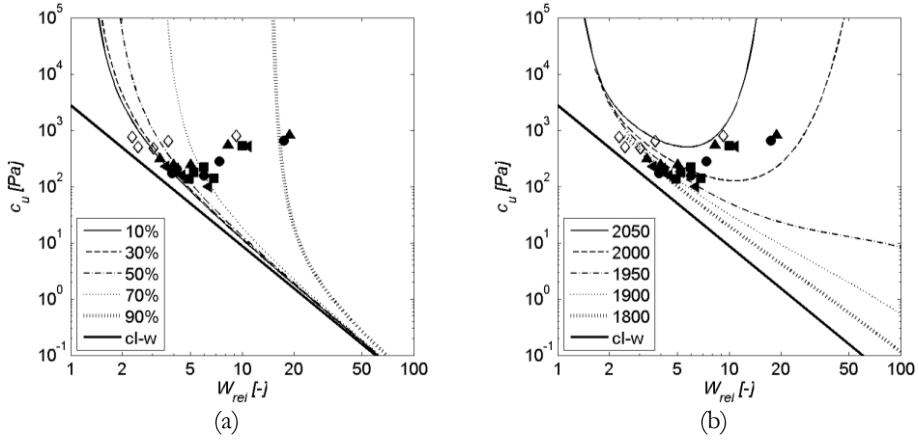


Figure 48. Modelled and measured c_u as a function of W_{rel} for sand-mud mixtures with varying ξ_{sa} (a) and varying ρ_{bulk} (b). The diagonal continuous line reflects c_u for mixtures of clay and water only (cl-w). For both (a) and (b) the clay-silt ratio (1:4) and clay mineralogy (kaolinite) are constant.

Figure 48(a) also shows that to maintain constant c_u , increasing W_{rel} requires increasing ξ_{sa} . The decrease of $c_{u,chw}$ due to increasing W_{rel} is then balanced by an increasing contribution of the granular fraction to c_u . Figure 48(b) shows decreasing and, subsequently, increasing c_u as a function of W_{rel} . This behaviour, including the transition between a sand-silt skeleton and a clay-water matrix at $W_{rel} \approx 4.5$, agrees with the results indicated in Figure 45(d). Figure 48(b) further indicates that with increasing ρ_{bulk} and constant W_{rel} (i.e. constant $c_{u,chw}$) c_u increases, which follows from increasing ϕ_{sasi} with increasing ρ_{bulk} .

c_u is almost independent of variations in ρ_{bulk} for a clay-water matrix (small W_{rel}), which confirms the dominant role of the PI . In case of a granular skeleton (large W_{rel}) and constant c_u , ρ_{bulk} decreases with increasing W_{rel} , which implies increasing W and decreasing ξ_{cl} . This behaviour is not trivial, as both the density and ξ_{cl} decrease, but c_u remains constant. However, as the clay-silt ratio is constant, the decrease of ξ_{cl} (as W_{rel} increases) leads to decreasing ξ_{si} and increasing ψ_{sasi} . Figure 42 indicates that $n_{sasi,min}$ decreases and $\phi_{sasi,max}$ increases for relatively low ξ_{cl} (sand-silt skeleton) and increasing ψ_{sasi} . The increase of $\phi_{sasi,max}$ results in larger λ and $c_u/c_{u,chw}$ (see Figure 47), which compensates for the decrease of $c_{u,chw}$ with increasing W_{rel} .

Finally, it is noted that for small W_{rel} the behaviour of the clay-water matrix changes from plastic to solid behaviour (see Figure 9), which changes the behaviour of $c_{u,chw}$, as described by Eq. (4.7). This effect is beyond the scope of the current study, and is not included in the model.

4.3 Coefficient of volume variation

4.3.1 Theory and experimental procedure

This section discusses the coefficient of volume variation m_v [$\text{m}^2 \cdot \text{N}^{-1} = \text{Pa}^{-1}$] for mixtures of sand and mud for conditions typically occurring during surface erosion. The subscript v indicates the vertical direction. Parts of the current section have been published in Jacobs *et al.* (2007a). m_v is also referred to as the compressibility or compression coefficient. However, m_v not only applies to plastic deformations during compressive loading, but also to elastic deformations during unloading conditions. Therefore, we refer to m_v as the coefficient of volume variation in the current study. To distinguish between m_v during compressive and swelling conditions, we refer to $m_{v,c}$ and $m_{v,s}$, respectively.

The theoretical discussion presented below is based on Terzaghi (1940), Terzaghi and Peck (1967) and Schofield and Wroth (1968). Vertical strain (ε [-]) due to one-dimensional (un)loading exhibits a logarithmic relation to the vertical stress:

$$\varepsilon = -\frac{1}{C} \ln \frac{p}{p_0} \quad (4.11)$$

where C [-] is the compression or swelling index, p [Pa] the vertical stress and p_0 [Pa] the initial vertical stress before loading. C is a material parameter and therefore independent of the applied stress condition. During compressive loading C is typically 10 – 100 for clay, 25 – 125 for silt and 50 – 500 for sand. By assuming small Δp compared to p_0 , the stress-strain relation yields (see also Eq. (3.11)):

$$\frac{\Delta \varepsilon}{\Delta p} = -\frac{1}{Cp} = -m_v \quad (4.12)$$

where m_v [Pa^{-1}] is the reciprocal of the soil-stiffness for a given stress condition.

For practical reasons Eq. (4.11) is generally written as a logarithmic function with base 10 ($\ln x = \log x / \ln 10$). Furthermore, the stress state for soils at rest is always located on the K_0 -stress path between the VCL and the CSL (Figure 21). The K_0 -stress path, CSL and SL are generally modelled as exponential functions of e ($\varepsilon \equiv \Delta e / (1 + e_0)$) to enable the projection of the stress state of soils on the p - e plane. Substituting the logarithmic function with base 10 and the void ratio, Eq. (4.11) becomes:

$$e = e_0 - C_i \log \frac{p}{p_0} \quad (4.13)$$

The material parameter C_i equals C_c or C_s for compression and swelling, respectively. C_c exhibits a constant relation with C_s for a particular soil mixture, which follows from the Critical State Theory. Generally, the stiffness of a soil upon unloading is approximately 10 times larger than during compression, which implies that $C_s \approx 0.1 \cdot C_c$.

The current study focuses on surface erosion during which pore water pressure gradients dissipate upon removal of overlying layers of sediment. This process of

swelling is characterised by C_s and $m_{v,s}$. Only cohesive soils exhibit a significant elastic response, which implies that it is difficult to accurately determine C_s for transitional and granular soils. However, by performing compression tests, and by assuming a constant relation between C_c and C_s , it is possible to indirectly determine C_s for both granular and cohesive sand-mud mixtures. In the following sections, both the results of compression and swelling tests are presented and discussed. Next, a general approach for the swelling behaviour of mixtures of sand and mud is formulated. Finally, typical $m_{v,s}$ values, as anticipated for the upper layer of a sand-mud bed during surface erosion, are presented.

By substituting Eq. (4.13) to Eq. (4.12) we can express $m_{v,s}$ as a function of C_s :

$$m_v = \frac{1}{\ln 10(1+e_0)} \frac{C_s}{p} \quad (4.14)$$

For compression the subscript v in Eq. (4.14) should be replaced by c . It is noted that for a large elastic response upon unloading (typically occurring for clays), relatively large C_s and $m_{v,s}$ values are found.

C_c and C_s were determined by performing Oedometer tests. During this standardized geotechnical test (ASTM 2435, NEN 5118) one-dimensional (vertical) loading and loading-unloading cycles were imposed on soil samples under horizontally confined conditions. Section 3.1.3 discusses soil-behaviour during Oedometer tests from a theoretical point of view (see also Figure 26). Progressively increasing vertical loading steps of 2, 6, 12, 24, 48, 96 and 140 kPa were applied to determine C_c . One unloading step after compression at 6, 12 and 24 kPa, and two unloading steps after compression at 48 and 96 kPa were applied to determine C_s .

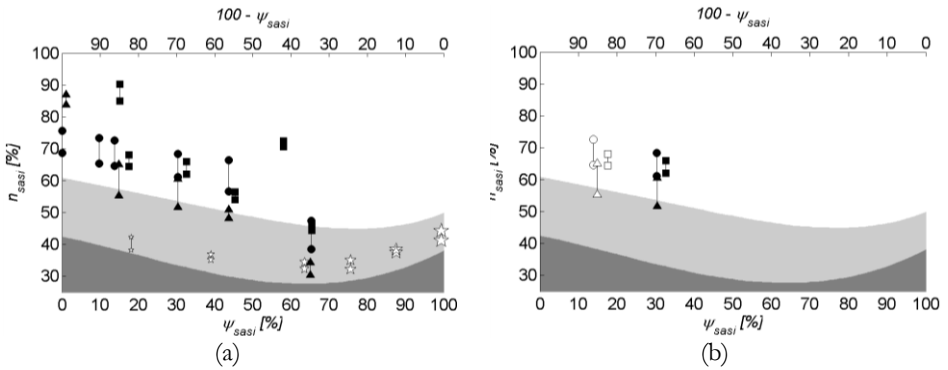


Figure 49. Granular porosity as a function of the sand-silt volume fraction ratio for sand-mud mixtures with kaolinite (\bullet), illite (\blacktriangle), bentonite (\blacksquare) and mixtures consisting of sand and silt (stars, marker size increases with increasing ξ_{sa}). Granular porosities for soil samples on which only compressive tests were executed are shown in (a), whereas for soil samples shown in (b) also unloading steps were applied. Solid markers in (b) indicate soil samples with $\xi_{cl} = 24\%$, the open markers refer to $\xi_{cl} = 28\%$. The upper and lower markers represent the states respectively before and after the Oedometer tests.

Soil sample compositions were chosen such that that cohesive, granular and transitional soil samples could be tested. For the compressive tests, six purely granular soil samples were applied, which exhibited six different sand-silt volume fractions ratios (Figure 49(a)). Furthermore, three groups of sand-mud mixtures with varying clay mineralogies (kaolinite, illite and bentonite) were tested. Each group consisted of four mixtures with varying clay content: 8, 20, 28 and 35%. Additionally, one soil sample consisting of 100% clayey material (as purchased) was tested for each group.

The bulk density was about $2000 \text{ kg}\cdot\text{m}^{-3}$ for purely granular soils, $1700 - 1900 \text{ kg}\cdot\text{m}^{-3}$ for transitional soils, and $1400 - 1600 \text{ kg}\cdot\text{m}^{-3}$ for purely cohesive soils. Loading-unloading cycles were applied for soil samples in each group which exhibited a dominant clay-water matrix ($\xi_{cl} = 24$ and 28% , $\rho_{bulk} = 1750$ and $1700 \text{ kg}\cdot\text{m}^{-3}$, respectively). The structures of these artificial mixtures are shown in Figure 49(b).

4.3.2 Results and discussion

Figure 50(a) shows logarithmic relations between e and p/p_0 (as in Eq. (4.13)) resulting from subsequent compressive loading steps on both purely granular soil samples and sand-mud mixtures with kaolinite. Upon loading, plastic, irreversible deformations are initiated which force the state of the soil samples to move in the direction of the positive p/p_0 -axis. The diagonal lines connecting the data points indicate the K_0 -stress path, whereas the slopes of the fit lines equal C_e .

Relatively steep slopes occur for sand-mud mixtures with a dominant clay-water matrix, whereas for mixtures with a sand-silt skeleton more gradual slopes occur (Figure 50(a)). The different slopes illustrate the larger compressibility of cohesive soils compared to the stiffer granular soil samples. Besides, the transition from relatively steep to more gradual slopes agrees with the expected transition from cohesive to granular behaviour, based on the structural classification shown in Figure 49(a).

Similar results were observed for sand-mud mixtures with illite and bentonite as for mixtures with kaolinite. However, larger slopes were observed for similar clay content when more plastic clay (bentonite) was utilized. This is attributed to the larger water-binding properties of such clays, and to the accompanying larger initial void ratio e_0 . The trend lines in Figure 50(a) for sand-mud mixtures with a granular porosity just above the maximum granular porosity (see Figure 49), but with varying clay mineralogy, similarly tend to the fit lines as observed for sand-silt mixtures.

Differences between the slopes of the sand-silt mixtures in Figure 50(a) relate to the degree of sorting. Relatively steep slopes occur for well-sorted mixtures (predominantly sandy or silty), whereas more gradual slopes are observed when the voids of the sand fraction are filled with smaller particles (i.e. poorly-sorted soils). Figure 50(b) shows a typical result of a loading-unloading cycle in the Oedometer, during which swelling is initiated upon unloading. The trend lines of data points along which the state of a soil sample moves (upon unloading) in the direction of the negative p/p_0 -axis indicate Swelling Lines (SL). The slopes of the SL equal C_s . Upon re-loading, the state of the soil moves back along the SL in the direction of the positive p/p_0 -axis towards its initial location on the K_0 -stress path, before moving further down in the direction of the positive p/p_0 -axis.

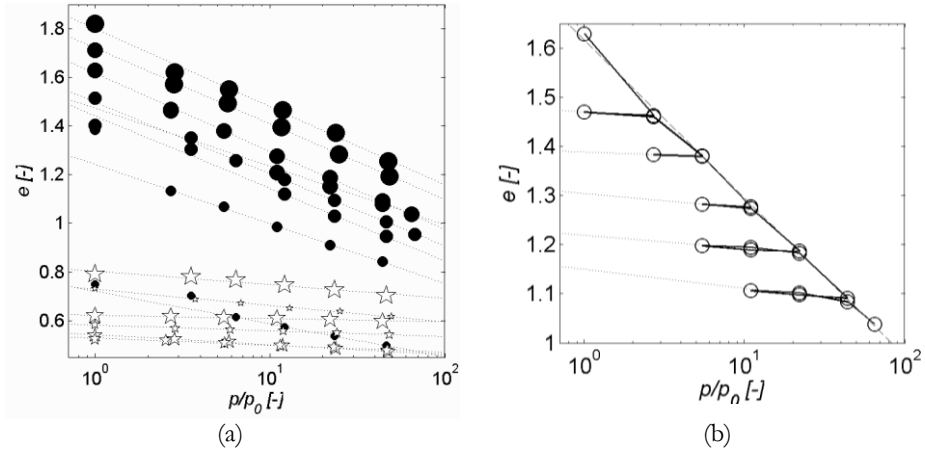


Figure 50. Typical Oedometer results of compressive (a) and loading-reloading (b) tests with the void ratio (e) as a function of the loading condition ($\log p/p_0$). The circles indicate the initial and final states after each loading / unloading step. The lines in (a) reflect the K_σ -stress path, with the slopes equal to C_c . Slopes of more gentle and more or less parallel swelling lines in (b) represent C_s . Results are shown for soil samples with kaolinite (\bullet (a) and \circ (b)) and sand-silt mixtures (stars (a)). The increasing size of the markers (a) indicates increasing ξ_{cl} (\bullet) or increasing ξ_{sa} (stars). Results in (b) are shown for a soil sample with kaolinite ($\xi_{cl} = 28\%$).

Only a limited number of unloading steps were applied and, therefore, each SL only exhibits two or three data points. However, it is shown that the swelling lines are more or less parallel, independent of the loading conditions, which confirms the applicability of C_s as a material property. Furthermore, similar results were obtained during swelling tests on soil samples characterised in Figure 49(b). Larger C_s are observed for soils with larger clay contents and/or for soils which contain more plastic clay. The behaviour of C_s as discussed here is in line with e.g. Schofield and Wroth (1968). For granular soils no swelling tests were executed, as anticipated elastic deformations are too small to record accurately.

The minimum strength (~ 100 Pa) of sand-mud mixtures (Figure 45) occurs for transitional soils for which the granular porosity tends to maximum (Figure 45(d)). This low strength results from a loosely packed granular fraction in combination with the low plasticity of the clay-water matrix, resulting from the low clay content. Most soil samples tested with the Oedometer exhibit such a low-strength transitional structure. Therefore, it was rather difficult to transfer representative sub-samples to the cylindrical containers used in the Oedometer without significant disturbances of the delicate sediment structure.

Another problem during the execution of the Oedometer tests related to the minimum stress conditions that could be prescribed in the Oedometers. This minimum stress (i.e. initial loading p_0 [kPa]) is governed by the weight of the porous

disc (~ 2 kPa), which was applied to transfer the vertical stress to the soil samples, simultaneously enabling the drainage of excess water. As p_0 was close to (and sometimes exceeded) the strength of the applied soil samples, liquefaction / fluidization often occurred during the first loading step.

Summarizing, it was rather difficult to obtain accurate data for the soil samples in the current study. Therefore, only a limited number of soil samples were tested. The accuracy of the results is not high, although the expected trends are still observed.

According to literature, the compression (C_c) and swelling (C_s) indices should be related to the Atterberg limits. Terzaghi and Peck (1967) present a relation for remoulded clays:

$$C_c = 0.007(LL - 10) \text{ for } LL > 10 \quad (4.15)$$

LL is zero for granular soils and up to about 130% for high plastic clays. This relation implies that C_c equals zero for sands and silts, 0.2 – 0.4 for low plastic clays, 0.4 – 0.75 for plastic clays and > 0.75 for high plastic clays. Seed *et al.* (1962) relate the swelling capacity of a soil to the activity of soils, which implies a relation between C_s and the Atterberg limits as well.

The A-line of a plasticity chart, which is an empirical boundary between inorganic clays and silty / organic soils, relates the plasticity index PI to LL (Casagrande, 1932):

$$PI = 0.73(LL - 20) \text{ for } LL > 20 \quad (4.16)$$

In the current study we apply the indirectly determined plasticity index PI^* (Eq. (4.1)) to express the plasticity of soils. By combining a constant relation between C_c and C_s (estimated at $C_c \approx 10 \cdot C_s$) with Eq. (4.15) and Eq. (4.16), we can express C_s as a function of PI^* :

$$C_s = 0.00096 \cdot PI^* + 0.007 \quad (4.17)$$

Figure 51 compares the experimentally determined C_c and C_s with Eq. (4.15) and Eq. (4.17), respectively. It is shown that C_s typically increases from 0.001, 0.01 to 0.025, for granular, transitional and cohesive soil samples. The data shown in Figure 51 are rather scattered (especially for soil samples with bentonite). However, the orders of magnitude of C_c and C_s roughly agree with those indicated by the theoretically derived relations for C_c and C_s . This supports the presumed relation between C_c and C_s . Furthermore, C_c for the sand-silt mixtures is clearly lower than for the cohesive mixtures.

The variation of C_c for sand-silt mixtures results from varying sand-silt ratios, which indicates that not only cohesive, but also individual granular particle characteristics and/or granular porosity may be important. These effects may cause the scatter in Figure 51 for sand-mud mixtures. Samples with constant PI^* may exhibit a variety in responses upon compression due to varying sand-silt ratios (Figure 49).

However, the scatter in Figure 51 is probably mainly due to the experimental procedure, i.e. the collection and transfer of the soil samples, as discussed in the previous section, and the state of the applied (relatively old) Oedometers. The latter may have caused friction between the perforated disc on top of the soil samples and

the metal ring which horizontally confines the samples. As a result, the decreasing character of e as a function of the loading condition as shown in Figure 50 may have been adversely influenced.

Due to limited data and a low level of accuracy of those data, it was not possible to derive a model for C_c and C_s as a function of soil characteristics. Besides, no data was obtained for soil samples consisting of clay and water only, which is required to study the behaviour of the granular and cohesive fraction separately before setting-up a combined model.

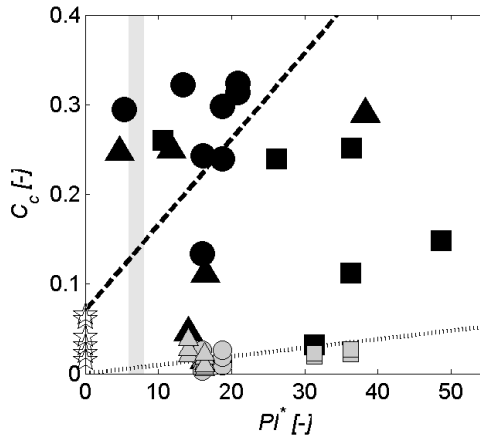


Figure 51. Compression (C_c , solid and open markers) and swelling indices (C_s , grey coloured markers) as a function of PI^* for soil samples with kaolinite (●), illite (▲), bentonite (■) and sand-silt mixtures (stars). The vertical grey line reflects the transition from granular ($PI^* < 7$) to cohesive soil behaviour ($PI^* > 7$). The dashed and dotted lines reflect Eq. (4.15) and Eq. (4.17), respectively for C_c and C_s .

Terzaghi and Peck (1967) present an empirical relation for cohesive soils between the isotropic (p) and deviatoric ($q \sim c_u$) stress ratio, on the one hand, and PI , on the other hand. This implies that the same model approach as applied for c_u (Section 4.2.2) may be applied to model the behaviour of C_c . However, it is questionable whether this model approach is also valid for sand-mud mixtures, as individual particle characteristics related to inter-particle friction (e.g. grain roughness, grain shape) may also play a role. This would imply that the application of bulk soil mechanical properties alone may be insufficient to model the behaviour of soil samples during compression.

In conclusion, insufficient and insufficiently accurate data are available to derive and validate the model for the behaviour of C_c . Therefore, it is recommended to develop a dedicated experimental set-up to obtain more (accurate) data for the compression and swelling behaviour of sand-mud mixtures. The availability of more data would also enable the derivation and validation of an adjusted model approach, incorporating both bulk and individual sediment parameters.

In the current study we apply the few data available to set up a conceptual diagram for C_c (Figure 51). To determine the coefficient of volume variation during surface erosion, typical values of $m_{v,s}$ are determined for granular, transitional and cohesive soils. Eq. (4.14) expresses $m_{v,s}$ as a function of C_s , the initial packing density e_0 , and the unloading stress p . The unloading stress during surface erosion equals the weight of the consecutively removed individual layers of sediment. The thickness of the eroded layers of cohesive sediments equals the erosion layer (δ_e), which is given by Eq. (3.32):

$$\delta_e = d_{50,m} \phi_{s,0}^{1/(n_{fr}-3)}.$$

Table 9. Typical soil properties of sand-mud mixtures as applied in the current study. These properties are applied to determine δ_e during surface erosion of sand and mud.

	W_{rel} [-]	ρ_{bulk} [kg·m ⁻³]	$\phi_{s,0}$ [%]	d_{50} [μm]	n_{fr} [-]	δ_e [mm]
Strong cohesive soils	0.9	1400	25	20	2.650	1.05
Cohesive soils	1.2	1500	31	30	2.675	1.08
Weak cohesive soils	2	1600	38	40	2.700	1.05
Sand-mud mixtures ($n_{sasi} \approx n_{sasi,max}$)	4	1750	47	70	2.725	1.10
Sand-mud mixtures ($n_{sasi} < n_{sasi,max}$)	10	1850	53	90	2.750	1.13
Sand or silt	∞	1950	59	130	-	1.30
Loosely packed sand-silt mixtures	∞	2000	63	150	-	1.50
Densely packed sand-silt mixtures	∞	2050	66	170	-	1.70

Table 10. Coefficient of volume variation $m_{v,s}$ as a function of typical soil properties and unloading pressure (both derived from Table 9) during surface erosion.

	e_0 [-]	p [Pa]	C_s [-]	$m_{v,s}$ [10 ⁻⁴ Pa ⁻¹]
Strong cohesive soils	3.0	14	0.0300	34.6
Cohesive soils	2.2	16	0.0250	31.3
Weak cohesive soils	1.7	17	0.0200	28.4
Sand-mud mixtures ($n_{sasi} \approx n_{sasi,max}$)	1.1	19	0.0100	16.1
Sand-mud mixtures ($n_{sasi} < n_{sasi,max}$)	0.9	21	0.0050	8.9
Sand or silt	0.7	25	0.0010	1.8
Loosely packed sand-silt mixtures	0.6	29	0.0010	1.7
Densely packed sand-silt mixtures	0.5	34	0.0010	1.6

Table 9 lists the soil characteristics of the samples treated in the current study to determine δ_e for surface erosion of sand-mud mixtures. d_{50} of the mud fraction ($d_{50,m}$) is assumed 30 μm, whereas the fractal dimension n_{fr} yields approximately 2.65 for purely cohesive flocs and 2.75 for flocs containing silt (Winterwerp and van Kesteren, 2004). For purely granular soils no flocs are present. For these soils δ_e is assumed equal to $10 \cdot d_{50}$ in order to obtain a smooth connection to δ_e for sand-mud mixtures. For granular mixtures we assume $d_{50} = 63$ and 170 μm, respectively for silt and sand

(based on fractions applied in the current study). The volume fraction $\phi_{s,0}$ follows from the bulk density; typical packing densities are based on Table 8.

The unloading stress during surface erosion ($p = \rho g \delta_e$, see Table 10) follows from Table 9 and is typically only 0.1 Pa, as the thickness of the subsequently removed layers of sediment is limited. $m_{v,s}$ as typically occurring during surface erosion, is determined by applying Eq. (4.14), the soil characteristics in Table 9 and unloading pressures shown in Table 10. Table 10 lists the coefficient of volume variation ($m_{v,s}$) during surface erosion of both cohesive and granular sand-mud mixtures.

Figure 52 illustrates the conceptual behaviour of $m_{v,s}$ as a function of W_{rel} for purely cohesive soil samples, sand-mud mixtures and purely granular soil samples. This conceptual plot is based on typical soil characteristics and unloading pressures during the removal of layers of sediment during surface erosion, as presented in Table 9 and Table 10. $m_{v,s}$ exponentially decreases with increasing W_{rel} , which follows from the low swelling capacities of granular soils. In this thesis, Figure 52 is applied to determine the coefficient of volume variation during surface erosion.

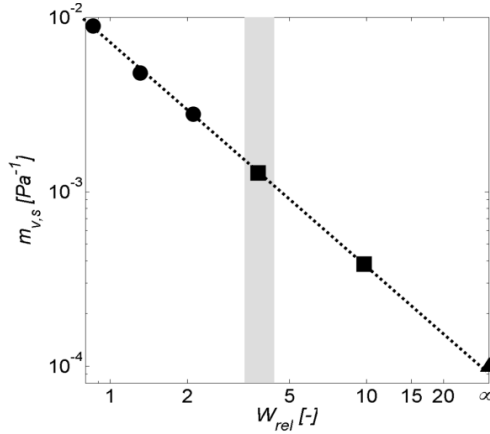


Figure 52. Conceptual behaviour of the coefficient of volume variation ($m_{v,s}$) during surface erosion as a function of the relative water content based on Table 9 and Table 10. The black markers represent typical $m_{v,s}$ for cohesive soils (●), sand-mud mixtures with a dominant sand-silt skeleton (■) and purely granular soils (▲). The light-grey shaded area reflects the transition from a granular structure ($W_{rel} > 4$) to a dominant clay-water matrix ($W_{rel} < 5$).

4.4 Permeability

4.4.1 Experimental procedure

The hydraulic conductivity k [$\text{m}\cdot\text{s}^{-1}$] is the proportionality parameter in Darcy's law, which relates the discharge through a porous medium to both the fluid physical properties (e.g. viscosity) and the applied pressure gradient, resulting from a head difference. For simplicity, the vertical hydraulic conductivity (k_v [$\text{m}\cdot\text{s}^{-1}$]) is referred to as the permeability in the current thesis. Parts of the current section have been published in Jacobs *et al.* (2007a). The permeability can be obtained both from Oedometer and Falling Head tests. These experimental set-ups are partly similar, as for both progressively increasing vertical compressive loading steps under confined horizontal conditions are applied to a circular soil sample with a height of about 1-2 cm. k_v obtained by an Oedometer test follows from the initial, linear relation between sample thickness and the square root of time. The linear part of the response reflects the consolidation stage, from which k_v indirectly follows.

Using the Falling Head test, the permeability is determined after the primary consolidation step. By applying a vertical head difference over a soil sample, an upward flow rate through a soil sample is generated, which yields a falling head as a function of time. The permeability follows directly from Darcy's law. Compressive loading is required to prevent vertical movement of soil samples due to the applied head difference, and to enable testing of multiple packing densities. For reasons of accuracy, a direct determination of k_v with Falling Head tests is preferred over the indirectly determined k_v following from Oedometer tests.

The Falling Head tests were executed both at the Delft University of Technology and at Deltares (institute for delta technology, which includes the former GeoDelft) following international standards (ASTM 5084, NEN 5124). Similar loading steps (2, 6, 12 and 24 kPa) were applied as for the Oedometer tests in Section 4.3. The minimum load resulted from the weight of a porous plate on top of the soil samples. Soil sample compositions were chosen such that the effect of the transition between a dominant sand-silt skeleton and a dominant clay-water matrix on k_v could be studied. The packing densities were also similar to the soil samples applied to determine c_u and m_v . Besides, three different clays were applied: kaolinite, illite and bentonite.

4.4.2 Results and discussion

Low-cohesive /granular soils exhibit little consolidation. Therefore, k_v for such soils cannot be determined accurately with a Oedometer (Section 4.3). Also for the Falling Head tests, it was not straightforward to obtain accurate k_v due to the characteristics of the soil samples which is explained below.

Sand-mud mixtures exhibit a minimum strength when the granular porosity tends to its maximum value (Figure 45(d)), which is the loosest packing of a granular skeleton. This low strength results from the loosely packed granular fraction, and the rather liquid character of the clay-water mixture (due to low clay content) in the voids of the granular fraction.

As a consequence of the low strength of the soil samples studied here, it was rather difficult to collect, and subsequently transfer representative sub-samples to the cylindrical containers applied for the Falling Head test, without (significant) disturbance of the delicate sediment structure. The second important consequence of the soil characteristics is that, for a dominant clay-water matrix, significant consolidation occurs during the first vertical loading step and/or when only a small head difference is applied. This implies that it was not possible to obtain steady state conditions during the tests for the sand-mud mixtures. It is therefore concluded that the Falling Head tests can only be applied for more consolidated soils.

In conclusion, no sufficiently accurate k_v -data could be derived from the Oedometer or Falling Head tests for the soil samples considered here. In addition, no other standardized method is currently available to obtain k_v for these soft soil samples. However, two alternative methods are currently being developed; these methods are briefly discussed.

First, Winterwerp and van Kesteren (2004) present the Seepage Induced Consolidation (SIC) test, which is designed to study the consolidation behaviour of soft mud. It may be possible to adjust this experimental set-up to induce a downward vertical flow by placing a small volume of water on top of a soil sample in combination with an underpressure below the soil sample. Although a much smaller vertical pressure gradient can be applied with an SIC test, compared to the conditions during Oedometer or Falling Head tests, it is unknown whether steady state conditions will occur. However, the same devices used to prepare the artificial soil samples can be used for the SIC test, which avoids the disturbance of the sediment structure due to the transfer of sub samples.

A second alternative to determine k_v is the *in-situ* Hydraulic Strength and Permeability (HPS) probe, which is based on the elasto-plastic soil response when injecting small volumes of water through a thin needle. The *in-situ* permeability follows from the observed pressure gradient as a function of time. The HPS probe is further discussed in Chapter 8. However, both the SIC test and the HPS probe are still under development and not yet fully operational.

Although the experimental data are not accurate, some data are briefly discussed below to indicate the typical range of k_v for the artificial soil samples elaborated in the current thesis. Figure 53(a) shows the results of the Falling Head tests executed at Delft University of Technology. k_v is determined after each loading step and plotted as a function of W_{rel} for soil samples with ζ_{cb} , ζ_{si} and ζ_{sa} of 8-20-28%, 32-45-65% and 60-35-7%, respectively. The water content increases (20, 32 and 50%) with increasing clay content. Three sets of artificial sand-mud mixtures with different clay mineralogy (kaolinite, illite and bentonite) were studied, which each characterized by mixtures with different clay contents (nine mixtures in total). Figure 53(b) indicates that the structure of the soils varies between a dominant sand-silt skeleton and a dominant clay-water matrix. Although the accuracy of the data is not high, Figure 53(a) allows for some general conclusions.

First, Figure 53 shows that k_v decreases with increasing clay content, as well as for an increasing packing density of the sand-silt skeleton. Furthermore, k_v for cohesive

soils typically ranges between 10^{-7} and 10^{-10} $m \cdot s^{-1}$ (Figure 53), whereas Falling Head results executed at Deltares on sand-silt mixtures indicate k_v ranging between 10^{-4} and 10^{-5} $m \cdot s^{-1}$. Comparison of these data with the lower permeabilities for sand-mud mixtures with a dominant sand-silt skeleton clearly indicates the effect of the presence of clay on k_v .

The literature reports large variations of the permeability for soil samples ranging from cohesive to granular (e.g. Mitchell, 1976; Schofield and Wroth, 1968). In general, k_v typically ranges between 10^{-12} and 10^{-8} for strongly to medium-consolidated clays, between 10^{-8} and 10^{-6} for silty and lightly consolidated cohesive soils, and between 10^{-6} and 10^{-3} for sandy soils. Smaller k_v for sand-mud mixtures compared to sand presumably results from the presence of clay, which blocks the flow through the granular skeleton. Furthermore, a larger plasticity index yields a larger volume fraction of clay (larger flocs), which explains the variation of k_v for soils with similar sand-silt ratio, density and clay content, but with varying clay mineralogy.

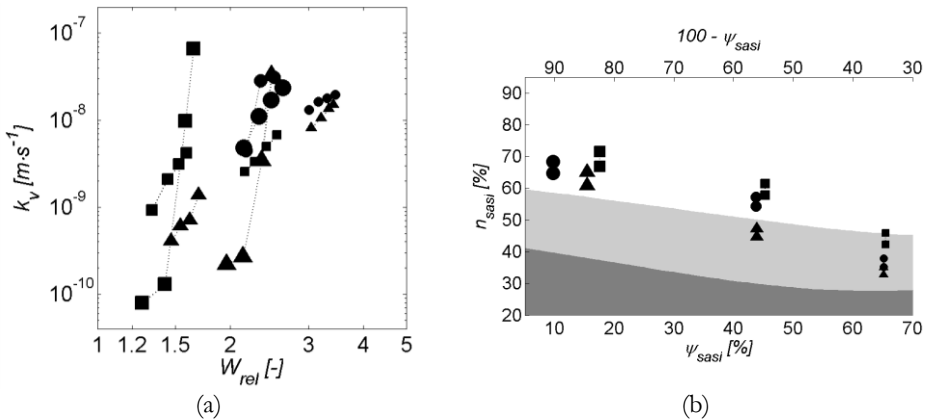


Figure 53. Results of Falling Head tests (a) with the permeability after each loading step as a function of the relative water content (clay content increases with decreasing W_{rel}) for soil samples with kaolinite (●), illite (▲) and bentonite (■). The increasing size of the markers indicates increasing clay content. In (b) the granular porosity as a function of the sand-silt volume fraction ratio for the first and final loading steps is indicated.

Finally, the lines in Figure 53(a) imply power law relations between k_v and W_{rel} , which is in line with a fractal approach for cohesive soils (Kranenburg, 1994). This also indicates that the permeability of sand-mud mixtures may be predominantly determined by the presence and characteristics of flocs. Furthermore, the fractal approach (Kranenburg, 1994) indicates that the permeability of soft mud may vary by orders of magnitude at small variations in density. This implies a fundamental problem with accurate determination with these types of soils.

The second conclusion following from Figure 53(a) concerns the behaviour of k_v for mixtures with a dominant clay-water matrix. k_v varies by orders of magnitude for only small variations (a few percent) of the density. This is most clearly observed for

the first three loading steps for soil samples with large illite and bentonite clay contents. However, the variation of k_v for the final two loading steps (lowest W_{rel}) exhibits a more gradual slope, which follows from the decrease of k_v for mixtures with a dominant sand-silt skeleton and similar density. This indicates that varying slopes of k_v for the most cohesive soils may be attributed to a transition from a clay-water matrix to a granular skeleton between loading steps 3 and 4.

However, the suggested dominance of the volume fraction of clay implies a power law relation as a function of W_{rel} , independent of the dominant structure. Therefore, another explanation is anticipated for the occurrence of the two different power law relations. In a granular skeleton, the clay flocs are expected to be compressed in particular between the contact points of granular particles, upon loading, as these particles are incompressible. This implies that the density of the clay-water mixture is locally strongly increased upon compression, although the increase of the overall density may be limited. This local increase may imply blocking of the overall flow rate, yielding a significant decrease of the permeability. This second explanation for the two different power law relations in Figure 53(a) requires further consideration.

Next, a theoretically derived model is proposed (see also Van Kesteren, 2008) for the permeability of sand-mud mixtures. Although only few data with low accuracy are available to validate and confirm this model approach, the combination of experimental data and data reported in literature enables the identification of a general trend for k_v . The model applies the fractal approach for cohesive sediments (Kranenburg, 1994), which implies that the permeability of a clay-water mixture (k_{clw} [$\text{m}\cdot\text{s}^{-1}$]) exhibits a power law relation as a function of the relative water content:

$$k_{clw} = CW_{rel}^D \quad (4.18)$$

where C [$\text{m}\cdot\text{s}^{-1}$] and D [-] are empirical coefficients.

The permeability of a sand-silt skeleton (k_{sasi} [$\text{m}\cdot\text{s}^{-1}$]) follows from the Kozeny-Carman formula (Kozeny, 1927; Carman, 1956):

$$k_{sasi} = \frac{g}{\nu_w} \frac{1}{k_0 S^2} \frac{e_{sasi}^3}{1 - e_{sasi}} \quad (4.19)$$

where ν_w is the kinematic viscosity of water, e_{sasi} [-] the void ratio of the sand-silt skeleton, S [$\text{m}^2\cdot\text{m}^{-3}$] the specific surface area per unit volume of solids ($S = N/d_{10}$), d_{10} [m] a solids diameter for which 10% is smaller by weight, k_0 [-] the Kozeny-Carman coefficient and N [-] a shape factor (e.g. round, angular). The permeability of a mixture of sand and mud is modelled as the sum of the reciprocals of the permeability of both the cohesive (Eq. (4.18)) and granular fraction (Eq. (4.19)):

$$\frac{1}{k_v} = \frac{1}{k_{clw}} + \frac{1}{k_{sasi}} = \frac{1}{CW_{rel}^D} + \frac{1}{\frac{g}{\nu_w k_0 S^2} \frac{e_{sasi}^3}{1 - e_{sasi}}} \quad (4.20)$$

Eq. (4.20) implies that k_v is determined by the lowest value of k_{clw} or k_{sasi} if these values are far apart. k_v is determined by the characteristics of the sand-silt skeleton (packing density, shape, d_{10}) when only few clay particles are present. For a dominant clay-water matrix k_v is predominantly determined by the plasticity of the clay fraction

in combination with the actual water content, whereas the effect of sand and silt particles is small. Figure 54 illustrates the typical behaviour of k_v as a function of W_{rel} for mixtures of sand and mud. These k_v are applied in the current thesis. Figure 54 is based on (1) the combined theoretical behaviour of k_{clw} and k_{sasi} , (2) the presented experimental data, and (3) typical data reported in literature.

Finally, some recommendations for future study concerning the further development of the proposed model approach are discussed. First, a correction may be applied in Eq. (4.18) accounting for the presence of sand and silt grains on the flow through a clay-water matrix, for example by multiplying Eq. (4.18) by $(1 - n_{sasi})$. Second, the Kozeny-Carman formula applies to uniformly graded granular material (e.g. Mitchell, 1976; Carman, 1956; Carrier, 2003), whereas the effect of non-uniformly graded material nor the effect of a varying maximum granular porosity as a function of the sand-silt volume ratio is incorporated. Therefore, it is suggested to apply the linear concentration (Section 4.2.2) rather than e_{sasi} to incorporate granular packing density.

The presented model may be further improved by replacing the viscosity of water in Eq. (4.18) by the viscosity of the clay-water mixture. Also the effect of local consolidation between the contact points of sand and silt particles should be further studied and possibly incorporated in Eq. (4.19). Moreover, more experimental data are required to validate the proposed model.

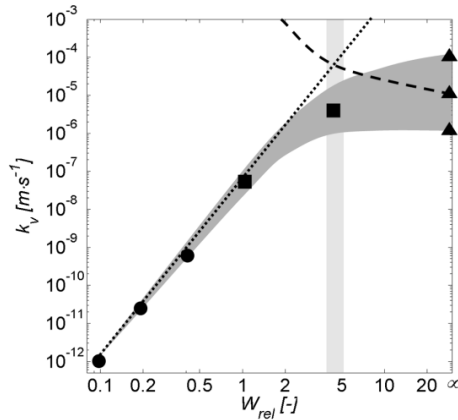


Figure 54. Conceptual behaviour of the permeability as a function of the relative water content for mixtures of sand and mud based on a theoretical approach, experimental data and data in literature. The black markers represent typical k_v for cohesive soils (●), sand-mud mixtures with a dominant sand-silt skeleton (■) and purely granular soils with varying sand-silt ratios (▲). The dotted and dashed lines reflect Eq. (4.18) and Eq. (4.19), respectively. The dark-grey shaded area illustrates Eq. (4.20), the widening of this area with increasing W_{rel} represents the effect of a varying sand-silt ratio. Poorly-sorted sand-silt mixtures exhibit relatively low k_v . The light-grey vertical shaded area reflects the transition from a granular skeleton ($W_{rel} > 4$) to a dominant clay-water matrix ($W_{rel} < 5$).

4.5 Coefficient of pore water dissipation

The coefficient of pore water dissipation c_v [$\text{m}^2 \cdot \text{s}^{-1}$] is the second soil mechanical parameter in the new erosion formulation (Eq. (3.36)), next to the undrained strength. During surface erosion, negative pore water pressure gradients originate from deformations of the bed upon removal of overlying sediments and from fluctuating flow-induced stresses. The deformations yield pore volume variations accompanied by negative pore water pressure gradients, resulting in swelling. The magnitude of the gradients depends on the stiffness of a soil and the unloading pressure; the rate at which the gradients dissipate depends on the permeability. The coefficient of pore water pressure dissipation $c_{v,s}$ characterises the (drained) dissipation process during swelling, and follows from the consolidation theory of Terzaghi (1940):

$$c_{v,s} = \frac{k_v}{m_v g \rho_w} \quad (4.21)$$

For cohesive sediments, a linear relation between settling and the square root of time exists during compression and swelling, which represents the dissipation of pore water pressure gradients. However, for more granular soils the dissipation phase is too short to accurately determine $c_{v,s}$. Therefore, $c_{v,s}$ is determined by substituting the coefficient of volume variation during swelling $m_{v,s}$ (Section 4.3) and the permeability k_v (Section 0) in Eq. (4.21). Results are shown in Table 11 and Figure 55.

Table 11. Coefficient of pore water pressure dissipation $c_{v,s}$ (at right, see also Figure 55) following from substituting $m_{v,s}$ (Figure 52) and k_v (Figure 54) in Eq. (4.21).

	W_{rel} [-]	$m_{v,s}$ [10^{-4} Pa^{-1}]	k_v [$\text{m} \cdot \text{s}^{-1}$]	$c_{v,s}$ [$\text{m}^2 \cdot \text{s}^{-1}$]
Strong cohesive (consolidated) soils	0.1	10^{-2}	10^{-12}	10^{-14}
Cohesive (consolidated) soils	0.2	10^{-2}	10^{-10}	10^{-12}
Weak cohesive (consolidated) soils	1	10^{-2}	10^{-8}	10^{-10}
Sand-mud mixtures ($n_{sasi} \approx n_{sasi,max}$)	4	10^{-3}	10^{-6}	10^{-7}
Sand-mud mixtures ($n_{sasi} < n_{sasi,max}$)	10	10^{-3}	10^{-5}	10^{-6}
Densely packed (sand-)silt mixtures	∞	10^{-4}	10^{-6}	10^{-6}
Loosely packed sand-silt mixtures	∞	10^{-4}	10^{-5}	10^{-5}
Sand	∞	10^{-4}	10^{-4}	10^{-4}

It is noted that the soil samples used in the current study generally concern sand-mud mixtures with a dominant structure close to the maximum granular porosity. This implies that $c_{v,s}$ typically ranges between 10^{-7} and $10^{-5} \text{ m}^2 \cdot \text{s}^{-1}$. Furthermore, both Table 11 and Figure 55 indicate that for more granular soil samples the permeability determines the behaviour of $c_{v,s}$. This follows from the relatively low swelling capacity of granular soils in combination with the relatively large permeability.

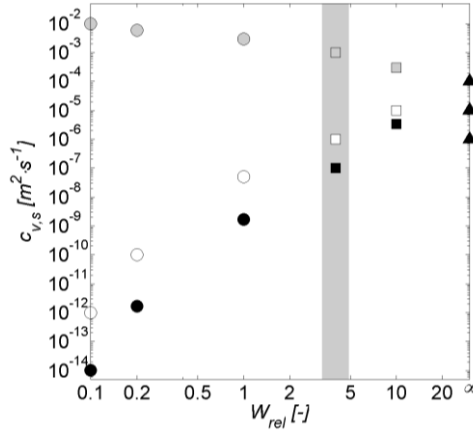


Figure 55. Conceptual behaviour of the coefficient of pore water pressure dissipation as a function of the relative water content (black coloured markers) for mixtures of sand and mud based on Eq. (4.21) by substituting $m_{v,s}$ (grey coloured markers, Figure 52) and k_v (open symbols, Figure 54). Circular markers represent cohesive soils, squared markers sand-mud mixtures with a dominant sand-silt skeleton, and triangular markers purely granular soils with varying sand-silt ratios. Poorly-sorted sand-silt mixtures exhibit relatively low $c_{v,s}$; larger $c_{v,s}$ relate to well-sorted mixtures. The light-grey area reflects the transition from a granular structure ($W_{rel} > 4$) to a clay-water matrix ($W_{rel} < 5$).

4.6 Conclusions

Two new bulk soil mechanical parameters are proposed: the relative water content and the granular porosity. The first combines the water content (\sim density) and the plasticity index (\sim cohesiveness). The granular porosity enables to distinguish between granular and cohesive soil behaviour. To obtain reproducible soil samples, to exclude biological and physico-chemical effects and to avoid disturbance of the (delicate) soil structure due to *in-situ* sample collection and subsequent transport to a laboratory, sand-mud mixtures were artificially generated in a dedicated experimental set-up.

The presented semi-empirical model to predict the undrained shear strength for sand-mud mixtures as a function of the soil sample composition nicely indicates how the separate Critical State Models for granular and cohesive soils can be successfully combined. Additionally, the power law relation between the undrained shear strength and the relative water content agrees with the fractal approach for flocs. This implies that the fractal approach can also be applied to denser mixtures of sand and mud.

Insufficient and insufficiently accurate data were obtained. The applicability of a similar model approach for the permeability and coefficient of volume variation could therefore not be fully assessed. Besides, both theory and experimental data suggest that not only bulk soil properties are important, but also particle characteristics. However, it

was possible to derive a conceptual diagram for the compressibility and permeability of sand-mud mixtures.

Problems concerning the determination of the permeability and the coefficient of volume variation are mainly related to the available experimental set-ups and inherent to the large sensitivity to variations of the density. These set-ups are designed for well-consolidated soils, rather than for low-strength mixtures of sand and mud. Also during the collection and transfer of sub samples to the experimental set-ups, two problems occurred. These two problems justify the current development of a new experimental device to *in-situ* measure the permeability and the coefficient of volume variation (which relates to the undrained shear strength) of intertidal sediments (Chapter 8). However, the large variation of the permeability of soft mud for small variations of the density following from the fractal approach may be a fundamental problem difficult to solve.

The soil samples are rather densely packed, whereas natural muddy intertidal sediments are often more loosely packed. However, the obtained insight and relations concerning the mechanical behaviour of sand-mud mixtures indicate that the results may also be applied to more loosely packed sediments. Additionally, the Critical State Model approach provides the possibility to incorporate biological and physico-chemical effects as encountered for natural intertidal sediments on soil mechanical behaviour. For example, the influence on the plasticity of soils by adhesion due to polymeric bonding or by pore water chemistry can directly be incorporated in the presented relations between the relative water content and soil mechanical behaviour.

Large-scale effects such as bioturbation require a different approach. Biota change the composition and structure of intertidal sediment beds, which implies that the relative water content itself is affected, rather than the relation between the relative water content and soil mechanical behaviour. This implies that for given relations between biota and relative water content, the effect of biota on soil mechanical behaviour can indirectly be determined using the presented relations. Clearly, the relation between biological and physico-chemical effects and soil mechanical behaviour should be further studied.

Chapter 5

Straight flume erosion experiments

Results of a large number of erosion tests on artificially generated and relatively dense sand-mud mixtures are discussed in this chapter. Soil sample compositions are varied with respect to clay-silt and sand-silt ratio, and clay mineralogy. The experimental set-up consists of a re-circulating, small-scale, rectangular erosion flume with unidirectional flow. The erosion threshold and erosion rate are studied through step by step increases of the flow velocity. Comparison of the results with theory (Chapter 3 and 4) and with large-scale erosion tests (Chapter 6) is presented in Chapter 7. Part of this chapter has been published in Jacobs *et al.* (2010).

5.1 Methods

Reproducible, homogeneously mixed and 100% saturated sand-silt-clay mixtures were generated using the experimental procedure described in Section 4.1.1. To prevent consolidation, tests were executed as soon as possible after generation of the sample. Compositions were chosen such that the effect of a transition in dominant structure (i.e. sand-silt skeleton or clay-water matrix) on erosion can be studied.

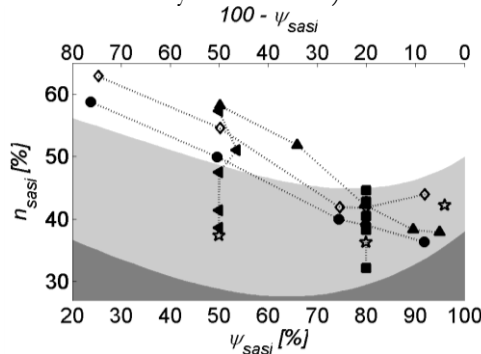


Figure 56. Granular porosity as a function of the sand-silt volume fraction ratio for soil samples shown in Table 12: Set 0 (stars), 1 (●), 2 (▲), 3 (■), 4 (◄) and 5 (◇). Each set exhibits a transition (at $n_{sasi} = n_{sasi,max}$) from a granular sand-silt skeleton (light-grey area) to a cohesive clay-water matrix (white area).

Four different sets of soil samples with increasing ζ_{cl} and varying clay-silt ratio (Set 1 and 2) and sand-silt ratio (Set 3 and 4) were tested (Table 12). Additionally, two different clay minerals were used: kaolinite (Set 1 – 4) and bentonite (Set 5). Set 5 had a similar granular composition as Set 1. Soil samples of Set 0 (i, ii and iii) consisted of sand and silt only, with n_{sasi} just above $n_{sasi,min}$. These Set 0 compositions are located on the lower ends of the dotted lines in Figure 56 (indicated by the stars). Their sand-silt ratios relate to Set 4 (no. i), 3 (no. ii) and 1, 2 and 5 (no. iii).

Table 12. Composition and bulk properties of the tested soils. For Set 1, 2 and 5 the clay-silt ratios are constant: 0.25, 0.4 and 0.25, respectively; for Set 3 and 4 the sand-silt ratio is constant: 0.8 and 0.5, respectively (see light-grey shaded cells). The applied clay mineral for Set 1 – 4 is kaolinite and for Set 5 bentonite. All soil samples are tested twice, which is reflected by two values for ρ_{bulk} , W , n_{sasi} and W_{rel} . The bold numbers in the column at left refer to soil samples exhibiting Feature 1 and 2 (see Table 13), respectively.

	<i>No</i>	ζ_{cl}	ζ_{si}	ζ_{sa}	ζ_{cl}/ζ_{si}	ψ_{sasi}	ρ_{bulk}	<i>W</i>		n_{sasi}		PI^*	W_{rel}		
		[%]	[%]	[%]	[-]	[%]	[kg·m ⁻³]	[%]		[%]		[%]	[-]		
Set 0	i.	2	49	49	0.05	50	2028	2040	21	21	37	37	0	-	-
	ii.	1	20	79	0.05	80	2029	-	21	-	36	-	0	-	-
	iii.	0	4	96	0.04	96	1948	-	27	-	41	-	0	-	-
Set 1	1.	2	8	90	0.25	92	2039	2017	21	22	36	38	1.3	15.5	16.4
	2.	5	19	76	0.25	80	2024	2077	22	19	39	36	3.2	6.7	5.8
	3.	6	24	70	0.25	74	2021	2046	22	20	40	39	4.0	5.4	5.1
	4.	11	45	44	0.25	50	1901	1947	30	27	50	47	7.5	4.0	3.5
	5.	16	64	20	0.25	24	1784	1804	40	38	59	58	10.7	3.7	3.6
Set 2	6.	2	5	93	0.40	95	2014	-	22	-	38	-	1.3	16.6	-
	7.	4	10	86	0.40	90	-	2028	-	21	-	38	2.7	-	8.0
	8.	7	19	74	0.40	80	1998	2020	23	22	42	41	5.0	4.6	4.4
	9.	12	30	58	0.40	66	1875	1920	32	28	52	49	8.0	4.0	3.5
	10.	17	42	42	0.40	50	-	1802	-	38	-	58	11.1	-	3.4
Set 3	11.	3	19	78	0.15	80	-	2120	-	17	-	32	2.0	-	8.2
	12.	5	19	76	0.25	80	2038	2079	21	19	38	36	3.2	6.5	5.8
	13.	6	19	75	0.32	80	2013	2022	22	22	40	40	4.0	5.5	5.4
	14.	7	18	74	0.40	80	1989	2002	24	23	43	42	5.0	4.8	4.6
	15.	8	18	74	0.44	80	1964	2005	25	23	45	42	5.4	4.7	4.2
Set 4	16.	2	49	49	0.05	50	2007	2091	23	18	39	33	1.6	14.1	11.2
	17.	5	47	47	0.12	50	1992	2017	24	22	41	40	3.7	6.4	6.0
	18.	8	46	46	0.19	50	1918	1931	29	28	47	47	5.7	5.0	4.9
	19.	12	41	47	0.29	54	1887	1872	31	32	51	52	7.8	3.9	4.1
	20.	16	42	42	0.39	50	1819	1816	37	37	57	57	11.0	3.3	3.3
Set 5	21.	2	8	90	0.25	92	-	1915	-	29	-	44	1.3	-	22.1
	22.	5	19	76	0.25	80	1976	-	25	-	42	-	5.0	4.9	-
	23.	6	24	70	0.25	75	1989	1997	24	23	42	41	6.6	3.6	3.5
	24.	11	44	45	0.25	50	1817	-	37	-	55	-	13.5	2.7	-
	25.	16	63	21	0.25	25	-	1704	-	49	-	63	19.7	-	2.5

Soil samples were comparable to those discussed in Chapter 4; the micro and meso-scale characteristics are discussed in Sections 4.1.2 and 4.1.3. Samples were relatively densely packed ($\rho_{bulk} \approx 1900 - 2000 \text{ kg}\cdot\text{m}^{-3}$) and exhibited relatively large c_u ($\approx 0.1 - 1 \text{ kPa}$). The latter resulted from n_{sasi} close to $n_{sasi,max}$, with $n_{sasi} \approx 0.45$ and $\xi_{cl} \approx \psi_{cl} \approx 10\%$ resulting in $n \approx 0.4$ and $\rho_{bulk} \approx 2000 \text{ kg}\cdot\text{m}^{-3}$ (Section 2.2.2). Finally, all sediment samples were generated twice; one was used for two erosion tests, the other to determine the undrained shear strength.

Erosion tests were executed using the small (1.20 m long, 8 cm wide and 2 cm high) and straight transparent flume ‘Erodimetre’ (Le Hir *et al.*, 2006, 2007b; Figure 57(a)) at the French research institute for Exploration of the Sea (Ifremer) in Brest. Sub samples with a thickness of 2 – 3 cm were obtained with a knife. These slices were placed in a cylindrical container with identical diameter, which was fixed to the flume (Figure 57(b)). Next, the surface of the soil sample was horizontally and vertically levelled with the bottom of the flume using four screws. The whole exposed surface area was presumed to contribute to erosion. The bottom of the flume was covered with sandpaper (with a roughness comparable to the applied sand fraction) to decrease differences in roughness with the sample. In practice, nearly no scour was observed at the upstream side of the samples.

A unidirectional flow generated by a re-circulating pump was accelerated step by step (average duration of a step approximately 150 - 200 seconds), until the sample was eroded by a few mm. The flow rate was controlled through a velocity meter in the pump. The volume of eroded sand was monitored at a sand trap downstream of the sediment sample, at the end of each velocity step. After the test, the total dry-mass of this material was determined. The grain size distributions of both the original soil samples and the sand trap material were determined using a laser-granulometer.

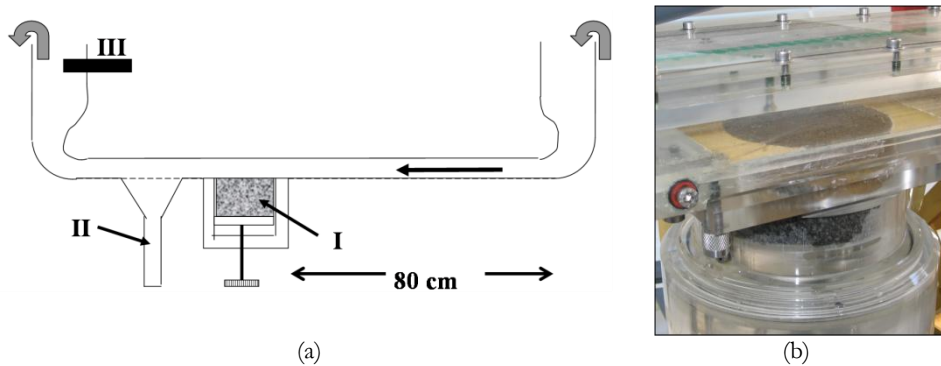


Figure 57. Re-circulating flume ‘Erodimetre’ as applied in the current study (after le Hir *et al.*, 2006, 2007b). The left panel shows a schematic depiction of the flume with the flow direction indicated by the black and grey arrows, and a soil sample by the shaded area (I). Downstream a sand trap (II) and turbidity meter (III) are mounted. The right panel shows a detail of a soil sample in the flume.

The suspended sediment concentration was derived from continuous measurements with an optical backscatter turbidity meter (*Seapoint*). Samples (~200 ml, replaced with clear water) were taken during 20 erosion tests to calibrate the turbidity meter. The soil samples were divided in three groups, based on the dominant fraction for sediments smaller than 63 μm : silt (soil samples i, ii, iii, 1, 6, 7 and 21), silt + kaolinite (2 - 5 and 8 - 20) or silt + bentonite (22 - 25). For each group a different calibration curve is applied (Figure 58); the observed scatter resulted from varying clay-silt ratios:

$$c = \begin{cases} 157 \cdot T & \text{for kaolinite} \\ 258 \cdot T & \text{for bentonite} \\ 289 \cdot T & \text{for illite} \end{cases} \quad (5.1)$$

where c [$\text{g}\cdot\text{l}^{-1}$] is the concentration of suspended sediments and T [mV] the turbidity meter output.

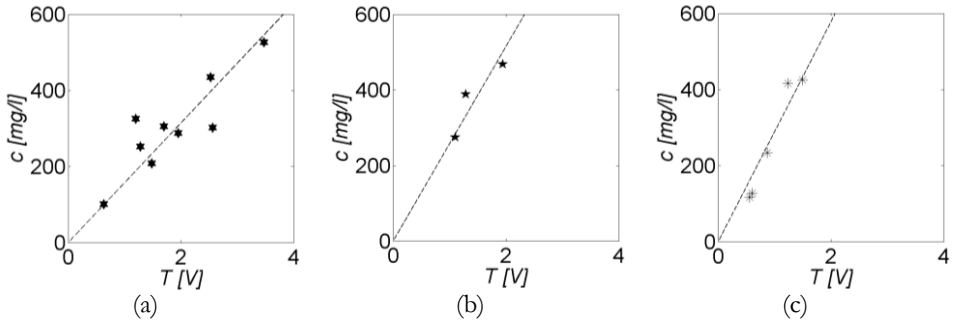


Figure 58. Calibration curves for the concentration [$\text{mg}\cdot\text{l}^{-1}$] as a function of the output T [Volt] of the turbidity meter for kaolinite (a), bentonite (b) and silt (c).

Calibration of the bed shear stress in the flume is not straightforward, as the bed roughness is likely to vary in space and even in time during the erosion process. However, a turbulent flow in the flume can be assumed, except for very low discharges. Then the bed shear stress is proportional to the square of discharge in the flume. The drag coefficient has been fitted so that the initiation of movement of monodisperse sand (test iii) is consistent with the critical mobility parameter given by the Shields diagram.

Off course, the calibration of τ_b is an estimation, for example due to the high sensitivity of the drag coefficient for small variations of the Reynolds number, especially when discharges are low. Furthermore, additional friction generated along the upper side of the test section is not taken into account in the assumption of the closed conduit flow. However, no alternative for the proposed calibration is currently available. The derivation of a more accurate calibration of the bed shear stress is the subject of ongoing study. In conclusion, the presented calibration of τ_b enables the discussion of relative variations of the critical bed shear stress for erosion, although care should be taken when discussing absolute values and/or when comparing results with previous studies.

Finally, the short duration of a test (2 hrs, including installation and cleaning), enabled the execution of a large number of tests. However, some tests failed due to problems with the experimental procedure (e.g. due to transferring soil samples from the core to the test-geometry in the flume). For this reason the results of one of the two tests on samples ii, 6, 7, 10, 11, 21, 22, 24 and 25 will not be discussed in the following sections.

5.2 Results and analysis

5.2.1 Erosion modes and features

Following the new classification scheme for erosion (Figure 36) in combination with the characteristics of the tested soil samples, two erosion modes are expected to occur during the erosion tests: floc and surface erosion. Observations from the erosion tests confirm that, even for low τ_b , individual flocs randomly erode from the sediment bed (i.e. floc erosion). For increasing τ_b a certain threshold occurs for all soil samples above which both sand and mud particles uniformly erode from the exposed surface area.

However, simultaneously with the occurrence of surface erosion two features are also observed above the surface layer of some soil samples. The first (Feature 1 in Table 13) is a transport feature and concerns the development of a sand wave on the bottom of the flume in between the soil sample and the sand trap. The second feature (Feature 2 in Table 13) concerns the development of cracks within the surface of the soil samples. Table 13 reveals for which soil samples continued these features, which are illustrated in Figure 59. It is noted that the eroding force for which these features occur is variable (see Appendix III).

Table 13. Overview of features observed during surface erosion, in relation to the accompanying soil samples characteristics.

	Feature 1	No feature	Feature 2
Sample no.	iii, 1, 6, 7, 21	i, ii, 2, 3, 8, 11-19, 22-24	4, 5, 9, 10, 20, 25
Dominant structure	Sand-silt skeleton	Sand-silt skeleton	Clay-water matrix
Mud content	$\zeta_{mu} < 10\%$, $\zeta_{sa} > 90\%$	$10\% < \zeta_{mu} < 56\%$	$42\% < \zeta_{mu} < 80\%$
Erosion mode	Floc, surface	Floc, surface	Floc, surface, lump
Bed load (sand)	Sand wave migration	Individual particles	Individual particles
Transport of mud	Suspended load	Suspended load	Suspended load + aggregates

A sand wave (Figure 59) occurred for sandy soil samples ($\zeta_{sa} > 90\%$). After the initiation of motion a sand wave developed, which traveled along the bottom of the flume towards the sand trap. The travel time of the wave caused a time lag between erosion and deposition in the sand trap. The duration of this time lag is in the order of

minutes and depends on τ_b . For sample iii the development and propagation of the sand wave prevented accurate determination of sand erosion rates. Therefore, instead of step by step increasing τ_b during one test, four tests at different τ_b were executed to obtain more accurate erosion rates.

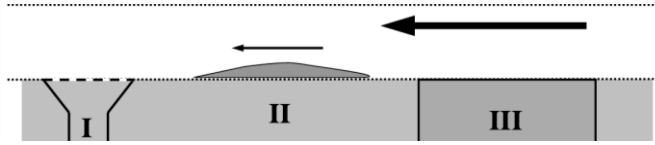


Figure 59. Schematic depiction of part of the flume showing the sand trap (I), a propagating sand wave (II) and a soil sample (III). The flow direction is indicated by the large black arrow; the horizontal dotted lines indicate the bottom and top of the flume. The sand wave reflects Feature 1, which is observed for sandy soils.

Cracks (Figure 60, Table 13) occurred for all soil samples with a dominant clay-water matrix and was characterised by cracks in the surface layer of the soil samples, and by uneven erosion patterns. These cracks expanded with increasing τ_b . Figure 60 shows that both radial cracks (mostly) and cracks parallel to the flow direction exist (longitudinal cracks). Before and during the formation of the cracks individual flocs and sand grains were simultaneously eroded. Also some aggregates of sediment randomly eroded from the cracks, which generated somewhat less accurate sand trap and concentration readings.

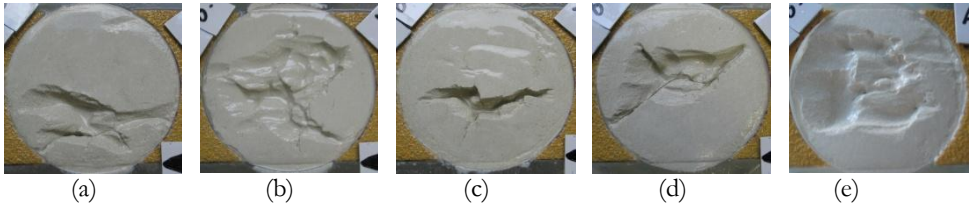


Figure 60. Photographs after erosion tests of soil samples 4(a), 5(b), 10(c), 10(d) and 20(e), showing Feature 2. Flow direction is from right to left. Radial cracks and longitudinal cracks are shown.

Most soil samples (Table 13) did not exhibit either of the features during the surface erosion of individual sand and mud particles. Sand arrives in the sand trap within seconds after erosion. Identical behaviour was found for soil samples with kaolinite and bentonite. The soil samples with no features exhibit a dominant sand-silt skeleton and $\xi_{mu} > 10\%$. Figure 61 shows an example for the transition ($n_{sasi} \approx n_{sasi,max}$) between surface erosion without (a – d) and with Feature 2 (e) when increasing ξ_{cl} . The smooth surfaces indicate surface erosion. Figure 61(e) indicates Feature 2, as the surface is irregular due to the presence of cracks and subsequent erosion of lumps of sediments. Identical transitions exist for Set 1 (between samples 3 and 4), Set 2 (8 and 9) and Set 5 (23 and 24). For Set 3 no sample exhibits Feature 2, as n_{sasi} for all samples is smaller than $n_{sasi,max}$.

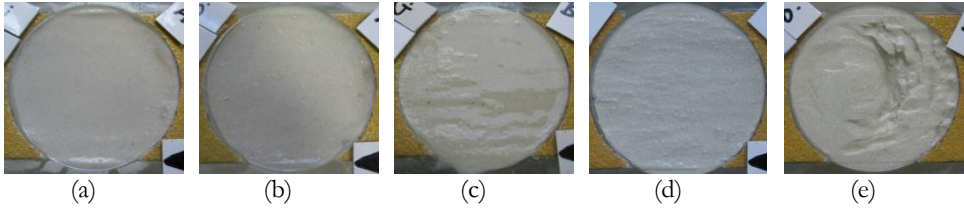


Figure 61. Surface of soil samples of Set 4 (samples 16 – 20) after erosion tests. Flow direction is from right to left. The clay content increases from (a) - (e). Surface erosion occurred for all 5 samples. However, for (a) – (d) surface erosion generated a flat surface, whereas in (e) Feature 2 is observed.

The occurrence of cracks generates random erosion of aggregates of sand and mud from the cracks. After erosion, these aggregates are transported as bed load and, subsequently, deposited in the sand trap. This is shown by Figure 62, which presents the results of grain size analyses on sand trap material. Larger ξ_{mu} for the sand trap material is found for soil samples which exhibit Feature 2. Yet, for some soil samples of Set 4 (16 - 18) and Set 0 (i - ii), for which $n_{sasi}/n_{sasi,max} < 1$, have a relatively large ξ_{mu} of the sand trap material, although these samples do not exhibit Feature 1 or 2.

These relatively large ξ_{mu} may be explained as follows. The mud of these samples is rather silty. After erosion, individual silt particles are assumed to be transported in suspension rather than along the bed. The presence of large ξ_{si} in the sand trap material may indicate that silt particles are eroded and, subsequently, transported along the bed in aggregates rather than in suspension. Apparently, these aggregates are relatively small, as the eroded surface does not exhibit an irregular character. Erosion of aggregates indicates that this type of erosion not only occurs for cohesive soils, but also for non-cohesive soils with relatively large ξ_{si} .

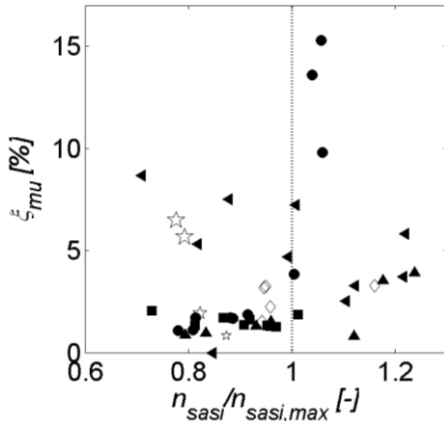


Figure 62. Mud content of the sand trap material as a function of the actual granular porosity (n_{sasi}) relative to n_{sasi} at the transition (see dotted line) between a sand-silt skeleton ($n_{sasi}/n_{sasi,max} < 1$) and a clay-water matrix ($n_{sasi}/n_{sasi,max} > 1$). Data are shown for Set 0 (stars), Set 1 (●), 2 (▲), 3 (■), 4 (◄) and 5 (◇, bentonite). The size of the markers of Set 0 (stars) increases with increasing silt content.

5.2.2 Concentration-time profiles

The concentration in the flume's water is continuously recorded by the turbidity meter, whereas the mass of eroded sand in the sand trap M_{sand} [kg] is recorded at the end of each step only. Water (with suspended fines) samples are subtracted from the flume during erosion tests for about one-third of the tests in order to calibrate the turbidity meter. However, the effect of varying clay-silt ratios is not taken into account, which may explain the scatter in the calibration of soil samples with a fines fraction consisting mainly of kaolinite (Figure 58(a)). Furthermore, the water samples are subtracted for $\tau_b \approx \tau_{e,s}$. Large c are, therefore, obtained by extrapolating the calibration curve, which further enhances the inaccuracy due to the scattering. In conclusion, one should realize that the accuracy of c may not be very high, especially for kaolinite soils with large c .

Figure 63 shows a typical example of c and M_{sand} as functions of t . Results for all soil samples are shown in Appendix III. Figure 63(b) shows that the concentration profile initially (low τ_b) exhibits a relatively sharp increase at the start of a new τ_b -step, followed by an equilibrium condition c . This logarithmic growth indicates that the erosion rate varies with time. Initially the erosion rate is high, after which it reduces to zero although τ_b was not changed. In the current thesis this behaviour is referred to as time-dependent erosion. This time-dependent behaviour exhibits a zero threshold, as erosion starts for any $\tau_b > 0$. It is further noted that at low τ_b only mud is eroded ($M_{sand} = 0$).

Figure 63 also shows that for larger τ_b , the concentration profile exhibits a linear increase with time for constant τ_b (Figure 63(c)). This indicates that the erosion rate is constant at specific τ_b . In the current thesis, this behaviour is referred to as time-independent erosion. Besides the linear increase of c with time, time-independent erosion is characterized by the simultaneous and uniform erosion of sand and mud particles.

The measured concentration profiles are fitted with an exponential function:

$$c(t) = A(1 - e^{-Bt}) \quad (5.2)$$

where A [$\text{g}\cdot\text{l}^{-1}$] and B [s^{-1}] are empirical constants. B^{-1} is the e -folding time scale for which the concentration coefficient decreases to $1/e$ of its previous value; it discriminates between a non-equilibrium and an equilibrium condition. It is noted that this fit-function is a mathematical tool to fit observed data only. The exponential character of the function is not based on a physical process.

Figure 63(b) and (c) show detailed views of a typical concentration profile for relatively low τ_b (small B^{-1}) and large τ_b (large B^{-1}), respectively. A and B^{-1} are relatively small and constant ($A = 0.01 - 0.05 \text{ g}\cdot\text{l}^{-1}$; $B^{-1} = 10 - 100 \text{ s}$) for time-dependent erosion. Time-independent erosion is characterised by an almost linear increase of c with t , which implies relatively large B^{-1} and A . The transition from time-dependent to time-independent (erosion rate constant with time) erosion is indicated by the moment at which both A and B^{-1} exhibit a sudden increase.

Time-dependent and time-independent erosion are clearly identified, and similar behaviours are observed for soil samples containing only silt, kaolinite and silt or bentonite and silt. However, in some cases for which time-independent erosion is expected, c tends towards equilibrium. This behaviour is attributed to the experimental procedure, and occurs for soil samples with relatively large ζ_{sa} and little or no ζ_{cl} (e.g. iii, 1, 6, 21). Maximum τ_b during these tests is relatively low (Appendix III), as the maximum erosion depth (for which the flow pattern over the eroding sample is not yet disturbed) is rapidly reached. These low τ_b suggest that fully-developed time-independent erosion was not yet obtained for these tests.

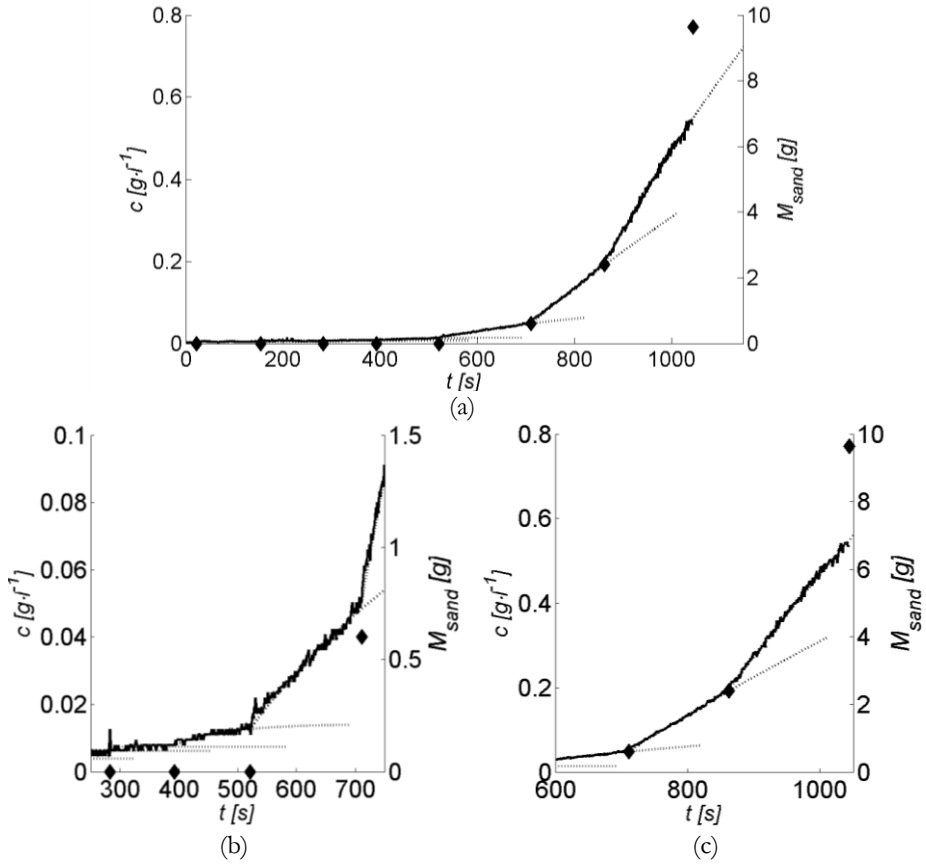


Figure 63. Typical example (soil sample 15) of the concentration (continuous line, left vertical axis) and the mass of eroded sand in the sand trap M_{sand} (\blacklozenge , right vertical axis) as a function of time. The dotted lines are the fitted concentration following from Eq. (5.2). Result of the complete test is shown in (a), with details for relatively low (b) and large bed shear stress in (c). Note the different vertical scales. For relatively low bed shear stress the concentration tends to equilibrium after an initial sharp increase (b), whereas for large bed shear stress the concentration exhibits an almost linear increase (c).

5.2.3 Erosion rates

The erosion rate for mud E_{mud} [$\text{kg}\cdot\text{m}^{-2}\cdot\text{s}^{-1}$] follows from the time-derivative of c . However, E_{mud} is highly sensitive for the time step Δt with which this derivative is determined. The effect of various Δt was therefore studied, and three conclusions are drawn. First, Δt should be sufficiently large to smooth the noise of the measured concentration (see e.g. Figure 63(a)). Second, Δt should be small as E_{mud} at the start of a velocity step significantly decreases with increasing Δt . Finally, it is concluded that the typical time-scale of the fluctuations of τ_b increases due to the increasing level of turbulence with increasing flow rate. This implies that Δt should increase with increasing τ_b to obtain identical smoothing for all velocity steps.

As the choice for Δt is highly subjective, the time-derivative of the fitted concentration is used to determine E_{mud} , which follows from Eq. (5.2):

$$\frac{\partial c}{\partial t} = AB e^{-Bt} \quad (5.3)$$

The erosion rate is determined by multiplying $\partial c/\partial t$ by the volume of water in the flume ($V_w \approx 18.5$ l) and subsequently dividing by the surface area of the test section ($A_{ts} \approx 64$ cm^2). E_{mud} is plotted as a function of t in Figure 64, which clearly shows time-dependent behaviour of E_{mud} in the first velocity steps, and time-independency in subsequent steps.

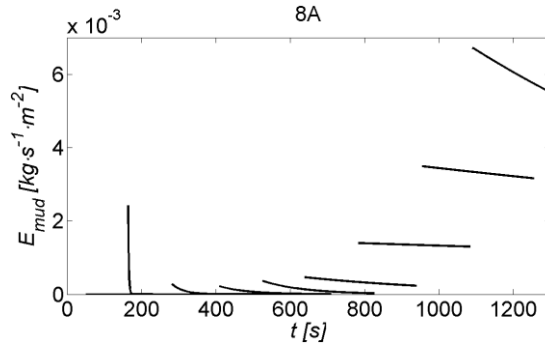


Figure 64. Typical example (Sample 8A in Table 12) of the mud erosion rate as a function of time (see also Figure 65). Time-dependent erosion in the first steps (E_{mud} tends to zero) precedes time-independent erosion (E_{mud} tends to a non-zero, constant value).

Time-dependent and time-independent erosion result from floc and surface erosion, respectively. The (almost) horizontal character of E_{mud} enables the derivation of the surface erosion rate (E_s [$\text{kg}\cdot\text{m}^{-2}\cdot\text{s}^{-1}$]), which follows from Eq. (5.3):

$$E_s = AB(V_w/A_{ts}) \quad (5.4)$$

Eq. (5.4) indicates that E_s is defined as the maximum erosion rate at the beginning of a velocity step ($t = 0 \rightarrow \partial c/\partial t = A\cdot B$). Figure 64 also shows that E_{mud} is not always completely time-independent towards the end of a test. However, the application of

Eq. (5.4) enables studying the initial erosion, without incorporating possible artefacts of the experimental set up (see next section) yielding a decrease of $\partial c/\partial t$ with t .

Maximum erosion rates for sand (E_{sand} [$\text{kg}\cdot\text{m}^{-2}\cdot\text{s}^{-1}$]) and mud as a function of τ_b are shown in Appendix III; a typical example is presented in Figure 65. Relatively large E_{mud} , (which sometimes fall beyond the domain of the figures) exist for time-dependent erosion in the first velocity steps. Furthermore, no single erosion threshold, but a range of τ_b exist at which flocs are eroded. E_{mud} and E_{sand} increase linearly with τ_b for time-independent erosion, which slope reflects the surface erosion parameter.

Figure 65 further indicates an erosion threshold when extrapolating the erosion rate to the x -axis. This threshold, which is comparable for sand and mud, equals the onset of transport rather than the initiation of motion (see Section 5.3.2). In the current study, the surface erosion threshold equals the average τ_b of the extrapolated E_{sand} and E_{mud} .

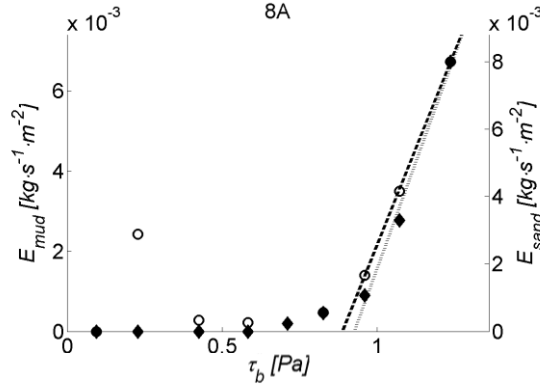


Figure 65. Typical example (Sample 8A in Table 12) of the mud erosion rate (\circ , left vertical axis) and the sand erosion rate (\blacklozenge , right vertical axes) as a function of the bed stress. The dashed and dotted lines relate to time-independent erosion for mud and sand, respectively.

5.2.4 Erosion threshold

Figure 66 shows $\tau_{e,s}$ for all soils listed in Table 12 as a function of the water content. Generally, it is presumed that $\tau_{e,s}$ decreases for a lower density, and therefore, with increasing W . However, Figure 66 clearly shows the opposite, as $\tau_{e,s}$ becomes larger for increasing W . Finally, Figure 66 indicates that $\tau_{e,s}$ for sand-mud mixtures with low ξ_{cl} and low W , tend to $\tau_{e,s}$ for mixtures of sand and silt only. These behaviours are further elaborated in sections 5.3.3 and 5.3.4. Next, $\tau_{e,s}$ is plotted as a function of PI^* in Figure 67 (see also Appendix III), from a which a power law relation between the erosion threshold and the plasticity index (for $PI^* > 2$) is derived:

$$\tau_{e,s} = 0.161PI^{*0.80} \tag{5.5}$$

where PI^* is the indirectly determined plasticity index (see Section 4.1.3). Although $PI^* \approx 5 - 7$ indicates the onset for cohesive behaviour, Eq. (5.5) applies to the behaviour of

τ_e for both a dominant sand-silt skeleton and a clay-water matrix. For $PI^* < 1$, $\tau_{e,s}$ tends to $\tau_{e,s}$ for mixtures of sand and silt, for which $\tau_{e,s}$ increases with increasing ζ_{si} .

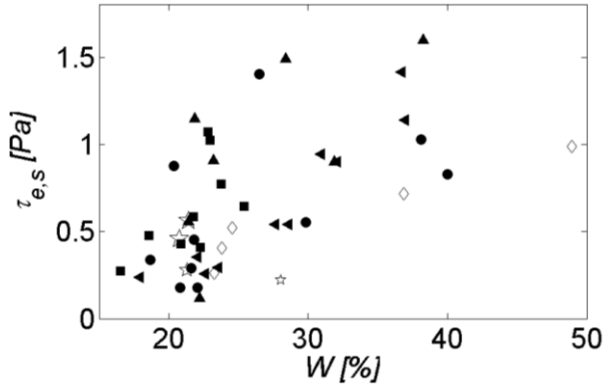


Figure 66. Surface erosion threshold as a function of the water content for soil samples of Set 0 (stars), 1 (●), 2 (▲), 3 (■), 4 (◄) and 5 (◇, bentonite). The size of the markers of Set 0 increases with increasing silt content.

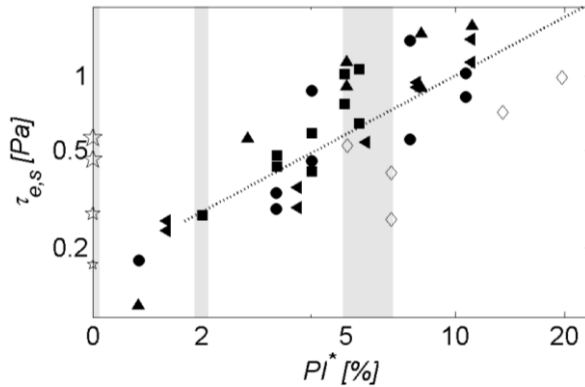


Figure 67. Surface erosion threshold as a function of the plasticity index (PI^*) for Set 0 (stars), 1 (●), 2 (▲), 3 (■), 4 (◄) and 5 (◇, bentonite). The size of the markers of Set 0 increases with increasing ζ_{si} . The grey-shaded areas indicate non-cohesive soils ($PI^* = 0$), the offset for cohesive effects ($PI^* \approx 2$), and the transition between a sand-silt skeleton and clay-water matrix ($PI^* \approx 5 - 7$).

τ_e for low cohesive soils ($PI^* < 2$) deviate from the power law function indicated by Eq. (5.5). These τ_e are plotted in Figure 68 as a function of ψ_{sa} in relation to ψ_{si} . It is shown that τ_e increases for increasing silt content, and that τ_e for soil samples of Set 1 – 5 with little clay similar τ_e exist as for Set 0 soils. The figure indicates a linear relation between ψ_{sasi} and τ_e for soil samples i, ii, iii, 1, 6 and 11, with larger $\tau_{e,s}$ for increasing ψ_{si} . τ_e for soil sample 16 deviates from this linear relation.

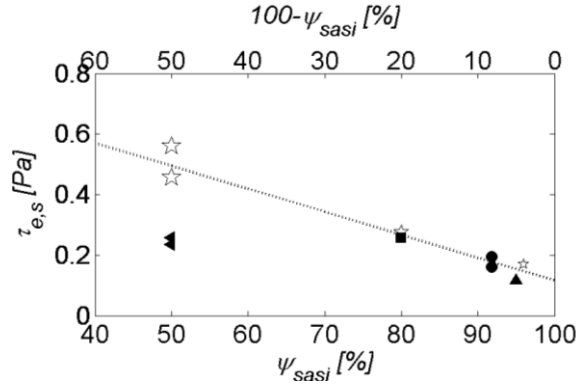


Figure 68. Surface erosion threshold as a function of the ratio between sand and silt volume fraction for Set 0 (stars), 1 (●), 2 (▲), 3 (■) and 4 (◄) for which the plasticity index < 2. The dotted line is the fit for all data, except for Set 4 (see Table 12).

5.3 Discussion

5.3.1 Erosion modes and features

The erosion of aggregates associated with Feature 2 (cracks) would suggest mass erosion. Section 3.2.3 indicates that the mass erosion threshold equals $f_w \cdot (2 - 5) \cdot c_u$ (with $f_w \sim 2 \cdot 10^{-3}$ Section 3.2.3). The c_u -value of the tested soil samples is ~ 1 kPa (Chapter 4), which results in a mass erosion threshold possibly in the order of τ_b during the tests (maximum ~ 3 Pa).

However, the observed behaviour does not agree with the failure mechanism of mass erosion (Figure 69(a)). Mass erosion exhibits flow-induced deformations in plastic material, which generate swelling in the flow direction and, subsequently, cracks perpendicular to the flow direction (transversal cracks). The characteristics of these cracks are markedly different from the longitudinal and radial cracks observed for Feature 2 (Figure 60).

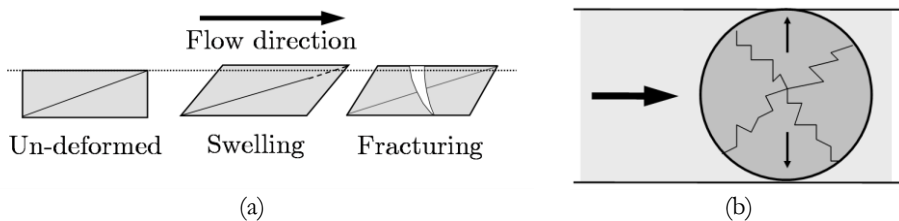


Figure 69. Failure mechanism of mass erosion (a, side view), with failure planes perpendicular to the flow direction (after Van Kesteren, 2008), and failure mechanism as observed in the current study (b, top view) for radial failure planes. The large black arrows indicate the flow direction.

Longitudinal cracks may be attributed to a combination of the (small) margin between the soil sample and the bottom of the flume, on the one hand, and the force exerted by the flow, on the other hand. Due to their plastic character, cohesive soils distort and exhibit cracks, whereas for more granular samples with a rigid sand-silt skeleton no distortion and cracks are observed. Such distortion is largest in the middle of soil samples and almost zero along the sides (e.g. Figure 60(c)). This difference is attributed to the circular shape of the exposed area. In the flow direction this area is longer in the middle of the flume, which induces more distortion and therefore, larger cracks.

Another effect of the margin between the soil sample and the bottom of the flume may be that the circular exposed surface area becomes slightly oval-shaped, as illustrated by the two little arrows in Figure 69(b). The upstream and downstream parts of the surface area act as a wedge and generate radial failure planes (e.g. Figure 60(b) and (d)). This mechanism generates dilating shear planes at low isotropic stress (Winterwerp and Van Kesteren, 2004).

Furthermore, true mass erosion yields undrained failure during which lumps of material are abruptly eroded. However, based on the observed slow rate at which the cracks developed, Feature 2 must be a drained process rather than an undrained process. The erosion of the lumps of material followed from the presence of cracks, which allow the dissipation of pore water pressure gradients at relatively large and random depth and, subsequently, the erosion of lumps of material.

The crack formation and the subsequent erosion of lumps of material can be compared with cliff erosion due to wave action as observed at the transition between tidal flats and marshes in estuaries. A dissipation front propagates horizontally into the cliff; erosion of lumps of material occurs when the flow-induced stresses (in combination with a gravitation component) exceed the drained strength of the cliff.

In conclusion, the longitudinal and radial cracks, which characterise Feature 2, are most likely artefacts of the experimental set-up. Furthermore, the cracks generate drained erosion of lumps of material which should not be confused with true mass erosion following Winterwerp and Van Kesteren (2004).

5.3.2 Flocculation and surface erosion

The determination of the erosion threshold is often subject of discussion, as there is no proper definition. This is primarily caused by the fact that for any given bed shear stress some particles are always moved and/or eroded, which results in a range of τ_e for the onset of time-dependent erosion. However, for time-independent erosion, which occurs for larger τ_b , a distinct threshold can be identified by extrapolating to a zero erosion rate. Observations from the erosion tests indicate that this threshold reflects the onset of uniform erosion of both sand and mud, whereas for time-dependent erosion only flocs were randomly eroded.

Time-dependent and time-independent erosion refer to, respectively, Type I and Type II erosion as defined by Parchure and Mehta (1985), see also Sanford (2006). However, they relate depth-limited (i.e. time-dependent) erosion to increasing bed

strength with increasing depth only. In the current study soil samples are isotropic with respect to packing density and composition, which indicates that vertical gradients in bed strength within the upper few mm are (presumably) too small to significantly decrease erodibility. Other possible causes for the occurrence of time-dependent erosion in the current study are briefly discussed below (a more thorough discussion is presented in Chapter 7).

The first possibility concerns the erosion depth; when it becomes too large it will locally affect the flow pattern in the flume and, therefore, the erosion behaviour. However, Figure 70 shows that the erosion depth for most tests is only about 2 mm (10% of the water depth), which is presumed too small to affect erosion.

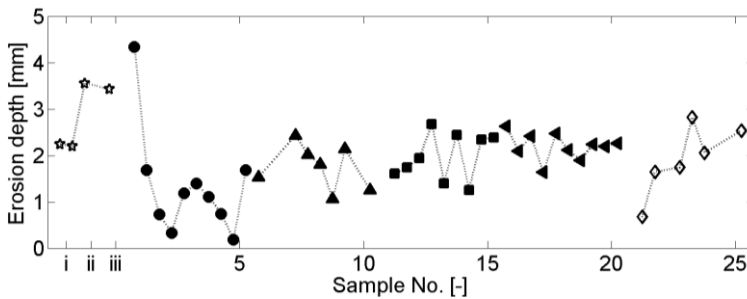


Figure 70. Maximum erosion depth as a function of soil sample number (Table 12) for soil samples of Set 0 (stars), 1 (●), 2 (▲), 3 (■), 4 (◄) and 5 (◇).

The second possibility is that during time-dependent erosion only flocs are eroded, due to which the remaining sand-silt skeleton consisting of larger particles is more difficult to erode (cf. armouring; e.g. Van Rijn, 1993). Also the occurrence of simultaneous erosion and deposition of mud (especially for high concentrations) may result in a zero net water-bed exchange. However, time-dependent erosion only occurs during the first velocity steps when concentrations are fairly low ($< 0.1 \text{ g}\cdot\text{l}^{-1}$) and deposition is not significant, whereas the effect of armouring and deposition are especially expected for relatively large τ_b and c .

The third possibility is that time-dependent erosion originates from the stochastic character of τ_b and, to a lesser extent, of τ_e . The decrease of the erosion rate with time is then explained as follows. Upon increasing mean τ_b towards mean τ_e , the peak shear stresses erode the weakest flocs at a relatively large rate. After some time, these weak flocs are mostly eroded, which induces a decrease of the erosion rate.

Also e.g. Vanoni (1964), Partheniades (1962, 1965), Grass (1970), Torfs (1995), Panagiotopoulos *et al.* (1997) and Righetti and Lucarelli (2007) relate the absence of a true erosion threshold for cohesive sediments to the stochastic character of the flow. As the bed shear stress is the sum of a mean value ($\bar{\tau}_b$) and turbulent fluctuations ($\hat{\tau}_b$), the erosion of particles may start for small τ_b when $\hat{\tau}_b$ exceeds τ_e .

These studies also observe a sudden increase in the size and quantity of flocs in the water column, as well as the start of the erosion of sand for larger τ_b ($\bar{\tau}_b > \tau_e$), which reflects Type II erosion. Partheniades (1962, 1965) further argues that the

horizontal distribution of the bed strength (and thus τ_e) further enhances time-dependent effects. However, in the current study it is presumed that this effect is small, as the exposed surface area is small and the soil samples are isotropic.

The stochastic approach agrees with the proposed erosion classification shown in Section 3.2.3. Floc erosion is the random (in both space and time) disruption of individual flocs from the surface of the bed by flow-induced peak bed shear stresses when the mean bed shear stress not yet exceeds the mean drained strength of the bed. In time, the weakest particles erode. This forces the probability density function of the bed strength to shift to larger values and, as a result, floc erosion ceases.

Surface erosion is a drained failure process (no pore water pressure gradients) which occurs when the maximum bed shear stress is larger than the maximum erosion threshold. As a result, the supply of sediments is unlimited yielding the simultaneous erosion of sand and mud from the whole surface layer of the sediment bed at constant rate. This is different from the random (in both space and time) character of floc erosion. Besides time-(in)dependency, it is also possible to apply the e -folding time scale to distinguish between floc and surface erosion. B^{-1} is about $> 0 - 300$ s for time-dependent erosion, whereas B^{-1} becomes suddenly an order of magnitude larger ($>1000 - 10000$ s) for $\tau_b > \tau_{e,s}$.

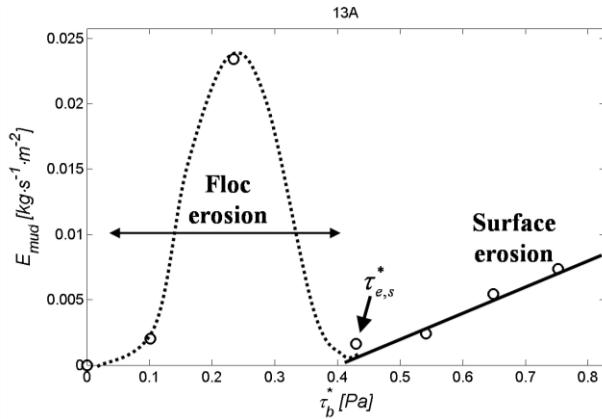


Figure 71. Typical example of the mud erosion rate (E_{mud} , \circ) as a function of the bed shear stress. The continuous line fits E_{mud} for surface erosion in case the bed shear stress exceeds the surface erosion threshold ($\tau_b > \tau_{e,s}$); the dotted line fits E_{mud} for floc erosion ($\tau_b < \tau_{e,s}$). The peak E_{mud} for floc erosion (e.g. for soil sample 13) exhibits a random character concerning occurrence and character.

The current study focuses on the surface erosion threshold, which relates to soil characteristics rather than to stochastic flow character as is the case for time-decreasing or floc erosion. The surface erosion coefficients are separately discussed in the following sections, whereas floc erosion coefficients are discussed immediately below.

Contrary to surface erosion, no single erosion threshold exists for floc erosion (for $0 < \tau_b < \tau_{e,s}$). Similar behaviour is observed for soil samples containing only silt,

kaolinite and silt or bentonite and silt. Floc erosion occurs for τ_b ranging from 0 - 1.5 Pa, which agrees with the floc strength c_d (typically a few Pa for freshly deposited clays, Section 3.1.1). Furthermore, Figure 71 shows that E_{mud} exhibits large peaks during floc erosion, for which E_{mud} typically varies between 10^{-3} to 10^{-2} $\text{kg}\cdot\text{m}^{-2}\cdot\text{s}^{-1}$. Mehta and Partheniades (1979) report similar results of E_{mud} and τ_b for floc erosion, with E_{mud} typically varying between $0.003\cdot 10^{-3}$ and $5\cdot 10^{-3}$ $\text{kg}\cdot\text{m}^{-2}\cdot\text{s}^{-1}$.

However, peak- E_{mud} exhibit rather random characters with respect to occurrence, maximum value and τ_b for which they occur. Furthermore, c within these first steps is still relatively low, which indicates that the mass of eroded material is small. Therefore, it is concluded that these peak- E_{mud} do not characterise the relation between floc strength and flow conditions, but that they can most likely be attributed to an artefact of the experimental procedure. An example may be the re-suspension of fines during the filling of the flume and the subsequent deposition on the bottom of the flume.

5.3.3 Surface erosion threshold for sand-mud mixtures

Figure 66 shows that $\tau_{e,s}$ typically varies between 0.1 – 1.5 Pa, which agrees with reported data for low-cohesive soil samples (e.g. Le Hir *et al.*, 2007a; Winterwerp and Van Kesteren, 2004). However, a negative correlation occurs for $\tau_{e,s}$ as a function of W , although in literature generally a decrease of the erosion threshold is expected for decreasing density (i.e. increasing W).

This increase of W can be explained by the water binding capacity of clay, which implies that as the clay content increases, the water content increases accordingly (whereas the overall-density decreases). The increase of the erosion threshold as a function of W (Figure 66) follows from the combined effect of increased cohesive bonding and a lower permeability of the sediment bed. The latter results from the relatively large volume fraction of mud flocs compared to sand and silt. Although the overall-density decreases, the increased space between sand and silt particles is occupied by the mud flocs, which decreases the overall permeability.

Furthermore, Figure 66 and Figure 67 confirm the presumed drained character of surface erosion, as the threshold relates to cohesiveness (PI^* , Figure 67) rather than to packing density (W , Figure 66). The scatter of the data in Figure 67 may be attributed to the (unknown) effect of varying clay-silt and sand-silt ratios on PI^* .

Next, the experimental data are compared (Figure 72) with the results of Smerdon and Beasley (1959) and Torfs (1995). Some assumptions are made concerning the composition of the soils used by Torfs (1995), as only limited information is available. Soils are relatively sandy mixtures of sand and mud with a presumed dominant sand-silt skeleton and with assumed activities of 0.4 for kaolinite, 0.5 for natural clay (mainly illite) and 1.34 for bentonite. These activities agree with the activities of the clay minerals used in the current study (kaolinite and montmorillonite) and with activities reported in literature (e.g. Head, 1980).

Smerdon and Beasley (1959) study natural, riverine mud with an activity of the clay fraction of 0.9. As for these soils $PI^* > 7$, a dominant clay-water matrix is

presumed for these soils. This is supported by the bulk densities of the soils, which ranges between 1580 and 1740 kg·m⁻³.

Neither Smerdon and Beasley (1959) nor Torfs (1995) distinguish between floc and surface erosion. Torfs (1995) defines τ_e as τ_b at which material starts to accumulate in the sand trap, in combination with a visually observed increase of the concentration of suspended fines. Smerdon and Beasley (1959) relate the erosion threshold to general movement of the soil composing the bed. This indicates that both studies define τ_e as τ_b for which transport is initiated, similar to the current study. This justifies the comparison of the results of the three studies.

Figure 72 shows that the power law relation (Eq. (5.5)) between PI^* and $\tau_{e,s}$ for the experimental data nicely agrees with the relation presented by Smerdon and Beasley (1959). Re-plotting the results of Torfs (1995) also indicates a power law relation, although $\tau_{e,s}$ exhibits significantly larger $\tau_{e,s}$ (factor 2 - 4). This difference may be attributed to the calibration method of τ_b , as Torfs (1995) determines the bed shear stress based on the slope of the water surface, which is a rather inaccurate method for short flumes. Another possible cause for the structural difference may be the application of different methods to determine ζ_{cl} , which can result in differences for ζ_{cl} up to 100% (Jacobs *et al.*, 2007a; Appendix I). An underestimation of the clay contents yields lower PI^* , which may explain the relatively large $\tau_{e,s}$ as found by Torfs (1995).

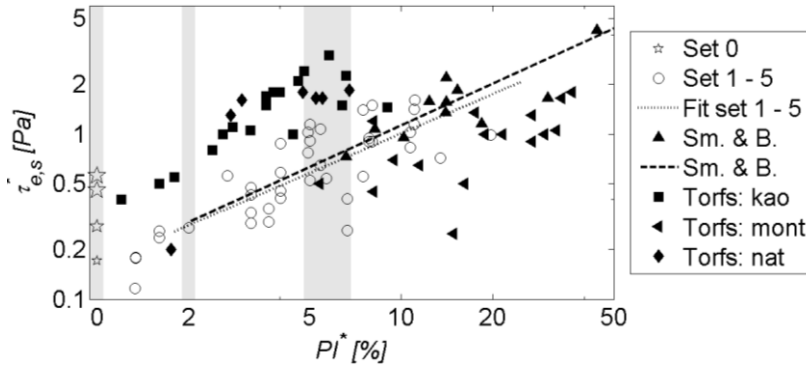


Figure 72. Surface erosion threshold as a function of the plasticity index (PI^*) for data of Set 0 – 5, Eq. (5.5), Smerdon and Beasley (1959, Sm. & B.) and Torfs (1995). The grey-shaded areas indicate $PI^* = 0$, $PI^* \approx 2$ and $PI^* = 5 - 7$, which refer to PI^* of sand-silt mixtures, the offset for cohesive behaviour, and the transition between a sand-silt skeleton ($PI^* < 5 - 7$) and clay-water matrix ($PI^* > 5 - 7$), respectively. The size of the markers of Set 0 increases with increasing silt content.

Summarizing, it is remarkable that for all three studies power law relations exists for $\tau_{e,s}$ as a function of PI^* , although sediment mixtures with varying structures and clay mineralogy are applied. This confirms the applicability of the plasticity index rather than the packing density to relate to the surface erosion threshold, and also confirms the presumed drained character of surface erosion and the, subsequently, dominant effect of the cohesiveness of the clay fraction.

5.3.4 Surface erosion threshold for granular mixtures

The erosion threshold for granular mixtures ($PI^* < 2$) deviates from the power law function given by Eq. (5.5). Furthermore, it is not useful to relate $\tau_{e,s}$ to W , as the packing density for samples of Set 0 exhibits only little variation (Figure 66). Therefore, $\tau_{e,s}$ is plotted as a function of ψ_{sa} in relation to ψ_{si} (Figure 68). The results show that $\tau_{e,s}$ linearly increases for increasing silt content, and that soil samples of Set 1 – 5 with a low clay content (soil samples 1, 6, 11 and 16) exhibit similar $\tau_{e,s}$ as found for Set 0. $\tau_{e,s}$ of soil sample 16 deviates from this linear relation due to the relatively large ξ_{mu} (50% for soil sample 16 and $< 25\%$ for i, ii, iii, 1, 6 and 11).

Next, $\tau_{e,s}$ of soil samples i, ii and iii are compared with the Shields stability criterion (Shields, 1936), for which the erosion threshold also follows from the extrapolated zero erosion rate as a function of bed shear stress. The Shields stability criterion exhibits an increasing threshold with decreasing d_{50} for fine sands ($< 100 \mu\text{m}$). Shields (1936) attributes this to the lower bed roughness of fine-grained beds compared to coarse-grained beds. Figure 73 shows the critical Shields parameter θ_{cr} [-] as a function of the dimensionless particle parameter d_* [-] = $[(s - 1)g/v_w^2]^{1/3}d_{50}$, where s [-] is the relative density (ρ_s/ρ_w), d_{50} [m] the median particle size of the mixtures and v_w [$\text{m}^2\cdot\text{s}^{-1}$] the kinematic viscosity of water.

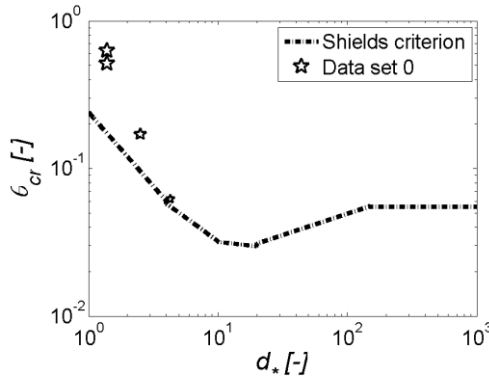


Figure 73. Shields stability criterion (dash-dotted line) with the critical Shield parameter θ_{cr} as a function of the dimensionless particle parameter d_* . Data for soil samples of Set 0 (stars) are shown, for which the size of the markers increases with increasing silt content.

A pronounced difference exists between the Shields stability criterion and $\tau_{e,s}$ presented in the current study. $\tau_{e,s}$ deviates from the criterion for an increasing silt content. A similar trend was found by Robberts *et al.* (1998), who studied the erosion of fine-grained granular mixtures. They report a relation between density and erosion rates for $d_{50} < 222 \mu\text{m}$ ($d_* < 5.6$), whereas for larger d_{50} erosion rates are independent of the density. This indicates that for small grained granular beds, bulk characteristics rather than individual particle characteristics become important.

A possible explanation is that the Shields criterion is calibrated for relatively coarse ($> 100 \mu\text{m}$) and well-sorted sediments, which implies that sorting effects are not incorporated. These effects concern a generally larger maximum density for poorly-sorted mixtures (small d_{90}/d_{10}) compared to well-sorted (large d_{90}/d_{10}) mixtures with similar d_{50} . Denser packing yields a larger internal friction which may enhance τ_e .

Another possibility is that due to a lower permeability (decreases with increasing d_{90}/d_{10} , see e.g. Head, 1982) the dissipation rate of pore water pressure gradients decreases, which augments failure resistance and, therefore, decreases erodibility. This will be subject of further study.

5.3.5 Surface erosion parameter

The current study defines the surface erosion parameter M_s as the sum of the slopes of $E_{s,sand}$ ($M_{s,sand}$) and $E_{s,mud}$ ($M_{s,mud}$) as a function of τ_b for $\tau_b > \tau_{e,s}$. This implies that M_s is expressed in $\text{kg}\cdot\text{m}^{-2}\cdot\text{s}^{-1}\cdot\text{Pa}^{-1}$ ($= \text{s}\cdot\text{m}^{-1}$), which agrees with the units of the new erosion parameter as presented in Section 3.3. However, M_s is often expressed in $\text{kg}\cdot\text{m}^{-2}\cdot\text{s}^{-1}$ (e.g. in the Ariathurai-Partheniades formulation, Section 2.4.3), as the slope of E as a function of τ_b is divided by $\tau_{e,s}$. In this way the combined effect of the erosion parameter and threshold is shown, whereas current study focuses on these parameters individually.

By definition, surface erosion is a drained process, which is governed by the inflow of water as a function of the permeability of soils. Subsequently, M_s is expected to relate to a combination of the packing density and clay content. This is confirmed by Figure 74, which shows that M_s does not exhibit a strong correlation with W or PI^* . This is explained by the absence of strong relations between sand-mud mixture permeability and W or PI^* .

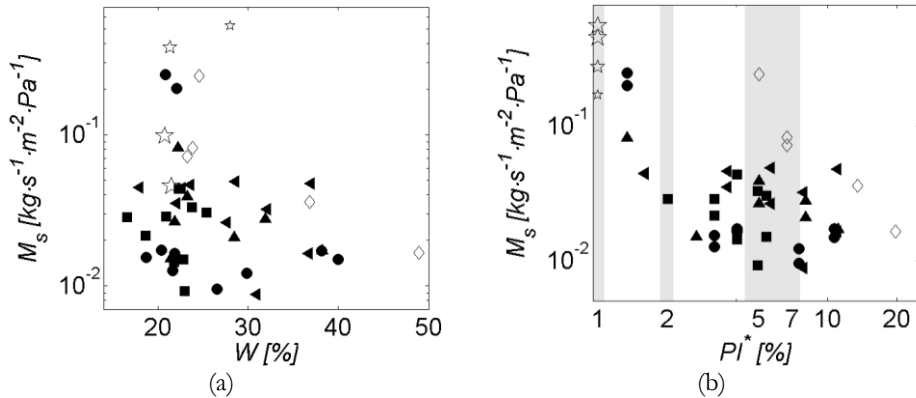


Figure 74. Surface erosion parameter (M_s) as a function of the water content W (a) and PI^* (b) for soil samples of (a) Set 1 (\bullet), (b) Set 2 (\blacktriangle), (c) Set 3 (\blacksquare), (d) Set 4 (\blacktriangleleft) and (e) Set 5 (\diamond , bentonite). The size of the markers for Set 0 (stars) increases with increasing silt content.

M_s is a function of c_u and c_v (Section 3.3), which both exhibit power law relations as a function of W_{rel} (Chapter 4). Therefore, M_s is plotted as a function of W_{rel} on a log-log scale in Figure 75 (see also Appendix III). M_s increases with increasing W_{rel} to M_s found for Set 0 at $W_{rel} \rightarrow \infty$, which indicates that the erodibility increases for decreasing clay content. Lowest M_s are found for soils with a dominant clay-water matrix. This cannot be attributed to higher clay contents and, subsequently, larger cohesive shear strengths only, as the occurrence of surface erosion implies (by definition) that the cohesive strength of individual flocs is exceeded by the turbulent shear stress of the flow. M_s as a function of W_{rel} is fitted with a power law function:

$$M_s = 3.8 \cdot 10^{-3} W_{rel}^{1.12} \quad (5.6)$$

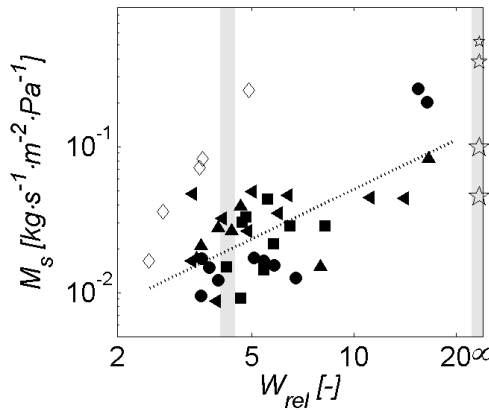


Figure 75. Surface erosion parameters: M_s [$\text{kg}\cdot\text{m}^{-2}\cdot\text{s}^{-1}\cdot\text{Pa}^{-1}$] as a function of the relative water content (W_{rel}) for soil samples of Set 0 (stars), Set 1 (●), Set 2 (▲), Set 3 (■), Set 4 (◄) and Set 5 (◇, bentonite). The grey-shaded areas indicate $W_{rel} = \infty$ and the transition ($W_{rel} \approx 4$) in dominant structure. The size of the markers for Set 0 increases with increasing silt content.

Scatter of this fit function may be attributed to the effect of varying clay-silt and sand-silt relations. This effect is especially important for soils with little clay, as M_s of these soils tends to M_s of mixtures of sand and silt only. M_s of these mixtures varies as a function of the sand – silt relation (see Figure 76(a)). Furthermore, it is noted that M_s for samples with bentonite exhibit a structural deviation from the data of Set 1 – 4, which may be attributed to a possible overestimation of the clay content (yielding an underestimation of W_{rel}) of the bentonite fraction (see also Section 5.3.3). Data for samples with bentonite are, therefore, not used for Eq. (5.6).

Next, M_s is plotted as a function of the relation between the volume fractions of sand and silt. When considering only particle size, a larger erodibility is expected for soils with smaller particles (i.e. more silt). However, Figure 76(a) shows the opposite, as M_s decreases with increasing silt content for sand-silt mixtures. This indicates the importance of bulk soil characteristics next to individual particle characteristics.

This importance is further confirmed by the strong correlation between M_s and d_{10} (i.e. the grain diameter for which 10% of the grains is passing) in Figure 76(b), which is an indicator for the permeability (e.g. Head, 1982). An increase of M_s with increasing d_{10} is expected, as larger d_{10} implies higher permeability and, subsequently, a larger erodibility as the in-flow of water upon removal of overlying layers of sediment is enhanced. M_s as a function of d_{10} can be fitted with a power law function:

$$M_s = 6.2 \cdot 10^{-6} d_{10}^{2.86} \quad (5.7)$$

where d_{10} is expressed in μm .

Next, experimentally obtained M_s are compared with literature. Figure 75 shows that M_s typically varies between $1 \cdot 10^{-2} - 1 \cdot 10^{-1} \text{ kg} \cdot \text{m}^{-2} \cdot \text{s}^{-1} \cdot \text{Pa}^{-1}$. M_s expressed in $\text{kg} \cdot \text{m}^{-2} \cdot \text{s}^{-1}$ is of the same order of magnitude, as $\tau_{e,s}$ ranges between 0.5 and 1.5 Pa. M_s values shown in Figure 75 are significantly larger than reported in Van Rijn (1993) and Winterwerp and Van Kesteren (2004). These studies report that M_s for soft natural mud typically varies between $0.01 \cdot 10^{-3} - 0.5 \cdot 10^{-3} \text{ kg} \cdot \text{m}^{-2} \cdot \text{s}^{-1}$. However, it is unknown on which studies these M_s are based and for what type of erosion they occurred. Besides, Winterwerp and Van Kesteren (2004) argue that M_s can be significantly larger or smaller than the indicated range, e.g. for mixtures of sand and mud or due to consolidation.

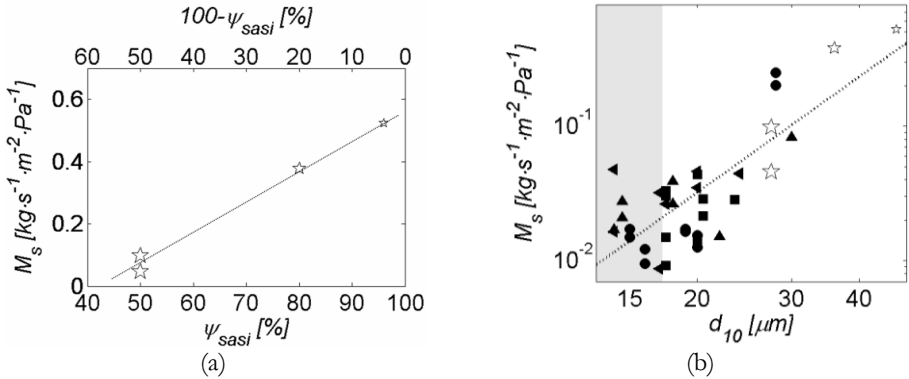


Figure 76. Surface erosion parameter (M_s) as a function of the relation between the sand and silt fractions (ψ_{sasi}) in (a) and as a function of d_{10} in (b) for soil samples of Set 0 (stars), Set 1 (\bullet), Set 2 (\blacktriangle), Set 3 (\blacksquare) and Set 4 (\blacktriangleleft). The size of the markers for Set 0 increases with increasing silt content. d_{10} is the grain diameter for which 10% of the grains is passing. The grey-shaded area in (b) indicates a dominant clay-water matrix.

Houwing (2000) reports erosion rates varying between $1 \cdot 10^{-5} - 1 \cdot 10^{-1} \text{ kg} \cdot \text{m}^{-2} \cdot \text{s}^{-1}$ for the erosion of a kaolinite bed under laboratory conditions. These rates are comparable to those found in the current study. Largest values exist for large τ_b at which the concentration linearly increases with time. Torfs (1995) presents surface erosion rates ($1 \cdot 10^{-4} - 1 \cdot 10^{-2} \text{ kg} \cdot \text{m}^{-2} \cdot \text{s}^{-1}$) for similar sand-mud mixtures as in the current study (concerning ρ_{bulk} , ζ_{cl} and clay mineralogy). Next, erosion rates are

compared with previous data for purely granular mixtures, although most studies focus on the erosion of mono-disperse and relatively coarse sands. Roberts *et al.* (1998) describe one of the few studies discussing the erosion of relatively fine grained sand-silt mixtures as a function of d_{50} and ρ_{bulk} . Reported data are of the same order of magnitude as found for Set 0.

Finally, it is noted that M_s is rather sensitive to the calibration methodology for the concentration sensor. As discussed in Section 5.2.2, this calibration is hampered by e.g. the effect of varying clay-silt and sand-silt ratios, which are not taken into account.

In conclusion, limited data are available concerning the surface erosion parameter for mixtures of sand and mud. In addition, different and often poorly described measurement and analysis methods are available. Furthermore, varying definitions for erosion modes are applied to determine and describe both E and M . Yet, some studies report comparable erosion coefficients for similar sand-mud and sand-silt mixtures as found in the current study.

5.3.6 Accuracy of results

The reproducibility of the experimental procedure is checked by comparing $\tau_{e,s}$ and M_s with the erosion coefficients of similar soil samples (Figure 77). Figure 56 and Table 12 show that soil samples 2 and 12, 4 and 19, 8 and 14 and 10 and 20 have comparable ξ_{sa} , ξ_{si} , ξ_{cl} , PI^* and n_{sasi} . Additionally, these soil samples are tested twice. The accuracy for $\tau_{e,s}$ is acceptable, whereas the M_s is relatively scattered. The latter is attributed to variations of W (see Table 12). Other possible causes for the scattering are errors due to the sample preparation, instrument calibration and/or measuring procedures.

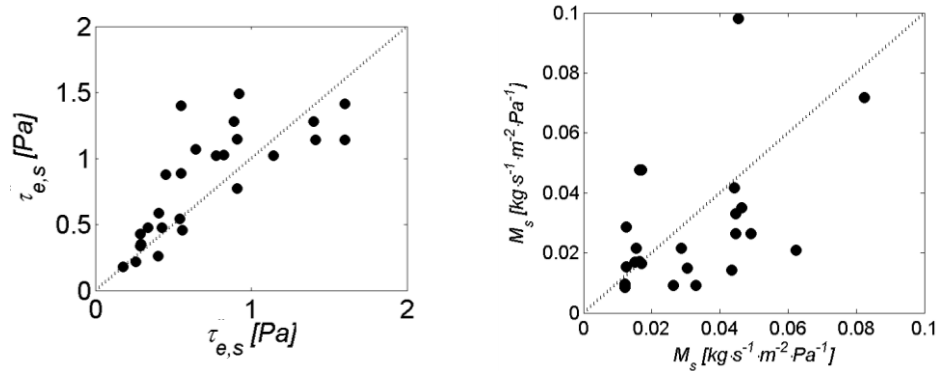


Figure 77. Reproducibility of the surface erosion threshold (a) and the surface erosion parameter (b) for soil samples with identical plasticity index and sand-silt and clay-silt ratio. The dotted lines indicate perfect agreement.

5.4 Conclusions

Results of about 50 erosion tests on soil samples with varying composition in terms of clay-silt and sand-silt ratio and clay mineralogy are presented. Sediment beds exhibit purely granular behaviour for a plasticity index smaller than 2. For larger plasticity indices two types of erosion exist: floc and surface erosion.

Floc erosion is most clearly observed at low bed shear stress. It is a time-dependent process (varying erosion rate with time) during which individual mud flocs are randomly eroded. Flocs are eroded at rather low mean bed shear stress, when peak bed shear stresses locally exceed the floc strength. This indicates the importance of the stochastic character of the flow. Floc erosion ceases when all erodible flocs are eroded.

For larger bed shear stress time-independent erosion (constant erosion rate with time) is observed, during which individual sand and mud particles are simultaneously and uniformly eroded. The erosion rate linearly increases with the bed shear stress beyond a specific threshold, which is defined as the extrapolated zero transport rate. Surface erosion properties are determined by material properties rather than by the stochastic properties of the flow conditions. The behaviour of the erosion rate as a function of time for floc (varying erosion rate with time) and surface erosion (constant rate) imply that only surface erosion can be described by an Ariathurai-Partheniades type formula.

The current study applies a geotechnical approach to characterize surface erosion as a drained process. This implies that only the cohesive sediment strength is determining for the surface erosion threshold, rather than the packing density. This geotechnical approach is confirmed by the experimental results.

Both the surface erosion threshold and the erosion parameter exhibit an inverse correlation with the water content, which is a measure for the packing density. However, a power law relation exists between the threshold and the plasticity index. This index is a bulk material parameter for the cohesiveness of a soil as a function of the clay content, the type of clay mineral and the effect pore water chemistry. The power law relation agrees with relations presented in literature, which is remarkable as soils with varying structure and clay mineralogy are applied. The erosion parameter exhibits a relation with the relative water content and with the particle size characterizing the smallest fractions (d_{10}), which indicates the importance of the permeability and, therefore, agrees with the definition of surface erosion.

The erosion threshold for granular mixtures partly agrees with the Shields stability criterion, as for small-grained and poorly-sorted mixtures a deviation with this criterion exists. Although more study is required, a possible explanation is that the threshold increases due to the existence of pore water pressure gradients, which results from a decreased permeability. The strong relation between plasticity index and erosion threshold for sand-mud mixtures nicely agrees with results presented in literature.

During surface erosion, two features (sand wave and cracks) in the upper layer of the sediment bed were observed. The experimental data show that the initial erosion process is not significantly affected by the occurrence of these features. This follows from the relatively small size of the test section, which prevents larger (eroded) particles from being deposited on the sediment bed. However, in natural environments

these features form a micro-bathymetry, which can significantly affect the flow pattern and, subsequently, lead to either a positive or negative feedback on erosion.

Surface erosion parameters and erosion rates agree with literature. However, comparison with previous studies is difficult, due to limited data and various definitions for erosion parameters and analysis methods. A qualitative discussion of the data indicates a strong relation between the erosion parameter for sand and the relative water content and d_{10} . A more quantitative discussion is presented in Chapter 7.

In conclusion, the recognition of time-dependent and time-independent erosion partly indicates that there is not a single erosion threshold for a particular soil. For time-dependent floc erosion a zero-threshold occurs, whereas for time-independent surface erosion a clear threshold occurs. Furthermore, results for artificially generated soil samples confirm the applicability of a geotechnical approach to study the erosion of sediment mixtures as proposed in Chapter 3. A similar approach for the erosion of natural soils is therefore suggested.

Furthermore, it is recommended to obtain more accurate calibration relations for the concentration and the bed shear stress. Concerning the concentration especially the effect of varying clay-silt and sand-silt ratios should be taken into account. For the calibration of the bed shear stress the additional friction source at the upper side of the test section should be taken into account.

Furthermore, erosion modes vary during erosion tests, e.g. from floc erosion to surface and finally mass erosion. This indicates that the character of resuspended material may vary during a test, from initially small clay-flocs, to larger flocs consisting of clay and silt and finally to aggregates of sand and mud. Therefore, it is recommended to take these varying properties of the suspension into account when deriving concentration calibration curves.

Chapter 6

Annular flume erosion experiments

Results of three large-scale erosion tests on artificially generated relatively dense mixtures of sand and mud are presented. The soil samples with constant clay mineralogy concern sandy, muddy and intermediate sand-mud mixtures with increasing clay content. The experiments were carried out in a large-scale rotating annular flume. Concentration profiles, erosion rates, erosion thresholds and erosion parameters are determined and analysed similarly as in Chapter 5. In Chapter 7, these erosion parameters are compared with the experimental results presented in Chapter 5, as well as with theoretically derived parameters in Chapter 4. Results of the three tests have also been presented in Laksanalamai (2007).

6.1 Methods

6.1.1 Annular flume and measurement techniques

Erosion tests were executed in the rotating annular flume at the Laboratory of Fluidmechanics at the Faculty of Civil Engineering of the Delft University of Technology (Figure 78). The diameter, width and height of the circular flow section of the flume are 3.7, 0.3 and 0.4 m, respectively. The volume of water in the flume was $\sim 0.9 \text{ m}^3$. Annular flumes exhibit three advantages compared to re-circulating straight flumes: (1) the absence of boundary effects due to their infinite length, (2) the absence of pumps which prevents adverse effects on the flow pattern and (3) on the break-up of suspended aggregates.

A tangential flow is driven by a ring shaped top lid (comparable to wind driven shear flow), rotating opposite to the direction of the flume. These oppositely directed tangential velocities generate two counter-rotating cells in the radial direction (Figure 79). The vertically varying tangential flow velocities generate variations of the centrifugal forces and, subsequently, a secondary flow. This flow is directed towards the outer bend, both along the sediment bed and along the top of the water column. The secondary flow is minimized by choosing a specific ratio between the angular velocities of the flume and lid. This ratio also generates a fairly uniformly distributed bed shear stress τ_b (Booij, 1994; 2003).

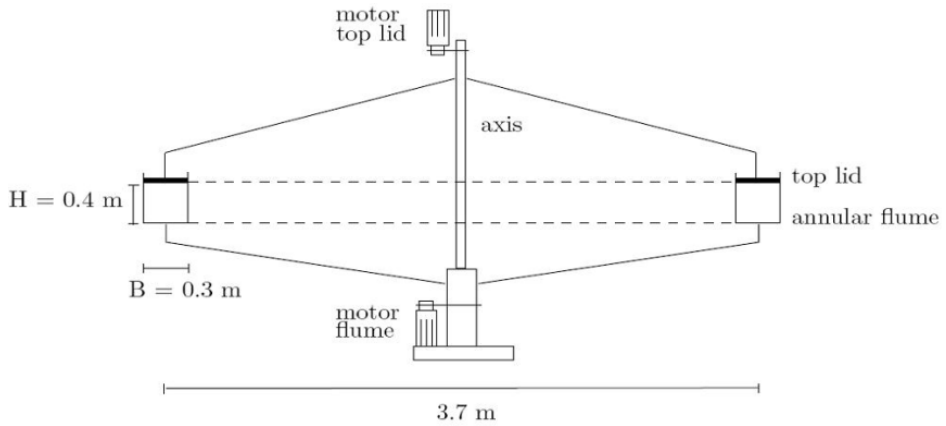


Figure 78. Cross section of the annular flume as applied in the current study (after Booij, 2003).

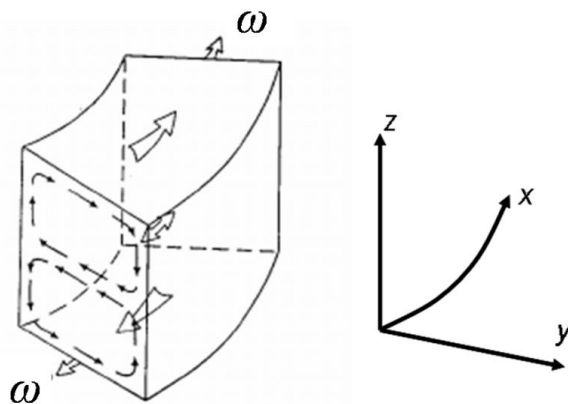


Figure 79. Schematized depiction of a section of an annular flume (Sheng, 1989). Two cells with opposing tangential flow (ω [rad·s⁻¹]) directions (block arrows) and counter rotating secondary cells (arrows) are shown in the cross-section. At right, the three-dimensional axes are shown.

During the tests, the angular velocities of the flume and lid were increased in 13 successive steps, each with an average duration of 10 min (Table 14). The optimum ratio between the angular velocities of the flume and lid to minimize secondary flow was constant for each test: 1.98 for a water depth of 0.27 m. The maximum angular velocities of the flume and lid are around 5.5 and 10.5 rad·s⁻¹, respectively. Maximum tangential flow velocity in the middle of the lower circulation cell (u_{av} [m·s⁻¹]) was about 1.15 m·s⁻¹.

Flow velocity and concentration were measured in two measuring stations at opposite sides of the flume (Figure 80). At each station an Electro Magnetic Flow

meter (EMF) determined the mean flow velocities in the x and z -direction. Flow velocities are derived from the potential difference generated by a flow-carried charge moving in a magnetic field in a coil with a diameter of 3 cm.

Table 14. Duration of velocity steps (T [min]) as imposed during the three erosion tests. ω_f and ω_l are the angular velocities of the flume and the lid, respectively; u_{av} is the average tangential velocity in the centre of the lower circulation cell (Figure 79) and τ_b is the accompanying average bed shear stress following from the LES model.

Step	T	ω_f	ω_l	u_{av}	τ_b
[-]	[min]	[rpm]	[rpm]	[m·s ⁻¹]	[Pa]
1.	7.5	-0.1	0.1	0.01	0.0003
2.	7.5	-0.5	1.0	0.11	0.0206
3.	7.5	-1.0	2.0	0.21	0.0752
4.	7.5	-1.5	3.1	0.33	0.1563
5.	10	-2.1	4.1	0.44	0.2640
6.	10	-2.5	5.0	0.53	0.3822
7.	10	-3.1	6.1	0.65	0.5601
8.	10	-3.6	7.1	0.76	0.7369
9.	12.5	-4.0	8.0	0.85	0.9010
10.	12.5	-4.4	8.8	0.94	1.0869
11.	12.5	-4.8	9.5	1.02	1.2543
12.	12.5	-5.2	10.2	1.09	1.4300
13.	12.5	-5.4	10.7	1.14	1.5805

The concentration (c_i [g·l⁻¹]) was measured using five (Figure 80) Optical Silt Measuring Instruments (Oslim). The subscript i refers to the Oslim number. Water with suspended sediment was continuously extracted from the flume by means of small (metal) tubes, which were connected to a pump and Oslim outside the flume. The Oslims measured c_i using the attenuation and scattering of light by passing particles. Three Oslims (range 0 – 30 g·l⁻¹) were positioned at Station I and two Oslims (range 0 – 2 g·l⁻¹) at Station II. The different vertical positions of the tubes enabled the determination of vertical c -profiles.

Before the tests, the Oslims were calibrated at varying suction speeds and for varying ratios of silt and clay, similar to the tested soil samples. To obtain representative Oslim measurements, the suction speed was more or less equal to the flow velocity in the flume. Three suction speeds were selected to reduce the number of calibrations applied for the mean flow velocity during step 1 – 4, 5 – 8 and 9 – 13. Sediment-water samples were withdrawn (at A between Oslims 4 and 5, see Figure 80) at about $\frac{3}{4}$ of the duration of each velocity step to obtain the reference concentration c_r [g·l⁻¹]. This concentration was determined by filtering, oven-drying and weighing and was, subsequently, compared with the output of the Oslims to perform an additional (Oslim) calibration. The volume of removed water (~150 ml) was replaced with clear water directly after extraction.

Flow properties should be measured at high resolution close to the bed in order to derive accurate τ_b . Such measurements with laser Doppler anemometry are difficult and labour intensive. Furthermore, c was too high after a few velocity steps to apply this technique. However, Booij (1994; 2003) performed detailed (laser Doppler) (clear water) measurements in a cross-section of this annular flume. Based on these measurements, a Large Eddy Simulation (LES) model with a resolution of 50 x 50 cells (y and z direction) for a hydraulically smooth (glass) bottom was calibrated. The input to the model concerned the water depth, the width of the flume and the angular velocities of the bottom and lid. The LES model nicely represented the tangential and radial flow patterns, provided insight in the optimal ratio to reduce the secondary flow, and enabled the determination of the spatially distributed τ_b .

In the current study this LES model was applied to determine τ_b . For each test 13 LES model runs were executed to simulate the flow properties for given water depth, ω_f and ω_l . The bed roughness of the sediment bed was assumed hydraulically smooth. The EMF (Electromagnetic Flow Meter) measurements are compared with the LES model results (Section 6.3.1) to check the validity of this assumption.

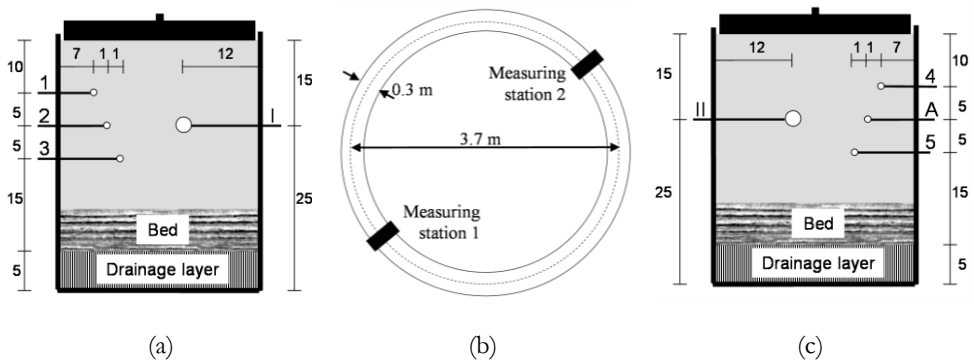


Figure 80. Cross sections at measuring Station 1 (a) and 2 (c) and top-view (b) of the annular flume showing the locations of EMF I (I in (a)) and EMF I (II in (c)), sampling tubes connected to the Oslims (1 - 5) and location (A) at which calibration samples are extracted (c). Units of the numbers left and right of the cross-sections are cm. Initial bed thickness for tests 1, 2 and 3 was 8.3, 9.1 and 8.7 cm, respectively.

6.1.2 Sample composition, preparation and placement

Three different mixtures of sand, silt and clay with different dominant soil structure were used during the erosion tests (Table 15 and Figure 81). These mixtures correspond to soil Samples 1, 3 and 5 in Chapter 5 (Table 12). Section 4.1.2 describes the micro-scale properties of the individual fractions. To obtain homogenous and 100% saturated mixtures, soil samples were artificially generated, similarly to the procedure described in Section 4.1.1. However, this small-scale set-up was not suitable to generate 0.4 m³ of sediment (required for a layer of 10 cm in the flume). Therefore,

a large vacuum mixer was applied to mix and saturate the soil samples in about 12 hrs. The 100% vacuum conditions imply that the use of CO₂ was not required.

After mixing, soil sample were placed in a cylindrical container, which was subsequently transported to the annular flume (~500 m). Two of these containers were required for one test. A hose with a 10 cm diameter was connected to the bottom of the cylindrical container, through which the material was poured by gravity into the flume to minimize air entrapment. In this way, two layers of 4 - 5 cm each formed the sediment bed. The surface of the bed was levelled after placement using a small shovel. The pouring procedure required sufficiently plastic material (i.e. sufficiently large W). However, sand and mud can segregate at too large W . Therefore, optimum W was experimentally determined (Laksanalamai, 2007), with optimum W at 30, 30 and 50% for Samples A, B and C, respectively.

Table 15. Composition (clay, silt and sand content; ratio sand-silt volume fraction) and bulk properties (bulk density, water content, granular porosity, plasticity index and relative water content) of the three tested soil samples. The clay mineral kaolinite is used and the clay-silt ratio is 0.25.

$No.$	ξ_{cl} [%]	ξ_{si} [%]	ξ_{sa} [%]	ψ_{sasi} [%]	ρ_{bulk} [kg·m ⁻³]	W [%]	n_{sasi} [%]	PI^* [%]	W_{rel} [-]
A.	2	8	90	92	1936	27	43	1.3	20.8
B.	6	24	70	74	2005	23	41	4.0	5.8
C.	16	64	20	24	1785	41	59	10.7	3.7

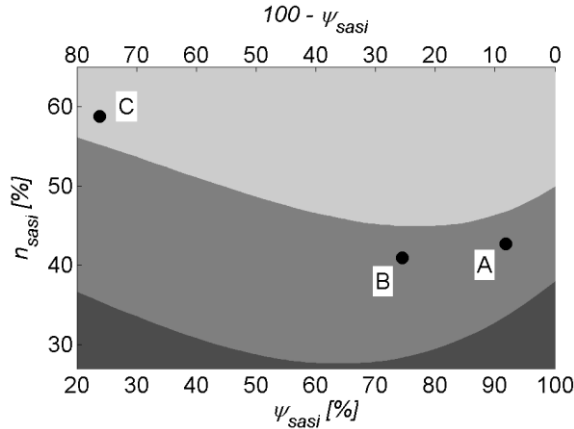


Figure 81. Granular porosity as a function of the sand-silt volume fraction ratio for soil samples tested in the annular flume. A, B and C refer to the soil samples listed in Table 15.

After placement, W of the soil samples was lowered to obtain comparable W as for the soil samples in Chapter 5, to facilitate a better comparison of the results. Self-weight consolidation is relatively slow and can lead to strong vertical gradients of bed properties, especially in the initial phase. This is inconvenient as varying bed

characteristics during erosion hamper the identification of relations between sediment characteristics and erosion behaviour.

To speed up consolidation and to prevent the formation of inhomogeneous bed characteristics, consolidation was enforced by means of an external load induced by a layer of water of 30 cm on top of the sediment bed. A plastic foil was placed on top of the bed and along the sides of the flume (Figure 82) to prevent the seepage of water through the bed. This load generated compaction of the sediment bed.

Excess water was drained from the bottom of the sediment bed. A perforated metal plate on top of a drainage layer consisting of gravel and bricks formed a permeable layer on the bottom of the flume. A filter fabric between the metal plate and the sediment bed prevented particles from washing out (Figure 82). Water was siphoned off from the water-filled drainage layer through two drainage holes in the bottom of the flume. The water level in the tubes connected to the drainage holes was equal to the bottom of the sediment bed in the flume.

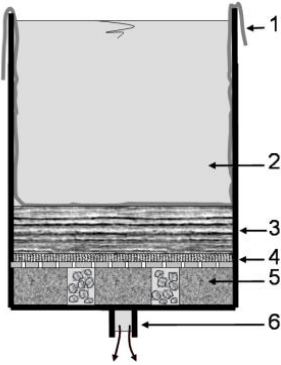


Figure 82. Cross section of the annular flume with plastic foil (1), water (2), sediment bed (3), filter fabric with perforated plate (4), drainage layer (5) and drainage hole (6).

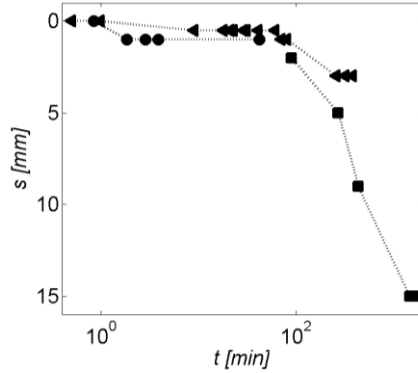


Figure 83. Settling (s [mm]) of the sediment bed as a function of time during forced consolidation for soil Samples A (\bullet), B (\blacktriangle) and C (\blacksquare), respectively.

The forced consolidation procedure was first tested in a small-scale set-up (Laksanalamai, 2007). Observations indicated typical consolidation behaviour (Figure 83). After an initial phase at little compaction, a clear consolidation phase occurred during which up to 1.5 cm settling was recorded for the most cohesive sample. After the settling phase the sample thickness was constant as internal stresses balanced the over-pressure.

As expected (Chapter 4), different consolidation behaviours existed for soils with either a sand-silt skeleton or a clay-water matrix (Figure 81). The length of the consolidation phase and the final settling were 50 min and 1 mm, 2 hr and 2 mm and 27 hr and 15 mm for soil Samples A, B and C, respectively. Accompanying dissipation coefficients (c_v) were about 10^{-4} , 10^{-6} and 10^{-8} $\text{m}^2 \cdot \text{s}^{-1}$ for soil Samples A, B and C,

which are comparable to the c_v given in Chapter 4. To ensure complete consolidation, samples were left to consolidate for 36 hrs in the annular flume.

After consolidation and before starting an erosion test, the plastic foil was carefully removed (without emptying the flume). Erosion tests were executed one day after the removal of the plastic to enable possible negative pore water pressure gradients to dissipate. Sediment cores with a diameter of 3.5 cm were obtained 1 m downstream of each measuring station before and after tests. Density profiles were determined by slicing and subsequently oven-drying the cores. The cavities in the bed were filled with coarse sand ($d_{50} = 1 - 2$ mm) to prevent disturbance of the flow pattern and/or subsequent scouring during tests. The total duration of the experimental procedure, including sample generation (2 days), transport, placement and consolidation (1.5 day) and erosion test (1 day) was 1 week.

6.2 Results

6.2.1 Computed and measured hydrodynamics

LES results clearly indicate the complex 3D flow pattern in the annular flume (Figure 84 and Figure 85). The simulations confirm the existence of two counter rotating circulation cells in radial direction, as argued by Sheng (1989) and illustrated in Figure 79. Results show that along the sediment bed the radial flow is directed towards the outer bend of the flume, with a downward flow along the inner bend and an upward flow along the outer bend (Figure 84). Maximum vertical velocities for step 13 are ~ 0.05 m·s⁻¹.

Also the tangential flow pattern (Figure 85) agrees with the expected flow behaviour. Along the sediment bed and walls, the flow is forced in the direction of the flume, whereas along the top of the water column the flow is forced by the counter rotating lid. As a result, the mean tangential velocities in the middle of the two circulation cells are oppositely directed. The white area in the middle of the cross section in Figure 85 indicates zero u_{av} .

τ_b is derived from the resultant of the frictional flow velocities (u_* [m·s⁻¹]) in the x and y -direction (Figure 79). u_* follows from the Reynolds' stresses computed with the LES model. Figure 86 shows that by applying an optimum ratio between the angular velocities of the bottom and lid, the horizontal distribution of τ_b in radial direction is rather uniform. Only for the last velocity steps, a maximum τ_b occurs at around 5 cm from the outer bend.

Figure 87 shows typical examples of the (a) tangential (u [m·s⁻¹]) and (b) vertical flow velocities (w [m·s⁻¹]) during a tests as measured with the EMF. The mean tangential flow velocities measured at the two stations (Figure 80) were identical. Therefore, the flow pattern is assumed homogenous in the tangential direction. The level of turbulence for u increases with increasing τ_b , although at constant τ_b (i.e. for an individual velocity step) the level of turbulence is more or less constant.

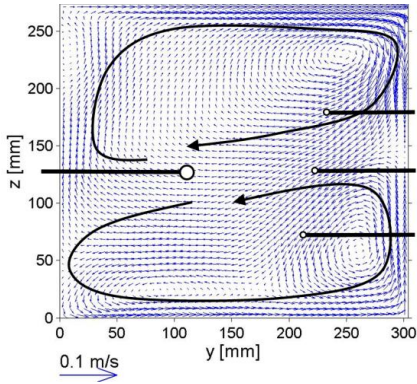


Figure 84. Typical (step 7) LES result for the radial flow in a cross-section of the flume (outer bend at right side), showing two counter rotating flow cells (black arrows). The tangential flow in the upper cell is directed away from the reader, whereas in the lower cell this flow is directed towards the reader. Locations of an EMF (at left) and three Oslims are indicated (at right).

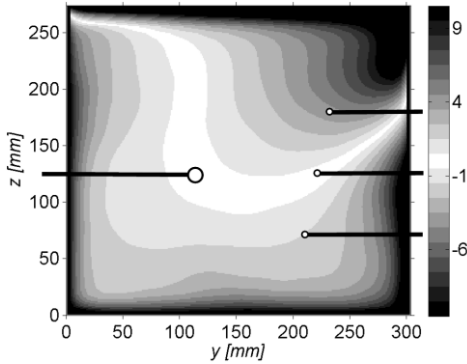


Figure 85. Typical (step 7) LES result for the tangential flow in a cross-section of the flume (outer bend at right side). The tangential flows in both circulation cells are oppositely directed. Values along the bar at right indicate flow velocities in $\text{cm}\cdot\text{s}^{-1}$. Positive (negative) velocities refer to a flow directed away (towards) from the reader, which occur in the upper (lower) circulation cell. Locations of the EMF and three Oslims are indicated.

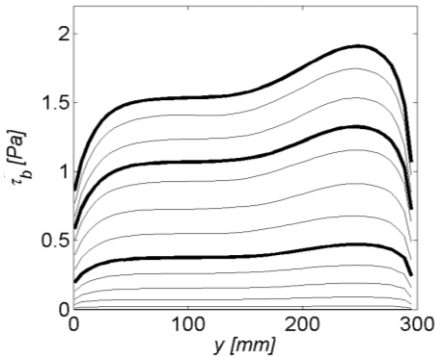


Figure 86. Typical LES result with the bed shear stress as a function of the distance from the inner bend of the annular flume (y [mm]) for all 13 velocity steps for hydraulically smooth conditions. The thick lines refer to velocity steps 6, 10 and 13. τ_b is reasonably uniformly distributed over the sediment bed, only for the last velocity steps a maximum exists at $y \approx 250$ mm.

The vertical velocities at the location of the EMF are rather small (Figure 87(b)). Turbulent fluctuations of w range between -0.1 and $0.1 \text{ m}\cdot\text{s}^{-1}$. Mean w is almost negligible for all three tests, varying between -0.005 and $0.005 \text{ m}\cdot\text{s}^{-1}$ only. No clear increasing or decreasing trend is observed for w with increasing τ_b . The stochastic character of w is shown by the significant level of turbulence indicated in Figure 87(b). Identical ranges of the level of turbulence existed at the two measuring stations. Unfortunately, one of the two EMF instruments malfunctioned in measuring w during tests B and C. Both EMF sensors worked properly for all tests in the u -measurements.

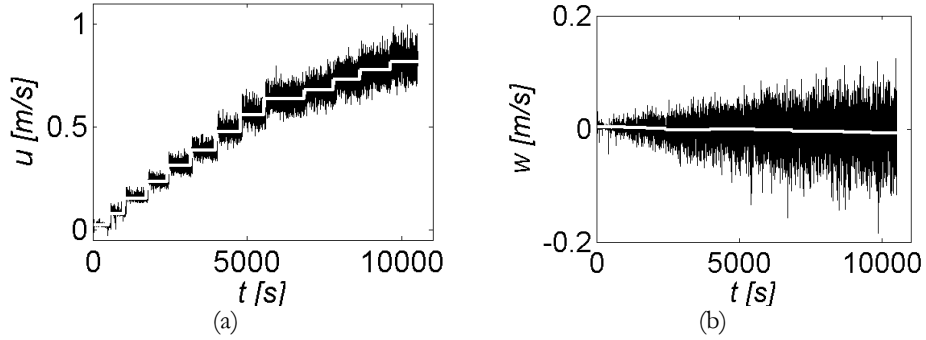


Figure 87. Typical examples of EMF measurement results for the (a) horizontal (u [$\text{m}\cdot\text{s}^{-1}$]) and (b) vertical flow velocities (w [$\text{m}\cdot\text{s}^{-1}$]) as a function of time during an erosion test. The white lines indicate the mean flow velocities.

6.2.2 Sediment bed properties

The thickness of the sediment bed after consolidation was 8.3, 9.1 and 8.7 cm for Samples A, B and C, respectively. Figure 88 shows vertical profiles of ρ_{bulk} as a function of depth below the surface. ρ_{bulk} slightly varies within the sediment bed: 1940 – 1980 ($W = 27 - 24\%$), 2000 – 2060 ($W = 23 - 20\%$) and 1770 – 1850 $\text{kg}\cdot\text{m}^{-3}$ ($W = 41 - 34\%$) for soil Samples A, B and C, respectively. Furthermore, no significant variation of ρ_{bulk} before and after the erosion tests was found. W of the upper 1 cm of the sediment bed is used to characterize the sediment bed during the erosion tests, as the maximum erosion depth was less than 1 cm for all three tests (Section 6.2.4). Variations of ρ_{bulk} within the upper 1 cm of the bed are too small to yield significantly varying soil properties.

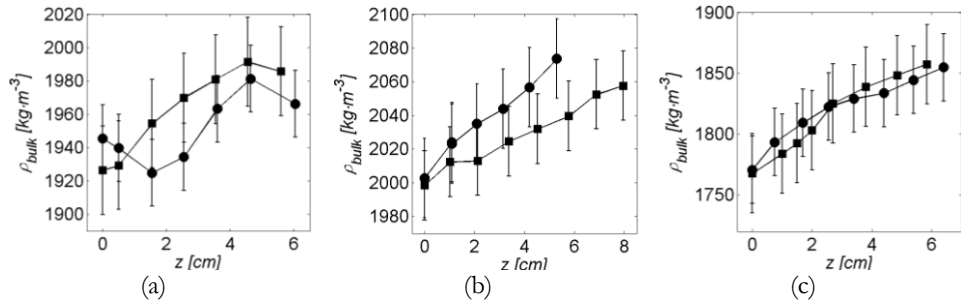


Figure 88. Mean (of two cores) profiles of the bulk density as a function of depth (z) for Sample A (a), B (b) and C (c), both before (●) and after (■) the erosion tests.

The plastic foil between the sediment bed and the water column left a wrinkled print on the surface of the bed (Figure 89). This micro-bathymetry was most clearly observed for soil Sample C. The typical length scale of the bed irregularities is 10 - 20 cm; the heights are about 1 - 2, 2 - 3 and 3 - 4 mm for soil Samples A, B and C, respectively.



Figure 89. Top view of the surface of soil Sample C before the erosion test, with the inner bend of the flume at the top (vertical scale of photo ~ 30 cm). The micro-bathymetry shown is the wrinkled print left by the plastic foil.

6.2.3 Erosion and transport modes and features

Table 16 gives an overview of the visual observations of the erosion and transport behaviour of sand and mud. Similar (but for varying τ_b) erosion modes and features were observed during subsequent velocity steps during the three tests. For the first steps only some small flocs were resuspended, which were mobilized during the removal of the plastic foil and, subsequently, deposited before starting a test.

Table 16. Visual observations of erosion and transport behaviour for all tests. Grey-shaded areas indicate transitions in behaviour: start of floc and surface erosion and sheet flow transport.

Step	A	B	C
1.	Re-suspension of fines	Re-suspension of fines	Re-suspension of fines
2.			
3.	Floc erosion		
4.		Floc erosion	Floc erosion
5.	Erosion of small aggregates and accumulation of sand		
6.			Erosion of small aggregates and sand
7.	Ripple formation in accumulated sand	Erosion of small aggregates and sand, ripple formation in accumulated sand	
8.	Sheet flow		
9.		Sheet flow	
10.			
11.			
12.		Random scour holes	Accumulation of sand
13.			

For increasing τ_b , floc erosion is observed, during which small flocs and small aggregates of flocs (for larger τ_b) come into suspension. The erosion of flocs is followed by the simultaneous erosion of flocs and individual sand grains. These grains are transported over the sediment bed towards the outer bend where they accumulate due to the radial flow above the bed (Figure 90(a)). The accumulating sand formed a triangular ridge along the entire perimeter of the flume (Figure 90(b)) during tests A and B. For test C only a limited amount of sand particles accumulated along the outer bend. The size of this volume (width – height ratio of 3:1, maximum width ~8 cm) progressively increases during the subsequent velocity steps. As a result, an increasing part of the originally exposed surface area of the sediment bed becomes sheltered from the flow (Figure 90(a)).

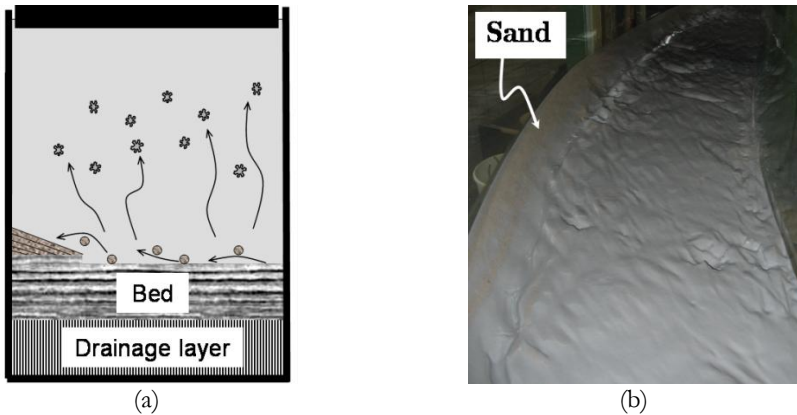


Figure 90. Schematic cross-section (a) and photograph (b) of the flume showing the triangular shaped volume of eroded sand along the outer bend (at left in both figures). Sand is transported along the bed and flocs become suspended after erosion (a). The diagonal lines (at left in (a)) indicate the increasing size of the volume of sand during subsequent erosion steps. In (b) small scour holes are shown, which mainly exist along the inner bend and toe of the accumulated volume of sand.

For increasing τ_b ripples developed in the sand ridge, which indicates the occurrence of bed load transport (Figure 91). The typical height and length scale of these ripples is 0.5 and 7.5 cm, respectively. Similar ripples developed during test A and B; for test C no ripples occurred. By further increasing τ_b , the surface of the sand ridge becomes flat as the ripples suddenly disappear and sand is transported within a thin (cm's) layer just above the sediment bed. Simultaneously with the disappearance of the ripples, the colour of the suspension, which was initially grey-white (due to suspended kaolinite and silt particles), becomes darker. This darker colour indicates the presence of sand in the suspension. Sand particles are also observed in the tubes connected to the Oslims. These observations indicate a sheet flow regime for sand transport (e.g. Dohmen-Janssen, 2001).

Water gradually stopped moving when stopping the rotating bottom and lid of the flume at the end of the tests. Due to the ongoing secondary circulation, the suspended

sand grains accumulated again along the outer bend of the flume. This sand was collected after the tests; the total mass of eroded sand was 13.5 and 21.3 kg for soil Sample A and B, respectively. The amount of accumulated sand along the outer bend of the flume during test C was too small to collect accurately.

After pumping the water out of the flume small scour holes are observed on the surface of soil Samples A and B (Figure 90(b)). These were predominantly found along the inner bend of the flume and at the toe of the triangular shaped ridge of sand. The average diameter of these holes was about 1 – 3 cm (test A) and 1 – 4 cm (test B) and their average depth was about 0.5 – 1 cm, both for test A and B. Observations indicate that these holes developed within the last velocity steps.

The properties of the sediment bed after erosion were markedly different for tests A and B, on the one hand, and test C, on the other. The bed of soil Samples A and B exhibits a distinct volume of sand along the outer bend of the flume, as well as small scour holes. The sediment bed after test C was not significantly different compared to the original bed, as only a layer of sediment was eroded from the top of the micro-bathymetry. The height of this wrinkled print was reduced with about 50%. Finally, the coarse sand is still situated in the small boreholes after the tests, which indicates no significant scouring during the tests. Therefore, it is concluded that these holes did not negatively influence the erosion process.



Figure 91. Side view of the outer bend of the flume showing propagating sand ripples on top of the sediment bed as observed for soil Samples A and B. Flow direction is to the left. Typical height and length of the ripples are 0.5 and 7.5 cm, respectively.

6.2.4 Concentration profiles and mass of eroded sand

The erosion behaviour of fines is derived from c_i as a function of t measured with the Oslims. First, c is checked to see if it exhibits a vertical distribution. Comparison of c_1 and c_2 , c_1 and c_3 , c_2 and c_3 and c_4 and c_5 (Figure 80) shows differences of less than 3 – 4% between measuring stations. These small differences indicate that the output of the Oslims are statistically comparable, and that no vertical gradient exists for c . This is a result of the complex 3D flow pattern with accompanying vertical velocities, which generate a well-mixed water body. Therefore, c is presumed uniformly distributed over the cross-section. The depth averaged c during the tests is obtained from averaging c_4 and c_5 ($0 < c < 2 \text{ g}\cdot\text{l}^{-1}$), and c_1 , c_2 and c_3 ($2 < c < 30 \text{ g}\cdot\text{l}^{-1}$).

Figure 92 shows c with c_r (from the withdrawn reference samples). These concentrations are determined for each velocity step; for soil Sample A calibration data is available for every second step only. Oslim and calibration c exhibit similar trends.

However, some differences also exist. For low c ($< 0.1 \text{ g}\cdot\text{l}^{-1}$) the mass of fines in the volume of extracted water was too small to accurately determine c_r . For soil

Sample B (Figure 92(b)) and C (c) the Oslims slightly overestimate c compared to c_r ($0.1 < c < 2 \text{ g}\cdot\text{l}^{-1}$). For larger c , c_i and c_r are comparable. The measuring procedures were carefully evaluated to account for this difference in concentrations, but a sound explanation was not found. However, some possible causes are discussed below. First, the Oslim calibrations before and after the tests are rather sensitive to small errors of the determination of c , especially for small c .

Second, the Oslims underestimate c relative to c_r from step 8 – 9 onward for test A (Figure 92(a)). Additionally, c exhibits a more oscillatory character ($c > 1 \text{ g}\cdot\text{l}^{-1}$) compared to lower c . This also occurs for tests B and C, although less obvious and not visible in Figure 92(b) and (c) as the scale of the vertical axis in both figures is larger than in (a). Both the underestimation and oscillations exist simultaneously with the occurrence of a sheet flow regime for the transport of sand (Table 16). Suspended sand particles (observed during sheet flow) may therefore have influenced the c measured by the Oslims, which are calibrated for clay-silt mixtures only.

Finally, the effect of suspended sand grains on the calibration c may be significant due to their relatively large individual mass. On the other hand, suspended sand grains are expected to affect the Oslim output only minimally, as the attenuation and scattering of light by sand grains is small compared to (the numerous) fines. Therefore, it is expected that the effect of sand grains is most significant for tests with relatively low c ($< 2 \text{ g}\cdot\text{l}^{-1}$) and a relatively large amount of suspended sand grains (as for test A).

c for each velocity step is fitted with an exponential function, similarly to that in Chapter 5 (Eq. (5.2)). The fitted profiles indicate a time-dependent behaviour at low τ_b . During these first steps c initially sharply increases, but becomes constant after increasing τ_b . Above a certain threshold τ_b , unlimited erosion (time-independent) exists, for which \bar{c} exhibits an almost linear increase with t . Figure 92 indicates that the transition between time-dependent and time-independent erosion occurs for steps 8 - 9, 7 - 8 and 10 - 11 for soil Samples A, B and C, respectively. For τ_b smaller than this threshold, $A < 0.2 \text{ g}\cdot\text{l}^{-1}$ and $B^{-1} < 200 \text{ s}$ (Eq. (5.2)) for all three soil samples. For τ_b larger than this threshold, all soil samples exhibit significantly larger values for A ($> 1 \text{ g}\cdot\text{l}^{-1}$) and B^{-1} ($> 1,000 \text{ s}$). Maximum A is about 10 - 30 of $\text{g}\cdot\text{l}^{-1}$; maximum B^{-1} is about 10,000 s.

The erosion depth (0.37, 0.72 and 0.12 cm for soil Samples A, B and C, respectively), from which the suspended fines are eroded and the mass of eroded sand as a function of t , follow from the mass balance. This implies that, by presuming the simultaneous erosion of sand and mud during time-independent erosion, the total (sand + mud) erosion rate and total erosion parameter for each velocity step can be derived from $c(t)$ multiplied by the volume of water, on the one hand, and the initial sediment composition, on the other.

The mass of eroded sand following from this mass balance analysis is 17.7, 28.7 and 1.1 kg for soil Samples A, B and C, respectively. These masses are $\sim 25\%$ larger than the mass of accumulated sand. Differences may be attributed to the thin layer of sand on top of the sediment bed, which was observed after emptying the flume. However, the majority of the sand accumulated along the outer bend of the flume.

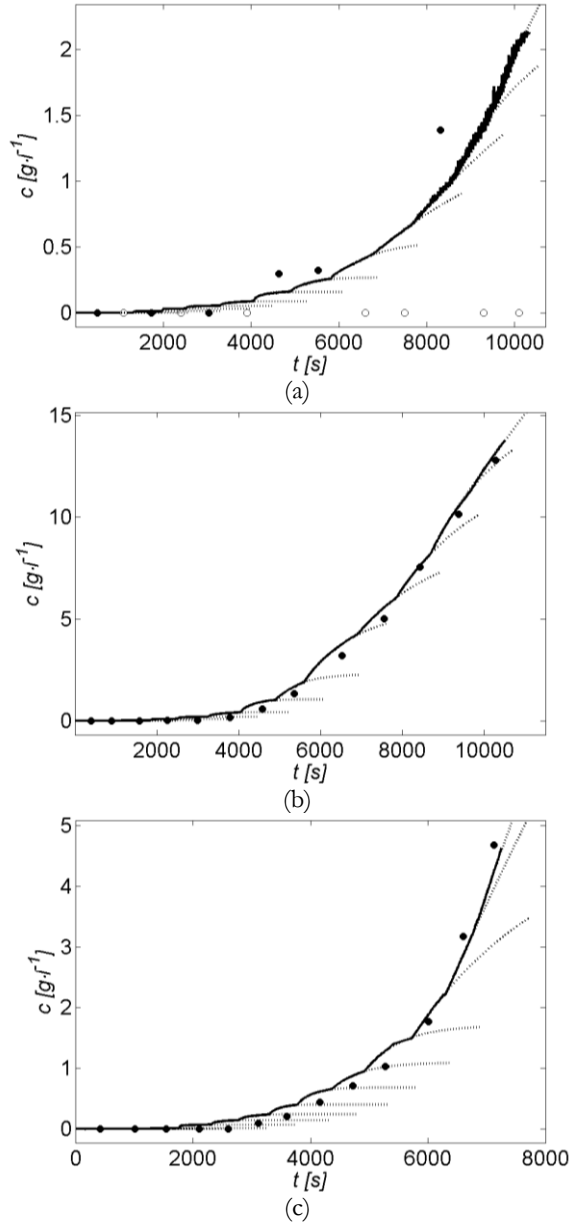


Figure 92. Depth-averaged concentration measured with the Oslims (continuous lines) and determined from the calibration samples (●) as a function of time for soil Samples A (a), B (b) and C (c). Note the different vertical scales of the three figures. Missing calibration concentrations are indicated (○) to display all velocity steps (a). The dotted lines are fits through the concentration measurements for each velocity step.

6.3 Discussion

6.3.1 Hydrodynamics

The applicability of the LES model to compute u and w during the tests is verified by comparing the LES and EMF output for identical horizontal and vertical positions. It is noted that this comparison is hampered by the varying vertical distance between the bed level and the EMF sensor. Although the vertical position of the EMF is fixed, the bed level exhibits vertical variations of ± 0.5 cm due to erosion and (propagating) micro-bathymetry. As a result, the EMF measuring position may vary relative to the two circulation cells. The complex 3D flow pattern indicates that flow properties may significantly vary over relatively small vertical and/or horizontal distances.

LES and EMF data exhibit similar general trends concerning u and w . Vertical velocities determined by both LES and EMF are comparably small. However, at the locations of comparison, the LES model overestimates the measured values of u by 10 - 13% for all three tests (averaged for all velocity steps). These differences are likely caused by the hydraulically smooth conditions assumed in the LES model. Applying hydraulically rough conditions would not only increase bed shear stresses through the roughness coefficient, but may also modify the flow pattern to an extent that explains the overprediction. As we were not able to re-run the LES model for hydraulic rough conditions, we apply τ_b following from the LES simulations to analyse the erosion data.

6.3.2 Erosion and transport modes and features

Figure 92 indicates transitions between time-dependent and time-independent erosion for steps 8 - 9, 7 - 8 and 10 - 11 for soil Samples A, B and C, respectively. Visual observations (Table 16) show that for the first velocity steps only flocs are eroded, followed by the erosion of aggregates at larger velocities. Therefore, time-dependent erosion (of flocs) is referred to as floc erosion, and time-independent erosion (of aggregates) as surface erosion. Chapter 7 further discusses whether these erosion behaviours agree with the proposed classification scheme (Chapter 3, Figure 36).

The transport of eroded sand forms an important feature in the annular flume tests. As sand is not collected after erosion (e.g. in a sand trap), it is transported along the sediment bed during which the erosion of material from the original sediment bed may be affected. Similar conditions are expected for natural circumstances. This bed load transport of sand is clearly observed, especially for mixtures with a dominant sand-silt skeleton (Samples A and B), with sand accumulating along the outer wall and the occurrence of bed forms and sheet flow transport. Next, characteristics of the latter two features are compared with literature.

For a specific range of τ_b , sand is transported by means of propagating mini-ripples on top of the accumulated sand. These ripples exhibit typical length scales (~ 7.5 cm) much smaller than the water depth (~ 29 cm). Van Rijn (1993) argues that the occurrence of bed forms depends on the particle diameter parameter (D_*) and the

bed shear stress parameter (T). Mini-ripples are expected for $1 < D_* [-] < 10$ and $0 < T [-] < 3$. This more or less agrees with the observed ripples in the annular flume, as $D_* \approx 4.5$ and $T \approx 5.0$. The occurrence of ripples also agrees with the observations from tests on sand-silt mixtures in Chapter 5.

Sheet flow transport of sand exists for $\theta > 0.8$ (e.g. Dohmen-Janssen, 2001), where $\theta [-]$ is the Shields parameter. A sheet flow regime exists from velocity step 8 onward for tests A and B (Table 16). Figure 73 shows that θ is 0.4 for a bed shear stress of 1 Pa and d_{50} of the applied sand fraction of 170 μm . This indicates that the bed shear stress along the outer bend may be larger than suggested by the LES simulations, which is attributed to the larger bed roughness generated by the presence of the ripples. Furthermore, the existence of a sheet flow layer may affect the erosion of the original sediment bed. However, these effects are not further analysed in the current study.

Two indications exist for the occurrence of suspended load transport of sand in the body of water above the sheet flow layer. First, the colour of the suspension becomes suddenly darker upon the start of sheet flow transport. Second, sand is found in the hoses connected to the Oslims, which indicates suspended sand particles as the vertical locations of the (Oslim) sampling points are well above the sheet flow layer (Figure 80). The presence of these sand grains generates an oscillating Oslim signal (Figure 92(a)), as well as an offset between c and c_r .

Finally, the occurrence of scour holes may suggest mass erosion. However, based on two observations these scour holes are considered artefacts of the experimental set-up. The first is that maximum τ_b is relatively small (~ 1.6 Pa) to generate sufficiently large stagnation stress to generate mass erosion ($> 2 - 5c_u$, Section 3.2.3), as c_u is in the order of kPa's (Section 4.2). For soil Sample C no scour holes were observed, which is probably due to the more cohesive character and lower permeability of this sample. The second observation is that the location of the scouring occurs at the location of the downward directed flow along the inner wall of the flume, which locally enhances erosion (Figure 84), and with maximum τ_b (Figure 86) at the toe of the accumulated sand.

6.3.3 Erosion rates

The erosion rate for mud ($E_{mud} [\text{kg}\cdot\text{m}^{-2}\cdot\text{s}^{-1}]$) is defined as the product of A [$\text{g}\cdot\text{l}^{-1}$], B [s^{-1}] and the volume of water in the flume, and divided by the actual surface area of the test section (Eq. (5.4)). The volume of accumulated sand generates a progressively decreasing surface area of the exposed sediment bed (Figure 90). The surface area decreased from 3.5 m^2 to 2.65, 2.45 and 3.30 m^2 during test A, B and C, respectively. Erosion rates were corrected for this decrease. Figure 93 shows E_{mud} and E_{sand} as a function of τ_b . Erosion rates for sand ($E_{sand} [\text{kg}\cdot\text{m}^{-2}\cdot\text{s}^{-1}]$) are determined similarly to E_{mud} , with A and B following from the fitted profiles of the mass of eroded sand as a function of t . These profiles follow from a mass balance analysis in combination with the presumed simultaneous erosion of sand and mud during time-independent erosion.

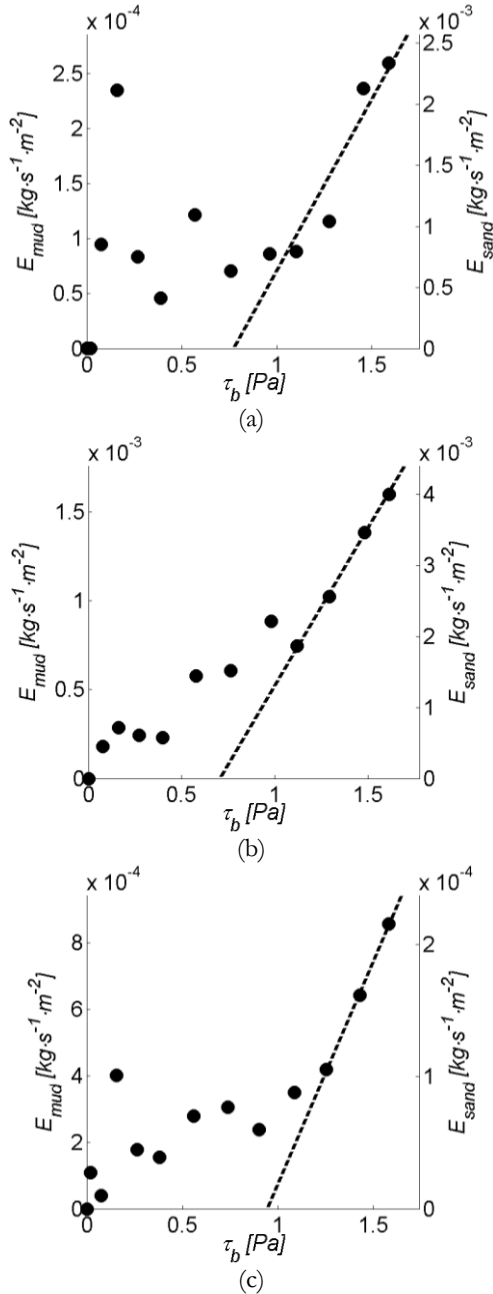


Figure 93. Erosion rates of mud E_{mud} [$\text{kg}\cdot\text{m}^{-2}\cdot\text{s}^{-1}$] (left vertical axes) and sand E_{sand} [$\text{kg}\cdot\text{m}^{-2}\cdot\text{s}^{-1}$] (right vertical axes) as a function of the bed shear stress for Samples A (a), B (b) and C (c). The dashed line fits E for surface erosion. Note the different vertical scales.

E_{mud} and E_{sand} are fitted with a linear function for τ_b larger than the time-dependent erosion threshold. τ_b (i.e. step 9, 10 and 11 for test A, B and C, respectively) was derived from the mutual sharp increase of A and B^I . Time-dependent erosion occurs at lower τ_b , for which relatively low c is observed (Figure 92). Figure 93 shows a few rather high anomalous erosion rates at the onset of the erosion experiments (low τ_b). These peaks are attributed to the resuspension of loose material produced upon removal of the plastic foil, and should therefore be considered artefacts. A similar behaviour was observed in Chapter 5.

6.3.4 Surface erosion threshold

Two methods are applied to determine the surface erosion threshold $\tau_{e,s}$. The first concerns visual observations from the tests (Table 16) and observed transitions for c as a function of t (Figure 92). The second applies E as a function of τ_b (Figure 93). Visual observations of $\tau_{e,s}$ concern the erosion onset of aggregates and the accumulation of sand. Minimum $\tau_{e,s}$ (for step 5, 7 and 6, i.e. 0.3, 0.6 and 0.4 Pa, for soil Sample A, B and C, respectively) indicate the onset of erosion of aggregates following from visual observations (see ‘ Δ ’ in Figure 94). Maximum $\tau_{e,s}$ (for step 8 - 9, 7 - 8 and 10 - 11 i.e. 0.9, 0.7 and 1.2 Pa for soil Sample A, B and C, respectively) resemble the transition between time-dependent and time-independent erosion.

The variation of visually observed $\tau_{e,s}$ is attributed to the less accurate methodology. Due to the significant turbidity of the water in the flume, only the sediment behaviour along the walls could be visually inspected. Furthermore, it is difficult to visually determine the moment of uniform failure of the bed. Also the onset of sand erosion is difficult to determine due to the time lag between erosion and accumulation along the outer wall.

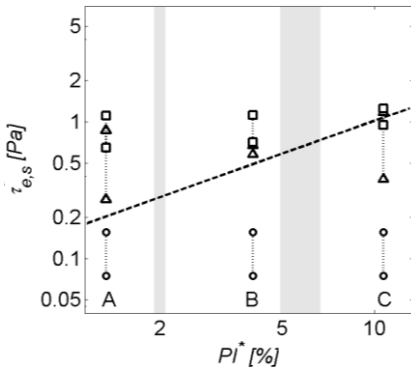


Figure 94. Surface erosion threshold $\tau_{e,s}$ as a function of the plasticity index PI^* following visual observations (‘ Δ ’, see Table 16 and Figure 92) and derived from the τ_b - E relation (‘ \square ’, Figure 93). Also the erosion threshold τ_e for time-dependent erosion is shown (‘ \circ ’). The grey areas indicate $PI^* \approx 2$ (offset for influences cohesive fraction) and $PI^* = 5 - 7$ (transition between a granular ($PI^* < 5$) and cohesive ($PI^* > 5 - 7$) structure. The dashed line reflects Eq. (5.5). The letters refer to the tests (Table 12).

Minimum values for $\tau_{e,s}$ indicated with ‘ \square ’ in Figure 94 follow from the abscissas of the linear fitted E as a function of τ_b (Figure 93). $\tau_{e,s}$ equals 0.9 Pa for Sample A (non-cohesive bed), 0.7 Pa for Sample B (transitional bed) and 0.9 Pa for Sample C (cohesive bed). However, the slope of the linear fit (i.e. M_s) is relatively small, which causes the abscissas to shift to relatively low τ_b compared to the accompanying τ_b of

the velocity step from which E is linear fitted. The latter τ_b are shown by the maximum $\tau_{e,s}$ indicated with ‘□’ in Figure 94 (step 10, 10 and 11, i.e. 1.1, 1.1 and 1.3 Pa for soil Sample A, B and C, respectively).

Figure 94 shows that the ranges for $\tau_{e,s}$ following from visual observations (Δ) and from E (\square) exhibit similar trends and partly overlap. $\tau_{e,s}$ derived from E is considered more accurate, as (especially the lower limit of the) visual observations are rather subjective. No obvious trend can be identified for $\tau_{e,s}$ as a function of PI^* , as $\tau_{e,s}$ is rather constant. However, $\tau_{e,s}$ is of the same order of magnitude as found from the relation between $\tau_{e,s}$ and PI^* , derived from the straight flume data (Eq. (5.5)). Only for the predominantly sandy soil Sample A $\tau_{e,s}$ is significantly larger compared to Eq. (5.5), which agrees with larger $\tau_{e,s}$ for granular soils as shown in Chapter 5 (Figure 67).

Finally, floc erosion is observed for all tests from step 3–4 onward, which explains the slight increase of c as a function of t (Figure 92). Accompanying τ_b are about 0.1 – 0.2 Pa (‘○’ in Figure 94), which agrees with the expected drained strength (c_d) of low cohesive material (kaolinite). Furthermore, the offset for floc erosion is more or less constant, which is expected as c_d is constant for constant clay mineralogy (Chapter 2).

6.3.5 Surface erosion parameter

Figure 95 shows the erosion parameter M_s [$\text{kg}\cdot\text{m}^{-2}\cdot\text{s}^{-1}\cdot\text{Pa}^{-1}$], which is the slope of the dashed lines in Figure 93, as a function of W_{rel} . M_s equals $3.1\cdot 10^{-3}$, $5.9\cdot 10^{-3}$ and $1.7\cdot 10^{-3}$ $\text{kg}\cdot\text{m}^{-2}\cdot\text{s}^{-1}\cdot\text{Pa}^{-1}$ for soil Samples A, B and C, respectively. These soil samples (Table 15) exhibit identical clay mineralogy and solid contents (ξ_i) of sand, silt and clay as soil Samples 1, 3 and 5 (Table 12) in the straight flume. Therefore, results of both studies are qualitatively compared; Chapter 7 presents a more quantitative discussion.

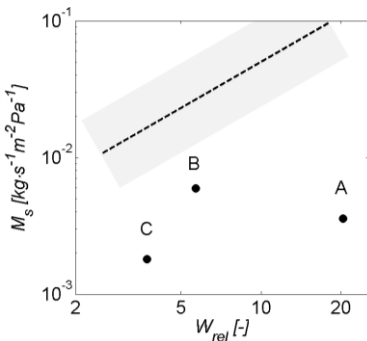


Figure 95. Surface erosion parameter M_s [$\text{kg}\cdot\text{m}^{-2}\cdot\text{s}^{-1}\cdot\text{Pa}^{-1}$] as a function of the relative water content W_{rel} , with the clay content increasing towards the left. The letters refer to the erosion tests (Table 15). The dashed line reflects Eq. (5.6) following from the straight flume tests (see Figure 75). The grey shaded area reflects the scatter of Eq. (5.6).

Comparing M_s obtained in the straight and annular flume indicates two differences. First, M_s for the soil Samples B and C is generally lower (factor 2 - 5) compared to straight flume results. The second difference concerns the two orders of magnitude smaller M_s for the sandy soil sample tested in the annular flume. This is too much to attribute to measurement errors or differences in bed roughness only.

Furthermore, bed properties (ζ_i and W) and forcing conditions are comparable, and cannot explain the deviating M_s for the sandy sediment in the annular flume.

A possible explanation for the differences in soil A concerns the different behaviour of eroded sand in both experimental set-ups. For the straight flume, eroded sand is transported only along the short test section, and subsequently collected in a sand trap. For the annular flume tests, however, the eroded sand remains part of the sediment bed. Therefore, the eroded sand may decrease the erodibility of the original sediment bed. This decrease may result from two phenomena.

The first concerns the bed load transport of sand. As a result, underlying sediments may become (partly) unavailable for erosion. Second, the presence of a sheet flow layer may reduce τ_b and, consequently, reduce erosion as well (e.g. Dohmen-Janssen, 2001). Although both effects cannot be studied in detail more, as no appropriate data is available, it is presumed that the significant difference between M_s of soil Samples A (annular flume) and 1 (straight flume) is caused by the bed load transport of eroded sand in the annular flume. Finally, the straight flume enables the study of ‘true’ erosion, as eroded sand is trapped and, consequently, does not reduce erosion. However, this reduction by eroded sand represents what may occur for natural conditions. Therefore, the annular flume enables the study of ‘natural’ erosion.

6.4 Conclusions

The LES model is a convenient tool to determine bed shear stress. It provides a good alternative for measuring the bed shear stress in an annular flume, which is difficult due to the complex 3D flow pattern. However, the computed bed shear stress is less accurate, as the model was calibrated for a glass bottom.

The general erosion behaviours of the three soil samples partly agree with the expected behaviour following the theory (Chapter 3), and with the results of the straight flume tests (Chapter 5). This especially concerns the (transition between) time-dependent floc erosion and time-independent surface erosion following from the concentration profiles. Also the erosion rates and thresholds agree with the results described in Chapter 5. However, the erosion parameters following from the annular flume tests are lower than for the straight flume. This is attributed to a reduced erodibility by eroded sand, which may indicate that in the annular flume tests not only the removal of particles from the bed is studied, but rather the net effect of erosion (of sand and mud) including the effect of bed load transport. The relatively small test section and the collection of sand in the sand trap indicate that with the straight flume tests only the removal of particles was simulated, without a reduced erodibility due to sand transport. This may explain the larger erosion parameters.

It is recommended to study the effect of eroded sand on the erosion of beds more carefully, as a similar behaviour is expected in nature. It is also recommended to re-calibrate the LES model for hydraulically transitional and/or rough conditions to enable its application for future erosion studies.

Chapter 7

Validation of new erosion approach

This thesis proposes a new approach for the erosion of sand-mud mixtures based on a geotechnical model for soil behaviour (Chapter 3). This approach concerns a classification for erosion modes (Figure 36), as well as a new surface erosion formulation. The current chapter discusses the validation of the new erosion approach. First, the erosion behaviours observed for the straight (Chapter 5) and annular flume tests (Chapter 6) are compared with the proposed erosion classification (Section 7.1). Next, the proposed erosion formulation is elaborated (Section 7.2) using experimental data following geotechnical (Chapter 4) and erosion tests (Chapters 5 and 6). In Section 7.3, the practical applicability of the new formulation for natural intertidal sediments is discussed.

7.1 Validation of erosion classification

7.1.1 Introduction

The new erosion classification (Figure 96) distinguishes between different erosion modes based on the type of eroded material and the role of the stochastic character of both the turbulent flow and sediment strength. The following sections aim to validate the classification by discussing erosion data of straight flume tests 1, 3 and 5 (Chapter 5) and annular flume tests ‘A’, ‘B’ and ‘C’ (Chapter 6). As during these test floc and surface erosion were observed, focus is on these two modes only.

The transition between the two erosion modes is discussed based on the behaviour of the suspended sediment concentration (c [$\text{g}\cdot\text{l}^{-1}$]) measured in the water column as a function of time (t [s]). Both straight and annular flume test results indicate an exponential increase of c as a function of t at relatively low τ_b , and a linear increase of c as a function of t at relatively large τ_b . The mass balance per unit area of eroded sediments brought into suspension in the water column is given by:

$$h \frac{d\bar{c}}{dt} = E - D = E - c_b w_{s,b} \quad (7.1)$$

where h [m] is the water depth, \bar{c} [$\text{g}\cdot\text{l}^{-1}$] the depth-averaged suspended sediment concentration, E [$\text{kg}\cdot\text{m}^{-2}\cdot\text{s}^{-1}$] the erosion rate, D [$\text{kg}\cdot\text{m}^{-2}\cdot\text{s}^{-1}$] the deposition rate and c_b [$\text{g}\cdot\text{l}^{-1}$] and $w_{s,b}$ [$\text{m}\cdot\text{s}^{-1}$] respectively the concentration and settling velocity of suspended sediment just above the sediment bed.

Eq. (7.1) indicates that the gradient of \bar{c} as a function of t relates to the rates of erosion and deposition. An exponential increase of the concentration c with t is referred to as time-varying or time-dependent erosion, which generally occurs at relatively low bed shear stress τ_b . A linear increase of c with t is referred to as time-independent erosion and generally occurs at relatively large τ_b . During erosion experiments E is generally larger than zero. Hence, time-dependent erosion is observed when E and D are not equal, or when E reduces to zero with t and D is negligible. Time-independent erosion behaviour is observed when E and D balance, or when E is constant and D is negligible.

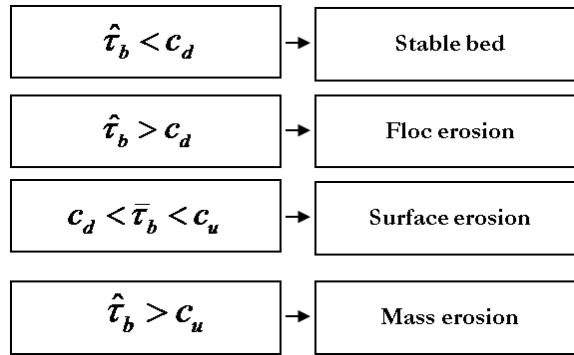


Figure 96. Classification scheme (see also Figure 36) for erosion modes based on erosion thresholds, which are reflected by the drained and undrained strength of the bed in relation to the mean and turbulent component of the deviatoric stress. It is noted that both floc erosion and surface erosion (for both $\hat{\tau}_b$ and $\bar{\tau}_b > c_d$), and surface erosion and mass erosion (for both $\hat{\tau}_b$ and $\bar{\tau}_b > c_u$) can occur simultaneously.

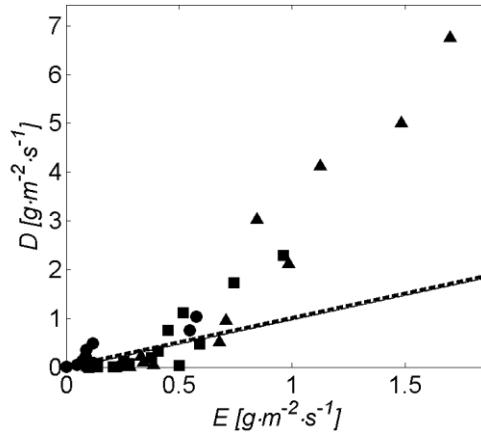
The validation of the classification consists of two steps. The first step is to verify the importance of the stochastic characters of the bed shear stress and erosion threshold for both the occurrence of time-dependent erosion and the transition towards time-independent erosion (Section 7.1.5). To eliminate other possible causes for time-dependency, first the effect of deposition (Section 7.1.2), vertical variations of sediment properties within the sediment bed (Section 7.1.3) and bed irregularities (Section 7.1.4) are discussed. The second step is to verify whether the type of eroded material and the way this material is removed from the bed agrees with the definition of floc and surface erosion (Section 7.1.6).

7.1.2 Effect of deposition

Balancing erosion and deposition rates may explain time-independent erosion. Besides, the experimentally determined erosion rates may be underestimated if significant deposition of suspended sediments did occur during the erosion tests. Therefore, it is investigated (using Eq. (7.1)) whether simulated D as a function of physically realistic values of w_s can balance experimentally determined E .

As the water column in both experimental set-ups is vertically well-mixed, it is assumed that the depth-averaged concentration (\bar{c}) equals the concentration just above the sediment bed (c_b) at the end of a τ_b -step. Winterwerp and Van Kesteren (2004) argue that $w_{s,b}$ as a function of concentration and flow characteristics may typically vary between 0.01 – 5 mm·s⁻¹. For $c \approx 3$ g·l⁻¹ mud particles flocculate, which implies relatively large $w_{s,b}$. As maximum c during both the straight and annular flume tests was only 1 – 1.5 g·l⁻¹, flocculation effects are not expected to play an important role. Therefore, $w_{s,b}$ is assumed constant throughout all erosion tests.

Computed D only balance with measured E for $w_{s,b} \approx 10 - 20$ mm·s⁻¹ for the straight flume test results. As discussed above, these large $w_{s,b}$ are physically unrealistic for the typical conditions during these flume tests. D only equals E for a physically realistic value of the settling velocity ($w_{s,b} \approx 0.5$ mm·s⁻¹, Figure 97) for the first velocity steps ($E < 0.5$ g·m⁻²·s⁻¹) for the annular flume test results. As D and E balance, deposition may have been important during the initial phase of these tests. However, Figure 97 shows that for $w_{s,b} \approx 0.5$ mm·s⁻¹ D becomes larger than E for increasing τ_b . D exceeding E yields decreasing c as a function of t , which is in contrast with observations from these experiments.



In conclusion, it is not possible to obtain balancing deposition and erosion rates for physically realistic values of $w_{s,b}$. This implies that deposition does not explain the observed time-dependency of c for $\tau_b > 0$. A similar conclusion was drawn by Parchure and Mehta (1985) for similar erosion tests. Furthermore, it can be assumed that $D \ll E$ at relatively large τ_b , which implies that accurate E can be derived from measured suspended sediment concentrations as a function of time.

7.1.3 Effect of decreasing erodibility with erosion depth

Next, we consider whether E can reduce towards zero at relatively low τ_b due to changing properties of the sediment bed with increasing erosion depth. Parchure and Mehta (1985) argue that time-dependent (Type I) erosion is depth-limited due to an increasing erosion threshold (\sim bed strength) with increasing depth. This increasing threshold results from vertical gradients in either the sediment composition or packing density (e.g. due to consolidation). This phenomenon is often observed for stratified beds (see e.g. Figure 16), for which erosion ceases when the strength of the bed exceeds the imposed bed shear stress.

Figure 98 shows the erosion depth as a function of simulated vertical τ_e -differences for the annular flume tests. The erosion depth is assumed uniform over the whole annular flume, and follows from combining the bed composition with the mass of eroded fines. This mass is the product of the volume of water in the flume and the measured concentration of suspended sediments at the end of each velocity step. The erosion threshold for each step is computed as follows.

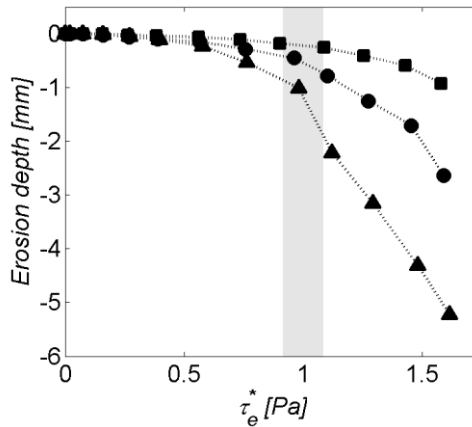


Figure 98. Behaviour of computed τ_e in relation with erosion depth for consecutive velocity steps as applied for annular flume tests ‘A’ (●), ‘B’ (▲) and ‘C’ (■). The grey vertical line indicates the range in which the experimentally derived surface erosion thresholds for these samples occur (Figure 94). The line reflects the transition from time-dependent (left) to time-independent erosion (right).

The concentration of suspended sediments at relatively low τ_b tends to a constant value. This implies that, following Parchure and Mehta (1985), the erosion threshold at the erosion depth and/or at the end of each step approaches τ_b . Therefore, it is assumed that τ_e at the end of each velocity step equals the imposed τ_b .

Figure 98 shows that, following Parchure and Mehta (1985), the upper 0.5 - 1 mm of the sediment bed should exhibit a rather strong τ_e -gradient (~ 1 Pa) in order to obtain time-dependent erosion. Similar patterns are required for the straight flume results, which exhibit comparable c -profiles, erosion depths and sediment characteristics. However, the computed strength-gradients are physically not realistic, as the sediment composition (clay mineralogy) is homogenous and no chemical and/or biological influences occur.

Additionally, the density within the upper 1 mm of the sediment bed is not expected to increase in such a way that strength-gradients as shown in Figure 98 can be generated. Therefore, we conclude that the time-evolution of c during the successive erosion steps for the discussed experimental results cannot be explained from a vertical gradient in bed properties.

7.1.4 Effect of bed irregularities

The next possible cause for time-dependent erosion is the effect of bed irregularities. It is hypothesised that E may locally reduce to zero either at or in-between these irregularities. Bed irregularities as observed for the erosion tests concern (1) morphological features like ripples and cracks, or (2) large particles surrounded by relatively small particles. Three possible scenarios for the possible effect of bed irregularities are discussed.

First, it is hypothesised that these features initially exhibit high erodibilities due to the locally increased bed roughness. As a result, the features will quickly smoothen and the erodibility will consequently decrease. During both the straight and annular flume tests, a rippled sediment bed was observed. An initial relatively strong erosion at the crest of these ripples may have ceased due to smoothening. However, visual observations indicate that these ripples formed well after the onset of surface erosion. This implies that ripples may only have influenced erodibility at relatively large τ_b . But as time-dependency was observed at relatively low τ_b , ripples cannot have generated time-dependent erosion.

The second morphological feature which possibly may have caused time-dependent erosion concerns the cracks in the cohesive soil samples tested in the straight flume (Figure 61). These cracks formed a similar pattern as the wrinkled print of the plastic foil on the sediment bed in the annular flume (Figure 89). Contrary to the ripples, both the cracks and the wrinkled print were present during the first velocity steps.

However, observations indicate that erosion from the cracks was rather random and mainly occurred at relatively large τ_b . This implies that the cracks cannot have structurally generated time-dependent behaviour. Besides, the cracks only occurred for cohesive soils, whereas time-dependent erosion was also observed for more granular sediment beds. The wrinkled pattern, on the other hand, did level off during the first

rotational steps of tests ‘A’ and ‘B’. This may indicate a possible relation with time-dependency. However, for soil Sample ‘C’ these features exhibited almost no erosion, although time-dependent erosion did occur. In conclusion, both the cracks and the wrinkled print cannot have generated time-dependent erosion.

The third possible effect of bed irregularities on the occurrence of time-dependent erosion concerns sheltering of small particles by larger particles (cf. armouring, see e.g. Van Rijn, 1993). It is hypothesised that due to erosion of small particles during the first velocity steps, the remaining larger particles provide shelter and, subsequently, decrease the erodibility of remaining finer particles.

However, Figure 98 shows that the maximum erosion depths observed during time-dependent erosion are about 750, 1000 and 250 μm for annular flume tests ‘A’, ‘B’ and ‘C’, respectively. These depths are of a similar order of magnitude or only slightly larger than the size of individual sand grains ($d_{50} = 170 \mu\text{m}$). It is unlikely that sheltering effects are sufficiently large to generate time-dependent erosion at these limited depths. Further, the average erosion depth during time-dependent erosion (i.e. in the first phase of the test) was even smaller than the indicated maximum depths. In conclusion, the presumed feedback of bed irregularities on (decreasing) erosion rates does not explain time-dependent erosion.

7.1.5 Effect of spatial inhomogeneity of erosion threshold and bed shear stress

A third possibility for time-dependent erosion resulting from a decrease of E with time concerns the spatial inhomogeneity of both the bed shear stress and the erosion threshold. Spatial inhomogeneity results from the stochastic characters of τ_b and τ_e . Also Partheniades (1962, 1965) and Parchure and Mehta (1985) recognize the importance of these stochastic characters for the erosion of (cohesive) sediments. However, these studies only apply these stochastic characters to explain the occurrence of a zero erosion threshold, but not the occurrence of time-dependent erosion.

The stochastic characters of τ_b and τ_e imply that these are not single values, but that they cover a range of values (Figure 99). For τ_b , this range results from the presence of coherent turbulent structures in the boundary layer of hydraulically smooth flows (Section 3.2.2). Figure 99 shows that these coherent turbulent structures generate a positively skewed (see e.g. Winterwerp and van Kesteren, 2004) probability density function (pdf).

The stochastic character of τ_e relates to the spatial variation of bed characteristics. Although not much information is available on the standard deviation of $\text{pdf}(\tau_e)$, it is generally presumed relatively narrow (Figure 99) compared to $\text{pdf}(\tau_b)$, especially for isotropic soil samples (Partheniades, 1962, 1965; Parchure and Mehta, 1985). As homogeneous soil samples were applied during the erosion experiments, $\text{pdf}(\tau_e)$ is assumed to exhibit a narrow character compared to $\text{pdf}(\tau_b)$.

Figure 99 further illustrates that erosion can occur at relatively low τ_b when $\bar{\tau}_b < \bar{\tau}_e$ due to peak bed shear stresses ($\hat{\tau}_b$) locally exceeding the erosion threshold of the weakest sediments. This implies that sediments are not eroded uniformly from the bed, but from horizontally distributed ‘hot-spots’. The erosion rate depends on the

overlapping surface area of the pdf's of τ_b and τ_e . Due to erosion of the weakest particles, the number of erodible particles decreases with time, as pdf(τ_e) becomes narrower.

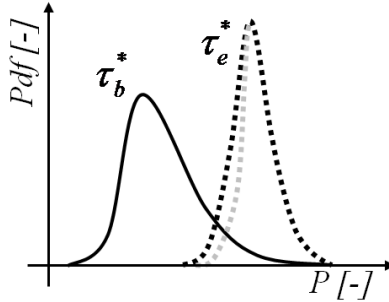


Figure 99. Schematic pdf of τ_b (continuous line) and τ_e (dotted lines) during floc erosion at the start of a velocity step (black-dotted line) and after some time (grey-dotted line). Erosion of sediments exists for $\bar{\tau}_b < \bar{\tau}_e$. Due to erosion of the weakest particles, the standard deviation of pdf(τ_e) becomes smaller during erosion (grey-dotted line), which implies that the bed becomes ‘stronger’.

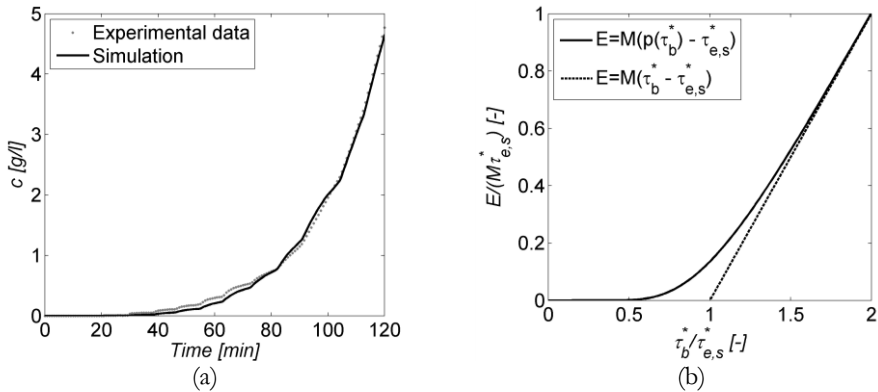


Figure 100. Comparison (a) of computed data including the stochastic character of τ_b and experimental data derived from annular flume test ‘C’ (Chapter 6). By including the stochastic character of τ_b the typical relation of the erosion rate (Figure 32) can be reproduced ((b), continuous line). The diagonal line in (b) reflects an erosion formulation in which τ_b is a single value (replotted after Van Prooijen and Winterwerp, 2010).

Van Prooijen and Winterwerp (2010) present a model to simulate the erosion of cohesive sediments, which incorporates the pdf's of τ_b and τ_e . Figure 100 shows that this approach was successfully applied to compute time-dependent erosion as observed during annular flume test ‘C’ (Chapter 6). Also the occurrence of a zero erosion threshold for $\bar{\tau}_b < \bar{\tau}_e$ was successfully computed. Therefore, it is concluded that the

stochastic character of erosion can explain the occurrences of time-dependent erosion as well as the zero erosion threshold, both at relatively low τ_b .

Additionally, Figure 100(a) nicely shows that the stochastic approach also explains both the occurrence of time-independent erosion and the transition from time-dependent to time-independent erosion. First, c exhibits logarithmic growth as a function of time at low τ_b (cf. Figure 63(b)), whereas c exhibits a linear behaviour towards the end of the test. As a result, E as a function of τ_b first exhibits a zero slope, followed by a constant non-zero slope at relatively large τ_b (Figure 100(b)). This constant slope yields a constant erosion parameter (M), which is characteristic of surface erosion as explained in the proposed classification.

The occurrence of time-independent erosion is further explained by Figure 101. Fully developed time-independent erosion occurs when $\bar{\tau}_b > \bar{\tau}_e$ and $\text{pdf}(\tau_b) > \text{pdf}(\tau_e)$, which implies that the whole $\text{pdf}(\tau_b)$ contributes to erosion (Figure 101(a)). The constant erosion rate at specific τ_b follows from the constant surface area of $\text{pdf}(\tau_b)$.

The transition from time-dependent to time-independent erosion is characterised by the sudden increase of the e -folding time scale (of c as a function of t), which is initially only seconds - minutes. Figure 101(b) shows that there is still some overlap between $\text{pdf}(\tau_b)$ and $\text{pdf}(\tau_e)$ in this transitional phase, as $\min(\hat{\tau}_b) < \max(\hat{\tau}_e)$. This implies that although $\bar{\tau}_b > \bar{\tau}_e$, not all turbulent components of τ_b contribute to erosion. As a result, erosion will cease after some time when all erodible sediments are eventually removed. However, this time-scale largely exceeds the duration of the executed tests.

Finally, it is noted that the importance of the stochastic characters of both τ_b and τ_e for erosion behaviour implies that care should be taken when comparing results of different experimental studies. The character of $\text{pdf}(\tau_b)$ strongly depends on the characteristics of the experimental apparatus, whereas $\text{pdf}(\tau_e)$ relates to differences in packing density and sediment and pore water composition. As a result, varying erosion rates for constant $\bar{\tau}_b$ and $\bar{\tau}_e$ may occur for different experimental studies.

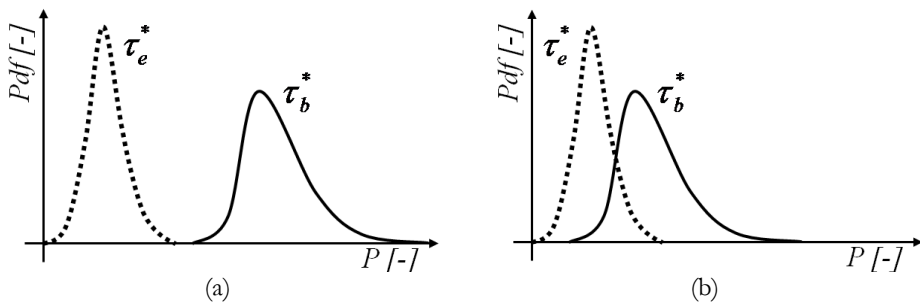


Figure 101. Schematic pdfs of τ_b (continuous line) and τ_e (dotted line) during fully developed time-independent erosion (a) for $\bar{\tau}_b > \bar{\tau}_e$ and $\text{pdf}(\tau_b) > \text{pdf}(\tau_e)$. In case both pdfs partly overlap but $\bar{\tau}_b > \bar{\tau}_e$ (b), a transitional phase occurs between time-dependent and time-independent erosion.

7.1.6 Type of eroded material

The first step of the validation of the new classification concerned the verification of the importance of the stochastic characters of the bed shear stress and erosion threshold for time-dependent and time-independent erosion. The second step verifies whether both time-dependent and time-independent erosion agree with floc and surface erosion, respectively.

Following the proposed classification, individual mud flocs are randomly eroded for $\tau_b > 0$. This is referred to as floc erosion. In contrast, sand and mud are eroded simultaneously and uniformly at relatively large τ_b during surface erosion. Furthermore, surface erosion is a drained process, with an erosion rate as a function of soil composition and packing density. In the following, the type of bed material as eroded during time-(in)dependent erosion as well as the accompanying erosion rates are discussed, for both the straight and annular flume tests. This allows verification of time-dependent and time-independent erosion agree with floc and surface erosion, respectively.

Visual observations and zero sand trap readings from erosion tests indicate that during time-dependent erosion, only flocs were randomly eroded. However, the properties of particles eroded during time-dependent erosion were not analysed; thus, the occurrence of floc erosion is not directly verified. Visual observations further indicate that during time-independent erosion, sand and mud were simultaneously and uniformly eroded from the surface of the bed. This agrees with the definition of surface erosion.

In addition, experimental data support the erosion of flocs only during time-dependent erosion, as well as the simultaneous and uniform erosion of sand and mud during time-independent erosion. Figure 102 shows the ratio of the masses of eroded sand (M_{sa}) and mud (M_{mu}) as a function of the normalized bed shear stress ($\tau_b/\tau_{e,s}$). M_{sa} follows from the mass in the sand trap, and M_{mu} is the product of c and the volume of water in the flume.

Figure 102 indicates that for $\tau_b/\tau_{e,s} < 1$ (time-dependent erosion) significantly more fines than sand are eroded, which indicates the erosion of mainly fines/flocs. In contrast, M_{sa}/M_{mu} tends to become constant for $\tau_b/\tau_{e,s} > 1$ (time-independent erosion). Constant M_{sa}/M_{mu} implies the simultaneous erosion of sand and mud. Furthermore, the variation of the constant M_{sa}/M_{mu} is relatively strong in Figure 102(a), and relatively small in Figure 102(b). This difference follows from the difference in sand-mud ratio of the tested soil compositions of Set 1 and Set 3 (Table 12). The constant ratios, as well as the agreement with the original composition of the soil samples as observed for time-independent erosion, nicely support the suggested erosion of subsequent layers of sediment during surface erosion.

It is noted that M_{sa}/M_{mu} is generally about 50% smaller than within the bed. Possible causes may be the Oslim-calibration of c and/or the determination of the grain size distribution. Furthermore, the ratios for the most sandy soil samples of both Set 1 (no. 1) and 3 (no. 11) are not shown, as the M_{sa}/M_{mu} ratio for these soils did not tend to a constant value for $\tau_b/\tau_{e,s} > 1$. This may be explained by their different erosion/transport behaviour (ripple formation) compared to more cohesive soils.

The new erosion approach (Section 3.2.3) argues that constant M_s can be explained by the dissipation of negative pore water pressure gradients within the sediment bed during erosion. During this dissipation process, the undrained sediment strength (c_u) decreases towards the drained sediment strength (c_d). The rate at which c_u tends to c_d is determined by the rate at which water flows into the sediment bed during this dissipation process. This flow rate is restricted, as it is a function of composition and packing density (Section 4.5).

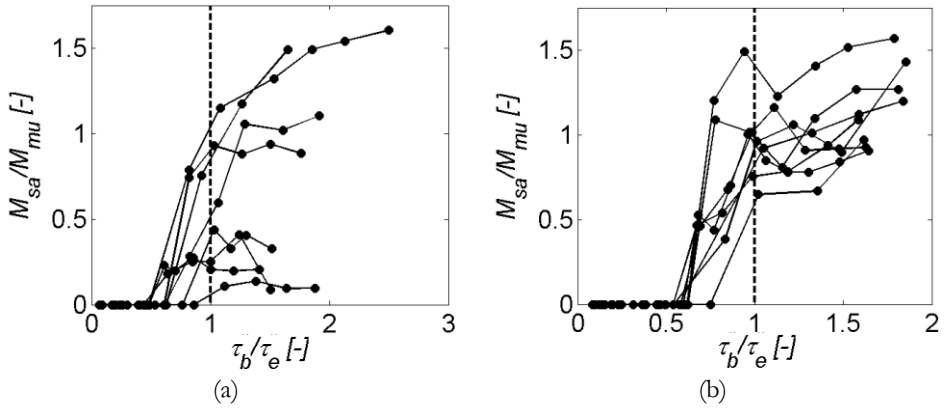


Figure 102. Ratio of eroded mass of sand (M_{sa}) and mud (M_{mu}) as a function of τ_b , normalized with $\tau_{e,s}$ for straight flume tests on soil samples 2 – 5 of Set 1 (a) and 12 – 15 of Set 3 (b) (Table 12). The vertical lines indicate the onset of time-independent erosion.

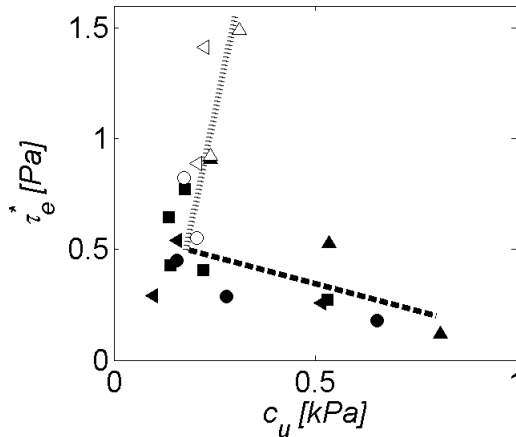


Figure 103. Relation between undrained shear strength (c_u) and surface erosion threshold (τ_e) for soil samples of Set, 1, 2, 3 and 4 as tested in the straight flume (Table 12). The clay content increases with increasing τ_e . A positive correlation between c_u and τ_e for soil samples with a dominant clay-water matrix (white-coloured markers) occurs, whereas for soil samples with a dominant sand-silt skeleton (black-coloured markers) an inverse correlation occurs.

The recognition of the importance of c_u for erosion is important, as studies on the erosion of (cohesive) sediments generally relate sediment strength to cohesive, adhesive and/or gravitational forces only. Furthermore, the bed shear stress and the threshold for time-independent erosion, on the one hand, and c_u , on the other, are typically in the order of Pa and kPa, respectively (Figure 103). This implies that it is important to define and experimentally determine sediment strength properly when discussing the erosion threshold in relation to sediment strength.

Finally, it is verified whether the observed time-independent erosion threshold agrees with the drained sediment strength, as is suggested in the new erosion classification. First, Figure 103 shows that the drained strength (c_d) of kaolinite clay (e.g. Le Hir *et al.*, 2007a; Winterwerp and Van Kesteren, 2004) and the (extrapolated) erosion thresholds following from the experimental data exhibit a similar order of magnitude (both a few Pa). Second, c_u is three orders of magnitude larger than τ_e , and c_u and τ_e partly exhibit a negative correlation (Figure 103). This indicates that pore water pressure gradients did not play a role upon the onset of time-independent erosion. In conclusion, time-independent erosion agrees with surface erosion concerning its threshold.

7.1.7 Conclusions

The new erosion classification is supported by the straight and annular flume data. This follows from the correspondences between the observed time-dependent erosion at relatively low bed shear stress and time-independent erosion at relatively large bed shear stress, on the one hand, and the proposed definitions for floc and surface erosion, on the other hand.

According to the classification, a stochastic approach is required to reproduce the relation between bed shear stress and erosion rate, as typically observed for cohesive sediments (see Figure 32 and Figure 100(b)). This typical relation mainly concerns a zero floc erosion threshold and the occurrences of time-dependent and time-independent erosion, which relate to a varying and constant erosion parameter, respectively. Deposition, vertical variations of sediment properties and bed irregularities are eliminated as alternative causes for time-dependency.

The proposed definitions for floc and surface erosion are also supported by the observed type of eroded material and erosion modes. Flocs are mainly eroded at random rates during time-dependent erosion, whereas during time-independent erosion subsequent layers of sediment are uniformly eroded at constant rates. Furthermore, the magnitude of the erosion threshold and the relation between the erosion parameter and sediment properties, as observed during time-independent erosion, support the suggested drained character of surface erosion.

Finally, properly defining and determining sediment strength, but also recognizing the stochastic character of both the bed shear stress and erosion threshold, is important when comparing experimental erosion studies.

7.2 Validation of surface erosion formulation

7.2.1 Introduction and soil composition

This section investigates whether the experimentally derived erosion rates (Chapters 5 and 6) can be represented by the newly proposed formulation for the surface erosion parameter M_s [$\text{kg}\cdot\text{m}^{-2}\cdot\text{s}^{-1}\cdot\text{Pa}^{-1}$], see Section 3.3 and Eq. (3.36):

$$M_s = \frac{c_{v,s}\rho_{dry}}{d_{50}\phi_{s,0}^{1/(n_{fr}-3)}c_u} = \frac{c_{v,s}\rho_{dry}}{\delta_e c_u} \quad (7.2)$$

Furthermore, the range in M_s for typical sediments beds, as found in estuaries and tidal lagoons, is investigated by substituting sediment properties from six sets of hypothetical soil samples in the formulation for the surface erosion parameter. Also sediment properties of the sediment mixtures used in the straight and annular flume tests ('flume soil samples') are similarly substituted. These theoretically derived M_s are compared with M_s values observed during the straight and annular flume tests.

Sedimentological properties of the flume soil samples were discussed in Chapter 5 and 6, respectively. The composition and structure of the hypothetical soil samples are described below and listed in Appendix IV. The structural composition of the flume and hypothetical soil samples is illustrated in Figure 104.

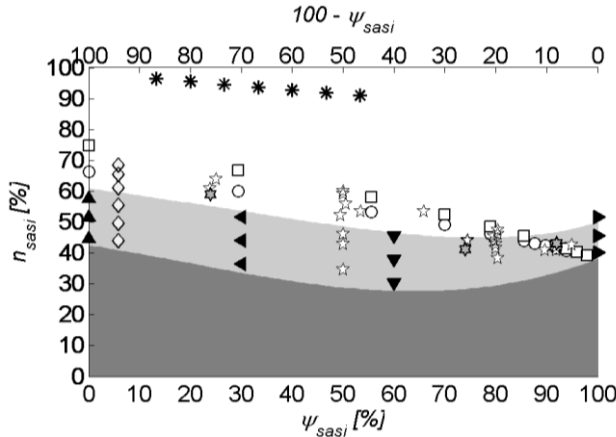


Figure 104. Granular porosity as a function of the sand-silt volume fraction ratio for the hypothetical samples: SM-A (\circ), SM-B (\square), GR-A (\blacktriangle), GR-B (\blacktriangleleft), GR-C (\blacktriangledown), GR-D (\blacktriangleright), CO-A and CO-B ($*$) and SI (\diamond), and for the flume soil samples applied in Chapter 5 (stars) and 6 (light-grey coloured stars).

The first two sets of hypothetical samples concern 10 sand-mud mixtures (SM-A and SM-B), as may be found in estuaries and tidal lagoons. These mixtures are comparable to the flume soil samples used in Chapters 4, 5 and 6. The samples of these sets exhibit increasing clay contents ($\xi_{cl} = 0 - 20\%$), yielding a transition from a dominant sand-silt skeleton to a dominant clay-water matrix. The clay-silt ratio of both

sets is constant ($\zeta_{cl}/\zeta_{si} = 0.25$), as often found in sediments in intertidal systems (Flemming, 2000). The difference between both sets is the cohesiveness of the clay fraction due to a variation in activity (0.67 and 2.00, respectively for SM-A and SM-B).

The third set (GR) concerns 12 purely granular sediments with a dominant sand-silt skeleton as may be found in tidal channels and river beds. This set is divided into four subsets (GR-A, GR-B, GR-C and GR-D) of three samples each. Each subset exhibits a varying sand-silt ratio ($\psi_{sasi} = 0, 30, 60$ and 100%, respectively); samples of one subset have a varying packing density.

The fourth and fifth set each consist of 7 cohesive sediment mixtures (CO-A and CO-B), which exhibit a dominant clay-water matrix resulting from a low granular content (15%). The sand-silt ratio of the granular fraction varies slightly. These cohesive sediments may be found in sheltered areas in marine systems and/or rivers. The activity of the clay fraction varies for both sets (0.67 and 1, respectively for CO-A and CO-B). Each set consists of samples for which the packing density strongly varies ($\rho_{bulk} = 1300 - 2000 \text{ kg}\cdot\text{m}^{-3}$). This yields a character ranging from liquid, plastic to solid. These characters represent freshly deposited and normally and strongly consolidated clay, respectively.

The final set (SI) concerns six predominantly silty sediments ($\zeta_{si} = 90\%$ and $\zeta_{sa} = \zeta_{cl} = 5\%$), as e.g. found in the Yellow River. These hypothetical sediments have a constant sediment composition but exhibit varying packing densities ($\rho_{bulk} = 1550 - 2000 \text{ kg}\cdot\text{m}^{-3}$), yielding a transition from a silt skeleton to a low-cohesive ($PI = 3.4\%$) clay-water matrix, as for quick sand.

7.2.2 Soil mechanical parameters

Bulk soil mechanical parameters c_u (undrained shear strength), $m_{v,s}$ (coefficient of volume variation during swelling) and k_v (permeability) are determined for both the hypothetical samples and the flume soil samples. Figure 105 shows c_u [Pa] following Eq. (4.10). c_u of the soil samples of Sets SM-A and SM-B follows the c_u -model (Figure 48(b)), whereas c_u of Set SI follows the c_u -model for soils with constant sand-silt ratio and varying ρ_{bulk} (Figure 48(a)). c_u of mixtures of CO-A and CO-B follows Eq. (4.7) for purely cohesive soils, as these mixtures contain little sand and silt.

Generally, c_u varies between 0.01 and 1 kPa. c_u is smaller than 0.01 kPa only for some loosely packed samples with little or no clay. Furthermore, c_u of these granular mixtures strongly increases to 10 - 100 kPa for only small variations of the packing density (n_{sasi}). This strong variation results from zero PI^* for granular mixtures, yielding an almost direct transition from liquid to solid behaviour (Figure 9).

The coefficient of volume variation during swelling $m_{v,s}$ [Pa⁻¹] follows from Eq. (4.14), and is a function of the swelling index C_s [-], the unloading pressure during surface erosion p [Pa] and the void ratio e [-] (Eq. (4.14)). The void ratio directly follows from ρ_{bulk} . p equals the soil pressure at the erosion depth ($p = \rho_{bulk}g\delta_e$), which has a maximum of about 30 Pa. Finally, C_s is a function of the plasticity index (Eq. (4.17)), and typically ranges between 0.01 - 0.1. Large $m_{v,s}$ yield a strong tendency for swelling, whereas low $m_{v,s}$ yields rather small volume increases upon unloading.

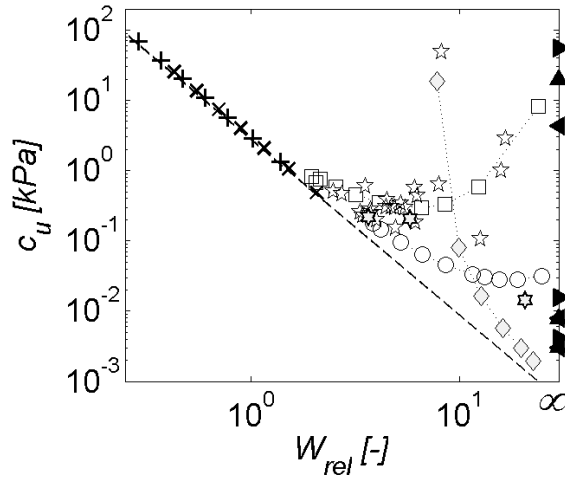


Figure 105. Undrained shear strength following Eq. (4.10) as a function of the relative water content for the hypothetical samples: SM-A (\circ), SM-B (\square), GR-A (\blacktriangle), GR-B (\blacktriangleleft), GR-C (\blacktriangledown), GR-D (\blacktriangleright), CO-A (+), CO-B (x) and SI (\diamond), and for the flume soil samples applied in Chapter 5 (stars) and 6 (light-grey coloured stars). The diagonal dashed line represents c_u for purely cohesive soils.

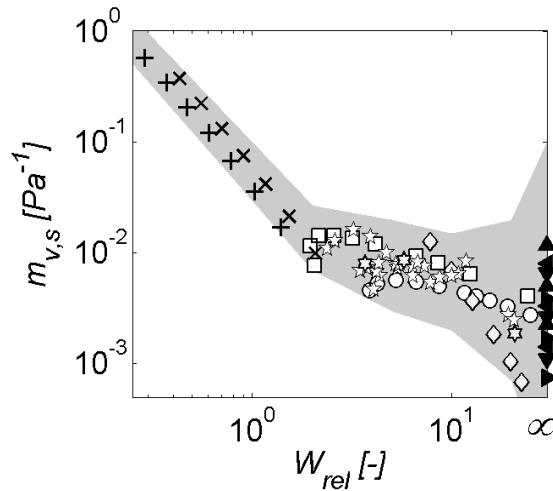


Figure 106. Coefficient of volume variation upon swelling following Eq. (4.14) as a function of the relative water content for the hypothetical samples: SM-A (\circ), SM-B (\square), GR-A (\blacktriangle), GR-B (\blacktriangleleft), GR-C (\blacktriangledown), GR-D (\blacktriangleright), CO-A (+), CO-B (x) and SI (\diamond), and for the flume soil samples applied in Chapter 5 (stars) and 6 (light-grey coloured stars). The grey-shaded area indicates the anticipated range of occurrence.

Figure 106 shows a variation of $m_{v,s}$ of about three orders of magnitude over the various mixtures. For the granular mixtures, $m_{v,s}$ ranges between 10^{-3} and 10^{-2} Pa $^{-1}$, with relatively large $m_{v,s}$ for densely packed silty soils and smaller $m_{v,s}$ for loosely packed sandy soils. For sand-mud mixtures, with a dominant sand-silt skeleton ($3 - 4 < W_{rel} < \infty$), $m_{v,s}$ not only varies as a function of W_{rel} , but also for constant W_{rel} . This is attributed to varying PI^* and varying sand-silt and clay-silt ratios. Finally, $m_{v,s}$ for cohesive soils strongly increases for decreasing W_{rel} . Relatively large $m_{v,s}$ in Figure 106 illustrate the strong swelling capacity of these types of (strongly consolidated) soils upon unloading.

As discussed in Section 4.4, no formulation is currently available to determine k_v [$m \cdot s^{-1}$] as a function of sediment properties. Therefore, the conceptual diagram of Figure 54 is applied to estimate the permeability of the hypothetical mixtures. Estimations of k_v are shown in Figure 107. Loosely packed sandy soils exhibit k_v of about 10^{-4} m \cdot s $^{-1}$. For increasing silt content and increasing packing density k_v decreases to about 10^{-6} m \cdot s $^{-1}$. This results from a larger specific surface area per unit volume (S in Eq. (4.20)) due to larger ρ_{bulk} and the smaller sized silt particles. Consequently, more friction is experienced by the flow, resulting in lower k_v . Therefore, k_v for the silty mixtures (SI) must be lower than for sand-mud (SM) mixtures at identical W_{rel} .

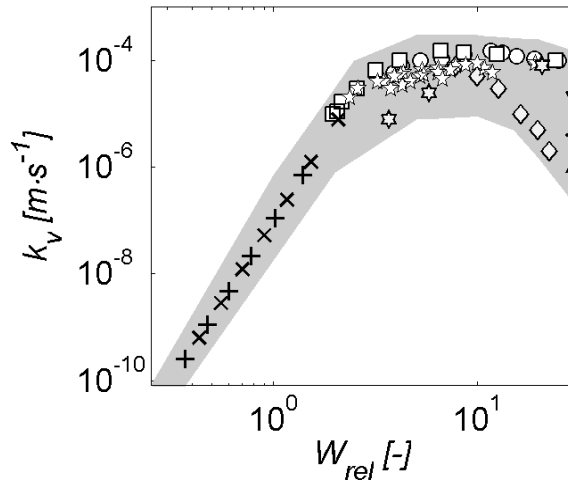


Figure 107. Permeability as a function of the relative water content for the hypothetical samples: SM-A (\circ), SM-B (\square), GR-A (\blacktriangle), GR-B (\blacktriangleleft), GR-C (\blacktriangledown), GR-D (\blacktriangleright), CO-A (+), CO-B (x), SI (\diamond) and for the flume soil samples applied in Chapter 5 (stars) and 6 (light-grey coloured stars). The grey-shaded area indicates the anticipated range of occurrence.

For sand-mud mixtures of SM-A and SM-B and for the flume soil samples, k_v increases slightly with increasing mud content (lower W_{rel}) when the clay content of the mixtures is low and they, consequently, exhibit a dominant sand skeleton. This increase of k_v results from the increasing volume fraction of mud, yielding an increased mutual distance between sand particles. The effect of varying sand-silt and clay-silt

ratios results in the occurrence of multiple k_v for constant W_{rel} . k_v strongly reduces for decreasing W_{rel} upon the transition from a granular skeleton to a clay-water matrix, as the character of the mixtures changes from loosely packed mud ($W_{rel} \approx 3 - 5$) to consolidated clay ($W_{rel} \approx 1 - 2$).

Finally, the coefficient of pore water pressure gradient dissipation during swelling $c_{v,s}$ [$\text{m}^2 \cdot \text{s}^{-1}$] is calculated as a function of $m_{v,s}$ and k_v following Eq. (4.21). Figure 108 shows that $c_{v,s}$ exhibits a similar trend as a function of W_{rel} as observed for k_v (Figure 107). Furthermore, $c_{v,s}$ of both the hypothetical and flume soil samples varies over orders of magnitude due to the strongly varying compositional and structural characters. These varying characters indicate a variation from (strongly) consolidated clay to loosely packed granular mixtures.

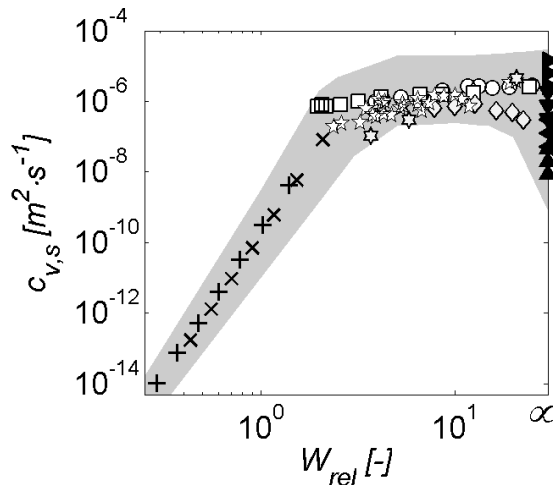


Figure 108. The coefficient of pore water pressure gradient dissipation during swelling following Eq. (4.21) as a function of the relative water content for the hypothetical samples: SM-A (\circ), SM-B (\square), GR-A (\blacktriangle), GR-B (\blacktriangleleft), GR-C (\blacktriangledown), GR-D (\blacktriangleright), CO-A (+), CO-B (x) and SI (\diamond), and for the flume soil samples applied in Chapter 5 (stars) and 6 (light-grey coloured stars). The grey-shaded area indicates the anticipated range of occurrence.

7.2.3 Erosion depth

The erosion depth δ_e or the thickness of the erosion layer relates to the spatial scale of the diffusion of pore water pressure gradients. Eq. (3.32) indicates that δ_e is a function of the median particle size of the mud fraction $d_{50,m}$ [μm], the fractal dimension n_{fr} [-] and the sediment volume fraction upon the onset of swell $\phi_{s,0}$ [%]:

$$\delta_e = d_{50,m} \phi_{s,0}^{1/(n_{fr}-3)} \quad (7.3)$$

$d_{50,m}$, n_{fr} and $\phi_{s,0}$ can only partly be derived for the available information and are therefore estimated, as is discussed below (see also Appendix IV).

Furthermore, δ_e for purely granular soils ($PI^* = 0$ for Set GR) is estimated at $2 \cdot d_{50}$ for densely packed soils ($n_{sasi} \rightarrow n_{sasi,min}$), $5 \cdot d_{50}$ for normally packed soils ($n_{sasi} \approx 0.5 \cdot (n_{sasi,max} - n_{sasi,min})$), and $10 \cdot d_{50}$ for loosely packed soils ($n_{sasi} \rightarrow n_{sasi,max}$). Winterwerp and Van Kesteren (2004) argue that the fractal dimension n_{fr} [-] of flocs in estuarine sediment beds varies between 2.65 - 2.85. A logarithmic relation between PI^* and n_{fr} is assumed ($n_{fr} = 2.80 - 0.05 \log PI^*$, see Figure 109).

The sediment volume fraction upon the onset of swell $\phi_{s,0}$ is assumed to equal the volume fraction derived from the applied ρ_{bulk} . This assumption is not valid for strongly consolidated sediments (e.g. the most dense soil samples of Sets CO-A and CO-B), as for these sediments $\phi_s < \phi_{s,0}$ before swelling.

The median particle size of the mud fraction ($d_{50,m}$ [μm]) follows from the median particle sizes of clay and silt. For sand-mud mixtures (SM-A and SM-B) $d_{50,m}$ is estimated at 30 μm . For the cohesive Sets CO-A and CO-B $d_{50,m}$ is varied between 16 and 10 μm ; for SI $d_{50,m} = 20 \mu\text{m}$. Mixtures of the granular Sets (GR-A - D) do not contain much mud. Therefore, the characterising grain size for these mixtures equals d_{50} rather than $d_{50,m}$, yielding 50 μm for GR-A, 90 μm for GR-B, 130 μm for GR-C and 170 μm for GR-D.

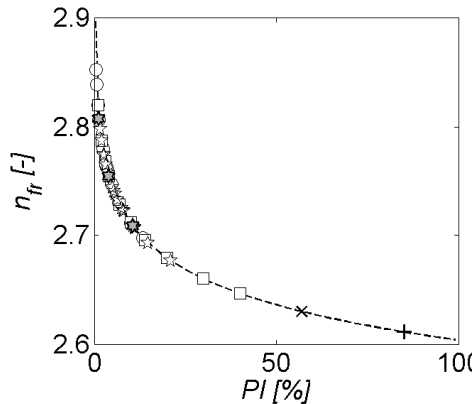


Figure 109. Assumed relation for the fractal dimension as a function of the plasticity index for the hypothetical samples of the five sets which contain a cohesive fraction: SM-A (\circ), SM-B (\square), CO-A ($+$), CO-B (\times) and SI (\diamond), and for the flume soil samples applied in Chapter 5 (stars) and 6 (light-grey coloured stars).

Figure 110 shows that the erosion depth typically ranges between about 0.01 to 10 mm. Small δ_e implies that the dissipation of pore water pressure gradients is a slow process, which is expected for (strongly) consolidated clay. Large δ_e relates to a fast dissipation process, yielding a larger surface erosion rate. This is typically expected for loosely packed and/or granular sediments with little or no clay.

Finally, Figure 110 shows more or less linear relations (on a log-log scale) for δ_e as a function of both c_u and $c_{v,s}$. These relations agree with the theory (Section 3.3), that

δ_e is a typical spatial scale of the dissipation of pore water pressure gradients. A fast dissipation of pore water pressures (large $c_{v,s}$) yields low undrained shear strength and large δ_e (and vice versa). These relations support the validity of assumptions applied to calculate δ_e and $c_{v,s}$.

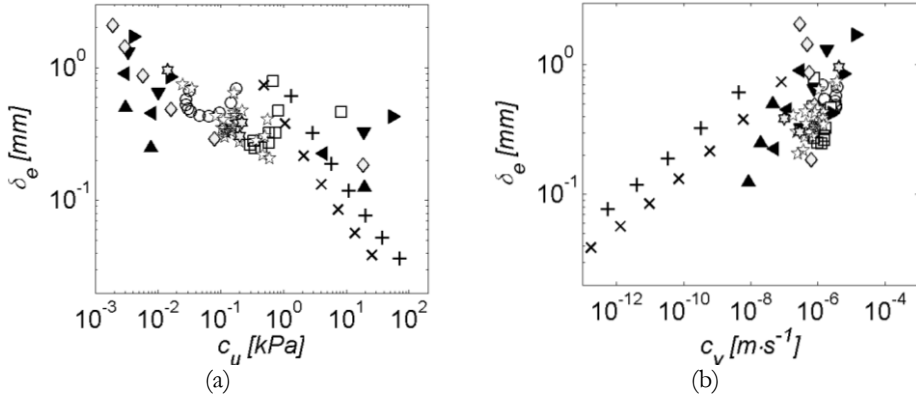


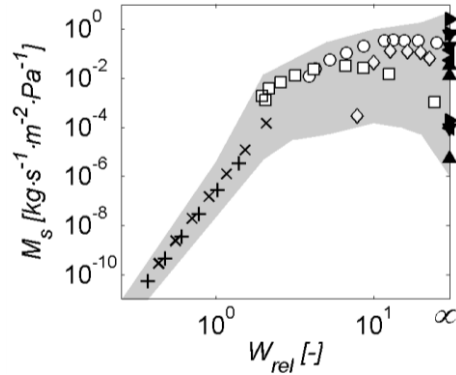
Figure 110. Erosion depth as a function of the undrained shear strength (a) and as a function of the coefficient of pore water dissipation during swelling (b) for the hypothetical samples: SM-A (\circ), SM-B (\square), GR-A (\blacktriangle), GR-B (\blacktriangleleft), GR-C (\blacktriangledown), GR-D (\blacktriangleright), CO-A (+), CO-B (x) and SI (\diamond), and for the flume soil samples applied in Chapter 5 (stars) and 6 (light-grey coloured stars).

7.2.4 Comparing theoretical and experimental erosion parameters

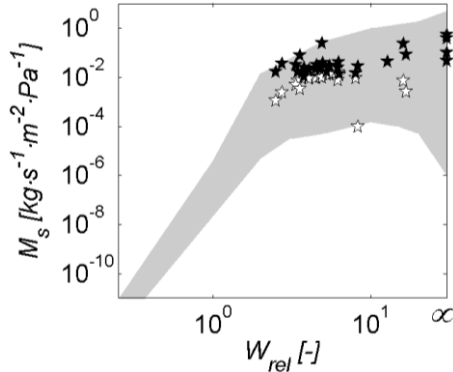
The surface erosion parameter M_s is established (Figure 111) for the six sets of hypothetical soil samples and for the flume soil samples applied in Chapters 5 and 6 by substituting both the calculated and estimated soil (mechanical) properties in Eq. (3.36). It is noted that larger M_s yields a larger erodibility. The first conclusion is that M_s can vary by orders of magnitude as a function of W_{rel} (Figure 111(a)). The second conclusion is that observed M_s can be successfully established by substituting soil (mechanical) properties in the new formulation for the surface erosion parameter (Figure 111(b) and (c)). Both conclusions are discussed further below.

The erodibility exhibits order of magnitude variations as a function of W_{rel} , especially for mixtures with a dominant clay-water matrix ($W_{rel} < 2$). M_s may increase from 10^{-10} to 10^{-4} $\text{kg}\cdot\text{m}^{-2}\cdot\text{s}^{-1}\cdot\text{Pa}^{-1}$, respectively for (strongly) consolidated clay to loosely packed mud ($0.1 < W_{rel} < 2$). This large variation of M_s implies that, for mixtures with a dominant clay-water matrix, the erodibility strongly increases as a function of a decreasing packing density and/or a decreasing plasticity index.

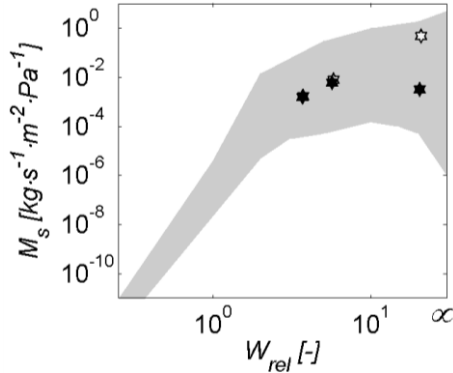
Variations of M_s for sand-mud mixtures ($2 < W_{rel} < 20$) are smaller ($10^{-4} < M_s < 10^{-1}$ $\text{kg}\cdot\text{m}^{-2}\cdot\text{s}^{-1}\cdot\text{Pa}^{-1}$) than for purely cohesive mixtures (Figure 111(a)). Generally, the erodibility slightly increases when n_{sasi} decreases below $n_{sasi,max}$ ($2 < W_{rel} < 10$), which results from a lower mud volume fraction and/or from a lower sand-silt density.



(a: Hypothetical soil samples)



(b: Straight flume soil samples)



(c: Annular flume soil samples)

Figure 111. Surface erosion parameter as a function of the relative water content for (a): SM-A (\circ), SM-B (\square), GR-A (\blacktriangle), GR-B (\blacktriangleleft), GR-C (\blacktriangledown), GR-D (\blacktriangleright), CO-A (+), CO-B (\times) and SI (\diamond). Computed (white markers) and observed M_s (black markers) for soils tested in the straight and annular flume are shown in (b) and (c), respectively. The grey-shaded areas indicate the typical range. Low W_{rel} reflect cohesive soil samples, whereas larger W_{rel} reflect more granular soil samples. For purely granular soil samples W_{rel} is not defined ($W_{rel} = \infty$).

For granular mixtures ($W_{rel} > 20$), M_s varies between 10^{-6} and $1 \text{ kg}\cdot\text{m}^{-2}\cdot\text{s}^{-1}\cdot\text{Pa}^{-1}$. Loosely packed and well-sorted (purely sand or silt) granular soils may exhibit relatively large erodibility, whereas more densely packed ($n_{sasi} \rightarrow n_{sasi,min}$) and poorly sorted (sand-silt mixtures) exhibit relatively low erodibility.

Next, computed and observed M_s are compared. Figure 111(b) and (c) compare observed M_s with M_s following from substituting soil (mechanical) properties in the new erosion formulation. The order of magnitude agreement between computed and observed M_s supports the applicability of the new erosion formulation, though some soil (mechanical) properties had to be estimated. This implies that it is possible to derive the erosion behaviour of both cohesive and granular sediment mixtures from a generic physically-founded formulation, which is an important improvement compared to currently applied empirical erosion formulae.

However, Figure 111(b) and (c) also indicate that computed and observed M_s can exhibit differences up to 1 – 2 orders of magnitude. Differences by an order of magnitude or less may result from measuring inaccuracies. Examples may be the calibration of the suspended sediment concentration (see also Sections 5.3 and 6.3) and/or the complex flow patterns in both flumes. These flow patterns hamper an accurate calibration of the bed shear stress and complicate the comparison of M_s derived from different flume studies, as well as the comparison with computed M_s .

Also estimations of soil properties required to compute M_s incorporate inaccuracies, such as the estimated permeability. The similar shape of the grey-shaded areas and the similar ranges of occurrence in Figure 108 and Figure 111 indicate that M_s is strongly influenced by k_v . However, it was not possible to accurately determine k_v , as no robust experimental method is currently available. Alternatively, k_v was estimated, which causes inaccuracies in the computation of M_s . This particularly concerns k_v for sand-mud mixtures, as k_v is assumed rather sensitive to varying sand-silt and clay-silt ratios.

k_v of the well-sorted sandy mixture tested in the annular flume (Figure 111(c)) is expected to vary between 10^{-5} and $10^{-4} \text{ m}\cdot\text{s}^{-1}$. However, unrealistically low k_v is required ($5\cdot 10^{-7} \text{ m}\cdot\text{s}^{-1}$) to establish the observed M_s . In addition, observations from this test indicate sand on top of the sediment bed. Section 6.3.5 discusses that eroded sand forms propagating ripples on the surface of the sediment bed, which protects the underlying sediment bed from erosion. Therefore, differences between computed and observed M_s larger than an order of magnitude (Figure 111(b) and (c)) may be attributed to a morphological feedback of eroded sand on erosion.

7.2.5 Conclusions

The order of magnitude of observed erosion parameters (M_s) can be established by substituting soil (mechanical) properties in the new surface erosion formulation. This supports the applicability of the new formulation for surface erosion of cohesive, granular and intermediate sediment mixtures, and forms an important alternative for the currently applied non-generic empirical erosion formulae. The new formulation

defines surface erosion as the drained removal of overlying layers of sediment, limited by the dissipation rate of pore water pressure gradients. Therefore, the fair agreement between computed and observed erosion parameters also supports the important role of these gradients as an additional retarding force for erosion, next to gravitational and/or cohesive forces.

The surface erosion parameter exhibits orders of magnitude variation, e.g. for highly consolidated cohesive soils, sand-mud mixtures with a transitional structure, and loosely packed granular soils. This strong variation follows from the spatial and temporal variations of the dissipation rate of pore water pressure gradients as a function of sediment composition and packing density.

Inaccuracies of observed erosion parameters are attributed to experimental procedures and set-ups, as well as to a possible morphological feedback of eroded sand on erosion. Inaccuracies of computed erosion parameters result from estimations of soil properties, e.g. the permeability or the fractal dimension. To further (quantitatively) validate the new erosion formulation, the permeability of sand-mud mixtures should be studied. But as discussed in Section 0, no robust experimental method is currently available. A first step to develop a new measuring device to measure permeability is presented in Section 8.2.

7.3 Real world applicability

7.3.1 Introduction

This section discusses both the new erosion classification (Figure 36) and the surface erosion formulation (Eq. (3.36)) in view of the erosion of natural sediment beds, in particular intertidal flats in estuaries and tidal lagoons. Only limited data is currently available to quantitatively validate the surface erosion formulation for natural conditions. However, the current study results in some important qualitative conclusions, remarks, and suggestions for the real world application of both the classification and formulation.

Natural intertidal sediment beds exhibit strong spatial (vertical and horizontal direction) and temporal variability, which mainly results from sedimentological (Section 2.3.2), physico-chemical (Section 2.3.2) and biological influences (Section 2.3.3). Additionally, the stochastic character of the flow and the interaction with bed roughness play an important role.

The next sections elaborate on the effect of sedimentological, physico-chemical and biological influences on the occurrence and characteristics of the three erosion modes as discussed in this thesis. This provides insight in the effect of these influences on the erosion threshold and rate, as well as in the occurrence of these modes and experimental procedures to study them.

The new erosion classification relates the occurrence of a particular erosion mode to the relation between the drained and undrained strength, on the one hand, and the bed shear stress and normal stress, on the other hand. Erosion rates and thresholds are

a function of individual particle characteristics and bulk soil properties. Therefore, a distinction is made between influences on (micro scale) individual particle properties and on (meso-scale) bulk soil properties.

7.3.2 Floc erosion

Floc erosion is defined as the erosion of loosely packed flocs from the surface of a sediment bed when flow-induced peak stresses exceed the strength of individual flocs (Section 3.2.3). Floc erosion strongly depends on the stochastic characters of both the flow conditions and floc strength and exhibits a rather low erosion threshold as it occurs at low (0.1 – 1 Pa) flow-induced stresses.

Furthermore, floc erosion exhibits a time-varying erosion rate, with large initial rates reducing to zero at relatively small time scale. Observations indicate that the typical time-scale (e -folding time scale, see Eq. (5.2)) at which these peak erosion rates reduce to zero is typically of the order of 10 – 100 seconds. The typical spatial scale at which floc erosion takes place equals the size of individual flocs, which is of the order of 10 – 100 micrometers.

It is anticipated that both the peak erosion rate and the typical e -folding time scale relate to the number of erodible flocs on top of the sediment bed and to the distribution and magnitude of the drained floc strength and flow-induced stresses. This implies that micro scale particle properties are more important than meso or larger scale sediment properties such as the packing density of the sediment bed.

The strength of individual flocs equals the drained bed strength, which is characterised with the plasticity index as a function of the clay content and the clay-activity. The activity of the clay fraction is determined by cohesive (as a function of clay mineralogy and pore water chemistry) and adhesive bonding (due to organic matter, see Figure 8). Although the clay mineralogy within a marine system is generally rather constant (determined by mineralogy of catchment area), physico-chemical influences and organic bonding may strongly vary, especially within the top layer (μm 's - mm 's) of the sediment bed.

Typical examples of organic bonding are biofilms produced by microphytobenthos (e.g. Orvain *et al.*, 2003; Montserrat *et al.*, 2008) on a sediment bed. In this thin film-layer adhesive bonding may exceed cohesive bonding. However, the occurrence of a biofilm strongly depends on the availability of light. Therefore, adhesive bonding and the effect on bed stability exhibits strong seasonal and even day-night variations (see e.g. Friend *et al.*, 2003).

Odell *et al.* (1960) and Malkawi *et al.* (1999) discuss the effect of organic matter on the plasticity index. Figure 112 shows that the plasticity index may either positively or negatively correlate with the organic matter content, depending on clay mineralogy. Malkawi *et al.* (1999) relate this contradictory effect to the two ways organic matter may affect the Atterberg Limits. Organic matter may increase the plasticity index of soils due to an enhanced water adsorption capacity. However, organic strings attached to clay particles cover (part of) their specific surface area, which reduces cohesive bonding. Dominance of either one of these factors depends on the type and content of

organic matter, on the one hand, and clay mineralogy, on the other. This illustrates the spatial and temporal variation of adhesive bonding within marine systems.

The effect of salinity on cohesive bonding is an example of a physico-chemical effect on the plasticity index (see e.g. Van Paassen, 2002; Van Paassen and Gareau, 2004). Figure 113 shows that the plasticity index relates to the salinity, which further depends on the water content and on the specific surface area and cation exchange capacity of clay particles. Other studies of physico-chemical effects on sediment properties are listed in Sections 2.1.3 and 2.4.5.

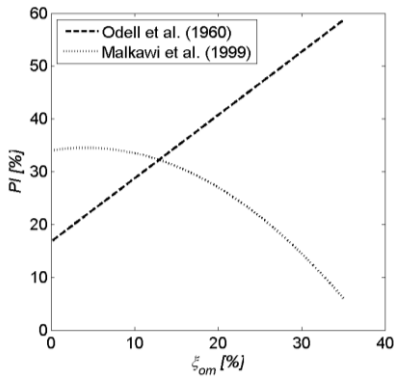


Figure 112. Plasticity index as a function of organic matter content ζ_{om} for a montmorillonite type of clay (Odell *et al.*, 1960) and for an illite type of clay (Malkawi *et al.*, 1999).

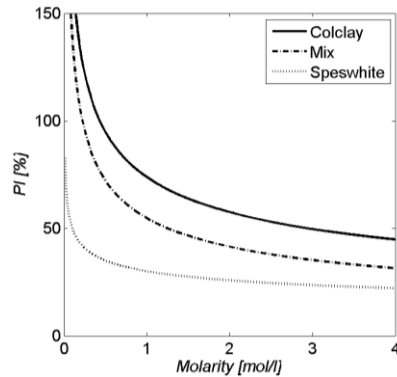


Figure 113. Plasticity index as a function of the salinity (NaCl) for Colclay (montmorillonite), Speshwhite clay (kaolinite) and a mixture of the two (after Van Paassen and Gareau, 2004).

The strong spatial and temporal variations of both adhesive and cohesive bonding on the plasticity index indicate that both the magnitude and probability distribution function of floc strength is difficult to quantify. Therefore, it is difficult to determine clear trends between floc erosion and intertidal sediment properties.

Next to floc strength, the amount of erodible flocs on a sediment bed is also important for floc erosion. The presence of flocs is determined by hydrodynamic properties (e.g. the duration of the slack tidal period), as well as by organisms which transport fine material from the subsoil to the surface of the bed (or vice versa). Additionally, the amount of erodible flocs may be reduced by organisms, which trap fines by means of adhesive / polymeric bonding. Examples are pelletisation by filter feeders (e.g. mussels, Prins *et al.*, 1996) or algae mats (e.g. Orvain *et al.*, 2003; Montserrat *et al.*, 2008).

Bed roughness is also important for floc erosion. The bed roughness of intertidal areas may strongly vary due to complex bed geometry (e.g. ripples) and biological effects. Examples of the latter are the mud shrimp (*Corophium volutator*, see e.g. Meadows and Tait, 1989), which generates a rough surface, and microphytobenthos, which generate a smooth biofilm surface.

In conclusion, floc erosion of natural sediments is a rather random process as both the character and availability of flocs strongly depends on biological and physico-chemical influences, which exhibit strong temporal and spatial variations, especially on intertidal flats. This implies that floc erosion rates are difficult to predict. Although floc erosion starts at rather low bed shear stress, only limited amounts of sediment are eroded from a rather thin (μm 's) surface layer of the bed. Therefore, it is anticipated that floc erosion is an important process only when studying the mass balance of fine material, or when predicting turbidity levels.

Floc erosion should be studied by relating the stochastic character of flow-induced stresses and floc strength (see e.g. Van Prooijen and Winterwerp, 2010). Floc erosion should be characterised by the magnitude of the initial concentration peaks and the typical time-scale at which these peaks reduce to zero. It is stressed that the study of floc erosion requires an accurate simulation of flow-induced stresses typically occurring in the natural environment.

7.3.3 Surface erosion

Surface erosion is the drained removal of subsequent layers of consolidated sediment by flow-induced bed shear stresses. An erosion threshold can be identified for a bed shear stress above which sediment is eroded at a rate, which is characterised by the erosion parameter. This parameter is constant for a uniform sediment bed, which illustrates that surface erosion is time-independent and supply unlimited. The surface erosion parameter is characterised by the process of pore water pressure gradient dissipation (i.e. swelling).

The erosion depth or the typical spatial scale at which surface erosion occurs is determined by the typical vertical spatial scale at which pore water pressure gradients dissipate. Section 7.2.3 and Figure 110 show that the erosion depth is typically 0.01 – 0.1 mm for consolidated clay, 0.1 – 1 mm for sand-mud mixtures and about 1 mm for loosely packed and/or granular soils.

Figure 114 shows a conceptual diagram for the surface erosion parameter, based on Section 7.2.4. The diagram illustrates the variability of the erosion parameter for intertidal sediments with a character ranging from cohesive to granular, and/or from loosely to densely packed. The diagram allows for the estimation of the typical temporal scale of surface erosion of intertidal sediments.

Typical flow-induced stresses on intertidal flats in estuaries and tidal lagoons are generally of the order of 1 - 10 Pa (Le Hir *et al.*, 2007a). The typical layer thickness of material which may be eroded during an ebb-flood or spring-neap tidal cycle is estimated at several cm's. As the current study indicates that surface erosion occurs at flow-induced stresses and bed strengths which may typically occur in estuaries and tidal lagoons, it is concluded that surface erosion is an important process in these systems.

The typical time scale of surface erosion follows from the product of the dry density and the eroded layer thickness divided by the erosion parameter and the bed shear stress. This results in time-scales of the order of seconds to minutes for loosely packed and/or granular sediment beds, tens of seconds to hours for sand-mud

mixtures with a granular skeleton and minutes to days for sand-mud mixtures with a dominant clay-water matrix.

For consolidated clay, the time-scale for the erosion of a layer of several cm's may increase up to several years and more. Morphological processes on intertidal flats exhibit much smaller (micro/meso) scales (Table 1). Therefore, it is concluded that surface erosion of consolidated clay on intertidal flats is not likely to be an important morphological process. However, the erosion of strongly consolidated layers of clay, which emerge after the removal of overlying sediments due to a migrating tidal channel, can be important for the (mega scale) development of estuaries and tidal lagoons. The erosion rate of these layers is much smaller than may be expected based on individual particle characteristics only, which is explained by the new erosion formulation.

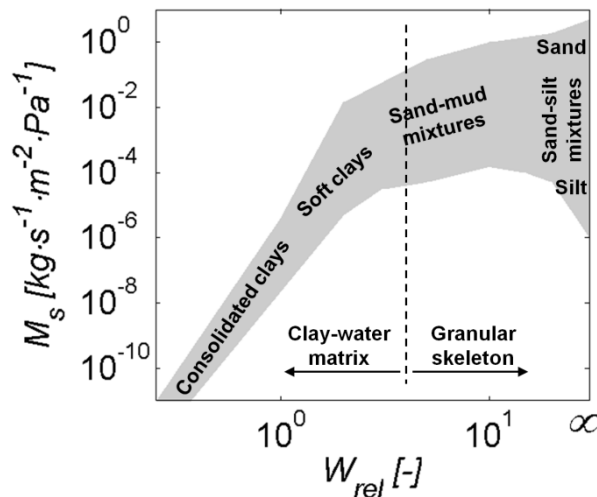


Figure 114. Conceptual diagram showing the typical range of the surface erosion parameter as a function of the relative water content (ratio of water content and plasticity index) for consolidated clay, mixtures of sand and mud and (mixtures of) sand and silt (see also Figure 111).

The dissipation of pore water pressure gradients during surface erosion implies that bulk (meso-scale) soil mechanical parameters are more important than individual particle characteristics. This is modelled by Eq. (3.36), in which the surface erosion parameter is a function of the undrained shear strength and the coefficient of pore water dissipation. Chapter 4 shows that these soil mechanical parameters are to a large extent determined by the character of the sediment structure, either a sand-silt skeleton or clay-water matrix.

This thesis shows (Figure 114) that small variations of the sediment structure can cause significant variations of soil mechanical properties and, consequently, varying erodibility. Variations of the dominant sediment structure are especially expected for mixtures for which the granular porosity is close to its maximum, as with sand-mud

mixtures. Sediment beds in estuaries and tidal lagoons generally consist of sand and mud. Only in areas with significant hydrodynamic forcing more sandy beds occur, whereas muddy beds favour more quiescent conditions.

In conclusion, soil mechanical properties of intertidal sediment beds are sensitive to small changes of the sediment structure. These small changes are likely to be generated by mixing and/or burrow digging organisms present in and on intertidal sediment beds (Section 2.3.3). Destabilizing of the sediment bed by biota is generated when pore water pressure gradient dissipation is enhanced, e.g. by loosening of the packing density. Stabilizing may e.g. result from the mixing of vertically stratified sediment beds, due to which the packing density increases and/or the permeability decreases. This implies that the overall erodibility of a sand-mud mixture may be significantly lower than the erodibility of individual layers of sand and mud.

Not only the occurrence of either a sand-silt skeleton or clay-water matrix, but also the character of the dominant structure is important for surface erosion. One example is the effect of physico-chemical effects on a clay-water matrix and, subsequently, on soil mechanical bulk properties like compressibility, permeability and strength (e.g. Kandiah, 1974; Mitchell, 1976; and Mitchell and Santamarina, 2005). However, few studies present generic relations between biota and soil mechanical bulk properties like the coefficient of pore water pressure gradient dissipation and/or the undrained shear strength.

Due to dissipation, the undrained strength of an over-consolidated bed decreases towards its drained strength during surface erosion. Surface erosion commences when flow-induced stresses exceed the decreasing bed strength. As discussed for floc erosion, the drained strength is a function of cohesive and adhesive bonding. These are both determined by micro-scale sediment properties and biological and physico-chemical influences. Also the erosion depth, which is the typical vertical scale at which surface erosion takes place, is a function of micro-scale mud characteristics: volume fraction, median size and fractal dimension. This indicates that surface erosion is not only determined by mechanical soil properties, but also by smaller scale sediment bed characteristics.

Biological and physico-chemical influences on the surface erosion threshold are similar to those for floc erosion. The difference with floc erosion is that not only the effect of these influences on surficial sediments is important for surface erosion, but also their effect on the properties of the subsoil, as during surface erosion subsequent layers of sediment are eroded. This implies that e.g. bioturbators, which oxidize the subsoil, may significantly influence the surface erosion threshold.

Furthermore, surface and floc erosion may simultaneously occur for flow-induced stresses close to the surface erosion threshold. This is supported by observations from both the straight (Chapter 5) and annular flume (Chapter 6) tests. It is noted that surface erosion is fully developed only when the complete probability density function (pdf) of the flow-induced stresses exceeds the pdf of the surface erosion threshold. This indicates that surface erosion is less sensitive to the stochastic characters of both the flow-induced stress and the drained sediment strength compared to floc erosion.

The typical spatial and temporal scales of surface erosion further indicate that other processes may influence surface erosion. Examples are the effect of propagating

bed forms (Figure 91) and a sheet flow layer above the bed, which both hamper the erosion of the underlying sediment bed, also under natural circumstances. Another example is the effect of deposition, which may alter the composition of the surface of the eroding bed.

The new erosion formulation relates the drained failure of surface erosion to soil mechanical parameters. This physically founded formulation is an improvement compared to the currently applied highly empirical relations. These relate the erosion threshold and erosion rate to individual particle characteristics, without incorporating larger scale effects like sediment structure or pore water chemistry. Consequently, these relations between erosion properties and individual particle characteristics exhibit a highly varying or even contradicting character, especially for natural sediments (Section 2.4.5).

7.3.4 Mass erosion

Mass erosion is the undrained disruption of lumps (cm's – dm's) of material (Section 3.2.3). Mass erosion occurs when the scale of the flow-induced deformations of the sediment bed is smaller than the scale at which pore water pressure gradients dissipate. This implies that the flow-induced (stagnation) stresses locally exceed the undrained shear strength. Generally, mass erosion occurs for cohesive sediment beds (low dissipation rates) in combination with large flow-induced stresses. However, mass erosion is also observed for purely granular beds which exhibit low permeability (e.g. for the silty sediment bed of the Yellow River, see Van Maren *et al.*, 2009).

The onset of mass erosion is generally characterised by the occurrence of cracks or failure planes perpendicular to the flow direction (see Figure 69(a)). Mass erosion is a random process which is characterized by an irregular surface of the sediment bed. The irregular erosion rates strongly depend on the stochastic character of the flow-induced stress, in particular normal stresses. The undrained failure mechanism of mass erosion exhibits a small temporal (seconds) scale.

As mass erosion is an undrained process, the drained strength and the dissipation rate of pore water pressure gradients are less important. Therefore, the mass erosion threshold and rate are expected to depend mainly on the stochastic characters of both the flow-induced stresses and undrained shear strength (see Section 3.2.3). Generally, large flow-induced stresses are required for mass erosion. However, often the undrained shear stress of relatively densely packed sand-mud mixtures is rather high. Additionally, this strength further increases with depth due to increasing packing density. Therefore, the layer thickness from which material may be eroded by means of mass erosion due to natural flow-induced stresses is limited. This implies that mass erosion is a supply-limited and time-dependent process, similarly to floc erosion.

Section 4.2 shows that the undrained shear strength is determined by the packing density of the granular fraction and by the relation between water content and plasticity index. Furthermore, the undrained shear strength of soils is generally orders of magnitude larger than the drained strength. This implies that biological and physico-chemical effects on adhesive and cohesive bonding, which determine the drained strength, are less important for mass erosion.

However, biota may significantly influence the soil structure as well as the sand-mud composition of intertidal sediment beds (Section 2.3.3). Section 4.2 shows that the undrained shear strength is rather sensitive to variations of the packing density, which implies a varying mass erosion threshold. More importantly, lower packing density yields an increasing pore water dissipation rate. As a result, the character of erosion may change from undrained mass erosion to drained surface erosion. This illustrates that biological and physico-chemical effects may not only influence erosion properties of a particular erosion mode, but also its occurrence.

Furthermore, confusion arises on the occurrence of mass erosion, which is often only related to the erosion of lumps of material from an irregular sediment bed. However, the current study defines mass erosion as an undrained process, whereas the erosion of lumps of material in nature may also result from a drained process. This implies the occurrence of an intermediate erosion mode (between surface and mass erosion). The drained removal of lumps of material may e.g. result from the presence of burrows or cracks in the upper layer of the sediment bed. Burrows are generated by biota, for example the lugworm *Arenicola Marina* (Figure 115(a)). Cracks may be generated by plant roots or drying clay (Figure 115(b)).



Figure 115. Example of bioturbation showing *Arenicola Marina* (white oval) burrows (a, vertical scale ~ 10 cm). In (b) a sediment bed consisting of dried clay is shown (horizontal scale ~ 1 m).

As a result of these burrows or cracks, pore water pressure gradients dissipate at larger depth than at the surface erosion depth (Eq. (3.32)). This may result in the erosion of lumps of material for flow-induced stresses which do not exceed the undrained shear strength. This drained failure shows similarities with surface erosion, although observations of an irregular bed surface may suggest the occurrence of mass erosion. This intermediate erosion mode is difficult to predict, as it depends e.g. on the scale and number of burrows or cracks.

An example of this intermediate mode was observed during the straight flume test. Irregular erosion patterns generated by the development of both longitudinal and radial cracks were observed for soils with a dominant clay-water matrix (Figure 59). Although the erosion of lumps of material suggested mass erosion, flow-induced

stresses were too low to exceed the undrained shear strength. Therefore, the erosion of lumps of material was attributed to artefacts of the experimental procedure rather than to true mass erosion. Also during the annular flume tests a locally irregular bed surface was observed (Figure 90(b), Section 6.3.2).

It is expected that mass erosion does not occur frequently in estuaries and tidal lagoons, as the flow-induced stresses in these systems are generally lower than the undrained shear strength of sand-mud mixtures, especially on intertidal flats. Larger flow-induced stresses may occur in tidal channels, but these generally exhibit loosely packed well-sorted granular sediment beds (Le Hir *et al.*, 2007a) which exhibit relatively low undrained shear strengths. Intertidal sediment beds at larger strengths only occur when an overlying layer of sediment is eroded (e.g. due to a shifting channel) and a (strongly) consolidated layer emerges.

In conclusion, true mass erosion is presumably not an important morphological process in estuaries and tidal lagoons. It is anticipated that the observed erosion of lumps of material in these systems is often a drained process, rather than the undrained process of true mass erosion. Finally, it is noted that mass erosion is difficult to study both *in-situ* and for laboratory conditions, especially in a quantitative way. First, rather large flow velocities are required. Second, the random character of mass erosion implies that a relatively large surface area should be studied to accurately determine mass erosion thresholds and rates. This surface area should be at least an order of magnitude larger than the typical size of the eroded lumps of material (dm's – m's).

7.4 Conclusions

The comparison of the straight and annular flume tests results as well as the successful reproduction of these experimental data support the new erosion classification and surface erosion formulation, both qualitatively and quantitatively. Floc erosion exhibits a stochastic and time-dependent character, a rather low erosion threshold, and initially large, random erosion rates. Surface erosion is characterised by time-independent character, a profound erosion threshold and the erosion of successive layers of sediment at constant rate.

The order of magnitude of observed erosion parameters can be established by substituting soil (mechanical) properties in the new surface erosion formulation. This supports the applicability of the new formulation for erosion of cohesive, granular and intermediate sediment mixtures, and forms an important alternative for the currently applied non-generic empirical erosion formulae. The successful establishment of the observed surface erosion parameters also supports the suggested important role of pore water pressure gradients as an additional retarding force for erosion, next to gravitational and/or cohesive forces.

However, reproducing observed data is hampered by a lack of a proper physical formulation for the permeability of sand-mud mixtures as a function of sediment properties. Therefore, the permeability was estimated based on preliminary experimental results and data reported in literature. As the surface erosion parameter is

rather sensitive to permeability, it is recommended to further study the permeability of sand-mud mixtures as a function of sediment properties. The sensitivity to the permeability especially accounts for sand-mud mixtures, for which the structure (and therefore the permeability) is rather sensitive to small variations of the sediment composition and packing density of the sand-silt skeleton.

The discussion of the three erosion modes for natural sediments supports that especially floc and surface erosion properties are sensitive to sedimentological, biological and physico-chemical influences. For mass erosion, it is expected that these influences affect the occurrence of this erosion mode rather than its threshold and/or rate. Floc and surface erosion are expected to be important for the morphological behaviour of estuaries and tidal lagoons, whereas mass erosion is only expected for rather particular, infrequently occurring conditions (e.g. episodic events). Furthermore, it is recommended to further study the relation between erosion, on the one hand, and transport processes (e.g. bed load transport) and deposition, on the other.

Chapter 8

In-situ sediment measuring techniques

In-situ sediment characterisation techniques are required to link micro/meso scale sediment properties to macro/mega scale processes. Sediment characteristics are usually obtained by core collection and subsequent laboratory analyses. Therefore, measuring campaigns covering the spatial and temporal variability of intertidal flats are time-consuming and expensive, which interferes with the increasing need for field data of a high spatial and temporal resolution. Besides, the extraction and transportation of sediment cores generates significant disturbances of the internal structure, and air-exposure negatively affects biological activity (Mitchell and Santamarina, 2005).

Available *in-situ* techniques to characterise sediments and/or their soil mechanical or erosion behaviour generally lack proper physical backgrounds. Quite different instruments are applied to determine poorly defined parameters (e.g. bed stability, erosion threshold or sediment strength). As a result, data obtained by different *in-situ* techniques exhibit highly varying results. This hampers the quantitative comparison of data obtained by different measuring techniques at different institutes.

Therefore, two new *in-situ* techniques are developed to measure properties and soil mechanical parameters of intertidal sediments. The Medusa RhoC device measures *in-situ* the density and sand/ mud content of intertidal sediments. From these data the plasticity index and the amount of organic matter can be derived using sedimentological interactions. The Hydraulic Permeability and Strength (HPS) probe determines the *in-situ* undrained shear strength and permeability, which are input parameters for the new erosion formulation. The Medusa RhoC and the HPS probe have been discussed in Jacobs *et al.* (2009) and Jacobs and van Kesteren (2009), respectively.

8.1 Medusa RhoC: in-situ sediment characterisation

8.1.1 Introduction

Alternative methods for *in-situ* sediment characterisation are currently under development. Remote sensing (using aircraft or satellites) uses the amount of backscatter of transmitted radar, laser or acoustic pulses. However, these techniques only characterise the composition of the surface layer of sediment beds (e.g. Eleveld,

1999; Van der Wal *et al.*, 2005), whereas also the vertical distribution of sediment properties is important to study (morphological) processes. Recently, radiometric sedimentology is applied to characterises sediment components using the concentration of natural γ -rays emitting radionuclides. The relation between the concentration of radioactive isotopes and the sediment composition forms the radiometric fingerprint. Sediments with a different fingerprint can be radiometrically distinguished, which enables the characterisation of the sediment composition (De Meijer, 1995; Gouleau, *et al.* 2000; Herman, *et al.* 2001).

An existing measuring system based on radiometric sedimentology is the Medusa system (Koomans, 2001; Roberti, 2001; De Groot *et al.*, 2002; Van Wijngaarden *et al.*, 2002a,b). Medusa is the acronym for Multi Detector system for Underwater Sediment Activity. This system is towed behind a ship and weighs about 30 kg. It consists of a γ -ray detector to measure the energy of natural γ -rays, which are subsequently translated into a depth-averaged sediment composition. The depth at which the composition is determined increases with decreasing density. Besides the depth-averaged sediment composition, also the degree of packing is required to characterise sediment behaviour.

A new handheld (about 8 kg) version of the Medusa system was deployed: the ‘Medusa RhoC’ system (Figure 116). ‘Rho’ refers to density and C [$\text{Bq}\cdot\text{kg}^{-1}$] to the activity concentration of decaying isotopes per unit mass of sediment. The system determines the depth-averaged sediment composition and vertical profiles of the bulk density (ρ_{bulk} [$\text{kg}\cdot\text{m}^{-3}$]) and the water content (W [%]) of the upper 15 - 20 cm of the sediment bed. The individual components of the system are calibrated for laboratory conditions (Tijss, 2007). However, the calibration of the complete system, the practical field applicability for intertidal flats, the accuracy and operating speed of the instrument in relation to traditional methods remain to be examined.

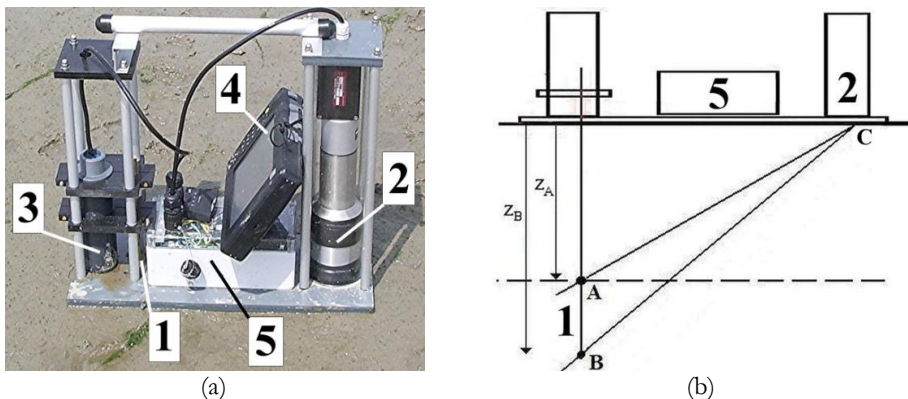


Figure 116. Photograph (a) and schematic depiction (b) of the Medusa RhoC system, showing the ^{22}Na source (1), γ -ray detector (2), TDR sensor (3), notebook (4) and data logger, GPS and power supply (5). The right panel indicates varying positions of the ^{22}Na source below the surface of the sediment bed (z_A and z_B) in relation to the position of the γ -ray detector ('C'). 'AC' and 'BC' reflect different path lengths over which ρ_{bulk} is measured. The TDR sensor and ^{22}Na source are jointly moved up and downward.

The potential and limitations of the new instrument are discussed. First, the accuracy of the Medusa RhoC data is assessed concerning sediment composition and ρ_{bulk} by using data of an extensive field campaign. Data are compared with results of traditional laboratory analyses and with results obtained by RhoC in a laboratory set up. Next, the practical applicability of the new instrument is assessed concerning the duration of the measurement procedure in relation to traditional methods. Finally, the existence of published sedimentological interactions is checked. The combination of these relations with data obtained by RhoC can significantly increase its applicability. A selection of field and laboratory data is presented; the complete data set is presented in Eelkema (2008).

8.1.2 Medusa RhoC: theory and methods

The amount of radioactive material is an indicator for the sediment composition, as natural fine sediments contain specific mixtures of radioactive isotopes (^{40}K , ^{232}Th and ^{238}U , e.g. Van der Graaf *et al.*, 2007). These isotopes especially adhere to fines. The sediment fingerprint is the relation between C and the grain size distribution. Fingerprints are site specific, as the clay fraction in a marine system exhibits a specific mineralogical composition and, therefore, a specific amount of adhered isotopes (Venema and De Meijer, 2001). This amount is more or less constant in a marine system, though may slightly vary due to a combined marine and fluvial input of fines. This implies that the required number of fingerprints to calibrate natural radiation depends on the size of the study area.

The energy of γ -rays (E_γ [eV]) is directly and uniquely related to the isotope by which it was released. γ -radiation interacts with atoms when penetrating a medium (Koomans, 2001). These interactions result in an attenuation of E_γ ; the degree of attenuation depends on the number of atoms per unit volume and on the distance travelled through a medium (e.g. Hussein, 2003a,b). When path length and attenuation coefficient are constant, the attenuation of γ -radiation solely depends on bulk density. This illustrates the applicability of γ -radiation for the determination of soil density.

The Medusa RhoC instrument holds a γ -ray detector (Caesium Iodine scintillation crystal and photomultiplier), a γ -ray source (^{22}Na), a Time Domain Reflectometry (TDR) sensor, a GPS, a power supply (12V battery) and a data logger (Figure 116). The dimensions of the system are 20 x 50 x 50 cm, for the width, length and height, respectively. The system is (wireless) connected to a notebook and can non-stop be operated for 8 - 10 hours. A small radioactive ^{22}Na source was placed in the tip of a brass rod with a diameter of 1 cm and a length of 20 cm. This rod is pushed into the sediment bed before starting a measurement. The attenuation of E_γ between the ^{22}Na source and the detector is related to ρ_{bulk} . The vertical position of the rod is automatically recorded.

The ^{22}Na source releases γ -rays with an energy level comparable to the natural radioactivity of sediments. Special permits to operate and transport the instrument are not required. The TDR sensor derives the dielectric constant of a soil from the travel time of an electromagnetic wave, which propagates along two metallic rods. This constant relates to W only, as it is independent of ρ_{bulk} , temperature, salinity or mineral

composition (Tijss, 2007). The TDR sensor and ^{22}Na source are jointly inserted in the sediment bed. The detector translates the energy of γ -rays released by natural isotopes and by the ^{22}Na source into C . Tijss (2007) and Eelkema (2008) give a comprehensive description of both procedures. The comparison of C with a previously determined radiometric fingerprint of a representative number of soil samples generates the sediment composition (ξ_{sa} and ξ_{mu}), which is discussed in Section 8.1.3.

The energy spectrum of ^{22}Na can easily be distinguished from natural isotopes (Tijss 2007). The bulk activity concentration (C_{bulk} [$\text{Bq}\cdot\text{kg}^{-1}$]) for known path length follows from this energy spectrum. However, not only solids but also water attenuates $E\gamma$. Therefore, C_{bulk} is corrected for the presence of water. W is measured by the TDR sensor. It is noted that both ρ_{bulk} and the sediment composition have to be corrected for W , as pore water attenuates γ -rays released by the ^{22}Na source and sediments.

Different vertical positions of the ^{22}Na source generate different path lengths between source and detector. Radiation intensity decreases with the inverse of the squared path length. When vertically varying the position of the source directly below the detector, the range of detected radiation intensity was too large to derive ρ_{bulk} accurately. Therefore, the position of the source was varied along a vertical axis at 40 cm from the detector (Figure 116(b)). This significantly reduced the variation of the path length and, therefore, the variation of radiation intensity between source and detector. The average densities along the trajectories ‘AC’ and ‘BC’ (Figure 116(b)) were applied to determine ρ_{bulk} as a function of depth (see also Jacobs *et al.*, 2009).

A typical measurement starts by pushing the ^{22}Na source and TDR sensor jointly ~ 15 cm into the sediment bed. Next, the depth-averaged sediment composition is determined. The duration of this measurement is set by the duration required to distinguish between background radiation (e.g. cosmic radiation) and radiation from sediments. Simultaneously, ρ_{bulk} , W , depth and GPS coordinates were recorded. In the second phase of the measurement, the ^{22}Na source and TDR sensor were pulled upward step by step. W and ρ_{bulk} were determined for each step.

As the current study discusses the testing and calibration of Medusa RhoC, multiple sediment cores with a length of 20 cm were collected close to each measurement station. Cores were carefully extracted and transported in an icebox to avoid the disturbance of sediment properties and to minimize ongoing biological activity. C , PI , n_{sasi} , W , ρ_{bulk} , dry density (ρ_{dry} [kg m^{-3}]), S , ξ_{sa} , ξ_{si} , ξ_{cl} and ξ_{om} were subsequently determined in a laboratory using traditional methods (e.g. Head, 1980). This procedure included freezing, slicing, freeze drying, weighing and grain size analyses (using a Malvern Mastersizer 2000), and the determination of carbon contents. The above properties were determined with a similar resolution as applied for the Medusa RhoC field measurements. C and PI were determined for complete cores. PI was determined according a geotechnical standard (ASTM D4318).

C (of dry material) was measured in a laboratory under controlled circumstances, using a similar detector as mounted on Medusa RhoC. Both the detector and the soil sample were placed in a box with a 10-cm thick lead shielding to exclude background radiation during the measurement. The laboratory set up to test RhoC for controlled

circumstances consisted of a wooden box (80 x 50 x 25 cm) filled with varying mixtures of sand and silt, for both saturated and dry conditions (Eelkema, 2008).

The field site concerned four tidal flats (within a range of 15 km) in the Western Scheldt Estuary (Section 2.3.5): Molenplaat, Walsoorden, Saeftinghe and Valkenisse (listed in the upstream direction). The Saeftinghe flat is the muddiest and the Valkenisse flat the sandiest. The mineralogical composition slightly varies along the estuary, but mainly consists of illite and smectite, with smaller amounts of kaolinite and chlorite (Fontaine, 2004). Measurement stations (35 in total) were located on 5 transects ranging from predominantly sandy to muddy sediments.

8.1.3 Results and analysis

The determination of the depth-averaged sediment composition at each measuring station takes about 15 - 20 min. The variation of this duration depends on the characteristics of the sediment bed. Sandy soils contain fewer isotopes than muddy soils, which yields a slightly longer measurement duration to obtain similar degrees of accuracy. Laboratory tests indicate that ρ_{bulk} data converge to a constant value after about 35 s. Within this period W can also be accurately determined.

The total duration of a ρ_{bulk} and W measurement at one position (z) takes about 1 minute, including time required to reposition the TDR sensor and ^{22}Na source vertically. The total duration of the measurement procedure at one measuring station depends on the desired vertical resolution. The current study applies a vertical resolution of 6 – 8 measuring points (mutual distance: 2 – 3 cm), which leads to a total length of the measurement procedure of about 20 – 30 min (i.e. 15 – 20 min for the composition and 6 – 8 times 1 min for a density profile). The collection of cores and repositioning to a new measuring station took both about 15 min.

Traditional laboratory analyses (W , ρ_{bulk} , ρ_{dry} , S , ζ_{sa} , ζ_{si} , ζ_{cl} and ζ_{om}) of sediment cores collected at 35 stations (executed by one person) took about two months. The determination of a fingerprint (C and a grain size analysis) took about 1 hour per sample. In the current study we determine fingerprints for all stations to evaluate the accuracy. The TDR sensor malfunctioned during laboratory and field measurements due to hardware problems. However, the sensor is a standard device and suitable for the determination of W of intertidal sediment beds according the supplier. W derived from the laboratory analyses is applied to determine sediment composition and ρ_{bulk} .

Eelkema (2008) shows all results of the RhoC measurements concerning sediment composition and ρ_{bulk} as measured by Medusa RhoC and laboratory analyses. Comparison of the depth-averaged ζ_{mu} as a function of C of the isotopes ^{40}K , ^{232}Th and ^{238}U measured *in-situ* by RhoC, as in the laboratory for dry sediment indicates a fair representation of the fingerprints by the new Medusa RhoC. The laboratory and field fingerprints for all isotopes exhibit identical correlation coefficients ($R^2 \approx 0.94$). Only for the Valkenisse flat the correlation is less strong ($R^2 \approx 0.56$). Besides, scattering of the fingerprints for ^{238}U is relatively large compared to ^{232}Th and ^{40}K .

The relations between ζ_{mu} and C for all flats exhibit the best correlation for ^{232}Th (Eelkema, 2008). Therefore, this fingerprint is used to determine the sediment composition. Comparing the field fingerprints for ^{232}Th for all tidal flats indicates that

3 of the 4 tidal flats are statistically comparable. The fingerprint for the more upstream situated Valkenisse tidal flat deviates from the other three, exhibiting larger ξ_{mu} . The correlation for RhoC results compared to traditional laboratory analyses for the depth-averaged ξ_{mu} is good ($R^2 = 0.87$, Figure 117), which indicates that Medusa RhoC generates a fair representation of the sediment composition.

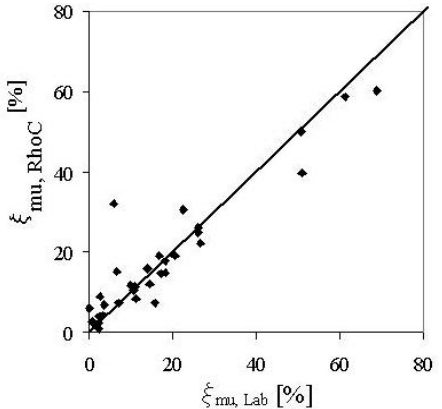


Figure 117. Comparison between data obtained by RhoC (vertical axis) and by traditional laboratory analyses (horizontal axis) for depth-averaged ξ_{mu} for all measuring stations. The continuous line represents perfect agreement. The correlation coefficient $R^2 = 0.87$.

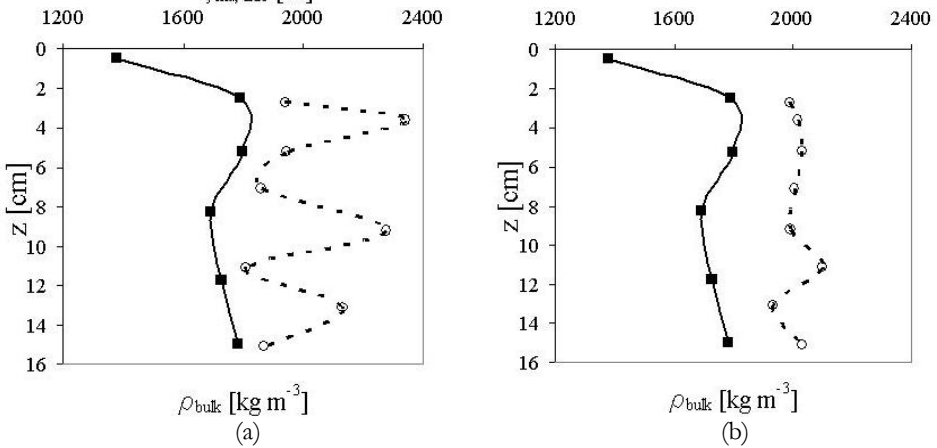


Figure 118. Typical ρ_{bulk} profiles measured with RhoC (\circ , dashed line) and traditional analyses (\blacksquare , continuous line) showing oscillations (a) and offset (b) between the data.

The minimum depth for operating the ^{22}Na source is 2.5 cm. For smaller depths, γ -rays travel not only along the diagonal line between source and detector, but also along the surface of the bed. This hampers the accurate translation of $E\gamma$ to ρ_{bulk} . Furthermore, vertical ρ_{bulk} profiles translated from the RhoC data deviate in two ways from the profiles determined with traditional analyses, which occurred for all measurements (Eelkema, 2008). First, results obtained by RhoC exhibit an oscillating character compared to the smoother laboratory profiles (Figure 118(a)). Second, RhoC results exhibit an offset with respect to laboratory profiles (Figure 118(b)).

The deviations indicate that the assessment of vertical ρ_{bulk} profiles from RhoC data is not satisfactory. A theoretical approach to understand and correct for the oscillations is proposed, as no laboratory data are available for further analysis. ρ_{bulk} measured by RhoC varies stochastically (standard deviation of about $15 \text{ kg}\cdot\text{m}^{-3}$). It has been shown theoretically that the random error of the RhoC measurement causes the oscillations (Eelkema, 2008). To minimize this effect, a three point smoothing procedure is proposed to obtain ρ_{bulk} profiles from the measurements of RhoC. For the upper and lower points of the profiles a two point interpolation is applied.

To understand the occurrence of the offset of ρ_{bulk} , the measuring procedures are carefully evaluated. It is unlikely that its cause lies in measuring (in)accuracies, sampling procedure, sample transport, storage and/or treatment. However, we found that the offset negatively correlated with the depth-averaged saturation degree S (Figure 119):

$$\Delta\rho_{bulk} = aS + b \tag{8.1}$$

with a ($= -8.2 \text{ kg}\cdot\text{m}^{-3}$) and b ($= 859 \text{ kg}\cdot\text{m}^{-3}$) as empirical coefficients. We have no physical explanation for this correlation. Moreover, the relation between the offset and S was not found for the laboratory tests (on artificially generated sand silt mixtures). Correcting ρ_{bulk} as measured by RhoC with the offset generates a good correlation ($R^2 = 0.77$) between $\rho_{bulk}(z)$ obtained by RhoC and traditional methods (Figure 120).

A homogeneous mineralogical composition in marine systems implies constant cohesive and water/organic material binding properties. Consequently, mud flocc properties are strongly related to this specific surface area, which generates specific relations between ζ_{cl} and ζ_{si} (Flemming, 2000), ζ_{cl} and ζ_{om} (Hedges and Keil, 1995; Middelburg and Herman, 2007) and ζ_{cl} and ρ_{bulk} (Flemming and Delafontaine, 2000).

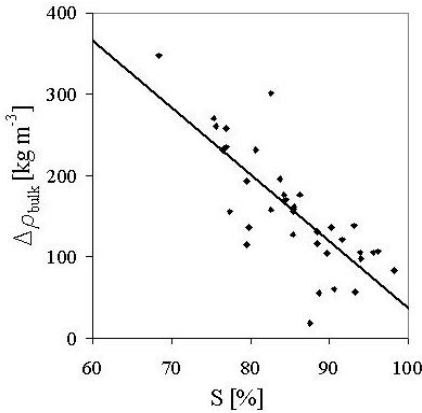


Figure 119. Depth-averaged ρ_{bulk} offset (i.e. the difference between depth-averaged ρ_{bulk} obtained by laboratory analyses and RhoC, $R^2 = 0.60$) as a function of the saturation degree S for the cores. A positive offset yields an overestimation of ρ_{bulk} by RhoC.

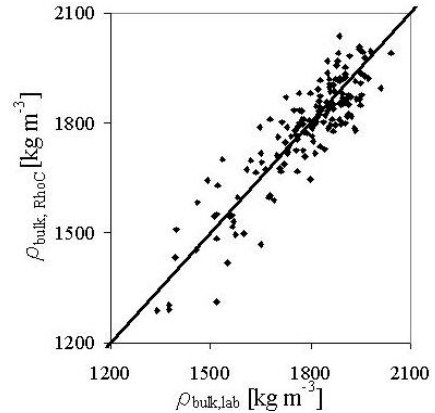


Figure 120. Comparison between $\rho_{bulk}(z)$ obtained by RhoC (vertical axis) and by traditional laboratory analyses (horizontal axis). The continuous line is the line of perfect agreement. The correlation coefficients $R^2 = 0.77$.

The third objective of the current study is to verify the existence of these sedimentological interactions for sediments ranging from predominantly muddy to sandy. Results are derived from traditional laboratory analyses of the sediment cores. Figure 121 shows strong relations between ζ_{cl} and ζ_{si} (a), as well as between ζ_{om} and ζ_{mu} (b). For soil samples for which $\zeta_{mu} > 25\%$, ρ_{bulk} decreases with increasing ζ_{mu} (Figure 121(c)). For granular samples ($\zeta_{mu} < 25\%$) the scatter is significantly larger. Finally, PI is determined for a representative number of soil samples (Figure 121 (d)). Differences in clay mineralogy and ζ_{om} are not incorporated. The slope (≈ 6) indicates the activity of the clay fraction.

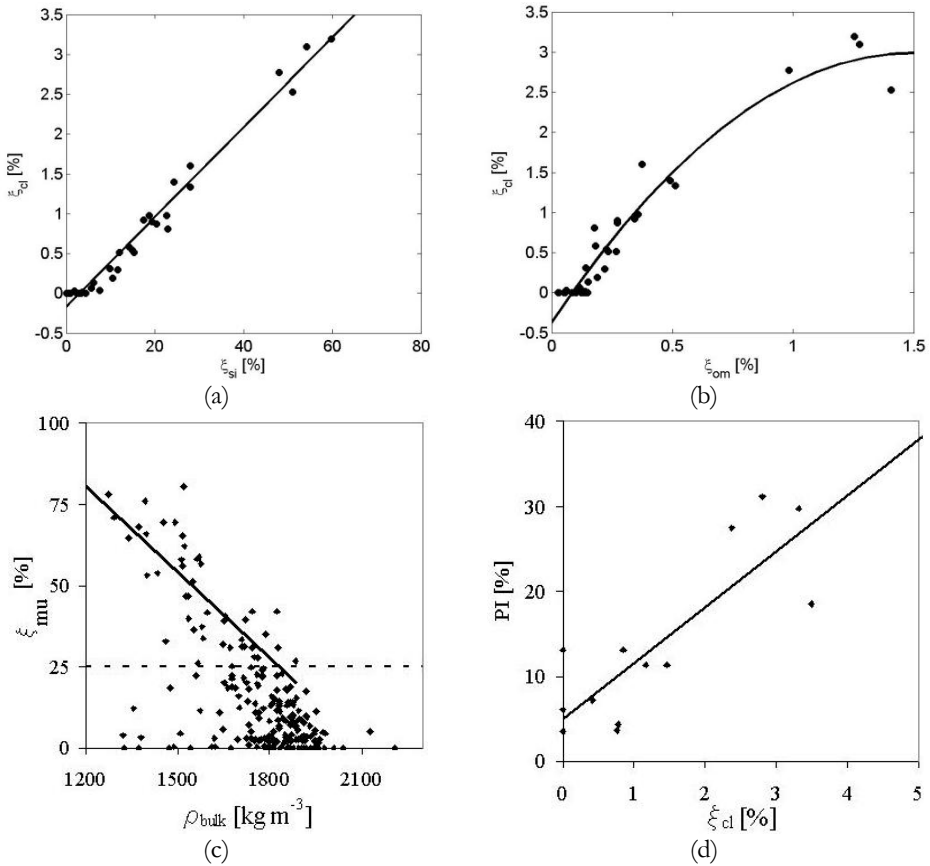


Figure 121. Relations between depth-averaged ζ_{si} and ζ_{cl} (a), ζ_{mu} and ζ_{om} (b), ρ_{bulk} and ζ_{mu} (c) and PI and ζ_{cl} (d) following traditional laboratory analyses of the sediment cores collected in the field. Correlation coefficients R^2 are 0.85, 0.91, 0.62 (for $\zeta_{mu} > 25\%$) for (a), (b), (c) and (d), respectively.

8.1.4 Discussion

The good agreement between the laboratory and field fingerprints using RhoC indicates that the depth-averaged sediment composition is accurately predicted by the Medusa RhoC system. Koomans (2001) and Van Wijngaarden *et al.* (2002a,b) report similar results. The proposed methods for smoothing and correcting for the offset (i.e. overestimation of $\rho_{bulk}(z)$ by RhoC) existing for partly saturated soils generates good results. However, the exact cause of the offset is not yet understood.

Fingerprints of different tidal flats vary slightly, most likely due to variations in the clay mineralogy. Fontaine (2004) shows this variation for the Western Scheldt Estuary. However, variations in clay mineralogy are too small to explain the markedly different fingerprint for the Valkenisse flat. It is assumed that the more sandy character of this flat, in combination with the fact that isotopes especially adhere to fines, generates a larger sensitivity to errors for the determination of ξ_{cl} for sandy soils. The relatively high level of scattering for ^{238}U is likely to be caused by the presence of feldspar (Koomans, 2001).

The good agreement between the laboratory and field fingerprints further indicates that the detected natural radioactivity is representative for the upper 15 cm of the sediment bed. Van Wijngaarden *et al.* (2002a) used soil samples obtained from a layer with a similar thickness to determine fingerprints (20 cm). The relation between ρ_{bulk} and the actual depth for which the sediment composition is measured is not studied. This depth decreases with increasing ρ_{bulk} , which may influence results of RhoC if the sediment composition at depths below 10 cm significantly varies.

The practical usage of Medusa RhoC in the field is good; the instrument is easily operated and transportable by a single person. The practical applicability of the system is further assessed by comparing the typical measurement durations of the new instrument and traditional laboratory analyses. Both procedures are compared concerning the duration of a field measurement, core collection and laboratory analyses. The duration of a measurement using RhoC (determination of depth-averaged sediment composition and vertical profiles of ρ_{bulk} , ρ_{dry} , W and S) without repositioning is 30 min.

Results show that a single fingerprint is sufficient to calibrate measurements on one tidal flat, whereas for the study of multiple flats multiple fingerprints are required (Eelkema, 2008). De Meijer (1995) and Van Wijngaarden (2002b) argue that 3 – 4 soil samples with varying ξ_{mu} are required to determine a representative fingerprint for a single flat. Roberti (2001) collected 20 - 30 soil samples to determine representative fingerprints for the Haringvliet Estuary in the Netherlands. It is concluded that 5 – 10 fingerprints are required to account for varying clay mineralogy on estuary scale.

The collection of calibration cores takes about 15 min per measurement station. The subsequent laboratory analyses to obtain similar parameters as with RhoC require about 4.5 hrs per sample. This duration follows from the total analysis procedure of 2 months divided by 35 soil samples, minus the time needed to determine (vertical profiles of) ξ_{om} , ξ_{cl} and ξ_{si} (these three parameters are not determined by RhoC). Formulations describing the duration of the traditional (T_{trad} [hrs]) and Medusa RhoC (T_{RhoC} [hrs]) measurement procedure yield:

$$T_{trad} = (0.25 + 4.5)x = 4.75x \quad (8.2)$$

$$T_{RhoC} = 0.5x + 3y \quad (8.3)$$

where x [-] is the number of measuring stations and y [-] the number of locations (e.g. tidal flats) for which a fingerprint is required (3 samples, 1 hr each). Comparison of Eq. (8.2) and (8.3) in Figure 122 shows that on estuary scale (8 – 16 fingerprints) the new instrument is significantly more time-effective for 10 or more measuring stations. For e.g. tidal flats this number is even lower.

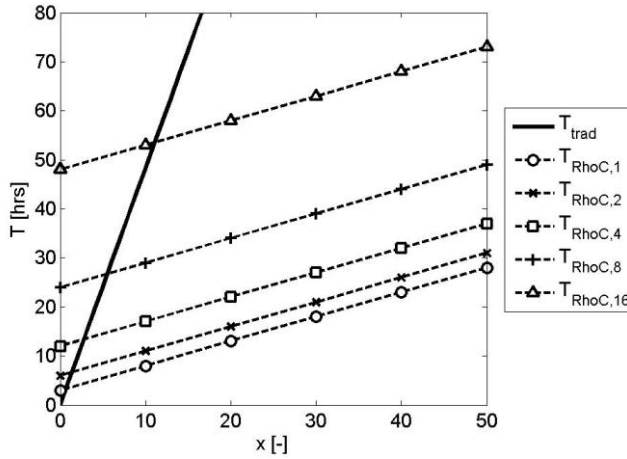


Figure 122. Comparison of measurement durations (T [hrs]) for traditional methods (T_{trad} [hrs]) and Medusa RhoC (T_{RhoC} [hrs]) as a function of the number of measuring stations (x [-]), with a vertical resolution of 6 - 8 measuring points. $T_{RhoC,i}$ refers to the required number of fingerprints, depending on the observed parts of a marine system (additional 3 hrs for each required fingerprint).

The availability of a large sedimentological data set enables the evaluation of sedimentological interactions reported in literature. The combination of these relations with data obtained by Medusa RhoC (or by traditional analyses) enables a relatively simple and fast derivation of additional sedimentological parameters. Data exhibit similar relations as reported in literature between ζ_{cl} and ζ_{si} (Flemming, 2000), ζ_{cl} and ζ_{om} (e.g. Herman *et al.*, 2001), ρ_{bulk} and ζ_{mu} (Flemming and Delafontaine, 2000) and ζ_{cl} and PI (e.g. Mitchell, 1976). The scatter of the relation is attributed to the little studied and sometimes contradicting effect of ζ_{om} on PI (Odell *et al.*, 1960; Malkawi *et al.*, 1999). The relation between ζ_{mu} and ρ_{bulk} follows from an increasing volume fraction of mud with increasing ζ_{mu} and, due to water binding capacity of mud, larger W and lower ρ_{bulk} .

The specific ratios of the four relations depend on the cohesive properties of the clay fraction and, therefore, on the existing clay mineralogy. These specific ratios are highly sensitive to the method applied to determine the grain size distribution. Variations up to 100% can occur for ζ_{cl} when applying different analyses methods

(Section 4.1.2, Appendix I). The existence of these relations significantly increases the number of parameters which can be derived from the RhoC data and saves a significant amount of time as the analyses (plus core collection) to obtain these additional parameters require an extra 2 – 3 hours per soil sample. These additional data are especially useful for the study of biological activity and mechanical behaviour of intertidal sediment beds, which relate to ζ_{om} (e.g. Widdows and Brinsley, 2002) and PI (e.g. Schofield and Wroth, 1968), respectively.

8.1.5 Conclusions and recommendations

The new Medusa RhoC instrument combines an existing technique to determine depth-averaged sediment composition with a new technique to measure vertical profiles of the bulk density for depths ranging between 2.5 – 20 cm. The instrument is calibrated and its applicability concerning field usage and duration of the measurement procedure is assessed. The depth-averaged sediment composition is well represented for intertidal sediment beds. A single fingerprint is sufficient for individual tidal flats. Varying calibration fingerprints are required to determine a system-wide sediment composition, as the clay mineralogy within marine systems may vary.

Vertical bulk density profiles show a structural overestimation as well as an oscillating character compared to the profiles determined by traditional laboratory analyses of sediment cores. The cause of the offset is not understood, although a relation exists with the degree of saturation. Correcting the results with this relation as well as with a smoothing procedure generates a good correlation between bulk density profiles of RhoC and of the sediment cores. Oscillations result from random measurement errors and from the applied algorithm to determine vertical bulk density profiles. An alternative method with multiple ρ_{bulk} readings at constant z is proposed, which results in smoother ρ_{bulk} profiles and a better agreement with laboratory profiles.

In conclusion, the Medusa RhoC instrument is a useful and practical tool to map sediment properties significantly faster and more cost effective than traditional methods. Furthermore, the combination of four confirmed sedimentological interactions with data obtained by RhoC further enhances the applicability of the new instrument, e.g. to study biological or morphological processes within the bed.

It is recommended to further analyze the offset in the density measurements in relation to the saturation degree, e.g. by considering the effect of partly saturated (natural) mud for controlled laboratory conditions. Second, it is recommended to study possibilities to measure bulk density in the upper 2.5 cm of the sediment bed, as this is the most active layer concerning morphological and biological processes. Furthermore, the accuracy of data following from the application of the sedimentological interactions to the Medusa RhoC data can be improved by coupling the depth-averaged sediment composition to vertical density profiles. This provides information on the specific thickness of the upper layer of the bed from which natural activity is recorded by the detector. Finally, the TDR sensor should be repaired and its working should be verified for field conditions.

8.2 Hydraulic Permeability and Strength (HPS) probe

8.2.1 Introduction

An often applied *in-situ* technique to characterise erosion of intertidal sediments is the Cohesive Strength Meter (CSM, Tolhurst *et al.*, 1999). However, Widdows *et al.* (2007) conclude that it is not possible to compare erosion properties obtained by erosion flumes on the one hand, and a CSM device on the other. Differences are mainly attributed to the applied forcing by a CSM, which does not induce shear flows. The CSM induces erosion by applying a downward directed vertical jet within a small water-filled chamber (Figure 123). This forcing is similar to the forcing in the EROMES device (e.g. Tolhurst *et al.*, 2000b), which is a laboratory erosion device applying a propeller generating a vertical jet. Both devices define τ_e as the water pressure at which the concentration of fines significantly increases.

The CSM device is applied to determine τ_e of artificially generated sand-mud mixtures (similar as applied in Chapter 4). Figure 124 shows that τ_e derived from CSM measurements is rather large (kPa's) compared to τ_e (Pa's) presented in Chapters 5 and 6 (see also Figure 103). Furthermore, a transition in the behaviour of τ_e exists for $W_{rel} = 5 - 7$, similarly as for c_u at the transition from a sand-silt skeleton to a clay-water matrix (Section 4.2). Both the transition and large strengths indicate that the CSM reflects c_u rather than τ_e . This implies that the CSM simulates a shear failure mechanism (e.g. following Prandtl, Figure 35) and, subsequently, undrained mass erosion, rather than drained surface erosion. Besides, the constant strength for sandy soils ($W_{rel} > 5 - 7$) indicates that it is difficult to obtain accurate thresholds for sandy soils. This is attributed to the different ways sand and mud particles behave upon being suspended. In conclusion, the CSM device cannot be applied to determine the threshold for surface erosion.

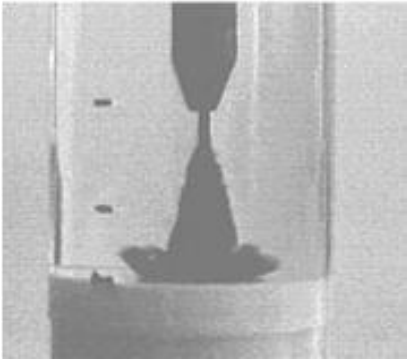


Figure 123. Visualization of the jet applied to the surface of a sediment bed in a CSM erosion device (Tolhurst *et al.*, 1999).

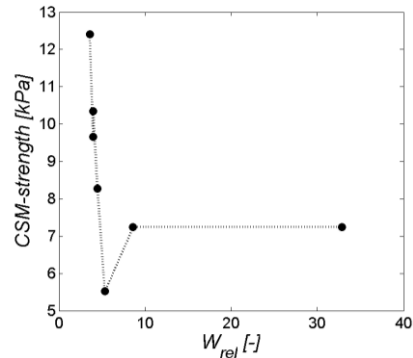


Figure 124. CSM data for artificially generated sand-silt-kaolinite samples (similar to the sediment mixtures applied in Chapter 4).

The example of the CSM demonstrates the difficulty concerning the *in-situ* simulation of natural flow conditions, which is required to derive erosion properties. However, this thesis shows that erosion behaviour relates to bulk soil mechanical parameters, which provides an alternative, indirect method to determine erosion properties. These bulk soil mechanical parameters concern the undrained shear strength c_u [Pa] and the coefficient of pore water dissipation c_v [$\text{m}^2 \cdot \text{s}^{-1}$], which is a function of permeability k_v [$\text{m} \cdot \text{s}^{-1}$] and compressibility m_v [$\text{m}^2 \cdot \text{N}^{-1}$]. As m_v can be derived from c_u , soil mechanical behaviour can be derived for known c_u and k_v . Both properties are individually determined, but by applying the shear modulus G [GPa] it is possible to check the measured c_u and k_v .

The Hydraulic Strength and Permeability (HPS) probe is based on a geotechnical theory of cavity and crack formation in soils. These cavities or cracks are induced by increasing pore water pressure gradients. The HPS determines c_u , k_v and G *in-situ*. This theory is based on Vesic (1972); see also Van Kessel (1998a,b) and Winterwerp and van Kesteren (2004). A laboratory version of the HPS probe is developed at Deltares. However, only some preliminary test results are available. A field version of the HPS probe was recently developed to determine c_u , k_v and G within the upper ~ 15 cm of sand-mud beds. Some preliminary tests were executed on tidal flats in the Western Scheldt Estuary. However, important steps have to be undertaken to enable the derivation of useful data, which was not possible at the time of writing this thesis.

The general objective of the current study is to derive bulk material properties from HPS data. More specifically, the objectives are to (1) elaborate the theory of the measuring principle, (2) determine a measurement protocol, (3) study the sensitivity of the measurement procedure and (4) calibrate the device under laboratory conditions.

8.2.2 Theory of elasto-plastic cavity growth

The HPS probe measures the water pressure while injecting small amounts of water at constant flow rate Q [$\text{m}^3 \cdot \text{s}^{-1}$] into a sediment bed at depth z below the bed surface through a thin needle with radius R_0 (Figure 125). The initial cavity radius is assumed to equal the needle radius. The initial cavity-volume is then given by:

$$V_0 = \frac{4}{3} \pi R_0^3 \quad (8.4)$$

When injecting water, the initial cavity is assumed to grow spherically. The pressure inside the cavity is a function of the cavity deformation, which may be an elastic or elasto-plastic process (Figure 126). For undrained conditions and elastic behaviour the pressure follows from (Vesic, 1972):

$$p = p_0 + \frac{4}{3} G \left(1 - \frac{V_0}{V} \right) \text{ for } V < V_p \quad (8.5)$$

and for elasto-plastic behaviour:

$$p = p_0 + \frac{4}{3} G \left(1 + \ln \left\{ \frac{G}{c_u} \left(1 - \frac{V_0}{V} \right) \right\} \right) \text{ for } V > V_p \quad (8.6)$$

in which G [Pa] is the shear modulus of a soil (i.e. the ratio between shear stress and shear strain), V_0 [m³] the initial cavity volume at the tip of the HPS injection needle following from Eq. (8.4), V [m³] the actual cavity volume ($= Q \cdot t$), and V_p [m³] the cavity volume at which plastic yielding of the cavity wall starts.

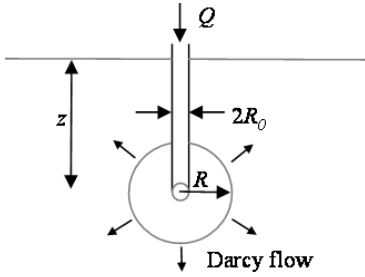


Figure 125. Schematic diagram of the injection of water into a sediment bed. R_0 and R reflect the initial and actual cavity radius, respectively.

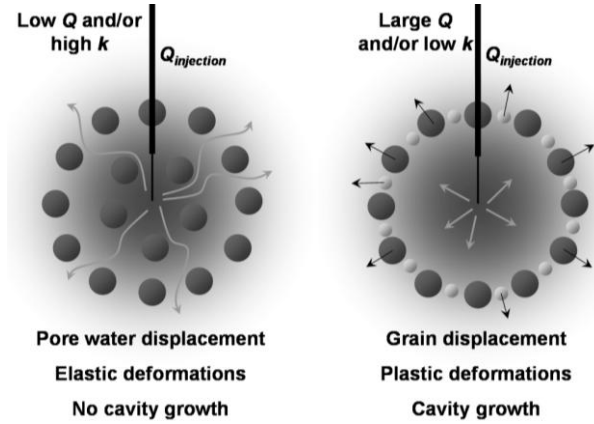


Figure 126. Schematic depiction of elastic (left figure, with Darcy flow indicated by the arrows) and elasto-plastic soil behaviour (right figure, with cavity growth indicated by the arrows) resulting from injection ($Q_{injection}$) of water through a needle (black vertical line) in a sediment bed (plotted after Winterwerp and Van Kesteren, 2004).

The isotropic pressure at depth z (p_0 [Pa]) yields:

$$p_0 = (\rho_{bulk} - \rho_w)gz \frac{2K_0 + 1}{3} \quad (8.7)$$

in which ρ_{bulk} [kg·m⁻³] is the bulk soil density, ρ_w [kg·m⁻³] the density of water, and K_0 [-] the ratio of horizontal and vertical stresses during self-weight consolidation. K_0 varies between 0.5 for fresh deposits and 1.0 for well-consolidated deposits.

It is important to realize that the isotropic soil pressure p_0 is the effective soil pressure corrected for the hydrostatic pressure. The pressure p_p [Pa] in the cavity upon plastic failure of the cavity wall yields:

$$p_p = p_0 + \frac{4}{3}c_u \quad (8.8)$$

When the cavity volume V grows to infinity, Eq. (8.5) and (8.6) predict the maximum pressure for elastic and elasto-plastic deformations, respectively. The pressure-volume relation for both types of deformations is shown in Figure 127 for $G/c_u = 100$. It is shown that only for small ΔV ($V \approx V_0$), the soil depicts an elastic response (i.e. for $p_p - p_0 < 4/3c_u$).

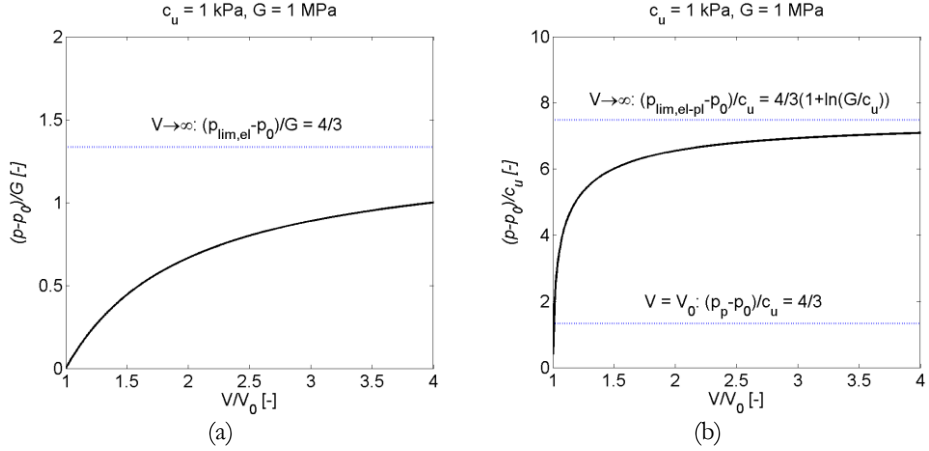


Figure 127. Schematic diagrams illustrating Eq. (8.5) (a) and Eq. (8.6) (b). Two important regions are distinguished in (b): elastic (el) soil behaviour with Darcy pore water flow for $(p - p_0)/c_u < 4/3$ and elasto-plastic (el-pl) soil behavior with zero Darcy pore water flow for $4/3 < (p - p_0)/c_u < 4/3[1 + \ln(G/c_u)]$.

Next to the undrained growth of the cavity, injected water can also generate a Darcy flow through a soil. For a radial flow at a certain cavity volume V with radius R , the drainage rate Q_d is given by Darcy's law:

$$Q_d = p \frac{4\pi kR}{\rho_w g} \text{ with } R = \left(\frac{3}{4\pi} V\right)^{\frac{1}{3}} \quad (8.9)$$

in which p [Pa] is the cavity pressure (relative to the pressure at infinite distance from the cavity). The cavity volume change during Darcy flow is described by a volume balance:

$$\frac{dV}{dt} = Q - Q_d = Q - p \frac{4\pi kR}{\rho_w g} \quad (8.10)$$

in which Q [$\text{m}^3 \cdot \text{s}^{-1}$] is the constant flow injected by the HPS probe.

The discharge through the needle is stopped when after a certain time, Q in Eq. (8.10) becomes zero and relaxation occurs. The pressure in the cavity drops and a radial Darcy flow through the soil towards the needle tip is generated. This flow can be considered as an elastic rebound; its governing differential equation can be obtained by substituting Eq. (8.5) and $R = R_0(V/V_0)^{1/3}$ in Eq. (8.10), and by eliminating Q :

$$\frac{dV}{dt} = -\frac{4\pi kR}{\rho_w g} \left[p_0 + \frac{4}{3} G \left(1 - \frac{V_0}{V} \right) \right] \left(\frac{V_0}{V} \right)^{\frac{1}{3}} \quad (8.11)$$

It is important to realize that cavities can only be generated in soils with relatively low k . For larger k no elasto-plastic deformations or pore water pressure gradients are generated, and no undrained soil behaviour occurs, as injected water directly flows through the sediment skeleton. This indicates that G and c_u can not be determined for relatively sandy soils with large k using the above formulations. An alternative method to determine k for sandy soils is presented below.

G can be determined in the elastic region of cavity growth by combining dV/dt at $t = 0$, for which $V = V_0$, $p = p_0$ and $R = R_0(V/V_0)^{1/3}$, and dp/dt derived from Eq. (8.5):

$$\left(\frac{dp}{dt} = \frac{4}{3} \frac{GV_0}{V^2} \frac{dV}{dt} \right)_{t=0} \xrightarrow{t=0} \frac{dp}{dt} = \frac{4}{3} \left(Q - \frac{4\pi k R_0 p_0}{\rho_w g} \right) \frac{G}{V_0} \quad (8.12)$$

By measuring dp/dt at $t = 0$ for multiple discharges (Figure 128), the shear modulus G can be determined from the slope of dp/dt as a function of Q (Figure 129). The maximum pressure should not exceed the pressure at which plastic failure of the cavity wall (Eq. (8.8) occurs. As dp/dt at $t = 0$ is applied to determine G , the elastic cavity growth is assumed zero and a Darcy flow is generated.

k follows from relaxation tests after each injection to determine G (Figure 128). During injections at which only elastic deformations occur, the cavity volume at the time of relaxation V_r [m³] can be assumed equal to V_0 . k then follows from Eq. (8.12), for $Q = 0$.

$$\frac{dp}{dt} = -\frac{16\pi k G R_0 p_0}{3 \rho_w g V_0} \Rightarrow k = \frac{3 \rho_w g V_0 \Delta p / \Delta t}{16\pi G R_0 p_0} \quad (8.13)$$

with $\Delta p / \Delta t$ following from the t - p relation, shown in Figure 128. It is important to note that k only follows from Eq. (8.13) for relaxation at constant p .

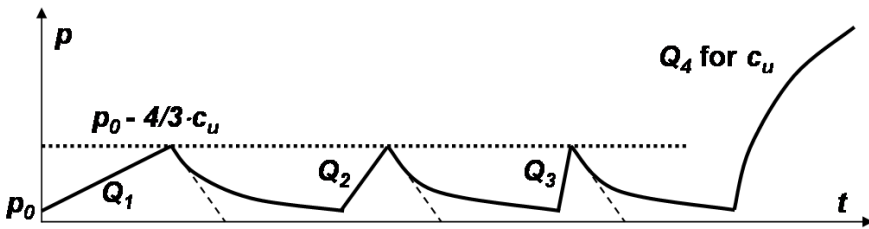


Figure 128. Experimental procedure to establish c_u , k_v and G with the HPS probe. dp/dt for multiple Q in the elastic region during injection and (subsequent) relaxation enables the determination of G and k , respectively.

Note that to determine p_0 (Eq. (8.8)) the unknown K_0 is required. K_0 can only be established in the laboratory with triaxial or Oedometer tests. However, the error in p_0 (hence in k) is maximal $\pm 15\%$ if one sets $K_0 = 0.75$. This error is small compared to

the error in k , which can vary easily by orders of magnitude. Furthermore, V_0 increases during the three consecutive relaxation-cycles as V_r does not return to the original V_0 . This results from (1), the slight increase of V_0 due to the elastic growth of the cavity, and from (2), the required long measurement time to enable relaxation of p to p_0 . To increase the accuracy of this method to determine k , it is possible to adjust V_r with the changed V_0 by recording the inserted Q (increase of V) in combination with dp/dt (decrease of V).

Alternatively, k can be determined for known G from the ordinate in Figure 129. Although the accuracy of this method can be poor due to the small value of the ordinate, this k can be compared with k from Eq. (8.13) to compare both procedures. Note that with this method, k cannot be determined for sandy soils (with relatively large k) due to the absence of elastic rebound. A Darcy flow is generated upon the injection of water, during which p at the needle tip is constant as p equals the pressure required to overcome friction of the grain skeleton. As no cavity is simultaneously generated, Q equals Q_D and k directly follows from Eq. (8.9).

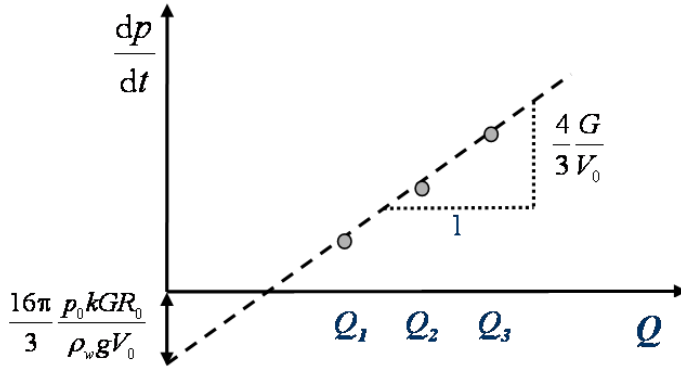


Figure 129. Determination of G (slope of Q - dp/dt relation) and k (ordinate of Q - dp/dt relation).

c_u can be obtained by a test with high Q inducing an increasing pressure following the curve sketched in Figure 128 ($p(t)$ for Q_4). At this high Q , we assume that Darcy flow is negligible and that only plastic soil deformations occur. Due to crack initiation around the needle, the maximum pressure for elasto-plastic behaviour ($p_{lim,el-pl}$) is normally not reached. However, the curvature of the pressure-volume relation is determined by c_u and G as shown in Figure 127(b).

The time-derivative of Eq. (8.6) as a function of $V^2/(V_0 - V)$ forms a straight line on log-log scale. c_u equals the slope of this relation, which indicates that c_u can be determined independently of G . However, differentiating data obtained by measurements may generate less accurate results due to possible oscillations. An alternative method to determine c_u for known G is to fit Eq. (8.6) to the measured pressure-volume relation.

Only dp/dt and not the isotropic soil pressure p_0 at depth z is required to determine c_u , k and G . An error in K_0 (and thus in p_0 , Eq. (8.8)) yields a translation of the curve only, and does not change its slope. This is convenient as K_0 (see Eq. (8.7)) is unknown. Furthermore, p_0 is the sum of the atmospheric pressure p_{atm} and the hydrostatic pressure p_{hydr} ($= \rho_w \cdot g \cdot z$, where z is the depth below the groundwater table):

$$p_0 = p_{hydr} + p_{atm} \quad (8.14)$$

p_{atm} is assumed constant during a test. However, when significant atmospheric pressure and/or temperature variations occur during the execution of a test (\sim tens of minutes), both p_0 and dp/dt are affected. This should be kept in mind when determining c_u , k and G , especially for field applications (see also Section 8.2.4).

Following the theory, a measurement procedure is proposed to determine c_u , k and G at one measuring station ('A') for constant depth. As c_u is required to know the upper limit for elastic behaviour, c_u should be determined first at another station ('B'). The horizontal distance of locations 'A' and 'B' should be minimized to ensure comparable conditions. Next, G and k are determined by applying three different Q without generating elasto-plastic behaviour. Subsequently, c_u is determined (in 'A') by applying large Q to generate elasto-plastic behaviour. Furthermore, it is possible to predict the appropriate injection Q using the expected c_u and k of the tested sediment bed. Maximum p follows from substituting c_u and $V = V_0$ in Eq. (8.6). p and k are subsequently substituted in Eq. (8.9) to determine Q at which Darcy flow is expected.

8.2.3 Description of the HPS probe

The HPS probe is mounted on a portable aluminium tripod with three 10 x 15 cm plastic plates to prevent its sinking in soft mud. The system consists of a water-filled reservoir, two pistons, an injection needle and a pressure sensor (Figure 130). A temperature sensor measures the temperature of the metal reservoir with an accuracy of 0.1°C. The needle connected to the reservoir is injected into the sediment bed. The pistons are connected to the storage chamber as well. By pushing down a piston, the pressure in the reservoir (p [Pa]) is increased and small amounts of water flow at constant rate through the needle into the bed. A pressure sensor records the pressure in the reservoir (0 - 1.7 bar) with a resolution of 0.1%.

The probe is moved vertically (max. speed is 0.96 mm·s⁻¹) to insert the injection needle into the sediment bed. The maximum insertion depth is \sim 15 cm. The steel injection needles are glued in a steel pipe with slightly larger diameter to provide more support to the flexible needles during insertion. In the current study, the needle has an inner diameter of 0.5 mm and a wall thickness of 0.1 mm. The pistons are automatically moved up and downward in two water-filled cylinders connected to the reservoir (Figure 131). The pistons are massive metal cylindrical bars which precisely fit in the cylindrical cavities. The pistons have different diameters (1 and 5 mm) to enable the generation of Q ranging from $2.7 \cdot 10^{-7}$ - $1.6 \cdot 10^{-4}$ $\mu\text{l} \cdot \text{s}^{-1}$ for piston 1, to $1.6 \cdot 10^{-4}$ - $9.6 \cdot 10^{-2}$ $\mu\text{l} \cdot \text{s}^{-1}$ for piston 2. When a piston has reached the lower end of the cylindrical cavity, it has to be lifted upward.

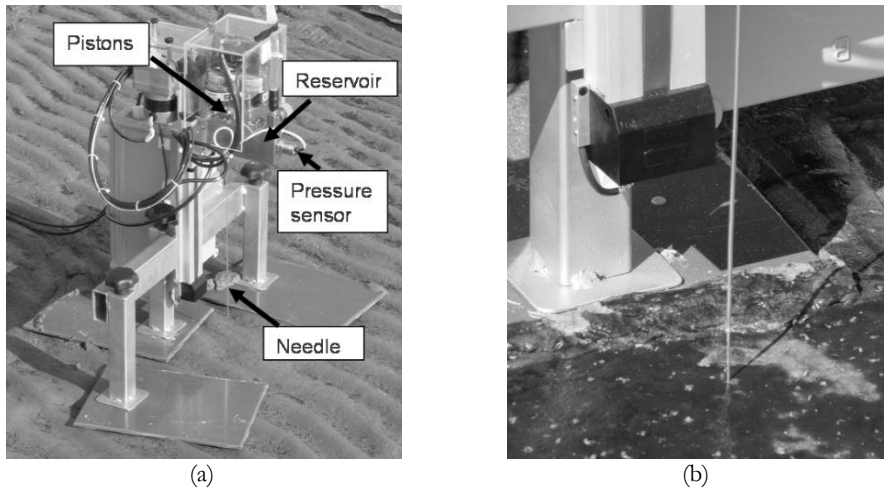


Figure 130. Photographs of the HPS (Hydraulic Permeability and Strength) probe mounted on a tripod (a) and of a detail of the needle as it is injected into the sediment bed (b).

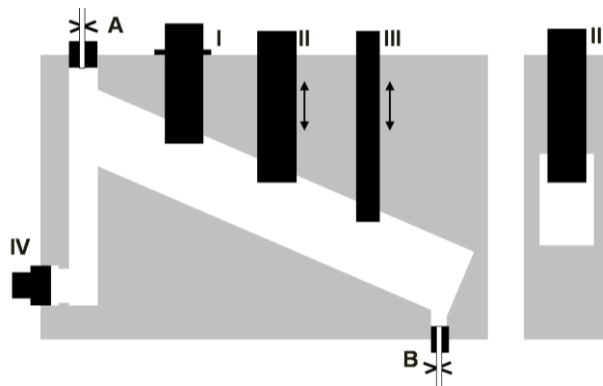


Figure 131. Detailed side views of the reservoir, with ‘A’ = valve at top reservoir, ‘B’ = valve between reservoir and needle, ‘I’ = plug at unused cavity, ‘II’ = piston / injector 1, ‘III’ = piston / injector 2, ‘IV’ = pressure sensor.

The reservoir is filled with demineralised water. Water is almost incompressible, whereas gas or water with dissolved gas can relatively easily be compressed, at small variations of p . Therefore, the entrapment of air (Figure 131) should be avoided. This requires a careful filling procedure of the system with de-aired water. Important points concerning the filling procedure are that (1) the system should be filled bottom-up in order to enable air to escape at the top of the system and to prevent the entrapment of air bubbles in the needle, and that (2) air entrapment behind the pressure sensor (at ‘IV’, see Figure 131) and along the plug in the unused cavity (‘I’) should be prevented. Filling is performed by creating (by mouth) an underpressure ($p \approx 0.9$ bar, see Figure

131) at ‘A’. A detailed description of this procedure is presented in Jacobs and Van Kesteren (2009).

The HPS probe weighs 10 kg and is transported in an aluminium box (3 kg) mounted on a metal frame (3 kg) which is carried as a backpack. The power supply of the HPS system consists of a battery (3.8 kg), which enables the operation of the system for about 10 hrs. The system is operated by a handheld water proof notebook (2.2 kg) with a built-in GPS. The dimensions of the probe are 50 x 50 x 36 cm and the weight of the system including transportation box is about 22 kg. The user-interface and the data output files display the pressure, temperature and piston location as a function of time.

8.2.4 Results and discussion

Preliminary tests were executed to check the sensitivity of the pressure in the closed reservoir (‘A’ and ‘B’ closed, see Figure 131) to atmospheric pressure and temperature variations. The latter two relate to p_0 (Eq. (8.14)), which is assumed constant during a measurement. Therefore, the sensitivity of p to variations of p_0 should be small compared to typical dp/dt resulting from soil behaviour. The effect of sunlight and the subsequent increase of the temperature are simulated using a standard lamp. Figure 132 shows that due to the radiation of the lamp, the temperature of the reservoir increases, which results in a significant effect on p ($\Delta p \approx 0.16$ bar in $\Delta t \approx 75$ min). p exhibits also a relatively large increase (0.02 bar increase of p in about 30 seconds) when warming the reservoir manually.

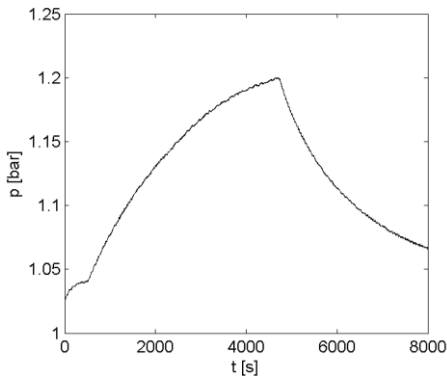


Figure 132. Increase of p as a function of t in the reservoir (valves ‘A’ and ‘B’ closed) as a result of increasing temperature in the reservoir induced by radiation of a standard lamp (from $t = 500$ to $t = 4500$).

The effect of the temperature (T [°C]) on p in the reservoir is further demonstrated in Figure 133(a). Temperature variations are caused by the heating system in the laboratory (switched off at night, switched on in the morning). A strong correlation between the behaviours of p and T as a function of t is shown. Atmospheric pressure (p_{atm}) effects are less important compared to the effect of T , as Figure 133(b) shows no correlation between p and p_{atm} .

Furthermore, the typical time scale of the fluctuations as observed for p_{atm} is much larger than the typical time scale of a measurement ($\sim 10 - 20$ min). Therefore, it

is sufficient to incorporate variations of p_{atm} in p_0 at the start of a measurement only. However, temperature fluctuations can cause significant fluctuations of p during a measurement. Therefore, a temperature sensor was installed, which enables the incorporation of the temperature on p when analysing the data.

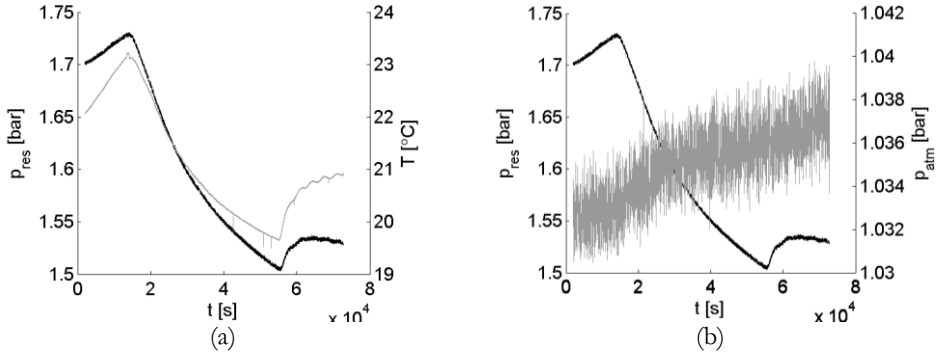


Figure 133. p_{res} in the reservoir (black lines, left vertical axes) as a function of t for a closed reservoir ('A' and 'B' closed) and a duration of ~ 20 hrs. In (a) also the temperature (grey line, right vertical axis) and in (b) also p_{atm} (grey line, right vertical axis) are shown.

Due to the low compressibility of water, a constant, relatively large increase of p with t is expected for a closed water-filled reservoir (without entrapped air) upon moving one of the two pistons downward. dp/dt then depends on the downward velocity of the piston. Furthermore, p should be constant for constant reservoir volume (i.e. for zero piston movement). However, two phenomena are observed which disagree with the abovementioned behaviour.

The first phenomenon concerns an increase of p with t (after a preceding decrease of p) as well as a decrease of p with t (after a preceding increase of p) for zero piston movement. Figure 134 shows an example of this behaviour for a step-by-step downward piston movement. After each increase of p , an exponential decrease at constant reservoir volume exists. The typical (e -folding) time-scale of this exponential character is about 5 – 10 min with an accompanying Δp of about 0.05 bar.

We anticipate the following explanation for this behaviour. It is possible that during the filling of the reservoir some air is entrapped. The volume of the (air in the) reservoir decreases and p subsequently increases upon moving the piston downward. This increase generates a change of the solubility of air in water (Henry's Law; see e.g. Van Kessel, 1998a). When, after a relatively rapid increase of p (dp/dt larger than the rate at which the solubility changes), the reservoir volume is kept constant, gas molecules continue to dissolve into the fluid, which generates a decrease of p . The same concept accounts for the step-by-step decrease of p (continuing evaporation and a subsequent increase of p).

The second phenomenon concerns a non-linear increase / decrease of p as a function of t during both the initial and final phase of downward / upward piston

movement. This behaviour is observed during hysteresis tests during which a piston was moved up and down at constant speed in a closed reservoir. This enables the study of the increase of p (from p_{atm} upwards) and decrease (until $p = p_{atm}$) as a function of t . Different tests were executed with varying maximum p (1.4, 1.7 and 2.0 bar) and varying injection speeds ($9.6 \cdot 10^{-2}$ and $0.05 \mu\text{l}\cdot\text{s}^{-1}$). The same tests were repeated after emptying and refilling the reservoir.

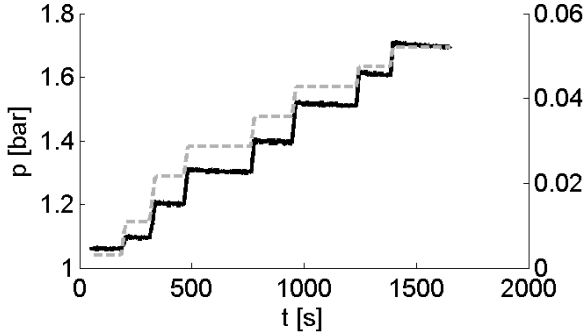


Figure 134. Typical example of a step-by-step increasing p as a function of t ($Q = 0.1 \mu\text{l}\cdot\text{s}^{-1}$). For constant piston position (i.e. constant reservoir volume) p exponentially decreases.

Figure 135 shows a typical result of such a hysteresis tests. It is clearly shown that dp/dt is not constant for constant up or downward piston velocity. This non-linear behaviour of p as a function of t could be reproduced by applying Gay-Lussac's gas law, which suggests the presence of entrapped air in the reservoir. The observed non-linear behaviour may be further enhanced by the varying solubility of the water in the reservoir. Finally, it is noted that similar dp/dt are found for hysteresis tests executed after refilling the reservoir. This indicates that the proposed filling procedure is consistent.

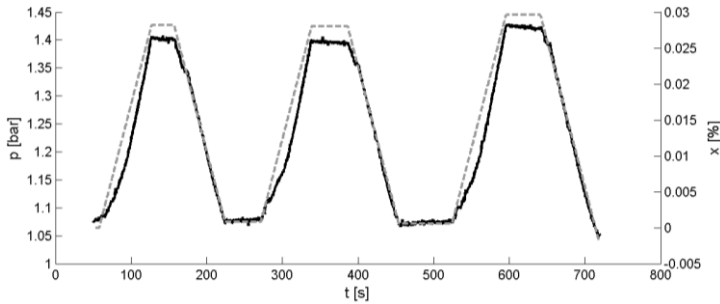


Figure 135. Typical result of hysteresis test with p in the reservoir (continuous black line, left vertical axis) and the relative (to upper most position) piston position (x [%], dashed grey line, right vertical axis) as a function of t .

Eight artificially generated (Section 4.1.1) sand-mud mixtures with either a sand-silt skeleton or a clay-water matrix (ζ_{sa} ranging 0 – 100%, clay-silt ratio = 0.25, clay mineralogy: kaolinite) were tested to check if the HPS probe represents soil behaviour

as expected following the theory. The measuring procedure concerned a step-by-step increase of Q (ranging from $2.7 \cdot 10^{-7} - 1 \cdot 10^{-1} \mu\text{l}\cdot\text{s}^{-1}$). Each step was followed by a subsequent relaxation period. Measurements were executed at constant depth (2 cm) and took about 20 – 25 min. As the temperature in the laboratory was constant (20°C), data of the temperature sensor are not analysed.

Figure 136 shows a typical result of an injection test for a soil with a dominant clay-water matrix. p clearly exhibits increasing dp/dt for increasing Q . Furthermore, different relaxation behaviours are identified for $Q = 0$. Varying dp/dt during both injection and relaxation agree with soil behaviour during elastic deformation as expected (Figure 128). Maximum p for elastic soil behaviour is reached at $t \approx 2700$ s, which yields failure of the soil. Following the theory, p as a function of t tends to $4/3c_u$ (see Eq. (8.8) and the upper horizontal line in Figure 127(b)) upon the transition from elastic to plastic soil behaviour. However, failure occurs before this limit value is reached. This is assumed to be attributed to the generation of small cracks, upon which the cavity volume suddenly increases and p , subsequently, drops.

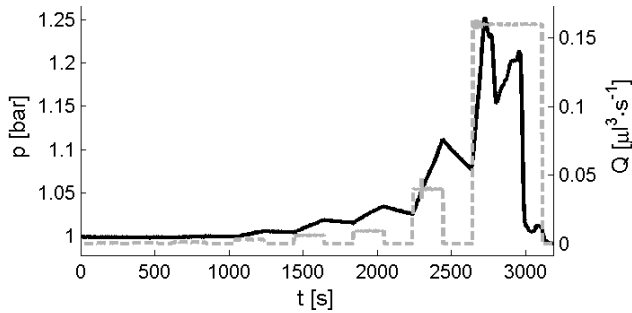


Figure 136. p (black continuous line, left vertical axis) and Q (grey dashed line, right vertical axis), both as a function of t for a soil sample for which $\xi_{cl} = 15\%$ and $W = 36\%$.

c_u has to be derived from the convex profiles of p as a function of t . However, dp/dt is almost constant in most cases (Figure 136), especially for relatively large Q . It is presumed that this linear character of p as a function of t results from the combined effect of the tendency to a convex profile due to elastic soil behaviour and the tendency to a concave profile due to the dissipation of entrapped gas molecules. This combined effect hampers the comparison of the HPS data with results obtained by traditional geotechnical tests.

Figure 137 shows a typical result of an injection test on a soil with a dominant sand-silt skeleton. It is clearly shown that for a granular soil a markedly different response is generated compared to a soil with a dominant clay-water matrix (Figure 136). p tends to a constant value rapidly after the start of injection. This indicates that no cavity is formed, during which p gradually increases due to cavity generation, but that a Darcy flow is generated following Eq. (8.9). The noise of p for relatively large Q is caused by a software error concerning the translation of imposed Q to actual injected Q (for relatively large Q only). This software error is the main reason why it is

also difficult for granular soils to compare HPS data with results obtained by traditional geotechnical tests.

The theory of the HPS probe applies to saturated soils only. Some preliminary tests have been executed to check the behaviour of partly-saturated soil during injection. Results clearly indicate no relation with the elasto-plastic behaviour as discussed in the theory. This is attributed to the generation of a Darcy-like flow to fill the voids in the skeleton. However, a different character is expected for a flow through an unsaturated skeleton than through a saturated skeleton, e.g. due to a different friction coefficient.

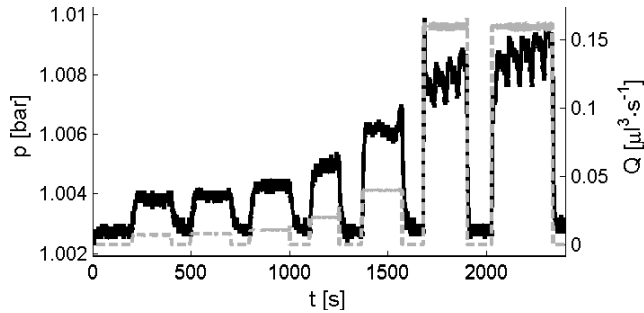


Figure 137. p (black continuous line, left vertical axis) and Q (grey dashed line, right vertical axis), both as a function of t for soil sample 1 ($\zeta_{cl} = 0\%$, $W = 30\%$).

8.2.5 Conclusions and recommendations

First, the theory of the measuring principle was elaborated. This enabled a thorough analysis of the sensitivity of the measurement procedure for laboratory conditions. Both the sensitivity to temperature and to atmospheric pressure fluctuations was studied. Especially the temperature has a significant effect on the pressure in the water-filled reservoir. Furthermore, hysteresis tests show that it seems difficult to obtain zero air-enclosure within the reservoir, although the sensitivity of the water pressure in the reservoir to the temperature indicates that the volume of entrapped air is limited.

A qualitative analysis of results of tests on artificially generated sand-mud mixtures with either a dominant sand-silt skeleton or a dominant clay-water matrix indicate soil behaviour as expected following the theory. Elastic and plastic soil behaviours are clearly shown, as the occurrence of a Darcy flow for more granular soils. However, the stiffness of the system is of the same order of magnitude as the anticipated stiffness of sediments during elasto-plastic behaviour. This is illustrated by similar pressure gradients during soil injection as when increasing the pressure for a closed reservoir. The relatively low stiffness of the reservoir is attributed to the entrapment of air in the reservoir. As a result, soil behaviour cannot be quantified and a comparison of the HPS data with data obtained by traditional (geotechnical) tests is not yet possible.

In conclusion, the HPS probe is a new and promising technique for the *in-situ* characterisation of bulk soil mechanical parameters without disturbing the existing

sediment structure too much. The HPS probe enables the study of processes and bed properties within the upper layer of the sediment bed. The most important recommendation for further development of the device concerns the entrapment of air, and the subsequent relatively low stiffness of the system.

First, alternatives for the filling procedure should be assessed to avoid air-enclosure. Second, hysteresis tests should be performed after filling the reservoir. Subsequently, the volume of entrapped air in the reservoir can be quantified by applying Gay-Lussac's gas law. Henry's Law can then be applied to determine the dissipation rate of air molecules as a function of pressure. The behaviour of the water pressure during soil injection can then be corrected for the dissipation of gas molecules. Finally, it is recommended to assess the maximum vertical resolution at a measuring station (expected to vary with varying soil compositions) and to apply Gay-Lussac to incorporate temperature variations in the data analysis.

8.3 Conclusions

In-situ sediment characterisation techniques are required to link micro/meso scale sediment properties to macro/mega scale processes and to determine the input for the new erosion formulation. Sediment characteristics are usually obtained by core collection and subsequent laboratory analyses. This is time-consuming and expensive. Besides, soils are significantly disturbed during collection and transportation. Available *in-situ* techniques generally lack a proper physical background. Therefore, two new techniques are developed to measure sediment properties and soil mechanical parameters following the geotechnical theory presented in Chapter 3.

The Medusa RhoC device applies radiometric sedimentology to characterize intertidal sediments concerning vertical distribution of the bulk density and depth-averaged sand and mud content. By deploying existing sedimentological interactions also the plasticity index and the organic matter content can be derived. The Hydraulic Permeability and Strength (HPS) probe determines vertical profiles of the hydraulic conductivity, shear modulus and undrained shear strength by recording pore water pressure gradients during elasto-plastic soil behaviour upon injecting small volumes of water. Medusa RhoC and the HPS probe data can be applied as input parameters for the new erosion formulation (Chapter 3).

Both new techniques are useful and practical tools to map sediment properties in a significantly faster and more cost effective way compared to traditional methods. Results obtained in the field and in the laboratory show a favourable agreement with results obtained by traditional analyses. However, some additional steps have to be taken concerning the accuracy (Medusa RhoC) and the calibration (HPS probe). Subsequently, both techniques can be applied to *in-situ* characterise the upper layer of intertidal sediment beds, and to study biological and/or morphological processes.

Finally, it is noted that both measurement principles can only be deployed above water (on tidal flats during low tide). However, by adjusting both devices as presented, it is believed that also submarine and/or subterranean soils can be characterised.

Chapter 9

Conclusions and recommendations

9.1 Research objectives

In the introduction to the current thesis three main gaps have been identified in the current knowledge on the mechanical behaviour and erosion of sand-mud mixtures in the marine environment in general, and on intertidal flats in estuaries and tidal lagoons, in particular (see also Section 1.3):

- Available relations between erosion properties and intertidal sediment characteristics are generally site-specific, highly empirical and often contradicting. This mainly results from the lack of a conceptual framework which identifies both erosion failure modes and its characterising soil parameters as a function of complex, multiple-scale sedimentological, biological, physico-chemical and hydro-dynamical interactions and feedbacks.
- It is not possible to accurately predict the behaviour of marine wetlands using the currently available highly empirical algorithms. Furthermore, combining these empirical relations to reflect spatial and temporal variations of intertidal sediment characteristics will result in large error margins.
- Available laboratory and *in-situ* experimental procedures to study relations between hydrodynamics and sand-mud stability are time-consuming, and therefore costly. Besides, measurement results often not correlate, e.g. due to different characters of flow-induced stresses, disturbances during the collection and transport of soil samples, and due to poorly defined soil characteristics.

This thesis aims at increasing our knowledge on said mechanical and erosion properties of natural sediment beds. The conclusions from the study described in the current thesis are categorized based on the three research objectives outlined in Section 1.4, addressing the above listed knowledge gaps:

1. Identify characterizing parameters for the mechanical behaviour of sand-mud mixtures.
2. Derive a generic formulation for the erosion of sand-mud mixtures.
3. Discuss and demonstrate the practical implications and applicability of the new erosion approach for sand-mud mixtures, and elaborate on in-situ experimental techniques to determine the required input-parameters.

9.2 Conclusions

Conclusions related to Objective 1: Identify characterising parameters for the mechanical behaviour of sand-mud mixtures.

- Intertidal sediments in estuaries and tidal lagoons generally concern a mixture of sand and mud. Both the classification and description of the morphological behaviour of these mixtures should, therefore, allow for the incorporation of the effect of both fractions. Current thesis shows that both fractions mutually influence the soil mechanical and, therefore, the morphological behaviour of sand-mud mixtures.
- The granular porosity and the relative water content are convenient soil parameters to characterise the soil mechanical and erosion behaviour of sand-mud mixtures. The granular porosity enables predicting the transition between cohesive and granular behaviour, which occur for a plastic clay-water matrix and a rigid sand-silt skeleton, respectively. The relative water content couples packing density and plasticity, which enables the characterisation of both cohesive and granular soils with varying fraction contents and mineralogy.
- A geotechnical approach is inevitable for studying and understanding the erosion behaviour of sand-mud mixtures. Different geotechnical failure mechanisms allow to distinguish between different erosion modes as a function of flow-induced stresses and soil mechanical parameters. It is shown that not only micro-scale soil properties, but also meso-scale (bulk) soil properties (packing density, plasticity and network structure) are important for soil mechanical behaviour. Based on this geotechnical approach an erosion classification scheme and a generic erosion formulation are derived.
- The absence of a universal proxy parameter for bed stability originates from a poor definition of sediment strength. Bed stability is generally related to gravitational, adhesive or cohesive forces, whereas in geotechnical engineering the (un)drained sediment strength is applied. Drained refers to cohesive and adhesive forces, whereas undrained refers to apparent cohesion. The latter occurs when the typical time-scale of flow-induced soil deformations exceeds the typical time-scale of the subsequently generated dissipative Darcy-inflow of water. The drained and undrained sediment strength may differ by orders of magnitude. The current thesis links bed stability to the (un)drained sediment strength.
- Semi-empirical functions for the undrained sediment strength and the coefficient of pore water pressure dissipation during swelling are introduced. The semi-empirical model for the undrained shear strength shows that the Critical State Models for granular and cohesive soils can be combined to describe the behaviour of sand-mud mixtures. The model for the dissipation coefficient is still highly empirical. This is mainly due to the lack of an accurate, standardized methodology for measuring the *in-situ* sediment permeability.

- A new classification scheme for erosion modes distinguishes between drained (floc and surface erosion) and undrained failure mechanisms (mass erosion), based on the relation between bed strength and flow-induced stresses. Floc and mass erosion are characterised by both the absence of a clear threshold and the random disruption of bed material. During surface erosion the initial undrained bed strength reduces to its drained strength owing to the Darcy-inflow of water. Subsequent layers of sand and mud are eroded at constant rate when flow-induced stresses exceeding the drained bed strength.

Conclusions related to Objective 2: Derive a generic formulation for the erosion of sand-mud mixtures under shear flow conditions.

- A new formula for surface erosion was derived, assuming that failure of the bed occurs at the critical state. As this critical state is met at the sediment surface, the bed swells to the local drained shear strength.
- This new surface erosion formulation reduces the degree of empiricism compared to currently available erosion formulations. The new formula relates the surface erosion rate to bulk soil mechanical properties: the erosion rate is a function of the packing density, the undrained sediment strength and the coefficient of pore water pressure gradient dissipation (i.e. a function of the permeability and compressibility). The surface erosion threshold relates to the plasticity index.
- The magnitude of observed erosion rates can be established by substituting soil (mechanical) properties in the new surface erosion formulation. This supports the applicability of the new formulation for erosion of cohesive, granular and intermediate sediment mixtures, and forms an alternative for the currently applied highly empirical erosion formulae. The successful establishment of the observed surface erosion rates also confirms the important role of negative pore water pressure gradients as an additional retarding force for erosion, next to gravitational and/or cohesive forces.
- The new erosion formula compares favourably with experimental results, in spite of difficulties in the accurate determination of erosion rates. In particular the bed shear stress, the suspended sediment concentration, and the clay content are difficult to establish. Moreover, reproducing observed data is hampered by a lack of a proper physical formulation for the permeability of sand-mud mixtures.
- Little is known on the relation between the stochastic character of flow-induced shear and normal bed stresses, on the one hand, and on the isotropic and deviatoric soil stresses induced by these shear and normal stresses in a semi-permeable sediment bed, on the other hand.

Conclusions related to Objective 3: Discuss and demonstrate the practical implications and applicability of the new erosion approach for sand-mud mixtures, and elaborate on *in-situ* experimental techniques to determine the required input-parameters.

- Soil mechanical properties of intertidal sediment beds are sensitive to small changes in the sediment structure, especially when the granular porosity is around its maximum value. These small changes may be generated by mixing and/or burrow digging organisms present in and on intertidal sediment beds, which either destabilize or stabilize the sediment bed.
- A qualitative discussion of the three erosion modes for natural sediments indicates that especially floc and surface erosion properties are susceptible to biological and physico-chemical influences. Floc and surface erosion are expected to govern largely the morphological behaviour of estuaries and tidal lagoons, whereas mass erosion is only expected to occur rather locally and infrequently.
- Both small-scale straight flume and large-scale annular flume tests indicate that eroded sand particles decrease the erodibility of the underlying sediment bed due to bed load transport, inducing propagating bed forms.. A similar behaviour is expected for sediment beds under more natural conditions.
- A theoretically derived conceptual diagram illustrates that the surface erosion rate for intertidal sediments with a composition ranging from cohesive to granular, and/or from loosely to densely packed, may vary over orders of magnitude. The diagram allows for the estimation of the rate and the typical spatial and temporal scale at which surface erosion may occur.
- Two promising *in-situ* techniques, the Medusa RhoC and Hydraulic Permeability and Strength (HPS) probe, are developed. These enable (1) the determination of input parameters for the new surface erosion formulation, (2) the *in-situ* study on micro-scale of sediment biological and/or morphological processes, and (3) to map sedimentological and soil mechanical properties in the upper layer (10 – 20 cm) of intertidal sediment beds. *In-situ* measurements avoid the need for sampling and subsequent laboratory testing, which disturbs the delicate sediment structure and is less time-consuming compared to traditional methods.
- Data obtained by the Medusa RhoC and HPS probe allow for a quick sedimentological characterisation of estuaries and tidal lagoons when combining their results with system-relations between clay content, on the one hand, and silt and organic matter content, density and plasticity, on the other hand.

Overall conclusions

- The current thesis is a step forward in the study of the mechanical and erosion behaviour of sand-mud mixtures. It presents a theoretical survey on sand-mud behaviour, which provides insight in the failure mechanisms and accompanying characterising soil parameters during the erosion of sand-mud mixtures. The results of standardized geotechnical tests as well as large and small-scale flume experiments provide an important data-set, especially because few data on sand-mud behaviour is available in open literature.

- Following a geotechnical approach, a new erosion scheme and erosion formulation for sand-mud mixtures are presented, which provides the following advantages:
 - The applied approach is highly instructive and provides insight in the failure mechanisms observed during the erosion of sand-mud mixtures, as well as in the characterising soil (mechanical) parameters.
 - Soil mechanical parameters can be studied using standardized and practical experimental procedures. This is in contrast with the study of erosion as a function of sediment properties directly, for which only highly laborious and poorly calibrated experimental procedures are available. This is especially important when studying the relation between sediment properties and erosion on different spatial and temporal scales in different marine systems.
 - Although the current thesis considers only artificially generated, relatively densely packed soils, a similar soil mechanical approach can potentially be applied to natural and/or more loosely packed intertidal sediments. This may concern studying biological and/or physico-chemical effects on geotechnical failure mechanisms, rather than studying the relation between these effects and erosion directly.
 - The number of parameters in the new erosion formulation is limited, and the utilization of soil mechanical parameters significantly reduces its degree of empiricism. This is especially important for the implementation of the formulation in numerical models.

9.3 Strategy for assessing soil mechanical behaviour

This thesis shows, based on theory and experimental data, which soil parameters determine the mechanical behaviour of sediment beds, and how these parameters are related. These parameters incorporate sedimentological, biological as well as physico-chemical effects. Semi-empirical functions have been established to link soil mechanical behaviour to bulk soil parameters. The empirical coefficients in these functions follow from experimental data of soil samples collected in the area of interest. The semi-empirical functions enable to interpolate and/or extrapolate site-specific experimental data, which significantly extends the applicability of these data.

The established semi-empirical functions in combination with experimental data can be applied as ingredients for the new erosion formula to assess the stability of sediment beds. This erosion formula allows to incorporate the understanding of the mechanical behaviour into predictive numerical sediment transport models, e.g. to predict the morphological behaviour of a tidal lagoon or estuary. The semi-empirical functions incorporate variations of mechanical behaviour on bed stability during model

simulations. These variations may arise from changing bed properties, e.g. due to erosion or deposition.

The strategy presented below proposes an experimental method to determine soil parameters required for the assessment of the mechanical behaviour of sediment beds. From these soil parameters, the input for the erosion formulation can be derived as well. First, measurement techniques for each parameter are discussed, followed by the spatial and temporal covering at which samples should be collected.

- Particle size distribution

The particle size distribution is determined in a laboratory using e.g. a laser granulometer. It is noted that the particle size distribution for especially the smallest sediment fraction (especially clay) is highly sensitive to the applied experimental procedure (Section 4.1.2 and Appendix II).

- Bulk and dry density

The bulk and dry density (Section 2.2.1) simply follows from weighing a specific sample volume both before and after oven drying. It is noted that the in-situ water content should be kept constant during the transport of the sample to the laboratory in order to determine e.g. the saturation degree and/or the degree of overconsolidation.

- Minimum and maximum granular porosity

The densest and loosest packing density of the sand and silt volume fraction provide insight in the soil structure, e.g. concerning the occurrence of granular and cohesive behaviour (Section 2.2.2 and 4.1.3).

- Atterberg Limits

The Atterberg Limits (Section 2.2.1) require around 0.5 litre of (remoulded) soil sample. A faster (but indirect) method to assess the plasticity of soils requiring much less material is the Methylene Blue method (Section 2.2.1).

- Undrained shear strength

The undrained shear strength follows from shear vane tests (Section 4.2.1) for granular, cohesive and mixed sediments. For soft, purely cohesive soils, also a rheometer may be applied.

- Coefficient of pore water pressure dissipation

The coefficient of pore water pressure dissipation can be derived in different ways, depending on the character of the tested soil sample. The Oedometer tests (Section 4.3.1) should be applied for relatively densely packed sand-mud mixtures. The Capillary Suction Time (CST, Huisman and Van Kesteren, 1998) test or the more advanced Suction Induced Consolidation (SIC) test may be applied for soft cohesive soils.

Most of these measurement techniques are standardized and cheap laboratory methods, which require about one litre of soil sample in total. To represent the in-situ conditions, the water content of the sample should be kept constant. Multiple laboratory tests may be executed on a soil sample by diluting it with water. Additionally, some biological and physico-chemical parameters (e.g. organic matter content, zeta potential, salinity and pH) may be determined to facilitate the interpretation of the measured soil mechanical parameters.

It is important to collect samples with sufficient spatial and temporal covering to incorporate the variability of soil mechanical behaviour, which may arise from hydrodynamical, geomorphological and biological effects. This implies that samples should be collected along spatial as well as temporal gradients of sediment characteristics within the area of interest.

Examples are the sand-mud gradient along the longitudinal axis of an estuary, and/or the vertical gradient of physico-chemical parameters within the upper layer of a sediment bed. It may also concern e.g. seasonal variability, which is required when studying the morphological behaviour of an estuary over multiple years. Studies on larger time scales also require information on the subsoil, further to information on the morphological active upper layer of the sediment bed.

To identify these gradients, different methodologies may be applied: satellite or aerial survey techniques (Section 8.1.1), visual inspections concerning e.g. biological activity and/or sedimentological character, or the Medusa system (Section 8.1). The latter system enables a relatively quick assessment of sedimentological gradients (sand-mud ratio) within the upper layer of the sediment bed. As mud content and organic matter are related, it also indicates biological gradients. Local vertical gradients may be lost by sampling. Therefore, the Medusa RhoC system and/or the Hydraulic Strength and Permeability (HPS) probe (Section 8.2) may be applied to study these gradients concerning bulk density and soil mechanical parameters, respectively.

Future practical experience should further detail the proposed strategy concerning both experimental techniques and spatial and temporal resolution at which samples need to be tested.

9.4 Recommendations for further study

- The current thesis shows that a geotechnical approach is inevitable to link hydrodynamic stresses to the erosion behaviour of intertidal sediments. However, this largely depends on how a turbulent flow induces stresses within the permeable sediment bed. Currently little is known on this translation. Therefore, the link between hydrodynamics and morphological sediment behaviour should be further studied. The same accounts for the effect of micro-bathymetry on the stochastic character of the flow-induced shear stresses.

- The current study focuses on erosion during shear flow conditions only. It is recommended to study the erosion of sand-mud mixtures as a function of cyclic forcing conditions as well, for example wind or ship waves. Furthermore, current thesis focuses mainly on floc and surface erosion. By studying erosion for larger (unidirectional) flow velocities also mass erosion may need to be studied. It is noted, however, that the size of the test sections in flumes should be at least an order of magnitude larger than the size of eroded aggregates of bed-material.
- Bed forms and/or bed load transport of sand decreases the erodibility of underlying sediments. Similar conditions may occur due to deposition. These effects should be further studied as they may play an important role during erosion of sand-mud mixtures in the natural environment. Also the occurrence, type and properties of bed forms in sand-mud mixtures as a function of both sedimentological as biological influences should be further studied, as these may significantly affect bed roughness.
- The surface erosion parameter is rather sensitive to the permeability and, therefore, to the coefficient of pore water pressure dissipation during swelling. Although the presented model for this dissipation coefficient is promising, it is still highly empirical and not very accurate. This mainly results from the lack of a standardized measuring methodology to determine the *in-situ* sediment permeability and from the limited availability and accuracy of Oedometer results. It is recommended to execute more Oedometer tests and to further develop the HPS probe.
- The current study mainly focuses on artificially generated sediment mixtures, which are only partly comparable to natural soils, which include organic material, gas and physico-chemical influences. However, the applied soil mechanical/bulk parameters provide the possibility to incorporate the effect of these influences as well (e.g. by means of the plasticity index). Therefore, it is recommended to study the relation between biological and physico-chemical effects and soil behaviour.
- Possibilities for studying the incorporation of biological effects may concern the effect of biota (1) on the translation from flow-induced stresses to the (stochastic character of) stresses within the upper layer of the sediment bed, (2) on the plasticity index and granular porosity, and/or (3) on the undrained shear strength and coefficient of pore water pressure dissipation.
- The Medusa RhoC and the Hydraulic Permeability and Strength probe should be further tested and calibrated to (1), provide in the growing need for more detailed spatial and temporal information of sediment characteristics, (2) to study the effect of biota on soil mechanical parameters and (3) because no alternative is currently available to study the *in-situ* permeability of intertidal sediment beds.

References

- Alvarez-Hernandez, E.M., 1990. The influence of cohesion on sediment movement in channels of circular cross-section. Ph.D. thesis. University of New Castle upon Tyne, New Castle upon Tyne.
- Amos, C.L., G.R. Daborn, H.A. Christian, A. Atkinson and A. Robertson, 1992. In situ erosion measurements on fine grained sediments from the Bay of Fundy. *Marine Geology*, Vol. 108:2, 175-196.
- Ariathurai, C.R., 1974. A finite element model for sediment transport in estuaries. Ph.D. thesis, University of California, Davis.
- Ariathurai, C.R. and Arulanandan, K., 1978. Erosion rates of cohesive soils. *Journal of the hydraulics division*, Vol. 104, 279-283.
- ASTM D2216, 2006. Standard Test Method for Laboratory Determination of Water (Moisture) Content of Soil and Rock by Mass. Annual Book of ASTM standards, American Society for Testing Materials, West Conshohocken.
- ASTM D2435-04, 2006. Standard test methods for one-dimensional consolidation properties of soils using incremental loading. Annual Book of ASTM standards, American Society for Testing Materials, West Conshohocken.
- ASTM D422-63, 2007. Standard Test Method for Particle-Size Analysis of Soils. Annual Book of ASTM standards, American Society for Testing Materials, West Conshohocken.
- ASTM D4254, 2006. Standard test for minimum index density and unit weight of sils and calculation of relative density. Annual Book of ASTM standards, American Society for Testing Materials, West Conshohocken.
- ASTM D4318, 2000. Standard test for Liquid Limit, Plastic Limit and Plasticity Index of soils. Annual Book of ASTM standards, American Society for Testing Materials, West Conshohocken.
- ASTM D4648, 2005. Standard test for Laboratory Miniature Vane Shear test for Saturated Fine-Grained Clayey Soil. Annual Book of ASTM standards, American Society for Testing Materials, West Conshohocken.
- ASTM D5084-03, 2006, Standard test methods for measurements of hydraulic conductivity of saturated porous material using a flexible wall permeameter. Annual Book of ASTM standards, American Society for Testing Materials, West Conshohocken.
- Austen, I., Andersen, T. J. and Edelvang, K., 1999. The Influence of Benthic Diatoms and Invertebrates on the Erodibility of an Intertidal Mudflat, the Danish Wadden Sea. *Estuarine, Coastal and Shelf Science*, Vol. 49, 99-111.
- Bagnold, R.A., 1954. Experiments on a gravity-free dispersion of large solid spheres in a Newtonian fluid under shear. *Proceedings of the royal society of London*, Vol. 225:1160, 49-63.
- Banta, G. T., Holmer, M., Jensen, M. H. and Kristensen, E., 1999. Effects of two polychaete worms, *Nereis diversicolor* and *Arenicola marina*, on aerobic and anaerobic decomposition in a sandy marine sediment. *Aquatic Microbial Ecology*, Vol. 19, 189-204.

- Bassoullet, P. and Le Hir, P., 2007. In situ measurements of surficial mud strength: a new vane tester suitable for soft intertidal muds. *Continental Shelf Research*, Vol. 27, 1200-1205.
- Black, K.S. and Paterson, D.M., 1997. Measurement of the erosion potential of cohesive marine sediments: a review of current in situ technology. *Journal of Marine Environmental Engineering*, Vol. 4, 43-84.
- Booij, R., 1994. Measurements of the flow field in a rotating annular flume. *Communications on Hydraulic Geotechnical Engineering*. Delft, Delft University of technology. Report No. 2-94.
- Booij, R., 2003. Measurements and large eddy simulations of the flows in some curved flumes. *Proceedings of the 5th International Symposium on Engineering Turbulence Modelling and Measurements*. In: *Engineering Turbulence Modelling Measurements*, Vol. 5, Elsevier Science, ISBN 0-08-044114-9. Rodi, W. and Fueyo, N. (Editors).
- Breugem, W.P., 2005. The influence of wall permeability on laminar and turbulent flows - Theory and simulations. Ph.D. thesis. University of Technology Delft, the Netherlands. ISBN 9090189246.
- BS 1377, 1990. Methods of test for soils for civil engineering purposes. General requirements and sample preparation. British Standards Institution. ISBN: 0580176924.
- Carman, P.C., 1956. Flow of gases through porous media. Academic, New York.
- Carrier, W.D., 2003. Goodbye Hazen; Hello, Kozeny-Carman. *Journal of geotechnical and geo-environmental engineering*, Vol. 129:11, 1054 - 1056.
- Casagrande, A., 1932. Research on the Atterberg limits of soils. *Public Roads*, Vol. 13, 121-136.
- De Boer, P.L. 1979. Convolute lamination in modern sands of the estuary of the Oosterschelde, the Netherlands, formed as the result of entrapped air. *Sedimentology*, Vol. 26, 283-294.
- De Boer, P.L., 1981. Mechanical effects of micro-organisms on intertidal bedform migration. *Sedimentology*, Vol. 28, 129-132.
- De Brouwer, J.F.C., Ruddy, D.K., Jones, T.E.R. and Stal, L.J., 2002. Sorption of EPS to sediment particles and the effect on the rheology of sediment slurries. *Biochemistry*, Vol 61, 57-71.
- De Groot, A.V., van der Klis, M.M.I.P., van Wesenbeeck, B.K., ten Have, R., de Meijer, R.J., Bakker, J.P., 2002. Natural radionuclides in salt marsh sediments; revealing spatial sediment patterns. *KVI annual report*, Vol. 62.
- De Meijer, R.J., Donoghue, J.F. 1995. Radiometric fingerprinting of sediments on the Dutch, German and Danish coasts. *Quaternary International*, Vol. 26, 43-37.
- De Vriend, H.J., 1991. Mathematical modelling and large-scale coastal behaviour, Part 1: Physical processes. *Journal of Hydraulic Research*, Vol. 29:6, 727-740.
- Defew, E.C., Tolhurst, T.J., and Paterson, D.M., 2002. Site-specific features influence sediment stability of intertidal flats. *Hydrology and Earth System Sciences*, Vol. 6:6, 971-982.
- Dohmen-Janssen, M., 2001. Grain size influences on sediment transport in oscillatory sheet flow (phase lags and mobile bed effects). Ph.D. thesis. Delft, Delft University of technology.
- Dyer, K.R., 1986. Coastal and Estuarine Sediment Dynamics. John Wiley and Sons. ISBN 0471908762.

- EC MAST-I, 1993. On the methodology and accuracy of measuring physico-chemical properties to characterize Cohesive Sediments. EC MAST-I research programme 1993.
- Eelkema, M., 2008. Measuring sediment properties in the field using Medusa RhoC. MSc thesis, Delft University of Technology. Available at (accessed 1 October 2010): <http://www.citg.tudelft.nl/live/pagina.jsp?id=4de0d195-5207-4e67-84bb-455c5403ae47&lang=en>.
- Eleveld, M.A., 1999. Exploring coastal morphodynamics of Ameland (The Netherlands) with remote sensing monitoring techniques and dynamic modelling in GIS. Ph.D. thesis, University of Amsterdam.
- Egiazaroff, I.V., 1965. Calculation of non-uniform sediment concentrations. *Journal of the Hydraulics Division*, Vol. 91:4.
- Fernandes, S., Sobral, P. and Costa, M.H., 2006. Nereis diversicolor effect on the stability of cohesive intertidal sediments. *Aquatic Ecology*, Vol. 40, 567–579.
- Fernandez-Luque, R., 1974. Erosion and transport of bed-load sediment. Ph.D. thesis, KRIPS Repro BV, Meppel, the Netherlands.
- Flemming, B.W., 2000. A revised textural classification of gravel-free muddy sediments on the basis of ternary diagrams. *Continental Shelf Research*, Vol. 20, 1125-1137.
- Flemming, B.W. and Delafontaine, M.T., 2000. Mass physical properties of muddy intertidal sediments: some applications, misapplications and non-applications. *Continental Shelf Research*, Vol. 20, 1179-1197.
- Flood, R.D., 1983. Classification of sedimentary furrows and a model for furrow initiation and evolution. *Geological Society of America Bulletin*, Vol. 94, 630-639.
- Fontaine, K., 2004. Waar komt het slib voor de Belgische kust vandaan? Een kleimineralogische benadering (in Dutch). M.Sc thesis, Katholieke Universiteit Leuven, Belgium.
- Friend, P.L., Collins, M.B. and Holligan, P.M., 2003. Day-night variation of intertidal flat sediment properties in relation to sediment stability. *Estuarine Coastal Shelf Science*, Vol. 53, 663-675.
- Gibson, R.E., England, G.L. and Hussey, M.J.L., 1976. The theory of one-dimensional consolidation of saturated clays. *Géotechnique*, Vol. 17, 261-273.
- Gillet, P. And Gorman, E., 2002. Population structure and secondary production of *Heteromastus filiformis* (Polychaeta: Capitellidae) in the Loire estuary, France. *Journal of the Marine Biological Association of the UK*, Vol. 82:3, 395-402.
- Gouleau, D., J.M. Jouanneau, D.M. Weber, P.G. Sauriau, 2000. Short- and long-term sedimentation on Montportail-Brouage intertidal mudflat, Marennes-Oléron bay (France). *Continental Shelf Research*, Vol. 20, 1513-1530.
- Grass, A.J., 1970. Initial instability of fine bed sand. Proceedings of the American Society of Civil Engineers. *Journal of the Hydraulics Division*, Vol. 96 (HY3), 619-632.
- Hansbo, S., 1957. New approach to the determination of the shear strength of clay by the fall cone test. *Proceedings of Royal Swedish Geotechnolgy Institute*, Vol. 15, 1-49.
- Head, K.H., 1980. Manual of Soil Laboratory Testing, Volume 1: Soil Classification and Compaction tests. Pentech Press London. ISBN 0-7273-1302-9.
- Head, K.H., 1982. Manual of soil laboratory testing. Volume 2: Permeability, shear strength & compressibility tests. Pentech Press London.
- Hedges, J.I. and Keil, R.G., 1995. Sedimentary organic matter preservation: an assessment and speculative synthesis. *Marine Chemistry*, Vol. 49, 81–115.

- Heip, C.H.R., Goosen, N.K., Herman, P.J., Kromkamp, J., Middelburg, J.J. and Soetaert, K., 1995. Production and consumption of biological particles in temperate tidal estuaries. *Oceanographic Marine Biology Annular reviews*, Vol. 33, 1–150.
- Herman, P.J.M., Middelburg, J.J., Heip, C.H.R., 2001. Benthic community structure and sediment processes on an intertidal flat: results from the ECOFLAT project. *Continental Shelf Research*, Vol. 21, 2055-2071.
- Houwing, E.J., 2000. Sediment dynamics in the pioneer zone in the land reclamation area of the Wadden Sea, Groningen, The Netherlands. Ph.D. thesis, Universiteit Utrecht, the Netherlands.
- Huisman, M. and Van Kesteren, W.G.M., 1998. Consolidation theory applied to the Capillary Suction Time (CST) apparatus. *Water Science and Technology*, 37(6-7), 117-124.
- Hussein, E.M.A., 2003a. Handbook on radiation probing, gauging, imaging and analysis: Volume I: Basics and techniques. Kluwer Academic Publishers, 66-69.
- Hussein, E.M.A., 2003b. Handbook on radiation probing, gauging, imaging and analysis: Volume II: Applications and design. Kluwer Academic Publishers, 465-466.
- Jacobs, W., 2006. Eco-morphology of estuaries and tidal lagoons: Literature review and experiments on sand-mud mixtures. TU report, No. 1-06. Delft University of Technology, faculty of Civil Engineering and Geosciences.
- Jacobs, W., Van Kesteren, W.G.M. and Winterwerp, J.C., 2007a. Permeability and consolidation of sediment mixtures as a function of sand content and clay mineralogy. *International Journal of Sediment Research*, Vol. 22:3, 180-187.
- Jacobs, W., Van Kesteren, W.G.M. and Winterwerp, J.C., 2007b. Strength of sediment mixtures as a function of sand content and clay mineralogy. Sediment and Ecohydraulics, IntercoH 2005, Saga, Japan. *Proceedings in Marine Science*, Vol. 9, 91-107. Kusuda, T., Yamanishi, H., Spearman, J. and Gailani, J.Z. (Editors).
- Jacobs, W. and Van Kesteren, W.G.M., 2009. Hydraulic Strength and Permeability (HPS) probe. A new device to measure *in-situ* material properties of intertidal sand-mud mixtures. Deltares report.
- Jacobs, W., Eelkema, M., Limburg, H. and Winterwerp, J.C., 2009. A new radiometric instrument for *in-situ* measurements of physical sediment properties. *Marine and Freshwater Research*, Vol. 60, 727-736.
- Jacobs, W., Cann, P., Le Hir, P and Van Kesteren, W.G.M., 2010. Erosion threshold of artificial sand-mud mixtures., IntercoH 2007, Brest, France. *Continental Shelf Research*.
- Jonsson, P.R., Van Duren, L.A., Amielh, M., Asmus, R., Aspden, R.J., Daunys, D., Friedrichs, M., Friend, P.L., Olivier, F., Pope, N., Precht, E., Sauriau, P.-G. and Schaaff, E., 2006. Making water flow: a comparison of the hydrodynamic characteristics of 12 different benthic biological flumes. *Aquatic Ecology*, Vol. 40, 409-438.
- Kandiah, A., 1974. Fundamental aspects of surface erosion of cohesive soils. Ph.D. thesis, University of California, USA.
- Kim, J., Moin, P. and Moser, R., 1987. Turbulence statistics in fully developed channel flow at low Reynolds number. *Journal of fluid mechanics*, Vol. 177, 133-166.
- Knaapen, M.A.F., Holzhauser, H., Hulscher, S.J.M.H., Baptist, M.J. and De Vries, M.B., 2003. On the modelling of biological effects on morphology in estuaries and seas. In: Sánchez-Arcilla, A. & Bateman, A. (Editors), RCEM 2003. *Proceedings of the Third LAHR Symposium on River, Coastal and Estuarine Morphodynamics*, 773-783. Madrid, Spain: IAHR. ISBN 90-805649-6-6.

- Koomans, R.L., 2001. Sand in motion: Effects of density and grain size. Ph.D. thesis, Rijksuniversiteit Groningen.
- Kozeny, J., 1927. Über kapillare Leitung des Wasser in Boden. Wien, Akad. Wiss., Vol. 136, 271.
- Kranenburg, C., 1994. The fractal Structure of Cohesive Sediment Aggregates. *Estuarine, Coastal and Shelf Science*, Vol. 39, 451-460.
- Kranenburg, C. and Winterwerp, J.C., 1997. Erosion of fluid mud layers – I: Entrainment model. *ASCE, Journal of hydraulic engineering*, Vol. 123-6, 504-511.
- Laksanalamai, J., 2007. Erosion tests with the annular flume. M.Sc. thesis, Delft University of Technology. Available at (accessed 1 October 2010): <http://www.citg.tudelft.nl/live/pagina.jsp?id=4de0d195-5207-4e67-84bb-455c5403ae47&lang=en>.
- Le Hir, P., Cann, P., Waeles, B., Jestin, H., and Bassoullet, P., 2006 (in French). Instrumentation légère pour la mesure de l'érodabilité des sédiments vaseux ou sablo-vaseux. *IXèmes Journées Nationales Génie Côtier-Génie Civil*, Brest, 12-14 Septembre 2006.
- Le Hir, P., Monbet, Y. and Orvain, F., 2007a. Sediment erodability in sediment transport modelling: Can we account for biota effects? *Continental Shelf Research*, Vol. 27, 1116–1142.
- Le Hir, P., Cann, P., Waeles, B., Jestin, H., and Bassoullet, P., 2007b. Erodability of natural sediments: experiments on sand/mud mixtures from laboratory and field erosion tests. Sediment and Ecohydraulics, Intercoh 2005, Saga, Japan. *Proceedings in Marine Science*, Vol. 9. Kusuda, T., Yamanishi, H., Spearman, J. and Gailani, J.Z. (Editors).
- Lucas, C.H., Widdows, J. and Wall, L., 2003. Relating spatial and temporal variability in sediment chlorophyll a and carbohydrate distribution with erodibility of an intertidal flat.
- Malkawi, A.I.H., Alawneh, A.S. and Abu-Safaqah, O.T., 1999. Effects of organic matter on the physical and the physicochemical properties of an illitic soil. *Applied Clay Science*, Vol. 14, 257–278.
- Mastbergen D.R. and van den Berg, J.H., 2003. Breaching in fine sands and the generation of sustained turbidity currents in submarine canyons. *Sedimentology*, Vol. 50, 625-637.
- McCave, N., 2006. Laser vs. settling velocity differences in silt grain size measurements: estimation of palaeocurrent vigour. *Pentech Sedimentology*, Vol. 53, 919-928.
- Meadows, P.S., Tait, J., 1989. Modification of sediment permeability and shear strength by two burrowing invertebrates. *Marine Biology*, Vol. 101, 75–82.
- Mehta, A.J. and Partheniades, E., 1979. Kaolinite resuspension properties. *Journal of the Hydraulics Division*, Proceedings of the ASCE, Vol. 105, 411-416.
- Merkelbach, L., 2000. Consolidation and strength evolution of soft mud layers. Ph.D. thesis, University of Technology Delft, the Netherlands, ISSN 016906548, Report No. 00-2.
- Middelburg, J.J. and Herman, P. J. M., 2007. Organic matter processing in tidal estuaries. *Marine Chemistry*, Vol. 106, 127– 47.
- Mitchell, J.K., 1976. Fundamentals of soil behaviour. John Wiley and Sons, Inc., New York, University of California, Berkeley. Series in soil engineering. ISBN 0471611689.
- Mitchell, J.K. and Santamarina, C.J., 2005. Biological considerations in geotechnical engineering. *Journal of geotechnical and geoenvironmental engineering*, Vol. 131-10, 1222-1233.
- Mitchener, H. and Torfs, H., 1996. Erosion of mud/sand mixtures. *Coastal Engineering*, Vol. 29, 1-25.

- Montserrat F., Van Colen C., Degraer S., Ysebaert T., Herman, P. M. J., 2008. Ecosystem engineering effects of a benthic community: a defaunation study. *Marine Ecology Progress Series*, Vol. 372, 43–59.
- Montserrat F., 2011. Estuarine Ecosystem Engineering: sediment-biota interactions and their implications in the estuarine intertidal. Ph.D. thesis, University of Technology Delft, the Netherlands.
- Murray, J. M. H., Meadows, A. and Meadows, P.S., 2002. Biogeomorphological implications of microscale interactions between sediment geotechnics and marine benthos: a review. *Geomorphology*, Vol. 47:1, 15-30.
- NEN 5104, 1989. Geotechnics: Classification of unconsolidated soil samples (in Dutch). Nederlands Normalisatie Instituut.
- NEN 5106, 1991. Geotechnics: Determination of undrained shear strength – in situ vane test (in Dutch). Nederlands Normalisatie Instituut.
- NEN 5118, 1991, Geotechnics. Determination of the one-dimensional consolidation properties of soil (in Dutch). Nederlands Normalisatie Instituut.
- NEN 5124, 1993. Geotechnics: Laboratory determination of permeability of soil by the falling head method (in Dutch). Nederlands Normalisatie Instituut.
- Nezu, I. and Nakagawa, H., 1993. Turbulence in open-channel flows. IAHR-Monograph, Balkema.
- Odell, R.T., Thornburn, T.H. and McKenzie, L.J., 1960. Relationships of Atterberg Limits to some other properties of Illinois soils. *Proceedings of the soil science society of America*, Vol. 24, 297-300.
- Orvain, F., Le Hir, P. Sauriau, P.G., 2003. A model of fluffy layer erosion and subsequent bed erosion in the presence of the bioturbator, *Hydrobia ulvae*. *Journal of marine Research*, Vol. 61, 823-851.
- Orvain, F., Sauriau, P.G., Bacher, U., and Prineau, M., 2006. The influence of sediment cohesiveness on bioturbation effects due to *Hydrobia ulvae* on the initial erosion of intertidal sediments: a study combining flume and model approaches, *Journal of Sea Research*, Vol. 55, 54–73.
- Orvain, F., Sauriau, P.-G, Le Hir, P., Guillou, G., Cann, P. and Paillard, M., 2007. Spatio-temporal variations in intertidal mudflat erodability: Marennes-Ole'ron Bay, western France. *Continental Shelf Research*, Vol. 27, 1153–1173.
- Paarlberg, A. J., Knaapen, M. A. F., De Vries, M. B., Hulscher, S. J. M. H. and Wang, Z. B., 2005. Biological influences on morphology and bed composition of an intertidal flat. *Estuarine Coastal Shelf Science*, Vol. 64:4, 577-590.
- Panagiotopoulos, I. and Voulgaris, G. and Collins, M.B., 1997. The influence of clay on the threshold of movement of fine sandy beds. *Coastal Engineering*, Vol. 32, 19-43.
- Parchure, T.M. and Mehta, A.J., 1985. Erosion of soft cohesive sediment deposits. *Journal of Hydraulic Engineering*, Vol. 111:10, 1308-1326.
- Partheniades, E., 1962. A study of erosion and deposition of cohesive soils in salt water. Ph.D. thesis, University of California, Berkeley.
- Partheniades, E., 1965. Erosion and deposition of cohesive soils. *Journal of the Hydraulics Division*, Proceedings of the ASCE, Vol. 91, 105-139.
- Partheniades, E., 1971. Erosion and deposition of cohesive materials. In: Shen, H.W. (Editor), *River Mechanics*, Fort Collins, CO, Ch. 25, 1–91.
- Paterson, D.M., 1997. Biological mediation of sediment erodibility, Ch 14, 215-229. John Wiley and Sons Ltd., University of St Andrews, UK.

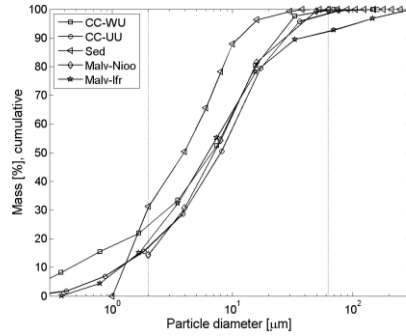
- Perillo, G.M.E., 1995. Geomorphology and sedimentology of estuaries: an introduction. In Perillo, G.M.E. (Editor), Geomorphology and sedimentology of estuaries. *Developments in sedimentology*, Vol. 53, 1-16. Amsterdam: Elsevier Science B.V.
- Prins, T.C., Smaal, A.C., Pouwer, A.J. and Dankers, N., 1996. Filtration and resuspension of particulate matter and phytoplankton on an intertidal mussel bed in the Oosterschelde Estuary (SW Netherlands). *Marine Ecology Progress Series*, Vol. 142:1-3, 121-134.
- Raudkivi, A.J., 1990. Loose Boundary Hydraulics. Oxford: Pergamon, ISBN 0080340741.
- Reading, H.G. (Editor), 1986. Sedimentary processes: Processes, Facies and Stratigraphy. Department of Earth sciences, University of Oxford. Blackwell Science. ISBN 0632012234.
- Righetti, M. and Lucarelli, C., 2007. May the Shields theory be extended to cohesive and adhesive benthic sediments? *Journal of Geophysical research*, Vol. 112.
- Roberti, J.R., 2001. Meten met Medusa (in Dutch). RIKZ Rijkswaterstaat 2001.035, 7.
- Roberts, J., Jepsen, R., Gotthard, D. and Lick, W., 1998. effects of particle size and bulk density on erosion of quartz particles. *Journal of hydraulic Engineering*, Vol. 124:12, 1261-1267.
- Roscoe, K.H. and Burland, J.B., 1968. On the generalised stress-strain behaviour of wet clay. In J. Heyman and F.A. Leckie, editors, Engineering Plasticity, pages 535-609. Cambridge: Cambridge University Press.
- Sanford, L.P. and Maa, J.P.Y., 2001. A unified erosion formulation for fine sediments. *Marine Geology*, Vol. 179, 9-23.
- Sanford, L.P., 2006. Uncertainties in sediment erodibility estimates due to a lack of standards for experimental protocols and data interpretation. *Integrated environmental assessment and management*. Vol. 2:1, 29-34.
- Santamarina, J.C., Klein, K.A., Wang, Y.H. and Prencke, E., 2002. Specific surface: determination and relevance. *Canadian Geotechnical Journal*, Vol. 39:1, 233-241.
- Schlichting, H., 1979. Boundary-Layer Theory. McGraw-Hill Book Company, New York, Series in Mechanical Engineering, 817. ISBN 10 0070553343.
- Schofield, A.N. and Wroth, C.P., 1968. Critical state soil mechanics. McGraw-Hill, London.
- Seed, H.B., Woodward, R.J. and Lundgren, R., 1962. Prediction of swelling potential for compacted clays. *Journal of soil mechanics*. Foundation Division, American Society of Civil Engineers, 88 (SM 3).
- Sheng, Y.P., 1989. Consideration of flow in rotating annuli for sediment erosion and deposition studies. *Journal of coastal research*, special issue, Vol. 5, 207-216.
- Shields, A., 1936. Anwendung der Aehnlichkeitsmechanik und der Turbulenzforschung auf die Geschiebebewegung. *Mitteilungen der Preussischen Versuchsanstalt für Wasserbau und Schiffbau*, Berlin, NW 87.
- Skempton, A.W., 1965. The colloidal activity of clay. *Proceedings of the 3rd International Conference on Soil Mechanics and Foundation Engineering*, I, 57-61.
- Smerdon, E.T. and Beasley, R.P., 1959. The tractive force theory applied to stability of open channels in cohesive soil. *Agricultural Experimental Stability Research Bulletin*, Vol. 715, 1-36.
- Terzaghi, K., 1940. Theoretical soil mechanics. Wiley, New York.
- Terzaghi, K., and Peck, R.B. 1967, Soil mechanics in Engineering Practice. John Wiley and Sons, Inc., New York.

- Tijss, M., 2007. RhoC: A novel system for soil water content, density and composition measurement. M.Sc. thesis, KVI internal report S-126, Medusa Explorations internal report P-063.
- Tolhurst, T.J., Black, K.S., Shayler, S.A., Mather, S., Black, I., Baker, K. and Paterson, D.M., 1999. Measuring the *in situ* erosion shear stress of intertidal sediments with the Cohesive Strength Meter (CSM). *Estuarine, Coastal and Shelf Science*, Vol. 49, 281-294.
- Tolhurst, T.J., Riethmüller, R. and Paterson, D.M., 2000a. In situ versus laboratory analysis of sediment stability from intertidal mudflats. *Continental Shelf Research*, Vol. 20, 1317-1334.
- Tolhurst, Black, K.S., Paterson, D.M., Mitchener, H.J., Termaat, G.R. and Shayler, S.A., 2000b. A comparison and measurement standardisation of four *in situ* devices for determining the erosion shear stress of intertidal sediments. *Continental Shelf Research*, Vol. 20, 1397-1418.
- Tolhurst, T.J., Friend, P.L., Watts, C., Wakefield, R., Black, K.S. and Paterson, D.M., 2006. The effects of rain on the erosion threshold of intertidal cohesive sediments. *Aquatic ecology*, Vol. 40, 533-541.
- Torfs, H., 1995. Erosion of mud/sand mixtures. Ph.D. thesis, Katholieke Universiteit Leuven, Belgium. ISBN 905682001.
- Uittenbogaard, R.E., 2008. Personal communication.
- Van den Berg, J.H., 1981. Rhythmic seasonal layering in a mesotidal channel fill sequence, Oosterschelde mouth, the Netherlands. *Special Publication of the International association of Sedimentologists*, Vol. 5, 147-159.
- Van der Graaf, E.R., Koomans, R.L., Limburg, H. and De Vries, K., 2007. In situ radiometric mapping as a proxy of sediment contamination: Assessment of the underlying geochemical and physical principles. *Applied radiation and isotopes*, Vol. 65, 619-633.
- Van der Vegt, M., 2007. Personal communication.
- Van der Wal, D. and Herman, P.M.J. and Wielemaker-van den Dool, A., 2005. Characterisation of surface roughness and sediment texture of intertidal flats using ERS SAR imagery. *Remote sensing and environment*, Vol. 98, 96-109.
- Van Duren, L.A., Herman, P.M.J. Sandee, A.J.J., Heip, C.H.R., 2006. Effects of mussel filtering activity on boundary layer structure. *Netherlands Journal of Sea Research*, Vol. 55, 3-14.
- Van Eck, G.Th.M., 1999. De ScheldeAtlas, een beeld van een estuarium (in Dutch).
- Van Kessel, T., 1998a. Belinitiatie en belgroei in sliblagen (in Dutch). Delft|Hydraulics report DM 18 (Z2314).
- Van Kessel, T., 1998b. Scheurvorming in slib: experimenteel onderzoek (in Dutch). Delft|Hydraulics report DM 21.
- Van Kesteren, W.G.M., 1996. Slope stability analysis Orange River mouth. Report No. Z2739. Delft: WL|DelftHydraulics.
- Van Kesteren, W.G.M., Cornelisse, J.M. and Kuijper, G., 1997. Dynaster bed model bed strength, liquefaction and erosion. In: *Cohesive Sediments* (Report No. 55). Delft: WL|DelftHydraulics and Rijkswaterstaat.
- Van Kesteren, W.G.M., 2004 & 2008. Personal communication.
- Van Ledden, M., 2003. Sand-mud segregation in estuaries and tidal basins. Ph.D. thesis, University of Technology Delft, the Netherlands, ISSN 01696548, Report No. 03-2.

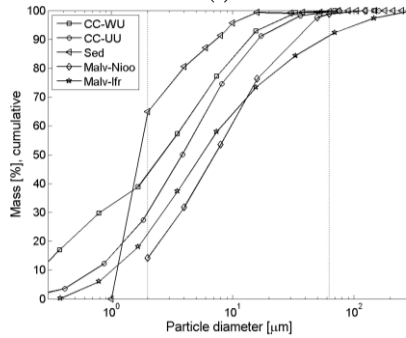
- Van Ledden, M. and Van Kesteren, W.G.M. and Winterwerp, J.C., 2004. A conceptual framework for the erosion behaviour of sand-mud mixtures. *Continental Shelf Research*, Vol. 24, 1-11.
- Van Maren, D.S., Winterwerp, J.C., Wang, Z.Y. and Pu, Q., 2009. Suspended sediment dynamics and morphodynamics in the Yellow River, China. *Sedimentology*. Vol. 56:3, 785-806.
- Van Paassen, L.A., 2002. The influence of pore fluid salinity on consolidation behaviour and undrained shear strength development of clayey soils. M.Sc thesis, Technical University Delft, The Netherlands. ISSN 13865072.
- Van Paassen, L.A. and Gareau, L.F., 2004. Effect of pore fluid salinity on compressibility and shear strength development of clayey soils. In: *Engineering geology for infrastructure planning in Europe*, Vol. 104, 327-340. Springer Berlin. ISBN 978-3-540-21075-7.
- Van Prooijen, B.C. and Winterwerp, J.C., 2010. A stochastic formulation for erosion of cohesive sediments. *Journal of Geophysical Research*, Vol. 115.
- Van Rijn, L.C., 1993. Principles of sediment transport in rivers, estuaries and coastal seas. Amsterdam: Aqua Publications, ISBN 9080035629.
- Van Wijngaarden, M, Venema, L.B. and De Meijer, R.J., 2002a. Radiometric sand mud characterisation in the Rhine-Meuse Estuary, Part A. Fingerprinting. *Geomorphology*, Vol. 43, 87-101.
- Van Wijngaarden, M., Venema, L.B. and De Meijer, R.J., 2002b. Radiometric sand mud characterisation in the Rhine-Meuse Estuary, Part B. In situ Mapping. *Geomorphology*, Vol. 43, 103-116.
- Vanoni, V.A., 1964. Measurements of critical shear stress for entraining fine sediments in a boundary layer. W.M. Keck Laboratory for hydraulics and Water Resources, California Institute of Technology, USA. Report No. KH-R-7, 47.
- Venema, L.B. and De Meijer, R.J., 2001. Natural radionuclides as tracers of the dispersal of dredge spoil dumped at sea. *Journal of Environmental Radioactivity*, Vol. 55:3, 221-239.
- Verhoef, P.N.W., 1992. The methylene blue adsorption test applied to geomaterials. Memoires of the Centre of Engineering Geology, Delft, the Netherlands, Vol. 101, 76.
- Verlaan, P.A.J., 1998. Mixing of marine and fluvial particles in the Scheldt estuary. Ph.D. thesis, University of Technology Delft, the Netherlands, Report No. 98-06.
- Vesic, A.C., 1972. Expansion of cavities in infinite soil mass. *Journal Soil Mechanics and Foundation Division, ASCE*, Vol. 98, 265-290.
- Watts, C.W., Tolhurst, T.J., Black, K.S. and Whitmore A.P., 2003. In situ measurements of erosion shear stress and geotechnical shear strength of the intertidal sediments of the experimental managed realignment scheme at Tollesbury, Essex, UK. *Estuarine, Coastal and Shelf Science*, Vol. 58, 611-620.
- Weaver, C.E., 1989. Clays, Muds, and Shales, *Elsevier, Developments in sedimentology*, ISBN 0444873813.
- Whitehouse, R.J.S., Bassoullet, P., Dyer, K.R., Mitchener, H.J. and Roberts, W., 2000. The influence of bedforms on flow and sedimeny transport over intertidal mudflats. *Continental Shelf Research*, Vol. 20, 1099-1124.
- Widdows, J., Brinsley, M. D., Bowley, N. and Barrett, C., 1998. A Benthic Annular Flume for In Situ Measurement of Suspension Feeding/Biodeposition Rates and Erosion Potential of Intertidal Cohesive Sediments. *Estuarine, Coastal and Shelf Science*, Vol. 46, 27-38.

- Widdows, J., Brinsley, M.D., Salkeld, P.N. and Lucas, C.H., 2000. Influence of biota on spatial and temporal variation in sediment erodability and material flux on a tidal flat (Westerschelde, The Netherlands). *Marine ecology progress series*, Vol. 194, 23-27.
- Widdows, J. and Brinsley, M., 2002. Impact of biotic and abiotic processes on sediment dynamics and the consequences to the structure and functioning of the intertidal zone. *Journal of Sea Research*, Vol. 48-2, 143-156.
- Widdows, J. Friend, P.L., Bale, A.J., Brinsley, M.D., Pop, N.D. and Thompson, C.E.L., 2007. Inter-comparison between five devices for determining erodibility of intertidal sediments. *Continental Shelf research*, Vol. 27, 1174-1189.
- Williamson, H.J. and Ockenden, M.C., 1993. Laboratory and field investigations of mud and sand mixtures. In: Wang, S.S.Y. (Editor), Proceedings of the First International Conference on Hydro-Science and Engineering, Washington, DC, *Advances Hydro-Science Engineering*, Vol. 1, 622–629.
- Winterwerp, J.C. and Van Kesteren, W.G.M., 2004. Introduction to the physics of cohesive sediment in the marine environment. *Elsevier, Developments in sedimentology*, ISBN 04444515534, ISSN 00704571
- Wood, R.G., Widdows, J., 2002. A model of sediment transport over an intertidal transect, comparing the influences of biological and physical factors. *Limnology and Oceanography*, Vol. 47-3, 848-855.
- Wood, R., Widdows, J., 2003. Modeling intertidal sediment transport for nutrient change and climate change scenarios. *The Science of the total environment*, Vol. 314-316, 637-649.
- Yallop, M.L., Paterson, D.M. and Wellsbury, P., 2000. Interrelationships between rates of microbial production, exopolymer production, microbial biomass, and sediment stability in biofilms of intertidal sediments. *Microbial Ecology*, Vol. 39, 116-127.

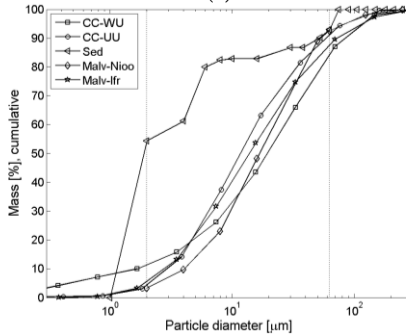
Appendix I: Grain size analyses



(a)



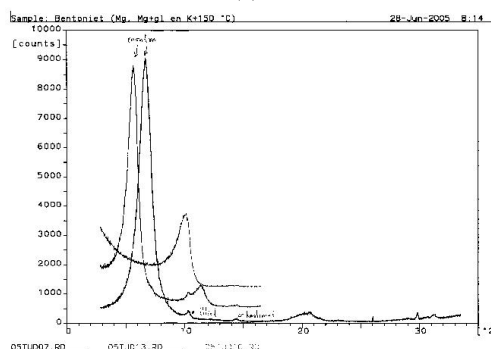
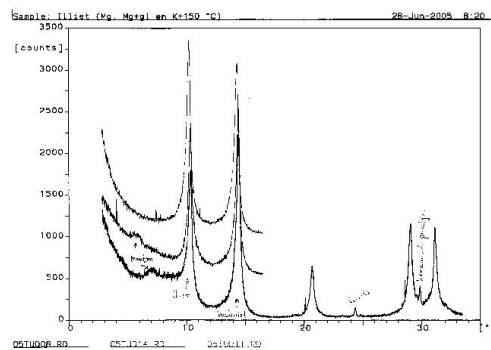
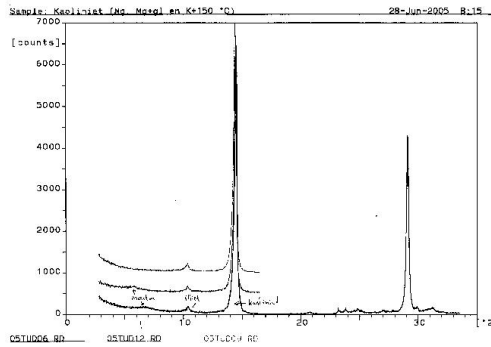
(b)



(c)

A.1. Results of different methods to determine the grain size analysis of kaolinite (a), illite (b) and bentonite (c). *CC-WU* refers to the Coulter Counter at the Wageningen University, *CC-UU* to the Coulter Counter at the Utrecht University, *Sed* to Sedigraph (GeoDelft/Deltares), *Malv-Nioo* to the Malvern at NIOO-Yerseke and *Malv-Ifr* to the Malvern at Ifremer-Brest.

Appendix II: Mineralogical analyses

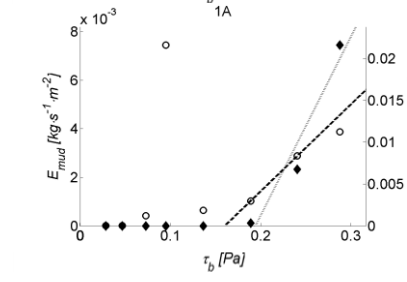
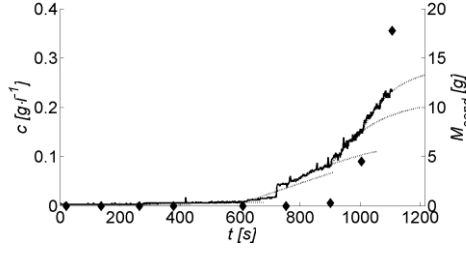
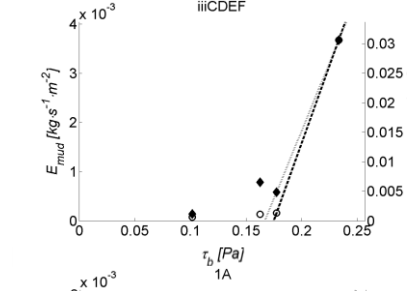
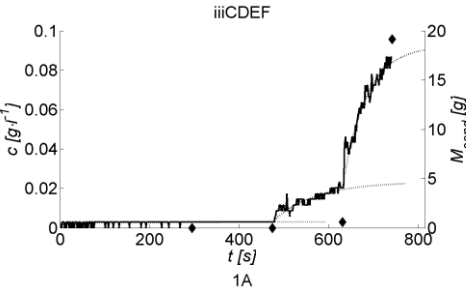
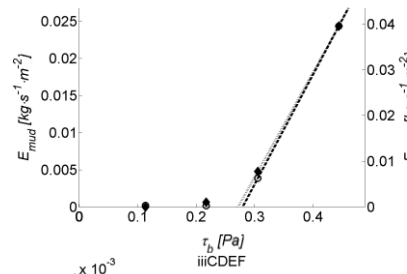
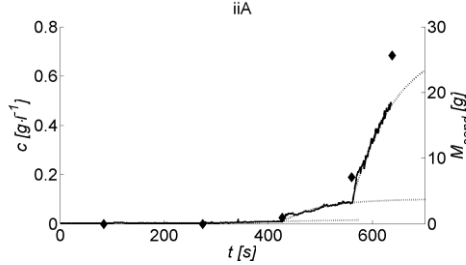
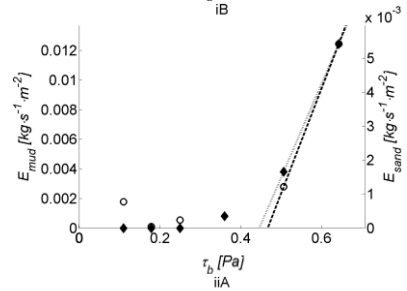
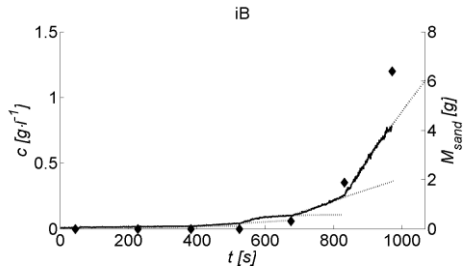
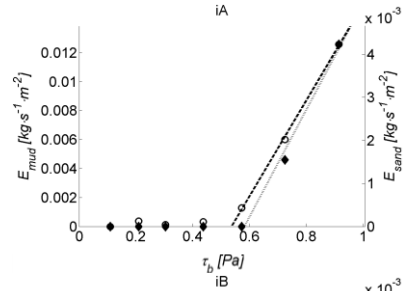
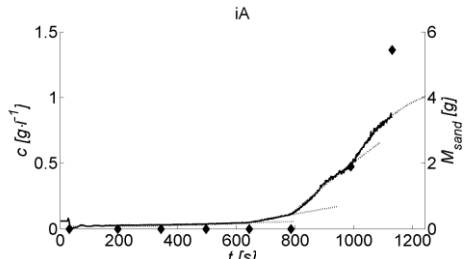


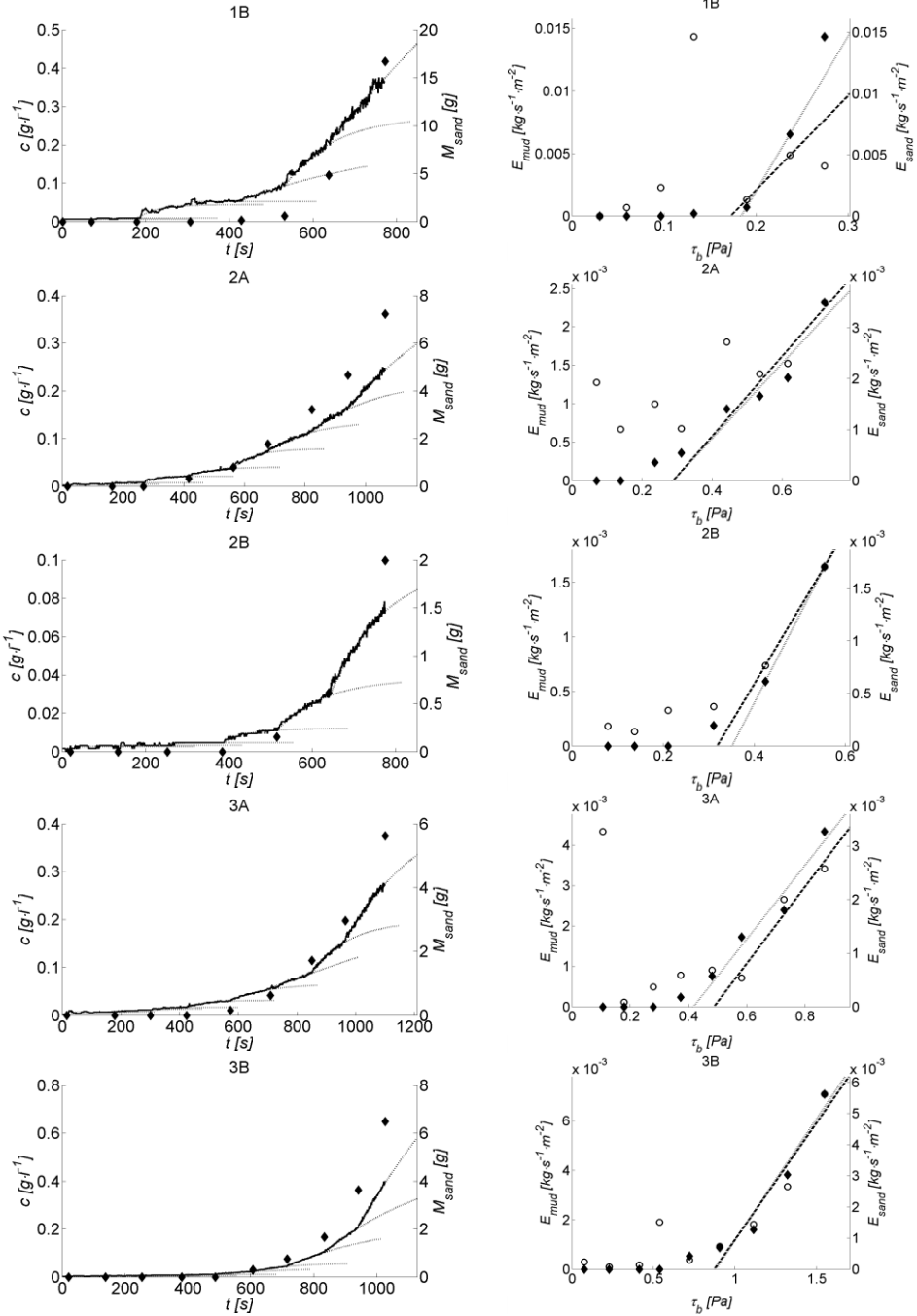
B.1 Results of X-ray mineralogical analyses on the purchased kaolinite (a), illite (b) and bentonite (c) with the counts per mineral as a function of the reflection angle. Peaks on the left indicate various clay minerals, whereas the peak on the right indicates quartz.

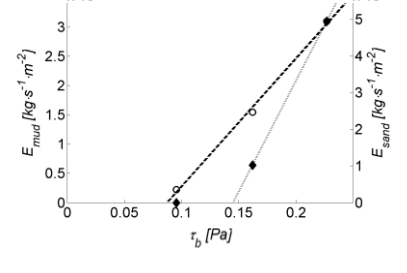
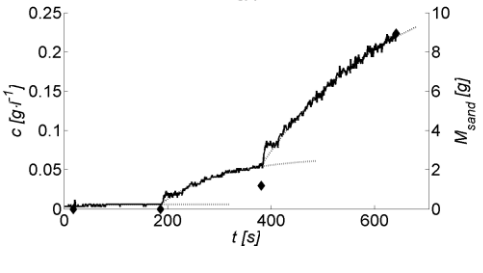
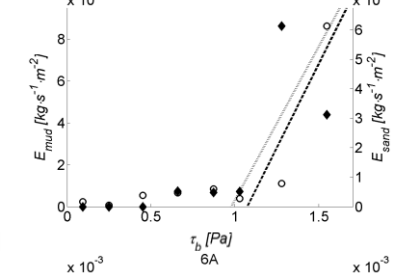
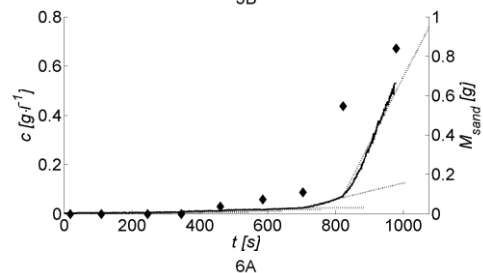
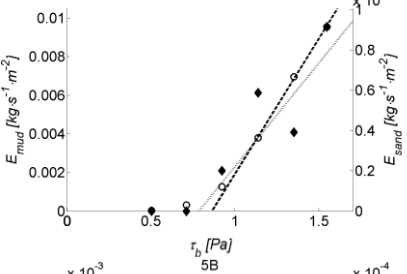
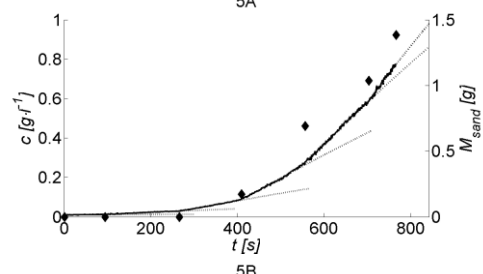
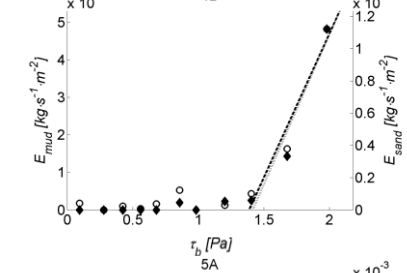
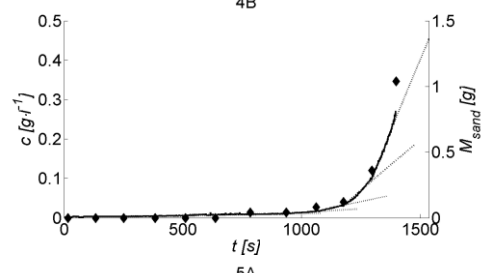
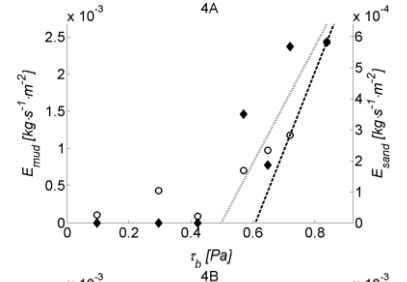
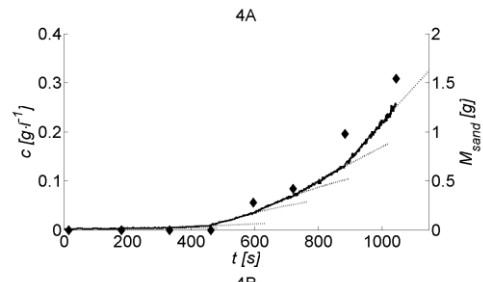
Appendix III: Results erosion tests CH 5

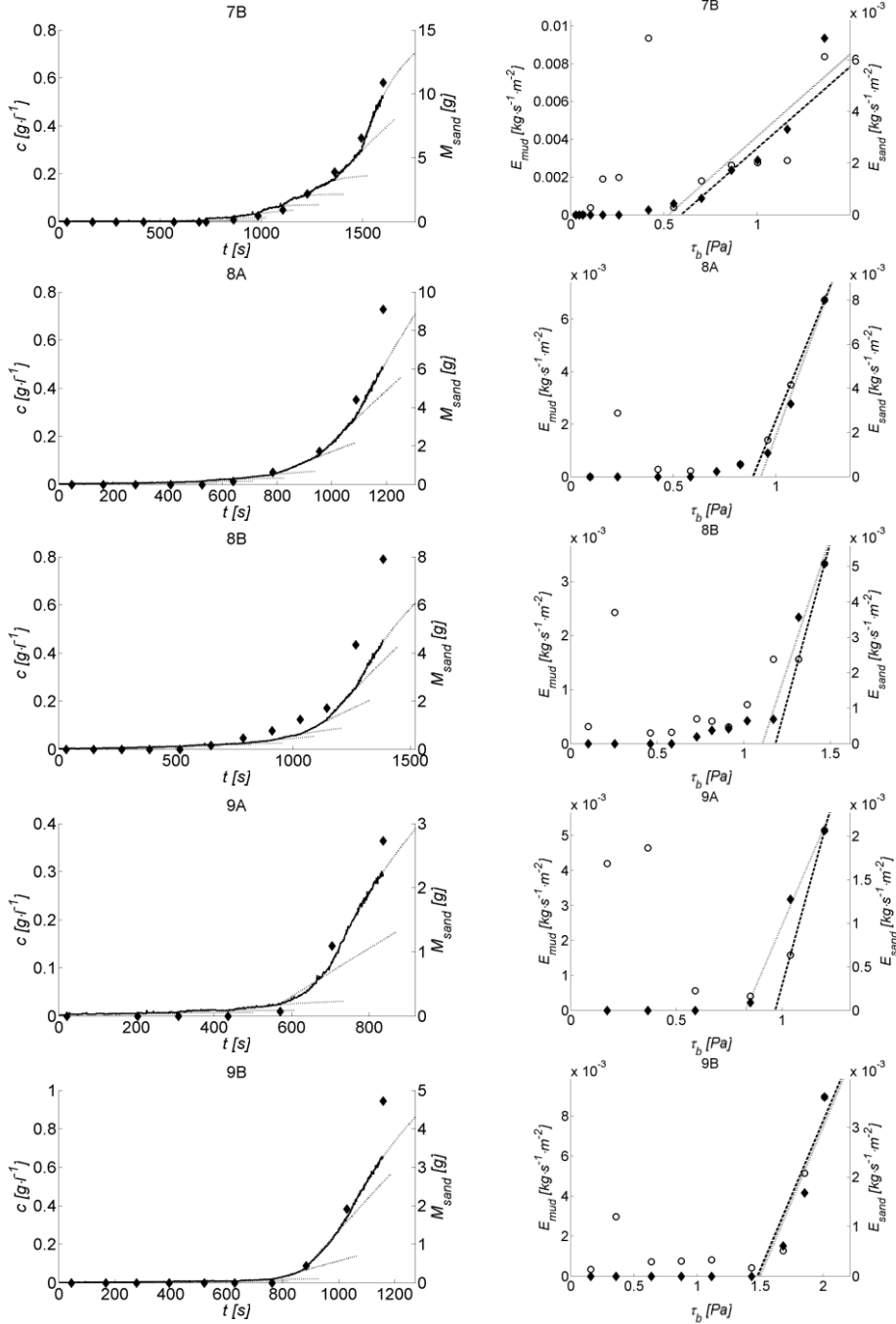
Below the erosion threshold τ_b and parameter M_s for surface erosion are listed in relation to PI and W_{rel} . The numbers refer to the sample number as listed in Table 12. Subsequently, the concentration profiles (left panels) and accompanying erosion rates (right panels) for all erosion tests using the small-scale straight flume are shown. The numbers above the figures indicate soil sample numbers as shown in Table 12. Panels at left show the concentration c [$g \cdot l^{-1}$] (left vertical axes) and mass of eroded sand M_{sand} [g] (\blacklozenge , right vertical axes) as a function of time [s]. Panels at right show the erosion rates of mud E_{mud} [$kg \cdot m^{-2} \cdot s^{-1}$] (\circ , left vertical axes) and sand E_{sand} [$kg \cdot m^{-2} \cdot s^{-1}$] (\blacklozenge , right vertical axes) as a function of the bed shear stress τ_b [Pa]. The dashed line fits E_{mud} , the dotted line E_{sand} . Note the different scales of the vertical axes in both panels.

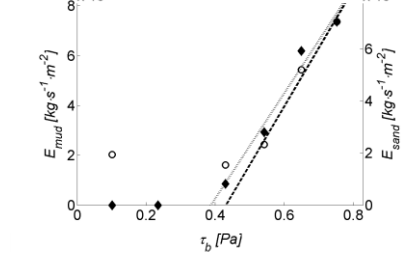
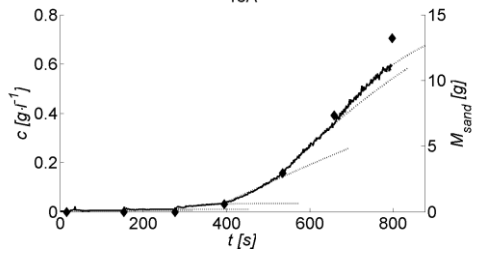
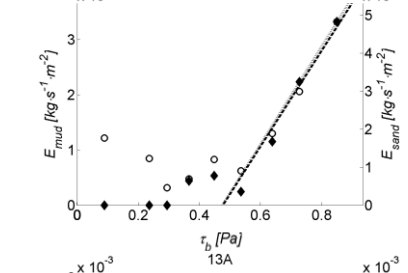
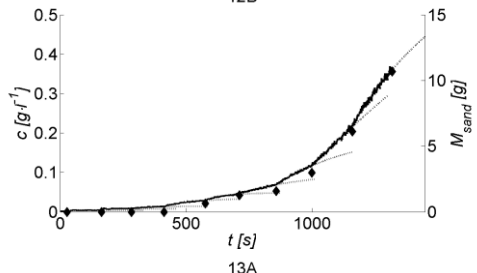
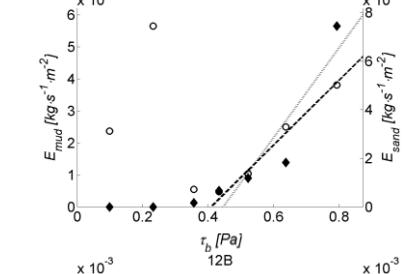
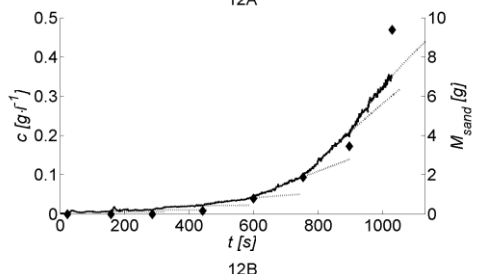
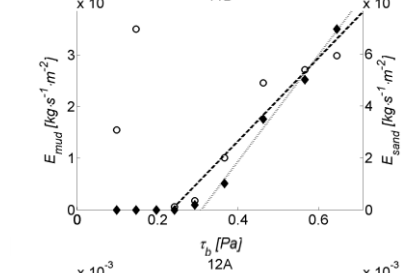
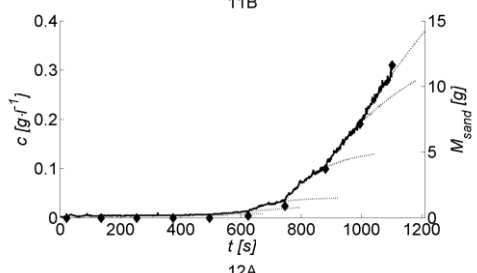
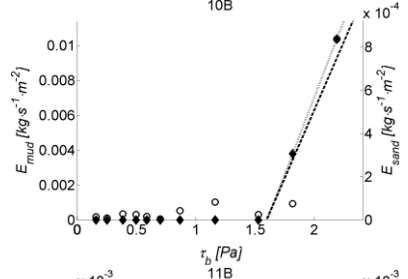
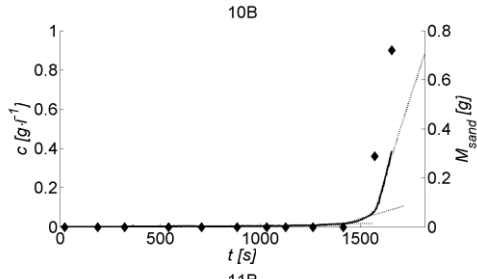
	No	PI^*	$\tau_{e,s}$	W_{rel}	M_s			
	[-]	[%]	[Pa]	[-]	[$kg \cdot m^{-2} \cdot s^{-1} \cdot Pa^{-1}$]			
Set 0	i.	0	0.56	0.46	-	-	0.0455	0.0982
	ii.	0	0.28	-	-	-	-	-
	iii.	0	0.17	-	-	-	0.5238	-
Set 1	1.	1.3	0.18	0.18	15.5	16.4	0.2496	0.2018
	2.	3.2	0.29	0.34	6.7	5.8	0.0126	0.0154
	3.	4.0	0.45	0.88	5.4	5.1	0.0164	0.0172
	4.	7.5	0.55	1.40	4.0	3.5	0.0122	0.0095
	5.	10.7	0.82	1.03	3.7	3.6	0.0149	0.0171
Set 2	6.	1.3	0.12	-	16.6	-	0.0821	-
	7.	2.7	-	0.56	-	8.0	-	0.0151
	8.	5.0	0.84	1.15	4.6	4.4	0.0389	0.0265
	9.	8.0	0.90	1.49	4.0	3.5	0.0277	0.0208
Set 3	10.	11.1	-	1.60	-	3.4	-	0.0171
	11.	2.0	-	0.27	-	8.2	-	0.0285
	12.	3.2	0.43	0.48	6.5	5.8	0.0287	0.0215
	13.	4.0	0.41	0.59	5.5	5.4	0.0437	0.0144
	14.	5.0	0.77	1.02	4.8	4.6	0.0330	0.0092
	15.	5.4	0.65	1.07	4.7	4.2	0.0304	0.0149
Set 4	16.	1.6	0.26	0.24	14.1	11.2	0.0443	0.0447
	17.	3.7	0.29	0.35	6.4	6.0	0.0464	0.0351
	18.	5.7	0.54	0.54	5.0	4.9	0.0492	0.0264
	19.	7.8	0.95	0.90	3.9	4.1	0.0088	0.0320
	20.	11.0	1.41	1.14	3.3	3.3	0.0164	0.0477
Set 5	21.	1.3	-	-	-	22.1	-	-
	22.	5.0	0.52	-	4.9	-	0.2438	-
	23.	6.6	0.40	0.26	3.6	3.5	0.0822	0.0718
	24.	13.5	0.72	-	2.7	-	0.0359	-
	25.	19.7	-	0.99	-	2.5	-	0.0165

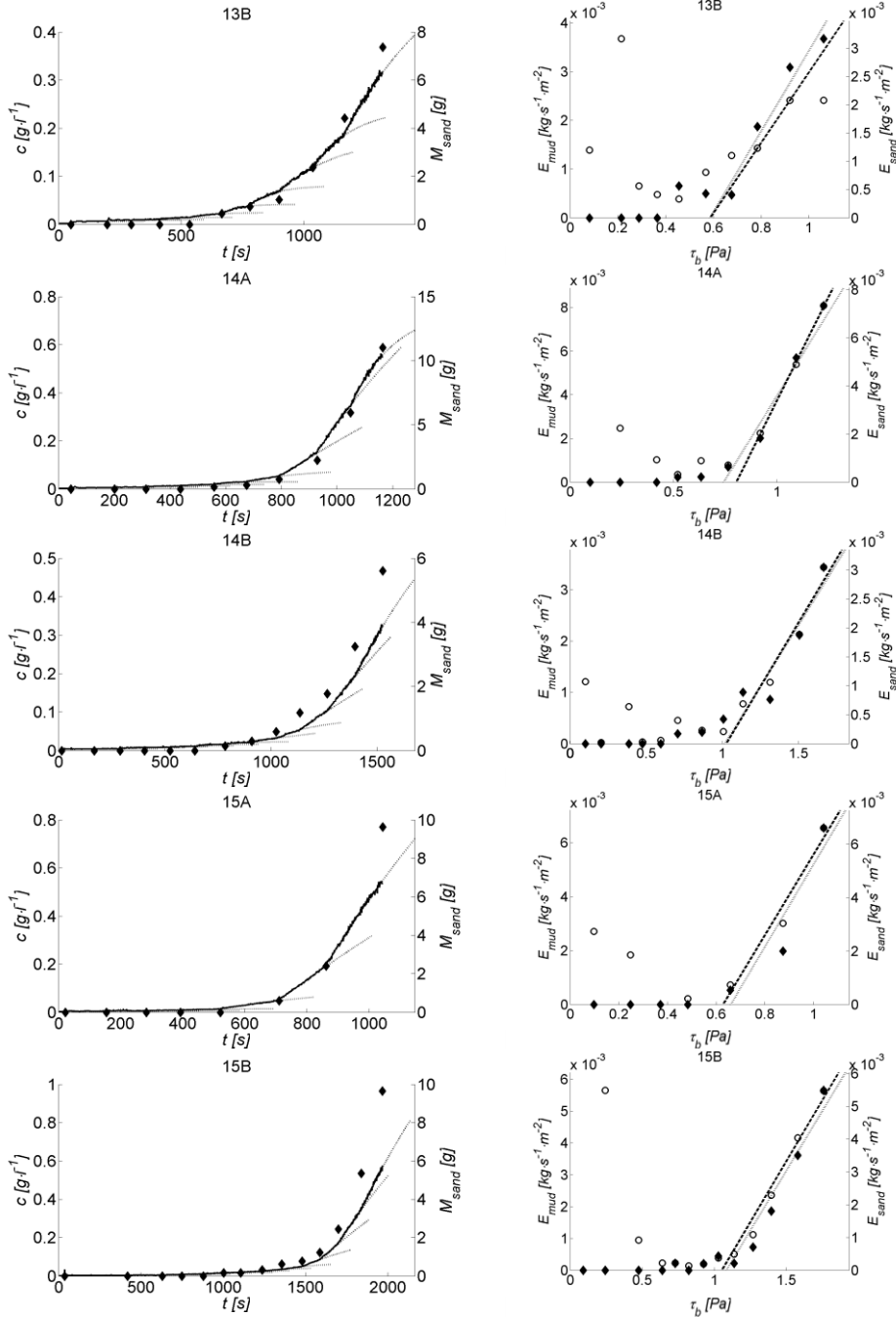


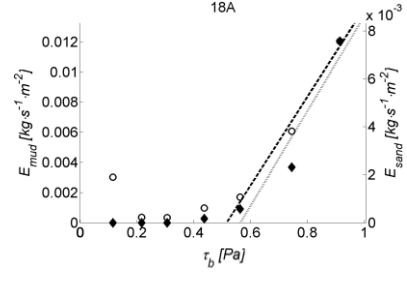
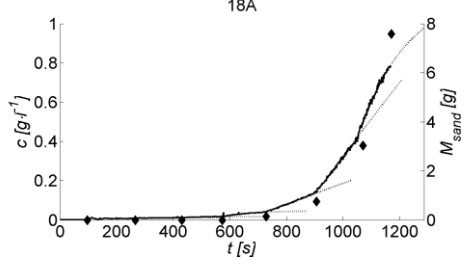
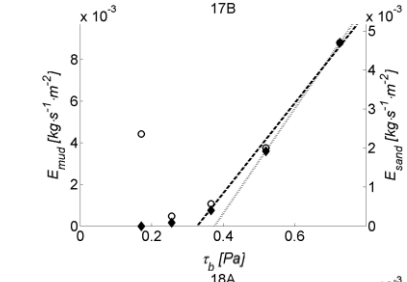
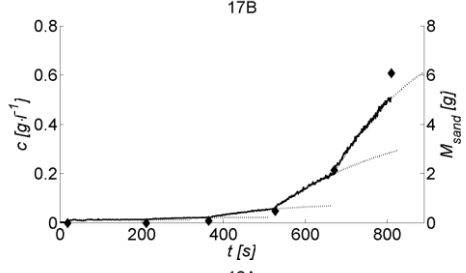
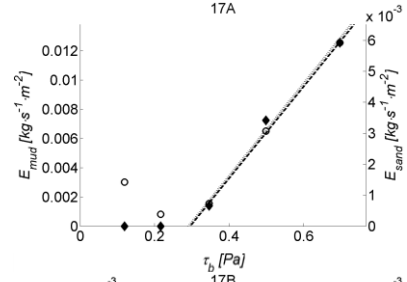
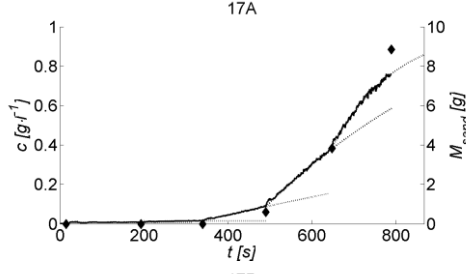
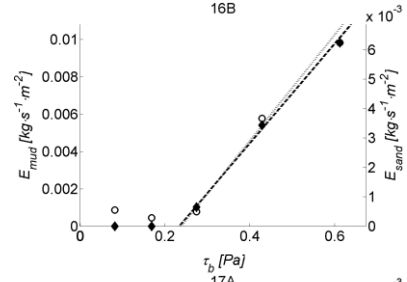
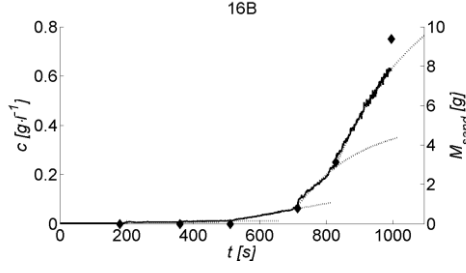
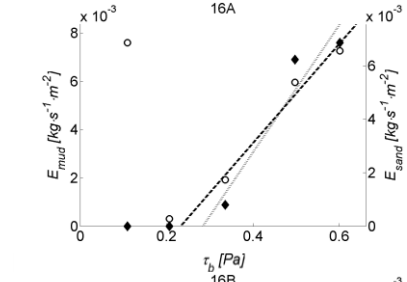
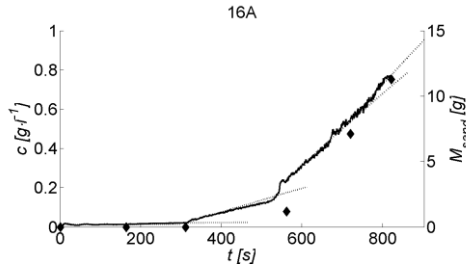


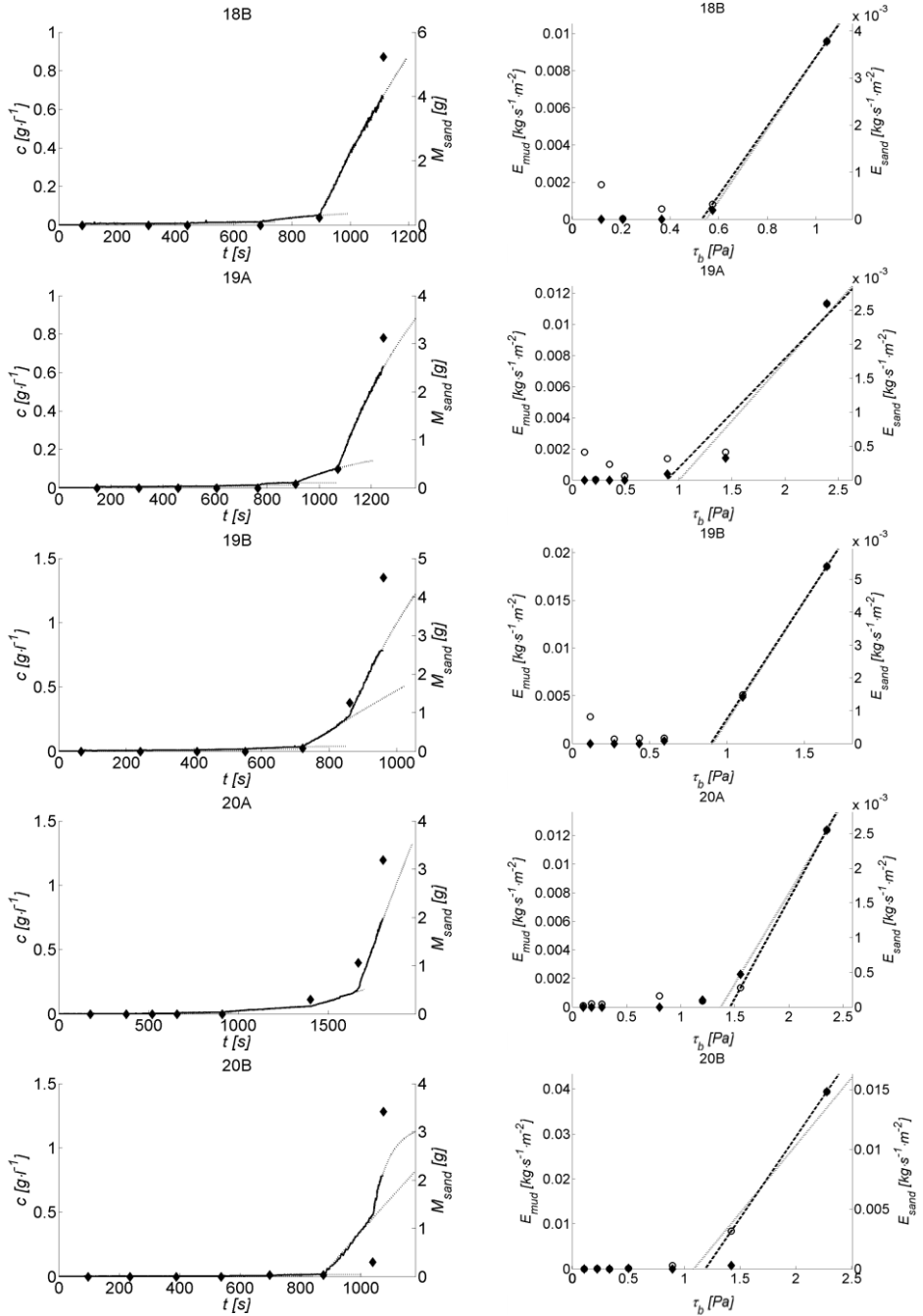


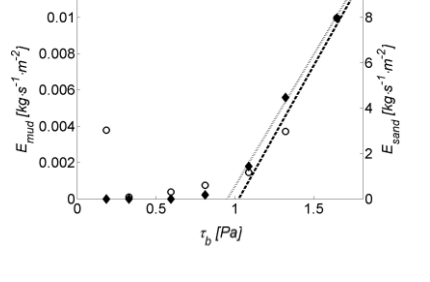
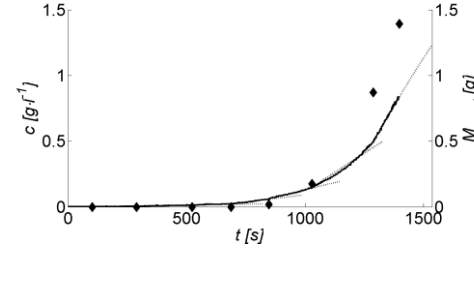
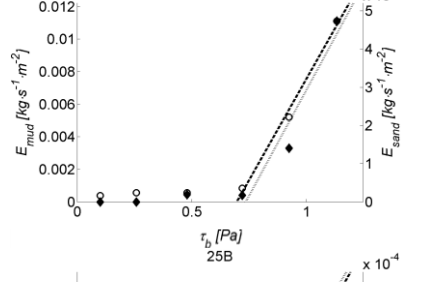
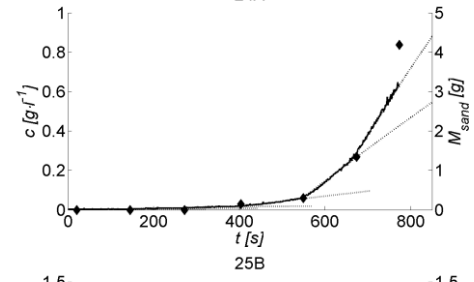
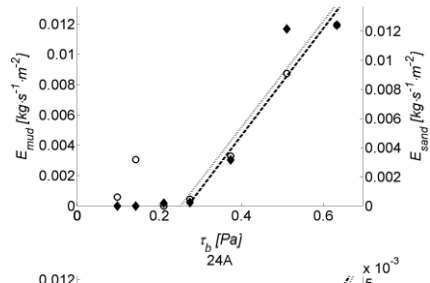
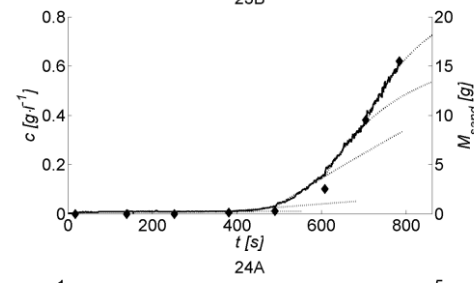
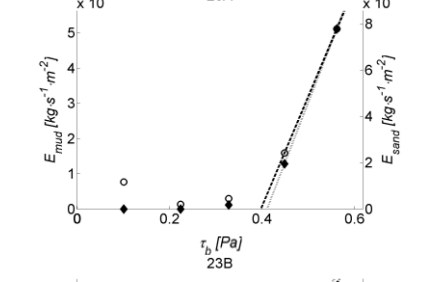
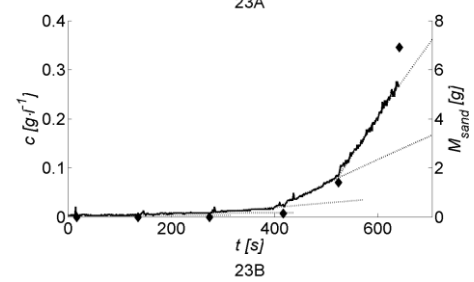
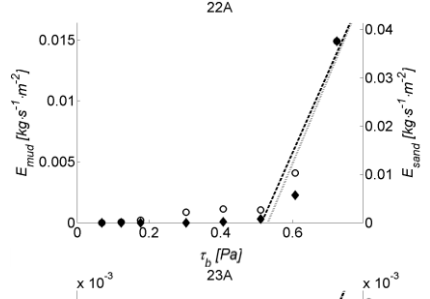
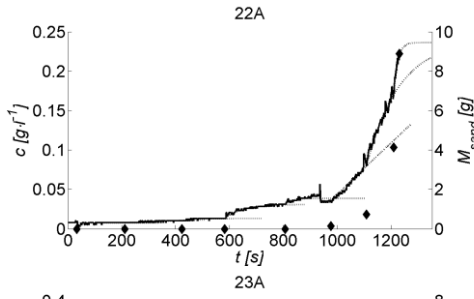












Appendix IV: Soil sample properties CH 7

The tables below list the properties for the hypothetical soil samples applied in Section 7.2. For each set two tables are shown: the 1st lists the sedimentological and bulk parameters of the soil samples, the 2nd all input parameters for the new surface erosion formulation.

Sand-mud mixtures (SM – A)

ζ_{cl} [%]	ζ_{si} [%]	ζ_{sa} [%]	ψ_{sasi} [%]	PI^* [%]	W [%]	n_{sasi} [%]	W_{rel} [-]
1.5	6	92.5	94	1	25	41	24.9
2	8	90	92	1.3	26	42	19.1
2.5	10	87.5	90	1.7	26	42	15.6
3	12	85	88	2	27	43	13.2
3.5	14	82.5	85	2.3	27	44	11.6
5	20	75	79	3.4	29	46	8.6
7	28	65	70	4.7	31	49	6.6
10	40	50	56	6.7	35	53	5.2
15	60	25	29	10.1	43	60	4.2
20	80	0	0	13.4	52	66	3.9

ρ_{bulk} [kg·m ⁻³]	$d_{50,m}$ [μm]	$\phi_{s,0}$ [%]	n_{fr} [-]	δ_e [mm]	c_u [Pa]	$m_{v,s}$ [Pa ⁻¹]	$k_v \cdot 10^6$ [m·s ⁻¹]	$c_v \cdot 10^6$ [m ² ·s ⁻¹]	M_s [kg·m ⁻² ·s ⁻¹ ·Pa ⁻¹]
1593	30	59	2.82	0.5	32	0.0037	100	2.79	0.2781
1580	30	58	2.81	0.4	28	0.0044	110	2.5557	0.3371
1568	30	58	2.8	0.4	28	0.005	120	2.4642	0.3502
1555	30	57	2.79	0.4	30	0.0054	140	2.6274	0.3675
1542	30	56	2.78	0.4	33	0.0058	150	2.6279	0.3466
1503	30	54	2.76	0.3	45	0.0066	130	1.9936	0.2014
1452	30	51	2.75	0.3	65	0.0073	110	1.545	0.1067
1375	30	47	2.73	0.3	96	0.0076	100	1.3501	0.0562
1246	30	40	2.71	0.4	145	0.0071	80	1.1467	0.0240
1118	30	34	2.7	0.5	175	0.0061	60	1.0044	0.0122

Sand-mud mixtures (SM – B)

ζ_{cl} [%]	ζ_{si} [%]	ζ_{sa} [%]	ψ_{sasi} [%]	PI^* [%]	W [%]	n_{sasi} [%]	W_{rel} [-]
0.5	2	97.5	98	1	24	39	24.1
1	4	95	96	2	25	40	12.4
1.5	6	92.5	94	3	26	41	8.5
2	8	90	92	4	26	42	6.6
3.5	14	82.5	85	7	29	45	4.1
5	20	75	79	10	32	48	3.2
7	28	65	70	14	36	52	2.6
10	40	50	56	20	43	58	2.2
15	60	25	29	30	59	67	2
20	80	0	0	40	82	75	2.1

ρ_{bulk} [kg·m ⁻³]	$d_{50,m}$ [μm]	$\phi_{s,0}$ [%]	n_{fr} [-]	δ_e [mm]	c_u [Pa]	$m_{v,s}$ [Pa ⁻¹]	$k_v \cdot 10^6$ [m·s ⁻¹]	$c_v \cdot 10^6$ [m ² ·s ⁻¹]	M_s [kg·m ⁻² ·s ⁻¹ ·Pa ⁻¹]
1618	30	61	2.82	0.5	8289	0.0041	100	2.5118	0.0011
1598	30	60	2.79	0.3	590	0.0064	130	1.7505	0.0146
1578	30	59	2.77	0.3	333	0.008	140	1.5249	0.0257
1558	30	58	2.75	0.3	294	0.0093	150	1.5376	0.0311
1498	30	55	2.73	0.2	347	0.0119	100	1.2856	0.0226
1437	30	52	2.71	0.3	450	0.0134	65	0.9877	0.0126
1357	30	48	2.7	0.3	588	0.0143	30	0.7821	0.0067
1237	30	42	2.68	0.3	747	0.0141	17	0.7218	0.0037
1036	30	33	2.66	0.5	819	0.0114	10	0.7134	0.0019
835	30	25	2.65	0.8	673	0.0077	11	0.7933	0.0013

Granular mixtures (GR - A, GR - B, GR - C, GR - D)

ξ_{cl} [%]	ξ_{si} [%]	ξ_{sa} [%]	ψ_{sasi} [%]	PI^* [%]	W [%]	n_{sasi} [%]	W_{rel} [-]
0	100	0	0	0	51	58	0
0	100	0	0	0	40	52	0
0	100	0	0	0	30	45	0
0	70	30	30	0	40	52	0
0	70	30	30	0	30	44	0
0	70	30	30	0	22	36	0
0	40	60	60	0	31	45	0
0	40	60	60	0	23	38	0
0	40	60	60	0	16	30	0
0	0	100	100	0	40	52	0
0	0	100	100	0	31	45	0
0	0	100	100	0	25	40	0

ρ_{bulk} [kg·m ⁻³]	$d_{50,m}$ [μm]	$\phi_{s,0}$ [%]	n_{fr} [-]	δ_e [mm]	c_u [Pa]	$m_{v,s}$ [Pa ⁻¹]	$k_v \cdot 10^6$ [m·s ⁻¹]	$c_v \cdot 10^6$ [m ² ·s ⁻¹]	M_s [kg·m ⁻² ·s ⁻¹ ·Pa ⁻¹]
1124	50	42	0	0.5	3	0.0023	1	0.0452	0.0330
1285	50	48	0	0.3	8	0.005	1	0.0202	0.0134
1470	50	55	0	0.1	19517	0.0116	1	0.0088	0.0000
1285	90	48	0	0.9	3	0.0014	4	0.291	0.1404
1486	90	56	0	0.5	8	0.0033	4	0.1244	0.0521
1686	90	64	0	0.2	4286	0.0079	4	0.0517	0.0001
1445	130	55	0	1.3	3	0.0011	20	1.8577	0.6096
1646	130	62	0	0.7	10	0.0026	20	0.7776	0.1937
1847	130	70	0	0.3	19277	0.0065	20	0.313	0.0001
1285	170	48	0	1.7	4	0.0007	100	13.7435	2.5489
1445	170	55	0	0.9	16	0.0017	100	6.0734	0.6598
1590	170	60	0	0.4	55222	0.0038	100	2.6804	0.0002

SAND-MUD EROSION FROM A SOIL MECHANICAL PERSPECTIVE

Cohesive mixtures (CO – A)

ζ_{cl} [%]	ζ_{si} [%]	ζ_{sa} [%]	ψ_{sasi} [%]	PI^* [%]	W [%]	n_{sasi} [%]	W_{rel} [-]
85	13	2	13	57	118	96	2.1
85	12	3	20	57	87	95	1.5
85	11	4	27	57	66	95	1.2
85	10	5	33	57	51	94	0.9
85	9	6	40	57	40	93	0.7
85	8	7	47	57	31	92	0.6
85	7	8	53	57	25	91	0.4

ρ_{bulk} [kg·m ⁻³]	$d_{50,m}$ [μm]	$\phi_{s,0}$ [%]	n_{fr} [-]	δ_e [mm]	c_u [Pa]	$m_{v,s}$ [Pa ⁻¹]	$k_v \cdot 10^6$ [m·s ⁻¹]	$c_v \cdot 10^6$ [m ² ·s ⁻¹]	$M_s \cdot 10^{-3}$ [kg·m ⁻² ·s ⁻¹ ·Pa ⁻¹]
642	16	4	2.63	0.7	485	0.0099	0.4	0.0812	0.1459
803	15	5	2.63	0.4	1052	0.0214	0.15	0.006	0.0121
964	14	5	2.63	0.2	2100	0.0415	0.04	0.0006	0.0013
1124	13	6	2.63	0.1	3993	0.0753	0.015	0.0001	0.0002
1285	12	7	2.63	0.1	7415	0.1308	0.005	0	0.0000
1445	11	8	2.63	0.1	13705	0.222	0.0015	0	0.0000
1606	10	9	2.63	0	25685	0.3734	0.0006	0	0.0000

Cohesive mixtures (CO – B)

ζ_{cl} [%]	ζ_{si} [%]	ζ_{sa} [%]	ψ_{sasi} [%]	PI^* [%]	W [%]	n_{sasi} [%]	W_{rel} [-]
85	13	2	13	85	118	96	1.4
85	12	3	20	85	87	95	1
85	11	4	27	85	66	95	0.8
85	10	5	33	85	51	94	0.6
85	9	6	40	85	40	93	0.5
85	8	7	47	85	31	92	0.4
85	7	8	53	85	25	91	0.3

ρ_{bulk} [kg·m ⁻³]	$d_{50,m}$ [μm]	$\phi_{s,0}$ [%]	n_{fr} [-]	δ_e [mm]	c_u [Pa]	$m_{v,s}$ [Pa ⁻¹]	$k_v \cdot 10^6$ [m·s ⁻¹]	$c_v \cdot 10^6$ [m ² ·s ⁻¹]	$M_s \cdot 10^{-5}$ [kg·m ⁻² ·s ⁻¹ ·Pa ⁻¹]
642	16	4	2.61	0.6	1319	0.0171	0.022	0.0042	0.3376
803	15	5	2.61	0.3	2863	0.0359	0.0054	0.0003	0.0279
964	14	5	2.61	0.2	5715	0.068	0.0025	0	0.0029
1124	13	6	2.61	0.1	10868	0.121	0.0007	0	0.0004
1285	12	7	2.61	0.1	20180	0.2066	0.0003	0	0.0000
1445	11	8	2.61	0.1	37297	0.3453	0.0001	0	0.0000
1606	10	9	2.61	0	69902	0.5727	0	0	0.0000

Silty mixtures

ζ_{cl} [%]	ζ_{si} [%]	ζ_{sa} [%]	ψ_{sasi} [%]	PI^* [%]	W [%]	n_{sasi} [%]	W_{rel} [-]
5	90	5	6	3.4	75	68	22.5
5	90	5	6	3.4	66	65	19.7
5	90	5	6	3.4	55	61	16.3
5	90	5	6	3.4	43	55	12.7
5	90	5	6	3.4	33	50	10
5	90	5	6	3.4	26	44	7.8

ρ_{bulk} [kg·m ⁻³]	$d_{50,m}$ [μm]	$\phi_{s,0}$ [%]	n_{fr} [-]	δ_e [mm]	c_u [Pa]	$m_{v,s}$ [Pa ⁻¹]	$k_v \cdot 10^6$ [m ² ·s ⁻¹]	$c_v \cdot 10^6$ [m ² ·s ⁻¹]	M_s [kg·m ⁻² ·s ⁻¹ ·Pa ⁻¹]
883	20	32	2.76	2.1	2	0.0007	2	0.2995	0.0661
964	20	35	2.76	1.4	3	0.001	5	0.4929	0.1118
1084	20	39	2.76	0.9	6	0.0018	10	0.5545	0.1193
1245	20	45	2.76	0.5	16	0.0037	30	0.8317	0.1301
1405	20	50	2.76	0.3	80	0.0069	50	0.7363	0.0444
1566	20	56	2.76	0.2	18844	0.0125	80	0.6517	0.0003

Mixtures as applied in the straight flume

ζ_{cl} [%]	ζ_{si} [%]	ζ_{sa} [%]	ψ_{sasi} [%]	PI^* [%]	W [%]	n_{sasi} [%]	W_{rel} [-]
2	8	90	92	1.3	21	37	16.0
5	19	76	80	3.2	20	38	6.3
6	24	70	74	4.0	21	40	5.2
11	45	44	50	7.5	28	49	3.8
16	64	20	24	10.7	39	59	3.6
2	5	93	95	1.3	22	38	16.6
4	10	86	90	2.7	21	39	8.0
7	19	74	80	5.0	23	42	4.5
12	30	58	66	8.0	30	51	3.8
17	42	42	50	11.1	38	59	3.4
3	19	78	80	2.0	17	33	8.2
5	19	76	80	3.2	20	37	6.1
6	19	75	80	4.0	22	41	5.5
7	18	74	80	5.0	23	43	4.7
8	18	74	80	5.4	24	44	4.4
2	49	49	50	1.6	20	37	12.7
5	47	47	50	3.7	23	41	6.2
8	46	46	50	5.7	28	48	5.0
12	41	47	54	7.8	31	52	4.0
16	42	42	50	11.0	37	58	3.3
5	19	76	80	5.0	25	42	4.9
6	24	70	75	6.6	24	42	3.5
11	44	45	50	13.5	37	55	2.7
16	63	21	25	19.7	49	63	2.5

SAND-MUD EROSION FROM A SOIL MECHANICAL PERSPECTIVE

ρ_{bulk} [kg·m ⁻³]	$d_{50,m}$ [μm]	$\phi_{s,0}$ [%]	n_{fr} [-]	δ_e [mm]	c_u [Pa]	$m_{v,s}$ [Pa ⁻¹]	$k_v \cdot 10^6$ [m·s ⁻¹]	$c_v \cdot 10^6$ [m ² ·s ⁻¹]	M_s [kg·m ⁻² ·s ⁻¹ ·Pa ⁻¹]
2053	50	64	2.81	0.5	1007	0.0041	90	2.2124	0.0073
2076	49	65	2.77	0.3	442	0.0088	80	0.9290	0.0120
2059	48	64	2.75	0.3	337	0.0095	70	0.7532	0.0129
1945	47	57	2.73	0.4	279	0.0085	60	0.7191	0.0108
1811	47	49	2.71	0.5	230	0.0059	50	0.8618	0.0092
2039	46	63	2.81	0.5	2875	0.0041	91	2.2463	0.0026
2053	45	64	2.77	0.3	637	0.0075	82	1.1183	0.0091
2033	44	63	2.74	0.3	379	0.0107	65	0.6217	0.0099
1917	43	56	2.72	0.4	240	0.0086	55	0.6506	0.0112
1820	42	50	2.71	0.5	231	0.0071	40	0.5744	0.0071
2148	41	70	2.79	0.2	49655	0.0118	70	0.6031	0.0001
2084	40	66	2.77	0.2	563	0.0112	65	0.5929	0.0076
2042	40	63	2.75	0.3	300	0.0105	60	0.5802	0.0126
2019	39	62	2.74	0.3	303	0.0111	55	0.5049	0.0107
2007	38	61	2.74	0.3	303	0.0114	50	0.4469	0.0094
2073	37	65	2.80	0.3	107	0.0072	60	0.8437	0.0438
2029	36	62	2.76	0.3	184	0.0101	45	0.4552	0.0160
1946	35	57	2.74	0.3	155	0.0091	40	0.4471	0.0148
1899	34	55	2.72	0.3	199	0.0096	35	0.3710	0.0087
1835	33	51	2.71	0.3	256	0.0096	30	0.3172	0.0048
1999	33	61	2.74	0.2	298	0.0120	50	0.4254	0.0099
2017	32	62	2.73	0.2	609	0.0167	40	0.2436	0.0034
1835	31	51	2.70	0.3	464	0.0127	30	0.2400	0.0024
1719	30	44	2.68	0.4	505	0.0106	20	0.1930	0.0011

Mixtures as applied in the annular flume

ζ_{cl} [%]	ζ_{si} [%]	ζ_{sa} [%]	ψ_{sasi} [%]	PI^* [%]	W [%]	n_{sasi} [%]	W_{rel} [-]
2	8	90	92	1.3	27	43	20.8
6	24	70	74	4.0	23	41	5.8
16	64	20	24	10.7	41	59	3.7

ρ_{bulk} [kg·m ⁻³]	$d_{50,m}$ [μm]	$\phi_{s,0}$ [%]	n_{fr} [-]	δ_e [mm]	c_u [Pa]	$m_{v,s}$ [Pa ⁻¹]	$k_v \cdot 10^6$ [m·s ⁻¹]	$c_v \cdot 10^6$ [m ² ·s ⁻¹]	M_s [kg·m ⁻² ·s ⁻¹ ·Pa ⁻¹]
1936	50	57	2.81	0.95	14	0.0019	80	4.406	0.4871
2005	40	61	2.75	0.30	205	0.0085	25	0.301	0.0078
1785	30	48	2.71	0.39	219	0.0080	80	0.102	0.0015

List of symbols

Latin symbols

a_i, A_i	Empirical coefficients	-
A	Activity of a soil	-
A_s	Specific surface of a particle	$\text{m}^2 \cdot \text{g}^{-1}$
A_{ts}	Surface area test section	m^2
b_i, B_i	Empirical coefficients	-
B	Inversed relaxation time scale for floc erosion	s^{-1}
c	Sediment concentration	$\text{kg} \cdot \text{m}^{-3}$
c	Soil strength for zero normal stress in Mohr diagram	Pa
c	Concentration of fines in suspension	$\text{g} \cdot \text{l}^{-1}$
\bar{c}	Depth-averaged suspended fines concentration	$\text{g} \cdot \text{l}^{-1}$
c^*	Deviatoric soil strength for $p = 0$ in CSM	Pa
C	Activity concentration of decaying isotopes	$\text{Bq} \cdot \text{kg}^{-1}$
c_b	Concentration of fines in suspension above the bed	$\text{g} \cdot \text{l}^{-1}$
C_{bulk}	Bulk activity concentration of decaying isotopes	$\text{Bq} \cdot \text{kg}^{-1}$
C_c	Compression index	-
c_d	Drained shear strength	Pa
c_d^*	Drained deviatoric strength for $p = 0$ in CSM	Pa
Chlorophyll-a	Chlorophyll-a content	$\mu\text{g} \cdot \text{g}^{-1}$
C_s	Swelling index	-
c_u	Undrained shear strength	Pa
c_u^*	Undrained deviatoric strength for $p = 0$ in CSM	Pa
$c_{u,ctw}$	Undrained shear strength of clay-water matrix	Pa
c_v	Pore water pressure dissipation coefficient	$\text{m}^2 \cdot \text{s}^{-1}$
$c_{v,s}$	Pore water pressure dissipation coefficient during swell	$\text{m}^2 \cdot \text{s}^{-1}$
d	Grain size	m
D	Deposition rate	$\text{kg} \cdot \text{m}^{-2} \cdot \text{s}^{-1}$
d^*	Dimensionless particle diameter	-
d_i	Grain size of fraction i	m
D_f	Diameter flocs	m
d_m	Mean grain size	m
D_p	Diameter primary particles	m
d_5	Grain size for which 5% smaller by weight	m
d_{10}	Grain size for which 10% is smaller by weight	m
d_{50}	Median grain size for which 50% is smaller by weight	m
$d_{50,m}$	Median grain size of the mud fraction	m
d_{60}	Grain size for which 60% is smaller by weight	m
d_{95}	Grain size for which 95% is smaller by weight	m
e	Void ratio	-

E	Erosion rate	$\text{kg}\cdot\text{m}^{-2}\cdot\text{s}^{-1}$
e_{CSL}	Initial void ratio for soil on CSL	-
E_f	Floc erosion rate	$\text{kg}\cdot\text{m}^{-2}\cdot\text{s}^{-1}$
$E_{f,max}$	Maximum floc erosion rate	$\text{kg}\cdot\text{m}^{-2}\cdot\text{s}^{-1}$
E_m	Mass erosion rate	$\text{kg}\cdot\text{m}^{-2}\cdot\text{s}^{-1}$
E_{mud}	Fines erosion rate	$\text{kg}\cdot\text{m}^{-2}\cdot\text{s}^{-1}$
E_s	Surface erosion rate	$\text{kg}\cdot\text{m}^{-2}\cdot\text{s}^{-1}$
E_{sand}	Sand erosion rate	$\text{kg}\cdot\text{m}^{-2}\cdot\text{s}^{-1}$
e_{SL}	Initial void ratio for soil on SL	-
$E_{s,mud}$	Surface erosion rate for fines	$\text{kg}\cdot\text{m}^{-2}\cdot\text{s}^{-1}$
$E_{s,sand}$	Surface erosion rate for sand	$\text{kg}\cdot\text{m}^{-2}\cdot\text{s}^{-1}$
E_{tr}	Erosion rate threshold	$\text{kg}\cdot\text{m}^{-2}\cdot\text{s}^{-1}$
e_{VCL}	Initial void ratio for soil on VCL	-
E_γ	Energy of γ -rays	eV
e_0	Initial void ratio	-
f_w	Friction factor	-
g	Gravitational acceleration	$\text{m}\cdot\text{s}^{-2}$
G	Shear modulus	Pa
h	Water depth	m
k_s	Nikuradse roughness coefficient	m
k_v	Permeability in vertical direction	$\text{m}\cdot\text{s}^{-1}$
$k_{v,s}$	Permeability in vertical direction during swelling	$\text{m}\cdot\text{s}^{-1}$
k_0	Kozeny-Carman coefficient	-
K_0	Coefficient of earth pressure at rest	-
LI	Liquidity Index	%
LL	Liquid Limit	%
m_v	Coefficient of volume variation	$\text{m}^2\cdot\text{N}^{-1}$
$m_{v,s}$	Coefficient of volume variation during swelling	$\text{m}^2\cdot\text{N}^{-1}$
M	Erosion parameter	$\text{kg}\cdot\text{m}^{-2}\cdot\text{s}^{-1}$
$M_{dry,i}$	Dry mass of fraction i	kg
$M_{dry,tot}$	Total dry mass	kg
M_E	Erosion parameter	$\text{m}\cdot\text{Pa}^{-1}\cdot\text{s}^{-1}$
M_f	Floc erosion parameter	$\text{kg}\cdot\text{m}^{-2}\cdot\text{s}^{-1}$
M_s	Surface erosion parameter	$\text{kg}\cdot\text{m}^{-2}\cdot\text{Pa}^{-1}\cdot\text{s}^{-1}$
M_{sand}	Mass of eroded sand	kg
M_{sed}	Mass of (dry) sediment	kg
$M_{s,mud}$	Surface erosion parameter for fines	$\text{kg}\cdot\text{m}^{-2}\cdot\text{Pa}^{-1}\cdot\text{s}^{-1}$
$M_{s,sand}$	Surface erosion parameter for sand	$\text{kg}\cdot\text{m}^{-2}\cdot\text{Pa}^{-1}\cdot\text{s}^{-1}$
M_w	Mass of water	kg
n	Porosity	-
N	Shape factor	-
n_{fr}	Fractal dimension	-
n_{sasi}	Porosity of a sand-silt skeleton	-
$n_{sasi,max}$	Maximum porosity of a sand-silt skeleton	-
$n_{sasi,min}$	Minimum porosity of a sand-silt skeleton	-
$n_{sa,max}$	Maximum porosity of a 100 sand skeleton	-

$n_{sa,min}$	Minimum porosity of a 100 sand skeleton	-
$n_{si,max}$	Maximum porosity of a 100 silt skeleton	-
$n_{si,min}$	Minimum porosity of a 100 silt skeleton	-
OCR	Over-Consolidation ratio	-
p	Isotropic stress	Pa
p	Cavity pressure	Pa
p_{atm}	Atmospheric pressure	Pa
p_b	Isotropic stress at sediment bed	Pa
p_e	Isotropic stress at onset of erosion	Pa
p_{ew}	Péclet number	-
pH	Pondus Hydrogenii	-
p_{hydr}	Hydrostatic pressure	Pa
p_i	Percentage of fraction i	%
PI	Plasticity Index	%
PI^*	Indirectly derived Plasticity Index	%
p_{K_0}	Isotropic stress at K_0	Pa
PL	Plastic Limit	%
p_w	Pore water pressure	Pa
p_w^u	Undrained pore water pressure	Pa
p_0	Initial cavity pressure	Pa
q	Deviatoric stress	Pa
Q	Discharge	$l \cdot s^{-1}$
Q_d	Darcy discharge	$l \cdot s^{-1}$
$Q_{injection}$	HPS probe injection discharge	$l \cdot s^{-1}$
q_b	Deviatoric stress at sediment bed	Pa
q_b	Bed load transport	$m^2 \cdot s^{-1}$
q_e	Deviatoric stress at onset of erosion	Pa
R	Cavity radius	mm
R_{e_s}	Reynolds number for a flow near a boundary	-
R_0	HPS probe needle radius / initial cavity radius	mm
s	Relative density	-
S	Degree of saturation	-
S	Specific surface area of solids per unit of volume	-
SAR	Sodium Adsorption Ratio	$(meq \cdot l^{-1})^{0.5}$
t	Time	s
T	Turbidity meter output	V
T	Temperature	$^{\circ}C$
T_{RhoC}	Duration MedusRhoC measurement procedure	hr
T_s	Typical time-scale for pore water pressure dissipation	s
T_{trad}	Duration traditional measurement procedure	hr
u_*	Bed shear stress velocity	$m \cdot s^{-1}$
v	Velocity in y-direction	$m \cdot s^{-1}$
w	Velocity in z-direction	$m \cdot s^{-1}$
V	Velocity scale	$m \cdot s^{-1}$
V	Cavity volume	m^3

V_e	Erosion velocity	$m \cdot s^{-1}$
$V_{e,max}$	Maximum erosion velocity	$m \cdot s^{-1}$
V_p	Cavity volume at which plastic yielding occurs	m^3
V_{por}	Pore volume	m^3
V_s	Velocity of swelling front	$m \cdot s^{-1}$
V_{sed}	Solids volume	m^3
V_{tot}	Total volume	m^3
V_w	Volume of water in flume	m^3
V_0	Initial cavity volume	m^3
W	Water content	%
W_{rel}	Relative water content	%
w_s	Settling velocity suspended sediments	$m \cdot s^{-1}$
$w_{s,b}$	Settling velocity suspended sediments above the bed	$m \cdot s^{-1}$
x	Horizontal coordinate, cross-shore	m
z	Vertical coordinate, distance from the bed	m
z_0	Roughness length	m

Greek symbols

α_i	Empirical coefficients	-
β	Empirical coefficient	-
α_c	Consolidation coefficient	-
δ_e	Erosion depth	m
δ_s	Swelling depth	m
Δ	Specific density of sediment	$kg \cdot m^{-3}$
ε	Vertical strain	-
ζ -potential	Double layer potential	V
η	Slope of stress path in p - q plane	-
η_{CS}	Slope of critical state line stress path	-
η_{flow}	Slope of the flow-induced stress path	-
η_w	Dynamic viscosity of water	$kg \cdot m^{-1} s^{-1}$ or Pa·s
θ_{cr}	Critical Shields parameter	-
κ	Von Kármán constant	-
κ	Soil material property for consolidation and swelling	-
λ	Soil material property for compression and dilation	-
λ	Linear concentration	-
v	Specific soil volume	-
ν_t	Turbulent diffusivity of water	$m^2 \cdot s^{-1}$
ν_w	Kinematic viscosity of water	$m^2 \cdot s^{-1}$
ξ_{cl}	Solids content of clay	%
$\xi_{cl,0}$	Critical clay content for cohesive behaviour	%
ξ_i	Solids content of fraction i	%
ξ_{mu}	Solids content of mud	%
$\xi_{mu,0}$	Critical mud content for cohesive behaviour	%
ξ_{om}	Solids content of organic matter	%

ζ_{sa}	Solids content of sand	%
ζ_{si}	Solids content of silt	%
ρ_{bulk}	Bulk density	kg·m ⁻³
ρ_{dry}	Dry density	kg·m ⁻³
ρ_{sed}	Specific density of sediment	kg·m ⁻³
ρ_w	Density of water	kg·m ⁻³
σ	Normal stress	Pa
σ	Effective shear stress in the Mohr diagram	Pa
σ'	Effective stress	Pa
σ_b	Normal stress on a sediment bed	Pa
$\hat{\sigma}_b$	Turbulent fluctuation of the bed normal stress	Pa
$\bar{\sigma}_b$	Mean isotropic bed stress	Pa
σ_d	Standard deviation	-
σ_n	Effective normal stress in the Mohr diagram	Pa
σ_{tot}	Total stress	Pa
σ_v	Normal principal stress in vertical direction	Pa
$\sigma_{1,2,3}$	Principal stresses (in x,y,z direction)	Pa
τ	Shear stress	Pa
τ_b	Bed shear stress	Pa
$\bar{\tau}_b$	Mean bed shear stress	Pa
$\hat{\tau}_b$	Turbulent fluctuation of the bed shear stress	Pa
τ_e	Critical bed shear stress for erosion	Pa
$\bar{\tau}_e$	Mean critical deviatoric bed stress for erosion	Pa
$\hat{\tau}_e$	Turbulent fluctuation of deviatoric critical bed stress	Pa
$\tau_{e,f}$	Critical deviatoric bed stress for floc erosion	Pa
$\tau_{e,m}$	Critical deviatoric bed stress for mass erosion	Pa
$\tau_{e,s}$	Critical deviatoric bed stress for surface erosion	Pa
τ_p	Peak shear strength for the shear vane test	Pa
ϕ	Internal friction angle in Mohr diagram	degrees
ϕ_{cl}	Volume concentration of clay	-
ϕ_f	Volume concentration of flocs	-
ϕ_{max}	Maximum internal friction angle	degrees
ϕ_{mu}	Volume concentration of mud	-
ϕ_{sa}	Volume concentration of sand	-
ϕ_s	Volume concentration sediment	-
ϕ_{sed}	Volume concentration of sediment	-
ϕ_{si}	Volume concentration of silt	-
$\phi_{s,0}$	Volume concentration at onset of swell	-
ψ_{cl}	Solids fraction of clay	%
ψ	Solids fraction of fraction i	%
ψ_{sa}	Solids fraction of sand	%
ψ_{sasi}	Solids fraction of sand and silt	%
ψ_{si}	Solids fraction of silt	%

Acknowledgements

Finally! The last few years have been an incredible experience, both in a professional and personal way. Starting after my MSc graduation I worked the first 4.5 years of my PhD research fulltime at the TU Delft. Getting familiar with research in general, and the topic in particular, was a big challenge. Being able to execute field and laboratory work, visiting conferences in Japan, China, France and Australia, meeting many nice and interesting people, was a privilege.

I wrote a large part of my thesis in my spare time, which was a challenge in itself. Although I can ensure that there are better ways to spend your weekends and late evenings, seeing all the pieces falling together is a satisfactory experience. During these years many colleagues, friends and family supported me, in many different ways. Either being advices on the contents of the research, showing interest or just by being there for me. I am very grateful and privileged for these supports.

First of all I would like to thank Han Winterwerp and Walther van Kesteren, who were my two supervisors. Han, I am grateful you persuaded me to 'do' a PhD after being also my supervisor during my MSc thesis work. You encouraged, corrected and advised me in many ways. Walther, I am impressed by your enormous expertise on a range of difficult topics. In combination with the willingness and patience to help me out, you have been both important and inspiring. I am grateful to my promoter, Huib de Vriend, for giving concise feedback on my thesis and for sharing your insights and knowledge.

My research was part of the STW project DCB 6334: 'Eco-morphology of estuaries and tidal lagoons', which was supported by the Dutch Technology Foundation STW, applied science division of NWO and the Technology program of the Ministry of Economic affairs. STW and Cor de Boer are gratefully acknowledged for their support. Also the members of the STW User Panel are thanked for their time, input and support throughout the project.

The project team also involved a Postdoc. First Maarten van der Vegt and later Bram van Prooijen filled this position. I greatly appreciate working with both, as they allowed me to test new ideas and provided me useful comments and support.

Although most of my thesis work took place in laboratories and offices, the multi-disciplinary character of the overall research project allowed me to participate in a number of interesting field trips in the Westerschelde Estuary. I would, therefore, like to thank the Netherlands Institute of Ecology (NIOO-KNAW) in Yerseke. In particular, I would like to thank Peter Herman, Tjeerd Bouma, Francesc Montserrat and Daphne van der Wal. Your enthusiasm and expertise are greatly appreciated and provided me a much wider view on estuarine sand-mud characteristics and behavior.

During my research, I spent two months at the French institute Ifremer in Brest. It was a privilege to execute part of my research at this famous research institute. The great facilities enabled me to collect an important data set for my thesis. The institute, overlooking the bay of Brest to one side, and the Atlantic, to the other, provided stimulating working conditions. Moreover, people at Ifremer were very helpful and friendly. In particular, I would like to thank Pierre le Hir, Philippe Cann, Philippe

Bassoullet and Ricardo Silva Jacinto, who welcomed, supported and advised me enormously.

The laboratory work at the Faculty of Civil Engineering of the Delft University of Technology was executed at the Laboratories of Fluid Mechanics, Sanitary Engineering and Geotechnology. I would like to thank the staff of these laboratories for their assistance and support and for using their laboratories and facilities.

Two MSc students, Jirat Laksanalamai and Menno Elkema, contributed greatly to the collection and analysis of experimental data presented in this thesis. Both put in a lot of effort and enthusiasm and successfully obtained their MSc degree. Jirat executed the annular flume tests at the Fluid Mechanics Laboratory, which involved handling of large volumes of slurry as well as the execution of detailed measurements. Menno tested the Medusa device, which required many hours in the NIOO laboratory and carrying a heavy backpack during the fieldwork. Thanks guys!

Working together with Medusa Explorations in Groningen was a pleasure. Developing a new measuring device together with Han Limburg, Ronald Koomans and Marco Tijs was interesting and fun. Visiting FC Groningen – Ajax even more!

During the past years, I got to know many people at Deltares. Discussing my work and related topics helped me a lot in the preparation of my thesis. Moreover, Deltares offered me the opportunity to continue working on the HPS probe for 4 months after my time at the TU Delft. I especially thank the people of the Coast and Sea Department as well as of the Physical-Chemical Laboratory for this interesting period.

As a member of the Hydraulic Engineering Section, but 'based' in the Fluid Mechanics Laboratory, I was lucky to be part of two groups of nice colleagues. I would like to thank everyone at both sections. In particular, I would like to thank my fellow-PhD candidates, both at the TU and other universities. Summer school at Texel, visiting conferences combined with holiday trips in Japan and Australia, field work in Zeeland and Normandy, together conducting oral examinations, sailing trip on the Wadden Sea and pizza in the lab made my time as a PhD candidate an unforgettable one. It was great hanging out with all of you, thanks!

Furthermore, I would like to thank my current employer, Boskalis / Hydronamic for the flexibility and support, allowing me to complete my thesis the last two years.

Finally, I would like to thank my family and friends. Support during the past years was ample and diverse, ranging from sincere interest in the research topic, to questions and remarks like 'Still not finished school?'. This support was and still is the most important motivation to obtain my goals and to keep seeing things in the right perspective. Special thanks, of course, to my parents and sister. Above all, Suzanne. Thanks a lot buddy, for your support, patience and love!

Publications

- Jacobs, W., 2004. Modelling the Rhine river plume with Delft3D, M.Sc. Thesis Delft University of Technology.
- Jacobs, W., 2006. Eco-morphology of estuaries and tidal lagoons: Literature review and experiments on sand-mud mixtures. TU report, No. 1-06. Delft University of Technology, faculty of Civil Engineering and Geosciences.
- Jacobs, W. (Ed.), 2006. Proceedings NCK workshop '*Water-bed exchange of cohesive sand-mud mixtures*'.
- Jacobs, W., 2006. Zand-slib mengsels. *Geotechniek*, Vol. 10-4.
- Jacobs, W., 2006. Eco-morphology of estuaries and tidal lagoons: Literature review and experiments on sand-mud mixtures. TU report, No. 1-06. Delft University of Technology, faculty of Civil Engineering and Geosciences.
- Jacobs, W., Van Kesteren, W.G.M. and Winterwerp, J.C., 2007. Permeability and consolidation of sediment mixtures as a function of sand content and clay mineralogy. *International Journal of Sediment Research*, Vol. 22-3, 180-187.
- Jacobs, W., Van Kesteren, W.G.M. and Winterwerp, J.C., 2007. Strength of sediment mixtures as a function of sand content and clay mineralogy. Sediment and Ecohydraulics, Intercohort 2005, Saga, Japan. *Proceedings in Marine Science*, Vol. 9, 91-107. Kusuda, T., Yamanishi, H., Spearman, J. and Gailani, J.Z. (Eds.).
- Jacobs, W. and Van Kesteren, W.G.M., 2009. Hydraulic Strength and Permeability (HPS) probe. A new device to measure in-situ material properties of intertidal sand-mud mixtures. Deltares report.
- Jacobs, W., Eelkema, M., Limburg, H. and Winterwerp, J.C., 2009. A new radiometric instrument for in-situ measurements of physical sediment properties. *Marine and Freshwater Research*, Vol. 60, 727-736.
- Jacobs, W., Cann, P., Le Hir, P. and Van Kesteren, W.G.M., 2010. Erosion threshold of artificial sand-mud mixtures. Intercohort 2007, Brest, France. *Continental Shelf Research*.
- Winterwerp, J.C., van Kesteren, W.G.M., van Prooijen, B., Jacobs, W. A conceptual framework for shear-flow induced erosion of soft cohesive sediment beds. Submitted to *Journal of Geophysical Research – Oceans*.

Curriculum Vitae

Walter Jacobs was born on the 11th of November 1977 in Leidschendam, the Netherlands. Shortly hereafter he moved to Zoetermeer, where he finished primary education. He completed secondary education at the 'Gymnasium Haganum' in Den Haag in 1997. After a year of travelling, he started his Civil Engineering study at the Delft University of Technology in 1998. During his studies he did an internship with Greek contractor Archirodon at the Palm Island Project in Dubai in the United Arab Emirates. In 2004 he graduated at the Section of Environmental Fluid Mechanics on the MSc thesis 'Modelling the Rhine River plume with Delft3D'. In September 2004 he started his PhD research at the Hydraulic Engineering Section of the Delft University of Technology, in cooperation with the Centre for Estuarine and Marine Ecology of the Netherlands Institute of Ecology. The study resulted in the current thesis. Part of the experimental work for this study was executed at the French research institute Ifremer in Brest, France. In 2008/2009 he worked four months as a researcher at the research institute Deltares. Since March 2009 he is employed as a project engineer at the 'Morphology and Marine Environment' discipline of Hydronamic, the engineering department of Royal Boskalis Westminster in Papendrecht.